



A University of Sussex PhD thesis

Available online via Sussex Research Online:

<http://sro.sussex.ac.uk/>

This thesis is protected by copyright which belongs to the author.

This thesis cannot be reproduced or quoted extensively from without first obtaining permission in writing from the Author

The content must not be changed in any way or sold commercially in any format or medium without the formal permission of the Author

When referring to this work, full bibliographic details including the author, title, awarding institution and date of the thesis must be given

Please visit Sussex Research Online for more information and further details



University of Sussex

**Development and Demonstration of a
High Bandwidth, Ultra Sensitive
Trapped Ion Magnetometer**

Ethan Robert Potter

Submitted for the degree of Doctor of Philosophy
Department of Physics, University of Sussex, United Kingdom.
September 2018

Declaration

I hereby declare that this thesis has not been and will not be submitted in whole or in part to another University for the award of any other degree.

Signature:

Ethan Robert Potter

UNIVERSITY OF SUSSEX

ETHAN ROBERT POTTER, DOCTOR OF PHILOSOPHY

DEVELOPMENT AND DEMONSTRATION OF A HIGH BANDWIDTH,
ULTRA SENSITIVE TRAPPED ION MAGNETOMETER

Abstract

This thesis describes an ion trap magnetometer, in which experimental hardware and theory for trapped ion magnetometry has been developed and demonstrated. Quantum magnetometry has been a fast expanding field in recent years due to the plethora of military, medical and security applications. The current quantum magnetometer literature has shown great improvements on the standard magnetometer success metrics such as sensitivity, spacial resolution, frequency tuneability, noise shielding and vector field resolution. Ion trap magnetometry could potentially boast several advantages over some of the better established methods such as, nano-meter spatial resolution, broadband tuneability over radio-frequency (RF) and microwave frequencies, and magnetic field noise shielding and sensitivity improvements through dynamic decoupling methods; all in room temperature environments.

The experimental setup discussed uses a micro-fabricated Paul trap for ion confinement due to the scalability of this technology. The method for sensing that was demonstrated utilises long-wavelength radiation dressed states to extend the coherence time of a single $^{171}\text{Yb}^+$ ion beyond the bare states and to allow for a high level of frequency tuneability. The coherence times measured were $T_2 = 0.645$ s for RF field sensing at 15.616 MHz and $T_2 = 1.153$ s for microwave field sensing at 12.658466 GHz. Sensitivities of $S_B = 125.857 \pm 26.155$ pT/ $\sqrt{\text{Hz}}$ for RF magnetic fields and $S_B = 102.054 \pm 11.046$ pT/ $\sqrt{\text{Hz}}$ for microwave magnetic fields were achieved experimentally.

A novel micro-fabricated Paul trap for trapping multiple ion clusters was developed to improve sensitivity values by increasing the total number of trapped ions. The design confines ions over a two-dimensional surface spanning 0.65×1.00 mm which would also allow for magnetic field gradient measurements.

Efforts have been made to miniaturise certain experimental hardware to further the development of portable trapped ion experiments. For this, a miniaturised RF resonator that could be used for radial confinement of ions within Paul traps has been developed. At the current stage of development it is capable of applying a peak RF voltage of 114.9 V with a Q value of 70 at a resonant frequency of $\Omega/2\pi = 12.65$ MHz.

Acknowledgements

General acknowledgements

I would like to thank my supervisor Prof. Winfried Hensinger for giving me the opportunity to work in the Ion Quantum Technology (IQT) group. Next, I would like to thank Dr. Altaf Nizamani, your relaxed demeanour made working with you a delight, your approach to supervision is second to none, probably because you always felt like my colleague never my superior. Thank to Dr. Seb Weidt for his continued supervision of my project towards the end of my Ph.D., your guidance considering your workload was greatly appreciated in these stressful times. Thanks to the IQT members that started with me, Anton Grounds for cementing my knowledge of electrical engineering to date, Adrian Rodriguez and Weikang Fan for endless entertainment at work during our first year, it's a shame both of you left Sussex so early on. Thanks to my project colleague, Harry Bostock for patiently working with me and learning to use Google as a useful tool. Thank you to the other IQT members Nick Johnson, Zak Romaszko, Foni Le Brun-Ricalens, Dr. Simon Webster, Dr. Joe Randall and Dr. Tomas Navickas; you have all contributed towards creating an enjoyable work environment within the IQT group and I hope that you continue to do so.

I would also like to thank the people external to my group that made my time in Sussex such an enjoyable experience. My house-mates Josh Salonga, Valentina Manzini, Victoria Kovalenko and George Allen, throughout the four years I've been at Sussex I've never felt like I was isolated in a shared house thanks to you guys, you're all good friends. My other Ph.D. buddies Ant Hayes, Oli Winston, Tristan Blackburn, Dan Wigmore and Tyler Alion, if there was ever a group I wish I met in Brighton I'm glad it was you guys. my climbing buddies Zach Payne, Steph Rayner and Callan Jobson, you guys were by far the chilliest reverse mountain surfers.

I would also thank my friends outside of Brighton, Linda Zhang, Tom Corbin and Matt Bryce, I honestly don't know how each of you have so much energy; I'm glad that I've been able to share some pretty great experiences with you guys while visiting each other the last four years and I hope that we continue to do so. My Essex friends Mark Acraman, James Diss, Ben Slater, Frank Street, Bradley Smith and James Schofield, I'm glad that we still get along like we did when we were kids, it's not something a lot of people have and I'll always appreciate that whatever paths we choose, we can always meet up and enjoy each others company.

Finally I would like to thank my parents and other family members, your continued emotional and financial support throughout my Ph.D. and the rest of my education is something that has allowed me to be where I currently am. I have nothing but gratitude for everything you do to make my life easier, I hope that someday I can do the same for you.

Detailed Acknowledgements

Some of the work presented in this thesis could not have been done without contributions from other members of the IQT group.

- Chapter 3, Weikang Fan and Zak Romaszko developed the fabrication process for the dual linear rail chip.
- Chapter 4, Dr. Tomas Navickas developed the laser locking scheme for the 369 nm laser. Anton Grounds developed the Labview program for the laser wavemeter. Dr. Altaf Nizamani developed the Labview program for manipulating the trap DC voltages. Harry Bostock and Dr. Simon Webster modified the Advanced Real-Time Infrastructure for Quantum physics (ARTIQ) programs used for the experimental procedures utilised in this thesis. Dr. David Murgia developed the direct digital synthesiser (DDS) boards used for the microwave and RF emitters and designed the front and back mounting structure for the ion trap. Dr. Altaf Nizamani designed the vacuum system used in this thesis. Harry Bostock assembled the DC filter box, the DC filter box was designed by Dr. Bjoern Lekitsch.
- Chapter 7, Anton Grounds helped with the development of the miniaturised RF resonator.

Publications in preparation

Ultra sensitive, tunable microwave magnetometer using a single ion

E. R. Potter, H. Bostock, A. Nizamani, S. Weidt and W. K. Hensinger

Contents

1	Introduction	1
1.1	Quantum magnetometry	1
1.1.1	Dynamic decoupling (DD)	3
1.2	Alternative approaches to quantum magnetometry	4
1.2.1	Nitrogen-vacancy (NV) centres in diamond	4
1.2.2	Spin exchange relaxation-free (SERF) magnetometer	5
1.2.3	Superconducting quantum interference device (SQUID)	6
1.3	Quantum sensing with trapped ions	7
1.4	Motivation and applications for trapped ion magnetometry	8
1.5	Thesis summary	9
2	Background theory for sensing with trapped ions	11
2.1	Energy level structure of $^{174}\text{Yb}^+$ and $^{171}\text{Yb}^+$	11
2.1.1	Ionisation	11
2.1.2	Doppler cooling	12
2.1.3	$^{171}\text{Yb}^+$ $^2\text{S}_{1/2}$ ground state manifold	14
2.2	Microwave and RF dressed states for sensing AC magnetic fields	16
2.2.1	Trapped ions for AC magnetometry	17
2.2.2	Three level dressed states	20
2.2.3	Microwave dressed states for RF frequency sensing	22
2.2.4	RF dressed states for microwave frequency sensing	25
2.2.5	Dressed state sensitivity limits	28
2.2.6	Multi-ion sensitivity improvements	32
2.3	Rabi oscillation numerical simulations for pulsed signals	32
2.3.1	Considerations for magnetic fields driving a two-level system	33
2.3.2	Numerical simulation method for magnetic field sensing	34
2.3.3	Pulsed signal driving a two-level system	35
3	Ion trapping for magnetometer applications	40
3.1	Electric fields, ion motion and stability in ion traps	40
3.1.1	Pseudopotential approximation and ion secular motion	42
3.1.2	Stability parameters and ion micro-motion	45
3.2	Methods for simulating 2D linear paul traps	48
3.2.1	Basis function technique	48
3.2.2	Analytical method and solution for simple linear chip design	50
3.2.3	Numerical method and solution for simple linear chip design and experimental results with numerical model	55
3.3	Dual rail linear chip for trapped ion magnetometry	60
3.3.1	Dual linear chip geometry optimization	61

3.3.2	Linear trap vs dual rail trap	64
3.3.3	Chip fabrication and design considerations	65
4	Demonstrator device setup	71
4.1	Vacuum system components	71
4.1.1	Ultra-high vacuum system	72
4.1.2	Chip carrier	77
4.1.3	Atomic ovens	79
4.1.4	Assembly, pumping and baking process	81
4.2	Laser setup	82
4.2.1	369 nm laser setup	83
4.2.2	Laser overlap	85
4.3	Trapping voltages	88
4.3.1	RF resonant circuit design and optimization	89
4.3.2	RF voltage capacitive probe	93
4.3.3	Trap DC voltage application	94
4.4	Ion imaging	95
4.5	Coherent manipulation magnetic fields	98
4.5.1	Static B-field coils	98
4.5.2	RF radiation	100
4.5.3	Microwave radiation	102
4.6	Master control setup	103
5	Initial experiments and magnetometer results	105
5.1	Initial trapping and cooling procedure	105
5.1.1	Initial trapping of $^{174}\text{Yb}^+$	105
5.1.2	Micro-motion compensation and secular frequency measurements	106
5.1.3	Initial trapping of $^{171}\text{Yb}^+$	108
5.1.4	Ion saturation limit and confirmation of micro-motion compensation effectiveness	109
5.2	Initial experiments	110
5.2.1	State preparation and detection	110
5.2.2	State detection fidelity	113
5.3	Experimental procedures	116
5.3.1	Frequency scans	116
5.3.2	Rabi oscillations	117
5.3.3	Ramsey T_2^* and T_2 spin-echo coherence time	117
5.4	Bare state experiments	119
5.4.1	Bare state frequency scans and Rabi oscillations	120
5.4.2	Bare state T_2^* and T_2 coherence time measurements	124

5.5	Microwave dressed states experiments	129
5.5.1	Microwave dressed state frequency scans	130
5.5.2	Microwave dressed state Rabi oscillations	131
5.5.3	Microwave dressed state T_2^* and T_2 coherence time measurements	132
5.6	RF dressed states experiments	135
5.6.1	RF dressed state frequency scans	136
5.6.2	RF dressed state Rabi oscillations	137
5.6.3	RF dressed state T_2^* and T_2 coherence time measurements	138
5.7	Dressed state system magnetometer	141
5.7.1	Magnetic field resolution and sensitivity results	141
5.7.2	Magnetometer results and theoretical limits comparison	147
6	Towards a portable ion trap magnetometer technologies	150
6.1	Portable ion trap magnetometer concept	150
6.2	Miniaturised RF resonator circuit	152
6.2.1	miniaturised RF circuit design process	153
6.2.2	Testing of the developed components	161
6.2.3	Improving power efficiency of the portable RF generator	164
6.2.4	Comparison with other portable RF resonator circuit	165
7	Colclusion	166
7.1	Summary	166
7.2	Future work	167
	Bibliography	168
A	Micro-fabricated chip numerical simulation meshes and mask	177
A.1	Numerical simulation meshes	177
A.2	Mask design	179
B	Chip glow	180
C	Workshop CAD designs	183
D	Normalising detection errors	185
D.1	Normalising detection errors conditional probabilities matrix	185
D.2	Normalising detection errors using maximum log-likelihood method	186

List of Figures

1.1	NV center experiment example	5
1.2	SERF experiment example	6
1.3	SQUID experiment example	7
2.4	Neutral ytterbium ionisation energy levels	12
2.5	$^{174}\text{Yb}^+$ Doppler cooling cycle	13
2.6	$^{171}\text{Yb}^+$ Doppler cooling cycle	14
2.7	$^2S_{1/2}$ ground state manifold of $^{171}\text{Yb}^+$	15
2.8	$^2S_{1/2}$ ground state Zeeman shifts	16
2.9	Bloch sphere illustration	19
2.10	Ion population probability function	20
2.11	"V" and "/" dressed state configurations	21
2.12	Microwave dressed states energy level diagram	23
2.13	RF dressed states energy level diagram	26
2.14	Sensitivity and Rabi frequency resolution limit	31
2.15	n ion improvement on sensitivity	32
2.16	Pseudo-random variate histogram for a Gaussian distribution	34
2.17	Rabi oscillations for different signal linewidths	35
2.18	Echo train pulse sequence	36
2.19	Pulsed signal waveform example	37
2.20	Pulsed signal driving a Rabi oscillation for different signal linewidths	38
2.21	Pulsed signal driving a Rabi oscillation for different signal Rabi frequencies	39
3.1	Hyperbolic electrode geometry for a ring trap	41
3.2	Hyperbolic electrode geometry for a linear trap	42
3.3	Pseudo-potential approximation	44
3.4	Ion motion in a harmonic potential	47
3.5	Basis function electrode	49
3.6	Analytical simulation result for a linear Paul trap	51
3.7	Stable and unstable trapping parameters for homogeneously mapped q parameter	54
3.8	Numerical simulation result for a linear Paul trap	56
3.9	Numerical simulation results for a linear Paul trap with DC voltages applied	58
3.10	CCD image of a 9 ion string	60
3.11	Linear electrode geometric factor κ_{RF}	62
3.12	Numerical simulation result for dual linear rail chip	64
3.13	Basic diagram of four major chip fabrication layers	65
3.14	Basic diagram of the chip fabrication layers	68
3.15	Micro-fabrication etching process	69
3.16	Microscope image of fabricated dual rail chip	70

4.1	System information flow diagram of the demonstrator device	71
4.2	Diagram of the vacuum system and internal components	72
4.3	Picture of fully assembled vacuum system	74
4.4	Back PCB for chip carrier	78
4.5	Front PCB for chip carrier	79
4.6	Ytterbium oven flux images	80
4.7	AOM and EOM setup for 369 nm laser	84
4.8	Laser overlap setup	86
4.9	3-axis periscope	88
4.10	Circuit for applying and probing RF voltages to an ion trap.	89
4.11	Resonator can dimensions	91
4.12	VNA port configuration for testing resonant circuit S-parameters	92
4.13	Demonstrator RF resonant circuit S-parameters	93
4.14	Capacitive divider calibration diagram	94
4.15	DC voltage four stage filter	95
4.16	Ion imaging setup	96
4.17	Static B-field coils setup	99
4.18	Induced B-field at the ions position	100
4.19	Circuit diagram for the RF radiation setup.	101
4.20	Experiment front viewport	102
4.21	Circuit diagram for the microwave radiation setup.	103
5.1	Graphical representation of the laser position sweep	106
5.2	$^{171}\text{Yb}^+$ cooling cycle transition polarisation dependencies	109
5.3	Single $^{171}\text{Yb}^+$ ion	110
5.4	State preparation time measurement	111
5.5	Cooling, state preparation and readout procedure	112
5.6	Experiment to prepare the ion in the bright state	113
5.7	State preparation histogram data	115
5.8	Experimental procedure for T_2^* Ramsey experiment	118
5.9	Experimental procedure for T_2 Ramsey experiment	119
5.10	Clock transition frequency scan and Rabi oscillation	121
5.11	1^{st} order sensitive bare state microwave transition frequencies and Rabi oscillations	123
5.12	1^{st} order sensitive bare state RF transition frequencies and Rabi oscillations	124
5.13	Clock transition T_2^* time	125
5.14	Clock transition T_2 time	126
5.15	Bare state microwave transition T_2^* time	128
5.16	Bare state microwave transition T_2 time	129
5.17	State preparation and detection protocol for microwave dressed states . . .	130
5.18	Microwave dressed state RF frequency scan	131

5.19	Microwave dressed state Rabi oscillation	132
5.20	Microwave dressed state T_2^* time	133
5.21	RF dressed state T_2 time	134
5.22	State preparation and detection protocol for RF dressed states	136
5.23	RF dressed state microwave frequency scan	137
5.24	RF dressed state Rabi oscillation	138
5.25	RF dressed state T_2^* time	139
5.26	RF dressed state T_2 time	140
5.27	MW dressed state frequency scan and long Rabi oscillation	142
5.28	RF dressed state frequency scan and long Rabi oscillation	143
5.29	Rabi frequency resolution $\delta\Omega'_S$ for RF field sensing	144
5.30	Rabi frequency resolution $\delta\Omega'_S$ for microwave field sensing	145
5.31	RF field sensing sensitivity graph	146
5.32	Microwave field sensing sensitivity graph	147
6.1	Concept for a portable ion trap magnetometer. Predicted total dimensions are $30 \times 20 \times 20$ cm.	151
6.2	An illustration of the portable RF device test circuit	152
6.3	Virtual ground and DC voltage supply circuit for portable RF resonator	154
6.4	Miniaturised resonator circuit	156
6.5	S-parameters for large toroid auto-transformer	157
6.6	S-parameters for small toroid auto-transformer with 19 turns	158
6.7	S-parameters for small toroid auto-transformer with 29 turns	159
6.8	Miniaturised resonator gain vs input voltage	161
6.9	Miniaturised resonator test circuit	162
6.10	Miniaturised resonator test circuit gain vs input voltage	163
6.11	Miniaturised resonator power consumption	164
A.1	Dual linear rail chip CAD file	177
A.2	Linear rail chip CAD file	178
A.3	Dual Linear CAD design used for photo-lithography mask, chip design is 8×10 mm total size.	179
B.4	CCD camera image of the dual linear chip glowing with $V_{RF} = 200$ V applied at a trapping frequency of $\Omega/2\pi = 18.5$ MHz.	180
B.5	Dual linear chip electrodes outside the vacuum system after the glowing shown in Fig. B.4.	181
B.6	Entire dual linear chip electrodes outside the vacuum system after the glow- ing shown in Fig. B.4 had occurred.	182
C.7	Single coil housing (Sec. 4.5.1) structure dimensions, units are in mm.	184

List of Tables

2.1	Ionisation and Doppler cooling wavelengths	12
3.1	Analytical and numerical simulation results for a linear Paul trap	56
3.2	Numerical simulation results for linear Paul trap with DC voltages applied	58
3.3	Dual rail chip numerical simulation results.	63
3.4	Dual rail chip and linear chip numerical simulation results.	64
4.1	Collimated laser beam diameters at beam overlap	88
5.1	Measured and theoretical results for RF and microwave field sensing using a single trapped ion	148
5.2	State of the art magnetometer comparison	148
6.1	Voltage gain data for large toroid auto-transformer	158
6.2	Voltage gain data for small toroid auto-transformer	159

1 Introduction

Metrology is the science of measurement, at its core it is the fundamental way in which we can quantify everything around us. In the recent few centuries standardised systems have been put in place to give a universal reference point for any type of measurement. There are two major branches of metrology, fundamental metrology, which is the field concerned with the establishment of the units of measurement; and applied metrology, which is concerned with the precision in which a measurement can be made. A large amount of industries are interested in applied metrology as progress in this field over the last century has been a fundamental tool for enabling continued human innovation.

In the last few decades there has been an increase of interest in quantum technologies, due to the numerous advantages they possess over their classical counterparts. This has been seen in the form of quantum clocks, quantum sensors, quantum simulators and quantum computers [1, 2]. The contents of this thesis falls into the quantum sensors category, which can be sub categorised into inertial, magnetic and electric field sensors. Due to the nature of the method used for sensing in this thesis, the trapped ion sensor measures the magnetic component of electro-magnetic fields, making it a magnetic field sensor.

Quantum magnetic field sensors, also known as quantum magnetometers, aren't inherently better than their classical counterparts. Depending on the application a classical sensor may be better suited to a specific task. Though with the current development of classical magnetometers being many decades ahead of quantum magnetometers, the true extent of classical magnetometers may be close to realisation, comparatively quantum magnetometers are still in their infancy. One advantage for quantum sensing is the potential to surpass the shot-noise limit of classical sensors through quantum entanglement [3, 4, 5]. Though there are many other advantages that quantum magnetometers may have over classical sensors, not only is there potential for improved sensitivity, but also vast improvements of spatial resolution, frequency tuneability and non-obstructive magnetic field noise shielding. Classical systems are typically limited when it comes to improving these characteristics due to issues determining the difference between noise and the desired signal to be sensed. Also, there are limitations on frequency tuneability and spatial resolution due to the systems being constrained to macroscopic sized structures that determine their pickup frequency and spatial resolution.

1.1 Quantum magnetometry

Quantum magnetometers implement a wide range of methods for sensing magnetic fields, the true extent of which is too detailed for the context of this section. Quantum magnetometers typically exploit some quantum effect to make a system sensitive to magnetic fields of a certain frequency. The best known methods implement magnetic field sensitive Zeeman states into the measurement scheme or solid-state circuits. Standard metrics used

to quantify the capabilities of a quantum magnetometer are as follows:

- Sensitivity
- Frequency tuneability
- Spatial resolution
- Vector field sensing
- Noise shielding

There are other elements like scalability and cost, but these normally only come into play as secondary concerns for industries. Sensitivity is a measurement of how fast the sensor can discern a magnetic field strength and is normally in units of $T/\sqrt{\text{Hz}}$. The frequency tuneability is the magnetometers capacity for detecting a range of frequencies. The spatial resolution is typically the volume of space in which the detector is occupying, it is what defines the resolution in which a magnetometer can determine a magnetic field gradient. Vector field sensing is used to determine the direction in which the magnetic field is coming from, this is generally quite difficult to attain and in the current literature comes at the expense of some other characteristics. Magnetic field noise is a problem for a lot of magnetometers, standard shielding mechanisms require large Faraday cages around the detector and emitter, which is quite impractical for a lot of applications. A way to circumnavigate this for some quantum magnetometers is to implement a dynamic decoupling scheme.

The need for improved sensitivity is homogeneous across all applications as it is the metric used for evaluating how much information about a magnetic field can be gathered in a period of time. This is important for industry, military and biomedical application as speed and detail are important for almost any application whether it be evaluating the properties of a piece of circuitry, detecting a magnetic anomaly such as a bomb or missile, or determining the properties of malignant tissue.

Though most sensors tend to trade frequency tunability for high sensitivity, having a wide range of frequencies that can be sensed can be greatly beneficial for the end user of such a device. The analogy for this trade off could be "master of one" vs "jack of all trades". If the end user requires multiple specialised sensors then it's likely to come with a high production cost, if the sensitivity is not of as much concern for the purpose then a sensor with better frequency tunability would be preferable.

The need for quality spatial resolution is highly dependent on the application. Having nm spatial resolution can only really offer benefits when measurements of similar sized objects is required.

Vector field sensing is likely a more application specific need than spatial resolution. Only if the application requires vector field sensing then this is off benefit. There is also

typically a dramatic reduction in sensitivity on vector field sensors due to the speed of acquisition having to be very short.

Noise shielding is also somewhat application specific but is typically offers a benefit for more applications than spatial resolution and vector field sensing, especially regarding military applications. When the environment of the sensor and target can be controlled, then noise shielding is typically passive like a Faraday cage. When the environment cannot be controlled then active noise shielding (such as dynamic decoupling described in 1.1.1) boasts a significant benefit.

1.1.1 Dynamic decoupling (DD)

A persistent problem with a lot of magnetometers is the separating desired field to be sensed from background noise. State of the art magnetometers usually have a mechanism that allows the sensor to be decoupled from the environment, quantum systems like ours often rely on fast pulses or continuous fields to dynamically decouple a quantum two-level system from it's environment. Dynamic decoupling (DD) works to reduce a large amount of unwanted electromagnetic frequencies that a quantum state might otherwise be sensitive to, it also decreases the rate at which a quantum state would recess back to a single atomic state. The most dominant source of decoherence is from low frequency magnetic field fluctuations constantly moving changing the transition energies between the bare atomic states being driven. The best metric for gauging the effectiveness of DD is the T_2 time, the value of T_2 tells us how long we can keep a two-level system in a quantum superposition before it recesses back to a single atomic state. Increasing the T_2 time is the dominant priority when trying to increase the sensitivity of a quantum magnetometer, this is because the larger the T_2 time, the longer a sensor can remain sensitive to the frequency field of interest, making it possible to detect smaller changes in magnetic field strength; this is described in greater detail in Sec. 2.2.

A standard form of DD is to use pulse sequences to cancel out unwanted noise and increase sensitivity, this is not the form of DD we use, but it is worth mentioning as it has achieved impressive sensitivities at lower frequencies. Using this form of DD for measuring high frequencies at high sensitivities requires a high pulse rate with high amplitudes [6, 7, 8]. This form of DD on a single Sr^+ ion has demonstrated scalar magnetic field sensitivities of $15 \text{ pT}/\sqrt{\text{Hz}}$ at a frequency of 312.5 Hz [9], this lock-in method requires the signal field to be resonant with the pulse rate of the decoupling field (pulsed DD). Higher frequencys up to 220 kHz have also been measured by using pulsed DD on NV centers, with sensitivities around $10 \text{ nT}/\sqrt{\text{Hz}}$ [8]. Sensitivities for such protocols typically fall off for larger frequency signals though, as faster pulse rates normally cause a decrease in pulse amplitude stability, meaning that a different protocol is required if high sensitivities at microwave frequencies are desired. Another method for selecting the desired signal to be sensed is by matching the Rabi frequency to that of the signal being sensed [10, 11]; again, this method is limited

to sensing lower frequencies as the rate you can induce Rabi oscillations is the limiting factor.

1.2 Alternative approaches to quantum magnetometry

To provide context for the trapped ion magnetometer outlined in this thesis, this section gives a brief overview of three alternative methods for quantum sensing, highlighting their advantages, disadvantages and current literature milestones.

1.2.1 Nitrogen-vacancy (NV) centres in diamond

NV centers in diamond arise due to impurities in diamond structures, a single nitrogen in place of a carbon atom creates a vacancy site which forms a spin $S = 1$ pair of electrons with one of the vacancy electrons from the carbon atoms. The Zeeman sub-levels of this spin state are utilized to detect microwave magnetic fields around the energy splitting of the $S = 0$, $S = 1$ transitions, though static magnetic fields are normally used to lift the degeneracy of the hyperfine states to allow for some degree of tuneability [12, 13]. Different frequency regimes ranging from kHz [14, 8] to MHz [7, 15, 11, 16] have also been detected by implementation of multi-pulse dynamic decoupling techniques.

NV centres are probably the most popular system used today for quantum magnetometry, this is likely due to the simplicity of the device. It boasts many benefits over other quantum magnetometers such as it being easy to operate in ambient conditions [7]. It's a highly scalable technology and comparatively cheap to other quantum magnetometers making it preferable for a lot of applications. NV centers have demonstrated scalar magnetic field sensing at microwave frequencies around 2.88 GHz with sensitivities of around ≈ 10 nT/ $\sqrt{\text{Hz}}$ [12], vector magnetometry has also been demonstrated in this frequency regime with a sensitivity of ≈ 1 $\mu\text{T}/\sqrt{\text{Hz}}$ [13]. There has been an increase in versatility through multi-pulse locking techniques where frequencies as low as a few kHz to a few MHz have been detected with sensitivities of ≈ 0.5 $\mu\text{T}/\sqrt{\text{Hz}}$ [14, 15, 11] to ≈ 10 nT/ $\sqrt{\text{Hz}}$ [8, 16]. Theoretical predictions for a fully optimised multi-pulse sequence used for extending the T_2 time of NV centers and improving the sensitivity have given values as high as ≈ 5 pT/ $\sqrt{\text{Hz}}$ [6]. One final advantage is the nano-meter scale spatial resolution that is achievable through using NV centers for magnetic field sensing [17].

The disadvantages of using NV centers typically come in the form of a ridged range of applications for each experiment due to the amount of customization that is required to change the range of frequencies the detector is sensitive to. Comparatively, other quantum magnetometers typically boast a higher sensitivity and NV centers typically have a trade off between spatial resolution and sensitivity [6]. Also, the T_2 coherence time of such devices is typically small, with maximum values typically of the order of a few milli-seconds [15, 6, 8] meaning that the absolute magnetic field amplitude measurements of such devices will be limited. This is due to the quantum states created being subjected

to larger amounts of noise from the neighbouring atoms. There are also some major limitations of the sensitivity of the pulsed dynamic decoupling techniques implemented for kHz to MHz sensing as the sensitivity sharply falls off for higher frequencies [8, 11].

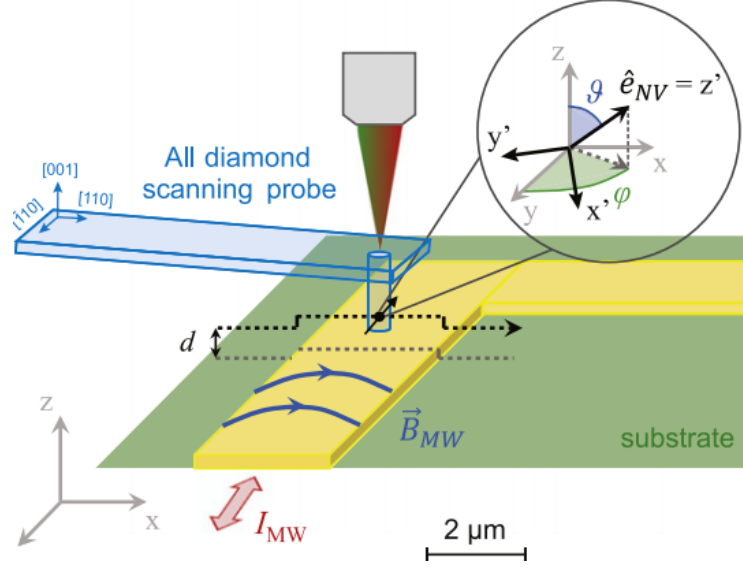


Fig. 1.1 Example of a NV center experiment. Credit goes to [12]

1.2.2 Spin exchange relaxation-free (SERF) magnetometer

SERF magnetometers, typically operate by trapping an Alkali-metal vapour by optically pumping the atoms using circularly polarised light. From this a static magnetic field aligned along the axis of the pump laser lifts the degeneracy of the atoms Zeeman states and align the spin of the atoms along the axis of the laser. This allows an orthogonal AC magnetic field to drive the Zeeman sub-levels to a state where the spin is no longer aligned along the axis of the pump laser, this reduces the total fluorescence which allows for the detection of the AC magnetic field [18].

SERF magnetometers are probably the most sensitive room temperature magnetometer in development, with sub-fT/ $\sqrt{\text{Hz}}$ sensitivities achieved for AC fields ranging from Hz [19, 20] to kHz [21, 18, 22] frequencies. By applying very large static magnetic fields, GHz frequencies have been detected [23] but with limited sensitivity only reaching $\mu\text{T}/\sqrt{\text{Hz}}$. Though this method boasts a broad frequency tuneability, this also highlights the frequency-sensitivity trade off for these types of magnetometers. Due to the nature of the detection scheme of SERFs, real time data acquisition can be utilized to perform vector field tracking by implementation of Faraday rotation probing [24, 25]. Vector field magnetometry using SERFs has demonstrated sub-nT/ $\sqrt{\text{Hz}}$ sensitivity at $50 \mu\text{m}$ spatial resolution [25].

Though SERF magnetometers can be operated at room temperature, they typically require shielding from ambient magnetic field fluctuations [26, 19, 22, 20, 18], due to the reliance on magnetic field sensitive hyperfine states. There is also a negative correlation

between spatial resolution and sensitivity, this is because increasing the number of atoms in the vapour increases sensitivity but also increases the space in which it is occupying. The sensitivities mentioned above are typically for spatial resolutions of the order of mm^3 to cm^3 .

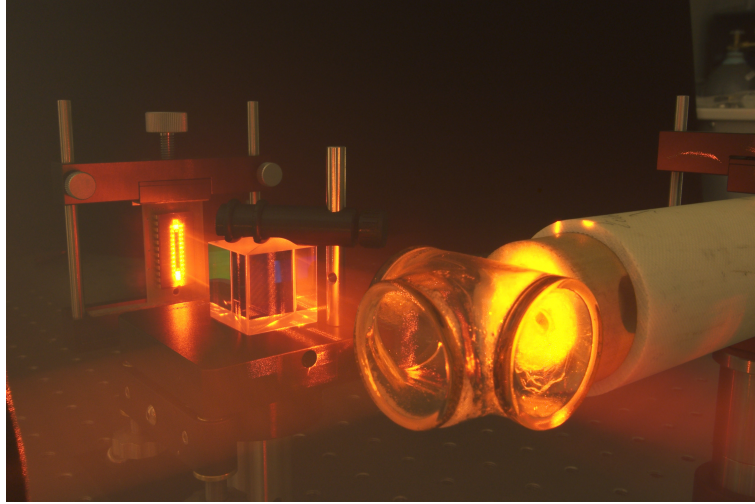


Fig. 1.2 Example of a SERF experiment. Credit goes to [27]

1.2.3 Superconducting quantum interference device (SQUID)

SQUID magnetometers are a superconducting circuit comprised of one or two Josephson junctions depending on whether the design utilises the AC or DC Josephson effect respectively. Unlike the Zeeman state based quantum magnetometers described above, this type of sensor utilises circuitry properties to achieve ultra-sensitive results. For DC SQUIDs [28] a magnetic field flux through the circuit induces a current on the circuit, as soon as the current passes a certain threshold a voltage across the junction is created, this is used to measure the magnetic field inducing the voltage. For AC SQUIDs [29] a single Josephson junction is part of a resonant circuit, as the magnetic flux through the junction changes so does the inductance of the junction and thus, the resonant frequency of the device. This can be measured to detect the magnetic field across the junction. AC SQUIDs typically have a lower sensitivity than DC SQUIDs, but offer a cheaper and simpler solution.

SQUID magnetometers are among the most sensitive quantum magnetometers currently being developed, with $\text{sub-fT}/\sqrt{\text{Hz}}$ sensitivities achieved [30]. They are typically used to detect frequencies ranging from a few kHz [30] to MHz [31]. With improvements in sensitivity stagnating over time for SQUID magnetometers, the demand for novel methods of sensing magnetic fields is being explored. An interesting proof of principle SQUID device for absolute magnetic field vector magnetometry has been demonstrated in [32] without the need for shielding.

Though SQUIDs boast a high sensitivity, this comes at a large cost. The requirement for cryogenics limits the portability of such devices, limiting the total amount applications. The spatial resolution is normally macroscopic as well and can only be reduced by reducing

the size of the Josephson junctions, and high RF or microwave frequency magnetometry has currently not been demonstrated with such devices.

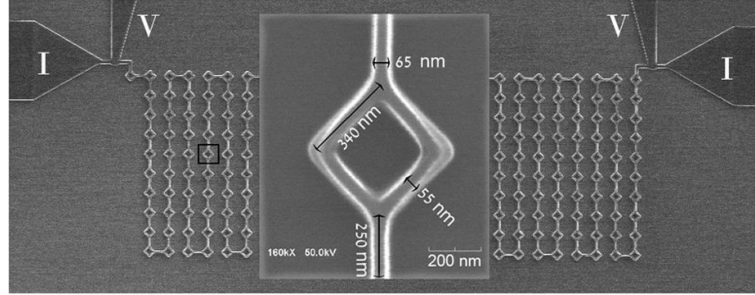


Fig. 1.3 Example of a SQUID experiment. Credit goes to [33]

1.3 Quantum sensing with trapped ions

This section is an introduction to the method in which the trapped ion magnetometer operates, current publications for trapped ion magnetometry, direct comparisons between trapped ion and other quantum magnetometers mentioned in the previous section, and potential improvements that could be made for the current literature on trapped ion magnetometers.

The sensing scheme outlined in this thesis utilizes the ground state hyperfine structure of the $^{171}\text{Yb}^+$ isotope to sense RF (MHz) and microwave (GHz) frequency fields. Here we implement a form of DD that utilises dressed atomic states via continuous application of on resonant, amplitude stable electromagnetic fields to bare atomic states. By using microwave dressed states in this manner, a scalar magnetic field sensitivity of $4.6 \text{ pT}/\sqrt{\text{Hz}}$ at a frequency of 14 MHz has been demonstrated in [34] with $^{171}\text{Yb}^+$ ions. This scheme can be altered by application of RF dressing fields to the ground state hyperfine structure of $^{171}\text{Yb}^+$ to sense microwave magnetic fields with similar sensitivities, as described in this thesis. Lower frequency magnetometry in the kHz range has also been performed by implementing a quantum analogue to a classical lock-in amplifier. This was demonstrated using Sr^+ ions with sensitivities of $15 \text{ pT}/\sqrt{\text{Hz}}$ demonstrated. [9].

Trapped ions typically fall in the middle of the quantum magnetometer spectrum in terms of sensitivity, typically attaining $\text{pT}/\sqrt{\text{Hz}}$ sensitivities. They tend to operate best in the low MHz frequency range, but can be easily tuned to higher MHz frequencies without too much of a loss in sensitivity due to their very large dressed state T_2 times. The T_2 coherence times are typically around three to four orders of magnitude larger than NV centers and two to three orders of magnitude larger than SERFs. Tunable GHz sensing can also be performed at $\text{pT}/\sqrt{\text{Hz}}$ sensitivities due to the novel dressed state scheme outlined in this thesis, making their sensitivity the highest achieved for this range of microwave frequencies. They also have nano-meter spatial resolution that rivals NV centers, the only limit to this being the ions secular motion within the trap. Unlike the most sensitive magnetometers, SQUIDs and SERFs, there is little need for shielding as

the DD scheme implemented shields the ion from small, slowly fluctuating magnetic fields. The Rabi frequency of the driving fields dictates what magnetic field noise the trapped ion magnetometer is sensitive to, meaning that there is some control over this value and it is typically of the order of 10s of kHz.

When compared to SQUIDs or SERFs, a short coming of a trapped ion magnetometer is its sensitivity, though it is typically a few orders of magnitude more sensitive than NV centers, it will likely remain a few orders of magnitude lower than SERF and SQUID magnetometers, even in a multi-ion ion case (s. 2.2.6). Its capacity to maintain $\text{pT}/\sqrt{\text{Hz}}$ sensitivities at a wide range of frequencies is something that other quantum magnetometer types cannot boast, making it by far the most sensitive quantum magnetometer for high MHz and GHz frequencies as demonstrated in Sec. 5.7. It can boast better spatial resolution than SQUIDs and SERFs, but NV centers are quite competitive in this metric. NV centers typically have a similar spatial resolution, but they also typically have lower sensitivity. Though all table top sized quantum magnetometers face difficulties in scalability, it may be harder for trapped ion magnetometers, this is because trapped ion experiments typically require a larger number of lasers and trapping voltages, higher resolution camera detection optics, and very low vacuum pressures.

So far only scalar magnetometry with single ions has been demonstrated within this thesis and other literature. As it currently stands, the main advantages trapped ions have over other quantum magnetometers is higher sensitivities at higher frequencies, and smaller spatial resolution. Potential improvements on the sensitivity can be made by increasing the number of trapped ions as the sensitivity scales as $1/\sqrt{n_i}$ (n_i = number of ions). This would consist of simultaneous scalar magnetic field measurements performed at multiple ion positions on an ion trap. Vector field magnetometry could also be performed as the two-level systems used for sensing magnetic fields in trapped ions are polarisation dependent. This means measurements of a field at different principal axis rotations (Sec 3.2.2) would result in different in different coupling strengths which could be used to give information about the direction of the magnetic field; a similar procedure was implemented for NV centers in [13].

1.4 Motivation and applications for trapped ion magnetometry

Pushing the limits of magnetometry is a prevalent focal point in research due to it's wide range of applications in military and medical industries which inevitably has a significant effect on the technologies we commonly use today. Microwave sensors have significant applications in magnetic anomaly and biomedical imaging. Whether for applications in security, like the microwave full body scanners currently being used as a non-invasive means of detection for metallic objects on a person [35]; or for biomedical imaging, like the malignant tissue imagers currently being developed for the next generation of diagnostic technologies [36]. Nuclear magnetic resonance (NMR) and nuclear quadrupole resonance

(NQR) imaging may also be feasible with the methods outlined in this thesis.

The current limitations for classical sensors are primarily regarding the trade off with sensitivity, spatial resolution and frequency tunability. The common issue with classical sensors is that the frequency to be sensed is constrained by the geometry of the sensor head as it is required to be of a similar size to the wavelength of the field being sensed. By proxy this limits the spatial resolution of the sensor and means that the sensitivity is limited by the geometrical precision in which the sensor is constructed. They are also limited when it comes to improving sensitivity due to issues determining the difference between noise and the desired signal to be sensed. This can be represented numerically by determining the Q value of resonant circuit used as the sensor.

In this thesis I propose a novel method for a sensitive and tunable RF and microwave magnetic field sensor based on the use of a single ion confined to a nano-meter sized region of space. The capabilities of the sensor rivals currently quantum based microwave magnetic field sensors and doesn't require cryogenic cooling or shielding. Further development of this technique has the potential to sense vector magnetic fields with nano-meter spatial resolution. There is also potential for a low power portable device, along with further improvements on the sensitivity and tuneability numbers quoted within this thesis.

1.5 Thesis summary

This thesis is structured as follows. Chapter 2 outlines the theoretical knowledge required for an understanding of the energy structure of the Ytterbium ion species used, how they are manipulated using lasers and long wavelength to perform quantum magnetometry within the context of this thesis, and how to numerically simulate such quantum models for novel applications.

Chapter 3 outlines the theory behind trapping ions by using Paul traps, how the ideal trap geometries can be manipulated to create 2D surface ion traps and how this can be optimised for sensing using trapped ions, and a micro-fabrication process currently utilises for creating such traps.

Chapter 4 outlines the development of the experimental setup that was built within the time frame of this thesis and later used to demonstrate trapped ion magnetometry. It contains information about all of the devices required for ion traps in general and how to construct such devices for ion trap experiments.

Chapter 5 outlines the initial experiment procedures utilised to trap ions within a short time frame, the initial experiments required to characterise the system and the novel results attained for a single trapped ion magnetometer. The novel results are based on the theory outlined in Chapter 2 and utilised RF and microwave dressed states to sense magnetic fields with high sensitivity.

Finally, chapter 7 outlines the concept of a portable trapped ion magnetometer and a novel, portable RF resonator design, potentially used for trapping ions in the portable

device. The work in this chapter can be expanded upon for certain applications where a portable or miniaturised device is required.

2 Background theory for sensing with trapped ions

This chapter will focus on the energy structure of Ytterbium ions and how they can be manipulated to become a trapped ion magnetometer. This information is essential for understanding the potentially vast applications for sensing magnetic fields using trapped ions as described in Sec. 1.4.

2.1 Energy level structure of $^{174}\text{Yb}^+$ and $^{171}\text{Yb}^+$

Though various ion species can be used for quantum magnetometry, all with inherent advantages and disadvantages, this section will describe the energy structure of $^{171}\text{Yb}^+$, used for quantum magnetometry, and $^{174}\text{Yb}^+$, used for optimizing trapping parameters. ^{171}Yb is one of seven naturally occurring stable isotopes of ytterbium, it is the only isotope with a nuclear spin of $1/2$. The non-zero nuclear spin means that the ion has a hyperfine structure that can be utilized for quantum magnetometry due to its sensitivity to magnetic fields. The low nuclear spin of $1/2$ means that the hyperfine structure is relatively simple to coherently manipulate when compared to large nuclear spin isotopes or ion species. $^{174}\text{Yb}^+$ is used for optimizing initial trapping parameters due to its zero nuclear spin giving it a simple energy structure that makes it far easier to trap when optimized trapping parameters that haven't been established (see Sec. 5.1).

2.1.1 Ionisation

To load our trap with ions, a neutral atomic flux is created via resistive heating of an atomic oven close to the ion trap (see Sec. 4.1.3). There are two atomic ovens, one containing a sample of natural ytterbium with a naturally occurring abundance of each isotope¹, the other contains a sample of enriched ytterbium which is $> 95\%$ ^{171}Yb . When heated, the atomic ovens produce a flux of ytterbium that is directed over the surface of the ion trap. They are then ionised via a two photon ionisation process involving two optical transitions as shown in Fig. 2.4. For the purpose of this experiment, the wavelength of a photon is calculated as the wavelength in a vacuum $\lambda = c/f$ where λ is the wavelength, c is the speed of light in a vacuum and f is the frequency.

The 399 nm wavelength is isotope dependent as are the other transitions later utilized for Doppler cooling. The 399 nm ionisation wavelength is also dependent on the orientation of the ovens to the laser, this is because there is a Doppler shift in the required wavelength due to the motion of the neutral ions being ejected from the oven. For the system described in Sec. 4 the atomic ovens are 90° to the laser. The Doppler shift on the ionisation wavelength can be calculated from [37]. A table of measured wavelengths for all the transitions utilized for $^{171}\text{Yb}^+$ and $^{174}\text{Yb}^+$ experiments can be seen in Table 2.1.

To ionise the neutral atomic flux, the ytterbium atoms are excited from their 1S_0

¹14.3% ^{171}Yb , 31.8% ^{174}Yb , 53.9% other.

ground state to the 1P_1 state via the 399 nm laser. The electron in the 1P_1 state can then be ejected into the continuum via a laser near 394 nm, for this process the 369 nm laser used for Doppler cooling is used. This is shown in Fig. 2.4.

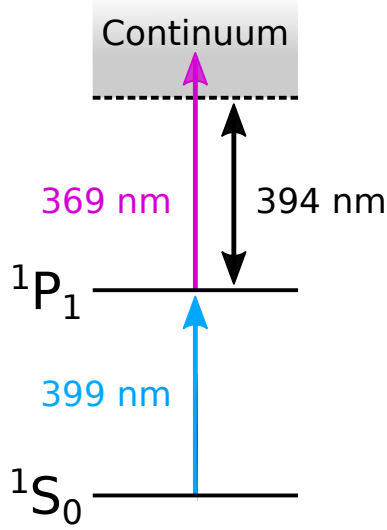


Fig. 2.4 Energy level diagram of the relevant levels in neutral ytterbium, showing the transitions required for two photon ionisation.

Isotope	$^1S_0 \leftrightarrow ^1P_1$ wavelength (nm)	$^2S_{1/2} \leftrightarrow ^1P_{1/2}$ wavelength (nm)	$^2D_{3/2} \leftrightarrow ^3[3/2]_{1/2}$ wavelength (nm)
^{174}Yb	398.91127	369.52504	935.17976
^{171}Yb	399.91067	369.52604 + AOM	935.18768

Table 2.1 All the wavelengths used in $^{174}\text{Yb}^+$ and $^{171}\text{Yb}^+$ experiments on the demonstrator system in this thesis. AOM (acousto optical modulator) represents the frequency shift induced on the 369 nm wavelength from the AOM described in Sec. 4.2.1.

2.1.2 Doppler cooling

Doppler cooling an ion works by removing momentum from the ion. If an incident laser is slightly detuned below the frequency of a transition in the ion, the ion will absorb more photons if it moves towards the laser source. Once excited the ion will emit a photon in a random direction, because the initial momentum change was in one specific direction and the subsequent was random, the overall momentum, thus speed, thus kinetic energy and temperature of the ion is reduced.

A closed Doppler cooling cycle can be formed using three lasers and one microwave field for $^{171}\text{Yb}^+$ and only three lasers for $^{174}\text{Yb}^+$, a figure of the transitions utilized in both cases can be seen in Figures 2.5 and 2.6. The main Doppler cooling cycle is the $^2S_{1/2} \leftrightarrow ^2P_{1/2}$ transition being driven by the 369 nm laser, population in $^2P_{1/2}$ decays

back to $^2S_{1/2}$ with a natural linewidth of $\Gamma/2\pi = 19.6$ MHz. In the case of $^{171}\text{Yb}^+$, off-resonant transitions sometimes populate the $^2P_{1/2} |F = 1\rangle$ state causing a decay into the $^2S_{1/2} |F = 0\rangle$ state. To avoid this an additional microwave field is required to drive the $^2S_{1/2} |F = 0\rangle \leftrightarrow ^2S_{1/2} |F = 1\rangle$ hyperfine transition near 12.6428121 GHz [38] to keep the ion in the cooling cycle. In 0.5% of cases the population in $^2P_{1/2}$ decays to $^2D_{3/2}$, from here it can be excited into the $^3[3/2]_{1/2}$ state via a laser near 935 nm, from where it can decay back into the $^2S_{1/2}$ state, closing the cooling cycle. In the case of $^{171}\text{Yb}^+$, additional laser power is recommended so that power broadening of all the hyperfine transitions in $^2D_{3/2} \leftrightarrow ^3[3/2]_{1/2}$ are driven. Occasionally a collision with background gas will cause population in the $^2D_{3/2}$ state to transition to the $^2D_{5/2}$ state, from which it can decay to the $^2F_{7/2}$ state. An additional laser near 638 nm can be used to transfer population from $^2F_{7/2}$ to $^1[5/2]_{5/2}$, from which it can decay back to either $^2D_{3/2}$ or $^2D_{5/2}$, this transition is very unlikely and it is not necessary to have a 638 nm laser to perform sensing experiments as this transition occurs approximately once per day. Due to time constraints a 638 nm laser was not introduced on the system described in this thesis but will be implemented in the future. Closed cooling cycles for $^{174}\text{Yb}^+$ and $^{171}\text{Yb}^+$ are shown in Fig. 2.5 and 2.6 respectively.

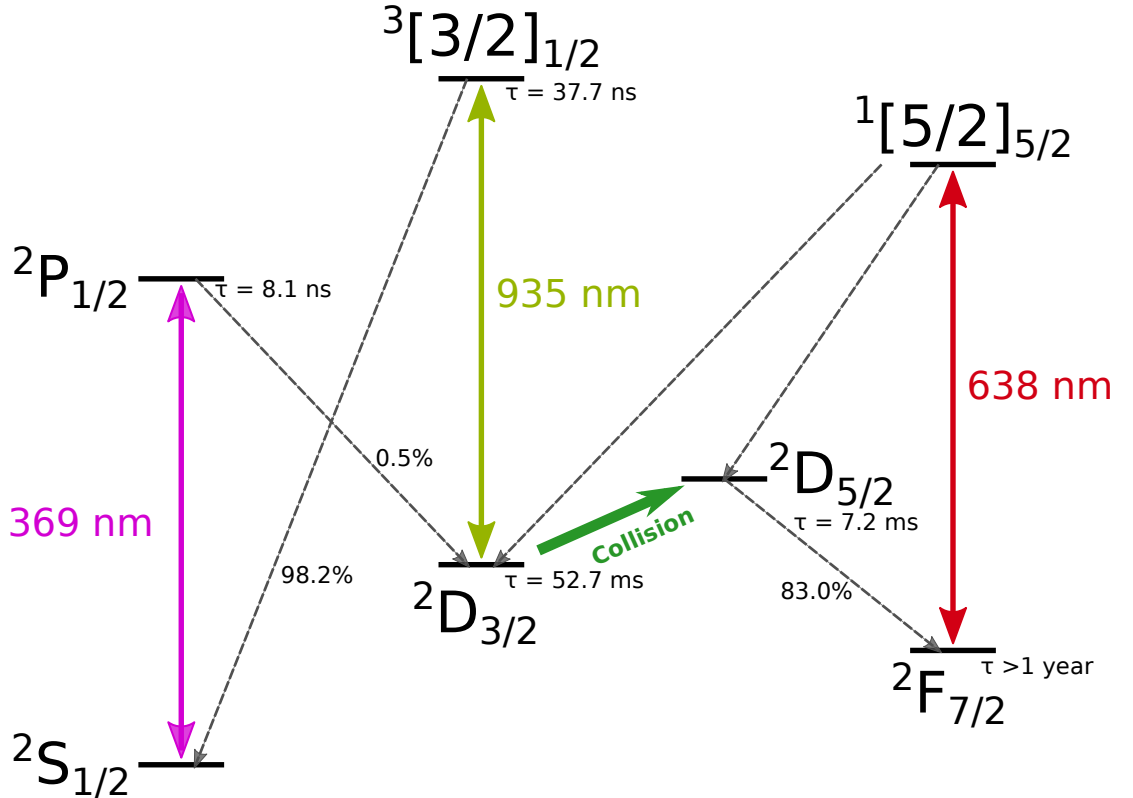


Fig. 2.5 Energy level structure of $^{174}\text{Yb}^+$ showing relevant energy levels and their decay modes. A closed Doppler cooling cycle can be performed with the three lasers driving the shown transitions on resonance. Linewidths, branching ratios and lifetimes are taken from [39, 40].

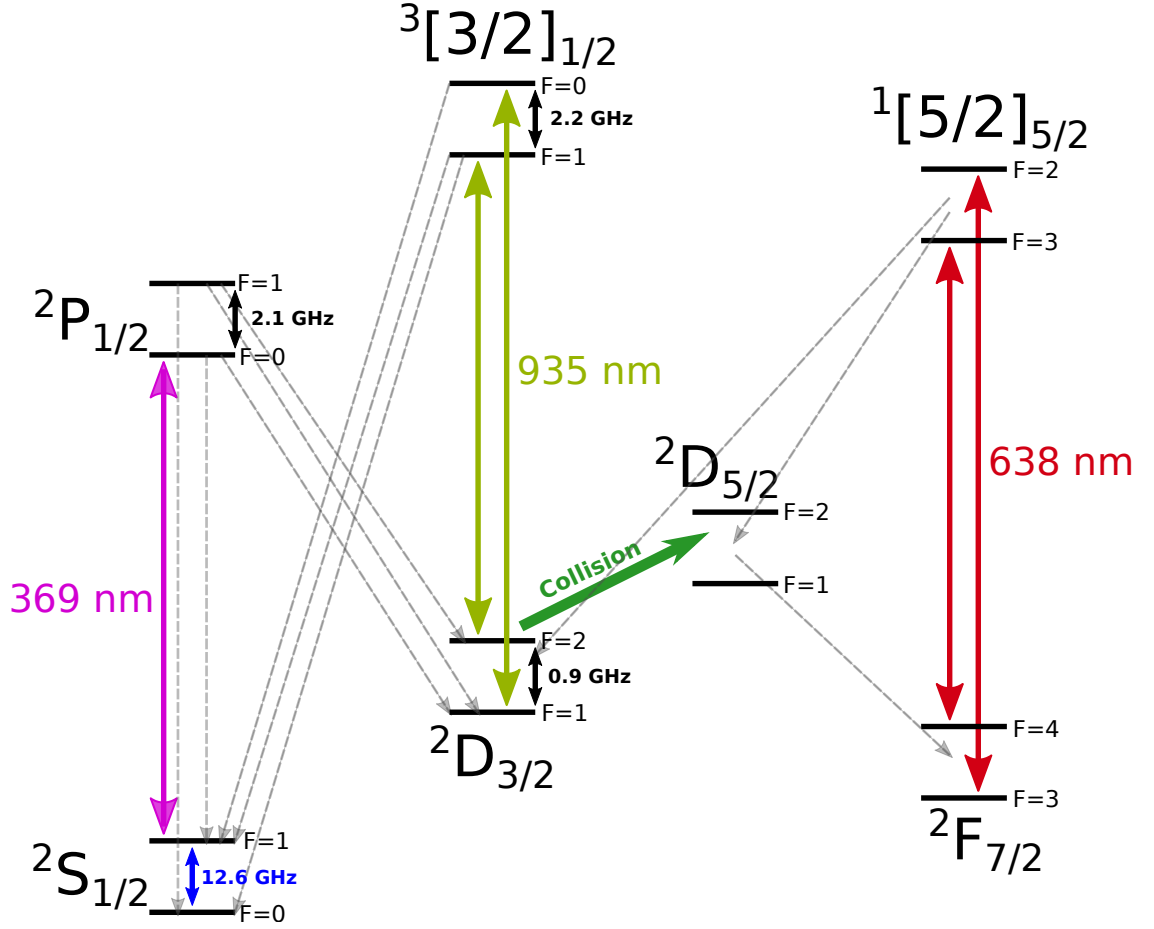


Fig. 2.6 Energy level structure of $^{171}\text{Yb}^+$ showing relevant energy levels and their decay modes. A closed Doppler cooling cycle can be performed with the three lasers and one microwave field driving the shown transitions on resonance. The $1/2$ nuclear spin means there is a hyperfine structure for each energy level, to keep the ion in the cooling cycle more 935 nm and 638 nm laser power is required to power broaden across all states. A microwave field near 12.6 GHz drives population out of the $^2S_{1/2}$ state to keep the ion in the cooling cycle.

2.1.3 $^{171}\text{Yb}^+$ $^2S_{1/2}$ ground state manifold

All sensing experiments conducted in this thesis are performed in the $^2S_{1/2}$ hyperfine ground state manifold of $^{171}\text{Yb}^+$. The manifold consists of the four states shown in an energy level diagram in Fig. 2.7. At zero static magnetic field, the state $|0\rangle \equiv ^2S_{1/2}|F=0, m_f=0\rangle$ is separated from the $|0'\rangle \equiv ^2S_{1/2}|F=1, m_f=0\rangle$ state by a frequency of $\omega_{hf} = 2\pi \times 12.6428121$ GHz [38]. The three states $|0'\rangle$, $|+1\rangle \equiv ^2S_{1/2}|F=1, m_f=+1\rangle$ and $|-1\rangle \equiv ^2S_{1/2}|F=1, m_f=-1\rangle$ are degenerate in the zero field case, the degeneracy is lifted in the presence of a magnetic field. The frequency associated with the energy splitting of the states when in the presence of a static magnetic field can be seen in Fig. 2.8. The equations describing the frequency splitting of the states can be derived from the

Breit-Rabi formula [41] and are given by [42]

$$\begin{aligned}\omega_B^+ &= \frac{\omega_{hf}}{2}(1 + \chi - \sqrt{1 + \chi^2}), \\ \omega_B^- &= -\frac{\omega_{hf}}{2}(1 - \chi - \sqrt{1 + \chi^2}), \\ \omega_B^0 &= \omega_{hf}\sqrt{1 + \chi^2},\end{aligned}\tag{2.1}$$

where $\chi = (g_J - g_I)\mu_B B / \hbar\omega_{hf}$ and B is the applied magnetic field. We can neglect the nuclear spin g-factor g_I as it is a few orders of magnitude lower than the electron g factor $g_J \approx 2$. From Eq: 2.1 it can be seen that the $|0\rangle \leftrightarrow |0'\rangle$ clock transition is 2nd order sensitive to magnetic field fluctuations (χ^2 term) while the $|0'\rangle \leftrightarrow |-1\rangle$ and $|0'\rangle \leftrightarrow |+1\rangle$ transitions are 1st and 2nd order sensitive. The frequency splittings of these states correspond to the frequencies that can be sensed by the ion, this is later described in this section.

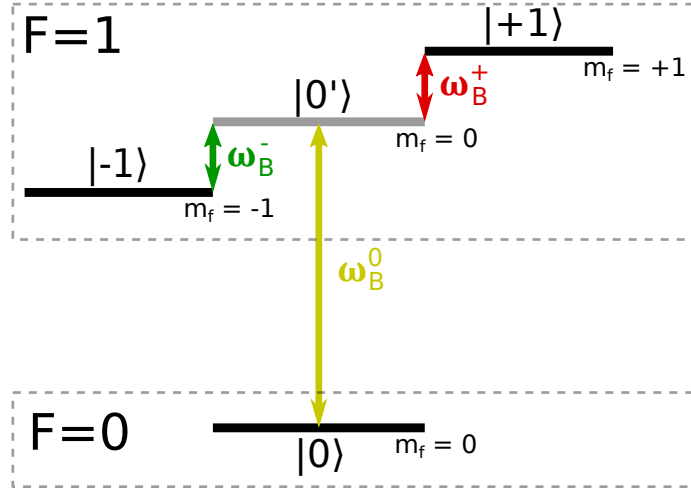


Fig. 2.7 Energy level diagram of the $2S_{1/2}$ ground state manifold of $^{171}\text{Yb}^+$. The state consists of two hyperfine manifolds $F = 0$ and $F = 1$, separated by a frequency of $\omega_B^0 = 2\pi \times 12.6428121$ GHz at zero magnetic field. An applied magnetic field lifts the degeneracy of the $F = 1$ manifold and three m_f sub-levels are produced with frequency splittings ω_B^- and ω_B^+ .

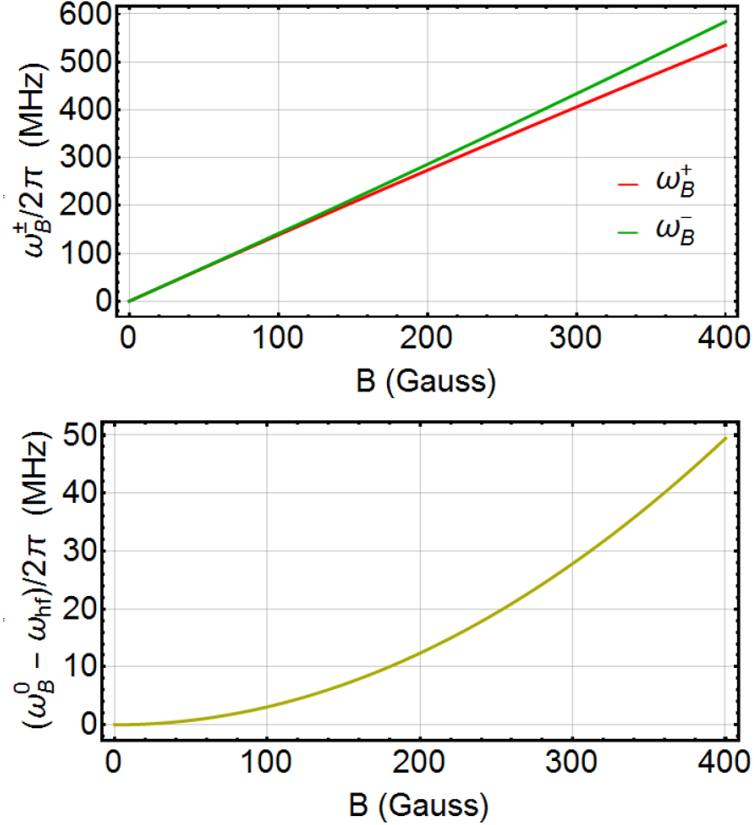


Fig. 2.8 Frequencies ω_B^+ , ω_B^- and $(\omega_B^0 - \omega_{hf})$ as a function of magnetic field B plotted from Eq. 2.1. $(\omega_B^0 - \omega_{hf})$ is equal to the frequency difference between ω_B^+ and ω_B^- , this equivalent to the 2nd order Zeeman shift.

2.2 Microwave and RF dressed states for sensing AC magnetic fields

This section will focus on a theoretical description for using dressed states in trapped ion magnetometry. The sensitivity of a ion trap magnetometer is dependent on the coherence time as $1/\sqrt{T_2}$ [34], meaning atomic transitions with long coherence times are essential to achieve the best sensitivity (See Sec. 2.40). The T_2 time is defined as the spin relaxation time time, in precise terms under the context of this thesis, this is the time in which the transverse magnetization of an ion to fall to approximately 37% ($1/e$) of its initial value.

The T_2 coherence time of the trapped ion sensor is dependent on how much noise is coupled to the hyperfine states. Fluctuating magnetic fields will cause decoherence on the ion, meaning a shorter T_2 time and worse sensitivity. To maximize the coherence time of our magnetometer, a dynamic decoupling scheme can be implemented to decouple the ion from as much environmental noise as possible. The method described in this section is based on the a form of dynamic decoupling that utilises tuneable dressed states [43, 44], instead of quantum states formed by bare atomic Zeeman states that are more sensitive to decoherence from magnetic field fluctuations. There are two ways of using dressed states to detect high frequency magnetic fields, the first uses microwave dressed states to detect RF frequencies (Sec. 2.2.3), and the second is using RF dressed states to detect mi-

crowave frequencies (Sec. 2.2.4). The dressed states are created in the $^2S_{1/2}$ ground-state hyperfine manifold of $^{171}\text{Yb}^+$ described in the previous section. The efficient preparation, detection and manipulation of the hyperfine structure of $^{171}\text{Yb}^+$ to sense magnetic fields using dressed states has been demonstrated and can be found in Sec. 5.

2.2.1 Trapped ions for AC magnetometry

The basis for AC magnetometry using trapped ions is to allow an oscillating electromagnetic field to drive the ion between two of its internal states and readout the rate at which the ion is rotating between these states to extract a magnetic field strength reading. Labelling the two states $|\downarrow\rangle \equiv (0, 1)^T$ and $|\uparrow\rangle \equiv (1, 0)^T$ and setting the zero point energy to be half way between the two states, the Hamiltonian term describing the two states is

$$H_0 = \frac{\hbar\omega_0}{2} \left(|\uparrow\rangle\langle\uparrow| - |\downarrow\rangle\langle\downarrow| \right), \quad (2.2)$$

where $\hbar\omega_0$ is the energy splitting of the states. For our scheme, the two states utilized are created in the hyperfine atomic levels, meaning there is no electric dipole coupling when a electromagnetic field is applied. Instead the ion is coupled to the electromagnetic field via magnetic dipole coupling, therefore the resulting Hamiltonian, with an applied electromagnetic field, is $H = H_0 + H_I$. H_I is given by

$$H_I = -\vec{\mu} \cdot \vec{B}, \quad (2.3)$$

where $\vec{\mu}$ is the magnetic moment and \vec{B} is the applied magnetic field. The applied magnetic field takes the form of $\vec{B} = \vec{B}_0 \cos(\omega t - \vec{k} \cdot \vec{r} - \phi)$, where \vec{k} is the wavevector, \vec{r} is the ion position, ω is the frequency of the oscillating field and ϕ is the phase. We can neglect the $\vec{k} \cdot \vec{r}$ term in the cosine by expanding in exponential form and approximating $e^{i\vec{k} \cdot \vec{r}} \approx 1$ because the wavelengths typically used (RF and microwave wavelengths) are much larger than spatial extent of the ions wavefunction, this is the magnetic dipole approximation. The Hamiltonian can be now be written in terms of its matrix elements in the $\{|\downarrow\rangle, |\uparrow\rangle\}$ basis as

$$\begin{aligned} H_I &= -\left(\langle\downarrow| \vec{\mu} \cdot \vec{B}_0 |\uparrow\rangle |\downarrow\rangle\langle\uparrow| + \langle\uparrow| \vec{\mu} \cdot \vec{B}_0 |\downarrow\rangle |\uparrow\rangle\langle\downarrow| \right) \cos(\omega t - \phi) \\ &= \hbar\Omega_0 \left(|\uparrow\rangle\langle\downarrow| + |\downarrow\rangle\langle\uparrow| \right) \cos(\omega t - \phi), \end{aligned} \quad (2.4)$$

where the Rabi frequency is defined as $\Omega_0 = -\langle\downarrow| \vec{\mu} \cdot \vec{B}_0 |\uparrow\rangle / \hbar = -\langle\uparrow| \vec{\mu} \cdot \vec{B}_0 |\downarrow\rangle / \hbar$ and the matrix elements are off-diagonal elements describing the transition from one state to another. From this we can move to the interaction picture with respect to H_0 as $H \rightarrow H' = e^{iH_0 t/\hbar} (H - H_0) e^{-iH_0 t/\hbar}$, giving

$$H' = \frac{\hbar\Omega_0}{2} \left(|\uparrow\rangle\langle\downarrow| e^{i\omega_0 t} + |\downarrow\rangle\langle\uparrow| e^{-i\omega_0 t} \right) \left(e^{i\omega t} e^{-i\phi} + e^{-i\omega t} e^{i\phi} \right). \quad (2.5)$$

For values of ω set close to the resonant frequency of the two states ω_0 , the interaction Hamiltonian H' will contain four rotating terms, two slowly rotating at a frequency $\delta = \omega - \omega_0$ (better known as detuning), and two much faster terms at a frequency of $\omega + \omega_0$. The rotating wave approximation (RWA) can be used in this instance to neglect the faster rotating terms, this is valid as long as $\Omega_0 \ll \omega_0$. Now under the RWA, H' becomes

$$H' = \frac{\hbar\Omega_0}{2} \left(|\uparrow\rangle\langle\downarrow| e^{-i\delta t} e^{i\phi} + |\downarrow\rangle\langle\uparrow| e^{i\delta t} e^{-i\phi} \right). \quad (2.6)$$

With this Hamiltonian we now want to find the unitary operator associated with it to formulate an equation to describe the ions population for any given magnetic field. To find the unitary operator we insert H' into the Schrödinger equation $i\hbar\frac{\partial}{\partial t} |\psi(t)\rangle = H' |\psi(t)\rangle$ and solve for an arbitrary spin state $|\psi(t)\rangle = c_\downarrow(t) |\downarrow\rangle + c_\uparrow(t) |\uparrow\rangle$. This gives a set of two coupled first-order differential equations

$$\dot{c}_\uparrow(t) = -\frac{i\Omega_0}{2} e^{i\delta t} e^{-i\phi} c_\downarrow(t), \quad (2.7a)$$

$$\dot{c}_\downarrow(t) = -\frac{i\Omega_0}{2} e^{-i\delta t} e^{i\phi} c_\uparrow(t). \quad (2.7b)$$

Differentiating Eq. 2.7a with respect to t and substituting into Eq. 2.7b allows the problem to be written as a single 2nd order differential equation in terms of $c_\uparrow(t)$

$$\ddot{c}_\uparrow(t) - i\delta\dot{c}_\uparrow(t) + \frac{\Omega_0^2}{4} c_\uparrow(t) = 0. \quad (2.8)$$

The general solution to this is

$$c_\uparrow(t) = e^{i\delta t/2} \left(a e^{-i\Omega_\delta t/2} + b e^{i\Omega_\delta t/2} \right), \quad (2.9)$$

where $\Omega_\delta = \sqrt{\Omega_0^2 + \delta^2}$ and, a and b are constants that depend on the initial state the ion is in. The solution for $c_\downarrow(t)$ can then be found by differentiating Eq. 2.9 with respect to t and substituting the solution into Eq. 2.7a, this gives the solution

$$c_\downarrow(t) = \frac{e^{-i\delta t/2} e^{i\phi}}{\Omega_0} \left(\delta(a e^{-i\Omega_\delta t/2} + b e^{i\Omega_\delta t/2}) - \Omega_\delta(a e^{-i\Omega_\delta t/2} - b e^{i\Omega_\delta t/2}) \right). \quad (2.10)$$

We can then find the unitary operator in the $\{|\downarrow\rangle, |\uparrow\rangle\}$ basis by setting the initial state at $t = 0$ to be $|\downarrow\rangle$, this gives $c_\downarrow(0) = 1$ and $c_\uparrow(0) = 0$. From this we find that $a = -b = \Omega_0 e^{-i\phi} / 2\Omega_\delta$. If the ion was to start in the $|\uparrow\rangle$, we would get the initial conditions $c_\downarrow(0) = 0$ and $c_\uparrow(0) = 1$ and find that $a = (1 + \delta/\Omega_\delta)/2$ and $b = (1 - \delta/\Omega_\delta)/2$. Inserting these two sets of parameters for the two initial conditions into Eq. 2.9 and Eq. 2.10, we obtain the unitary operator

$$U(\delta, \Omega_0, \phi, t) = \begin{pmatrix} e^{i\delta t/2} \left[\cos(\Omega_\delta t/2) - \frac{i\delta}{\Omega_\delta} \sin(\Omega_\delta t/2) \right] & -\frac{i\Omega_0}{\Omega_\delta} e^{i\delta t/2} e^{-i\phi} \sin(\Omega_\delta t/2) \\ -\frac{i\Omega_0}{\Omega_\delta} e^{-i\delta t/2} e^{i\phi} \sin(\Omega_\delta t/2) & e^{-i\delta t/2} \left[\cos(\Omega_\delta t/2) + \frac{i\delta}{\Omega_\delta} \sin(\Omega_\delta t/2) \right] \end{pmatrix}. \quad (2.11)$$

In the Bloch sphere, this unitary operator rotates the Bloch vector by an angle $\theta = \Omega_0 t$ around an axis at an angle ϕ in the $x - y$ plane, this is visually shown in Fig. 2.9.

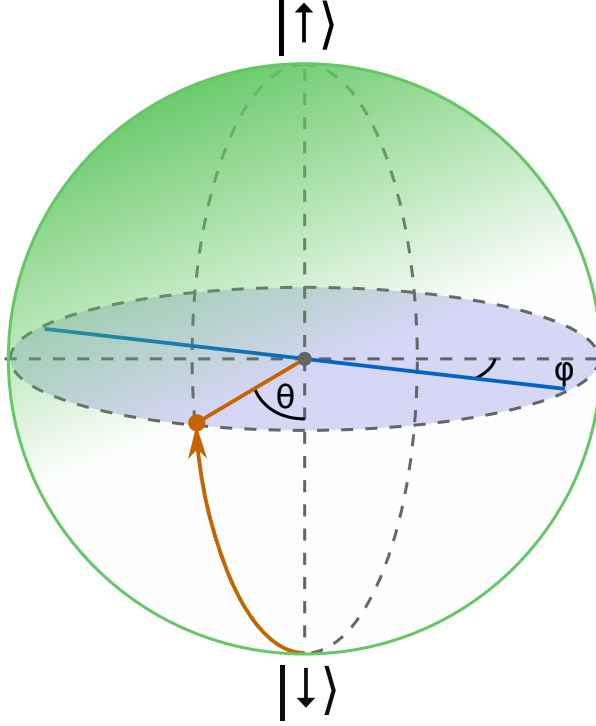


Fig. 2.9 Bloch sphere illustration of the effect the unitary operator (Eq. 2.11) has on a two-level system initialised in $|\downarrow\rangle$. The Bloch vector (orange) rotates by an angle $\theta = \Omega_0 t$ around an axis (blue) in the x-y plane. Sequences of pulses with an angle θ and phase ϕ perform arbitrary rotations on the Bloch sphere.

Although the experiments in this thesis focus on simple magnetometry where the phase ϕ of the field being sensed doesn't change and the detuning of the field from resonance is zero $\delta = 0$. In experiments the probabilities P_\uparrow and $P_\downarrow = 1 - P_\uparrow$ are measured, it is therefore useful to calculate these probabilities to compare with experimental data. For a state initialised in $|\downarrow\rangle$, the probability to be in the state $|\uparrow\rangle$ is found to be

$$P_\uparrow(t, \delta) = \frac{\Omega_0^2}{\Omega_\delta^2} \sin^2(\Omega_\delta t/2) = \frac{\Omega_0^2}{2\Omega_\delta^2} (1 - \cos(\Omega_\delta t)). \quad (2.12)$$

This can be applied to any two energy levels within the $^2S_{1/2}$ manifold being driven by a magnetic field, this includes the dressed states described in the next section. Plots for $P_\uparrow(t, \delta)$ as a function of time and detuning are shown in Fig. 2.10.

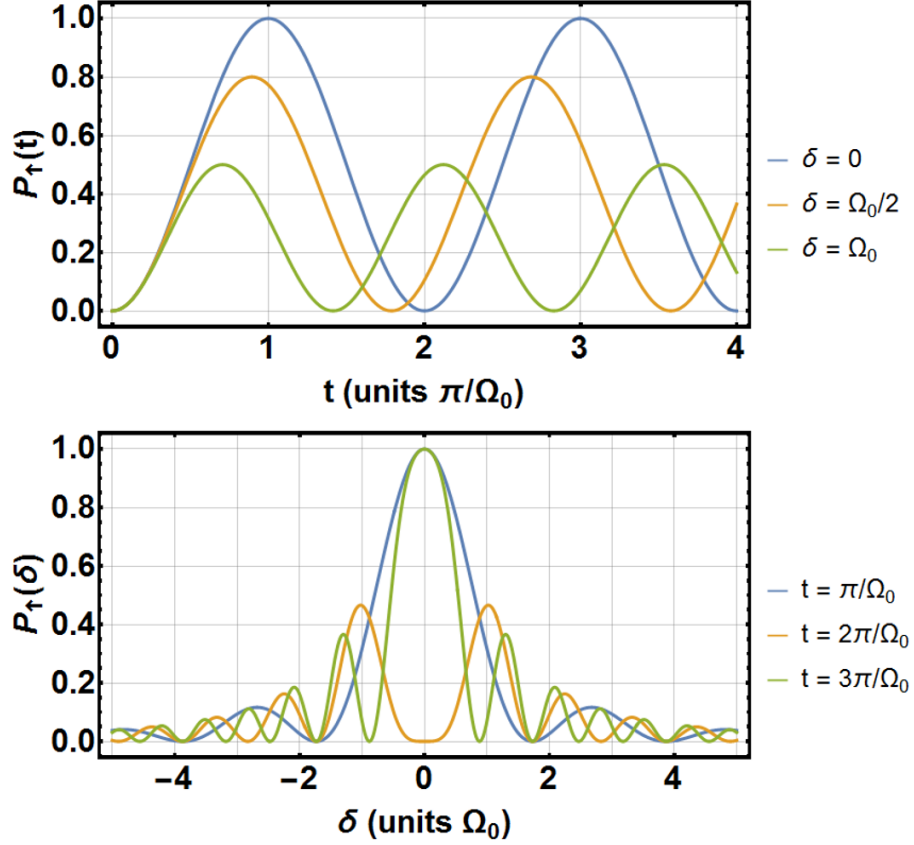


Fig. 2.10 Probability of the ion being in the $|\uparrow\rangle$ state when applying a near resonant field as a function of time (top) and detuning (bottom) when the state is initialised in $|\downarrow\rangle$. These are plotted from Eq. 2.12, it can be seen that large detuning gives rise to faster frequency oscillations with lower amplitude, making on resonant fields being a priority for sensing, as detuning would result in a faulty magnetic field strength reading. It can also be seen that if the pulse time is an odd integer multiple of π/Ω_0 , the population will have transferred completely to the $|\uparrow\rangle$ state.

2.2.2 Three level dressed states

A dressed state is an eigenstate of the Hamiltonian which describes an atomic system being driven by near-resonant electromagnetic fields (dressing fields). By applying dressing fields, the ion can be decoupled from noise that would otherwise couple to the bare states within the $^2S_{1/2}$ manifold. This extends the T_2 coherence time of a two-level system in the dressed state basis beyond that of the bare state basis, thus, improving the sensitivity for any AC magnetometry (see Sec. 2.40).

There are two configurations for dressed states that are utilized in this thesis, these are shown in Fig. 2.12 and 2.13. One uses microwave frequency dressing fields on resonance with the $|0\rangle \leftrightarrow |-1\rangle$ and $|0\rangle \leftrightarrow |-1\rangle$ transitions, while the other uses RF dressing fields on the $|0'\rangle \leftrightarrow |-1\rangle$ and $|0'\rangle \leftrightarrow |-1\rangle$ transitions. When analytically deriving the dressed states and dressed state Hamiltonian the two setups are for the most part equatable. To

avoid repetition, the two configurations for three level dressed states shown in Fig. 2.11 will be described using the same basis vectors $\{|0\rangle, |1\rangle, |2\rangle\}$. One needs to simply assign $|0\rangle \rightarrow |0\rangle$, $|1\rangle \rightarrow |-1\rangle$ and $|2\rangle \rightarrow |+1\rangle$ for the microwave dressed state system (Sec. 2.2.3); and assign $|0\rangle \rightarrow |0'\rangle$, $|1\rangle \rightarrow |-1\rangle$ and $|2\rangle \rightarrow |+1\rangle$ for the RF dressed state system (Sec. 2.2.4).

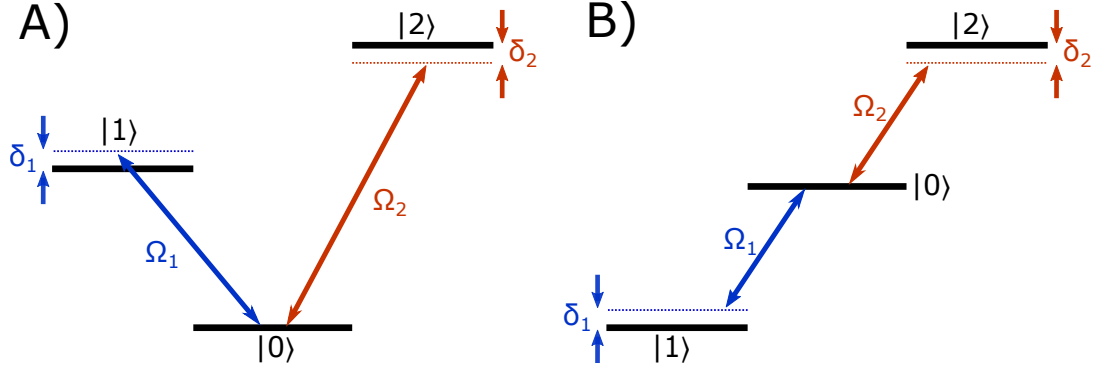


Fig. 2.11 A) Three level dressed state basis in "V" configuration, this represents the configuration used for the microwave dressed states in Sec. 2.2.3. B) Three level dressed state basis in "/" configuration, this represents the configuration used for the microwave dressed states in Sec. 2.2.4.

To start, three states $|0\rangle \equiv (0, 0, 1)^T$, $|1\rangle \equiv (0, 1, 0)^T$ and $|2\rangle \equiv (1, 0, 0)^T$ have two applied magnetic fields to the $|0\rangle \leftrightarrow |1\rangle$ and $|0\rangle \leftrightarrow |2\rangle$ transitions with Rabi frequencies Ω_1 and Ω_2 , and detunings δ_1 and δ_2 . The resulting Hamiltonian is

$$H_{dr} = \frac{\hbar\Omega_1}{2} (|1\rangle\langle 0| e^{-i\delta_1 t} e^{i\phi_1} + |0\rangle\langle 1| e^{i\delta_1 t} e^{-i\phi_1}) + \frac{\hbar\Omega_2}{2} (|2\rangle\langle 0| e^{-i\delta_2 t} e^{i\phi_2} + |0\rangle\langle 2| e^{i\delta_2 t} e^{-i\phi_2}), \quad (2.13)$$

where ϕ_1 and ϕ_2 are the phases for the fields. The two parts to this Hamiltonian can be derived in the same way as Eq. 2.6. This Hamiltonian can be made time independent by transforming into an interaction picture with respect to $H_\delta = \hbar(\delta_1 |1\rangle\langle 1| + \delta_2 |2\rangle\langle 2|)$ giving

$$\begin{aligned} H'_{dr} &= e^{iH_\delta t/\hbar} (H_{dr}(t) - H_\delta) e^{-iH_\delta t/\hbar} \\ &= \frac{\hbar}{2} \begin{pmatrix} -2\delta_2 & 0 & \Omega_2 e^{i\phi_2} \\ 0 & -2\delta_1 & \Omega_1 e^{i\phi_1} \\ \Omega_2 e^{-i\phi_2} & \Omega_1 e^{-i\phi_1} & 0 \end{pmatrix}. \end{aligned} \quad (2.14)$$

In general, the eigenenergies and eigenstate coefficients of this Hamiltonian cannot be written down in concise algebraic form, for a full derivation see Ref. [45]. For convenience, we define the phases of both the microwave fields to be equal to zero ($\phi_1 = \phi_2 = 0$), we also set the two microwave fields on resonance ($\delta_1 = \delta_2 = 0$) and at equal Rabi frequencies ($\Omega_1 = \Omega_2 = \Omega$). The resulting eigenstates reduce to

$$\begin{aligned}
|D\rangle &= \frac{1}{\sqrt{2}}(|2\rangle - |1\rangle), \\
|u\rangle &= \frac{1}{2}|2\rangle + \frac{1}{2}|1\rangle + \frac{1}{\sqrt{2}}|0\rangle, \\
|d\rangle &= \frac{1}{2}|2\rangle + \frac{1}{2}|1\rangle - \frac{1}{\sqrt{2}}|0\rangle,
\end{aligned} \tag{2.15}$$

with corresponding eigenenergies

$$\begin{aligned}
E_u &= + \frac{\hbar\Omega}{\sqrt{2}}, \\
E_d &= - \frac{\hbar\Omega}{\sqrt{2}}, \\
E_D &= 0.
\end{aligned} \tag{2.16}$$

In this case the energy of the dressed state $|D\rangle$ is independent of the dressing field Rabi frequencies and therefore protected from Rabi frequency noise [44]. It's important to understand the decoupling from noise that is achieved through dressed states, this can be seen by introducing a perturbation to represent magnetic field fluctuations coupling to the 1st order sensitive states

$$H_p = \hbar\lambda_0(t)(|2\rangle\langle 2| - |1\rangle\langle 1|), \tag{2.17}$$

where $\lambda_0(t)$ is an arbitrary time-dependent function. In the dressed state basis, Eq. 2.17 becomes

$$H_p = \frac{\hbar\lambda_0(t)}{\sqrt{2}}(|D\rangle\langle u| + |D\rangle\langle d| + |u\rangle\langle D| + |d\rangle\langle D|). \tag{2.18}$$

This shows us that magnetic field fluctuations will drive population between the three dressed states, but these states are separated by an energy gap of $\hbar\Omega/\sqrt{2}$, therefore only magnetic field fluctuations with a frequency at of near $\Omega/\sqrt{2}$ will drive transitions between these dressed states. It is preferable to attain the largest value of Ω possible to decouple the ion from environmental noise and potential noisy kHz sources typically expelled by most electronic devices.

2.2.3 Microwave dressed states for RF frequency sensing

In this case, two microwave fields are used for putting the ion into the dressed state basis. The signal to be sensed is on resonance with the transition frequency of $|0'\rangle \leftrightarrow |D\rangle$, where $|D\rangle$ is the hyperfine dressed state comprised of the 1st order magnetic field sensitive states $| -1\rangle$ and $| +1\rangle$, and $|0'\rangle$ is a 1st order magnetic field insensitive bare state. An energy level diagram showing the fields applied and the microwave dressed states can be seen in Fig. 2.12, this corresponds to the "V" configuration in Fig. 2.11. The degeneracy of the Zeeman states is lifted by a static magnetic field, induced via a pair of coils (Sec. 4.5.1), the frequency splittings ω_B^0 , ω_B^+ and ω_B^- are described in Sec. 2.1.3.

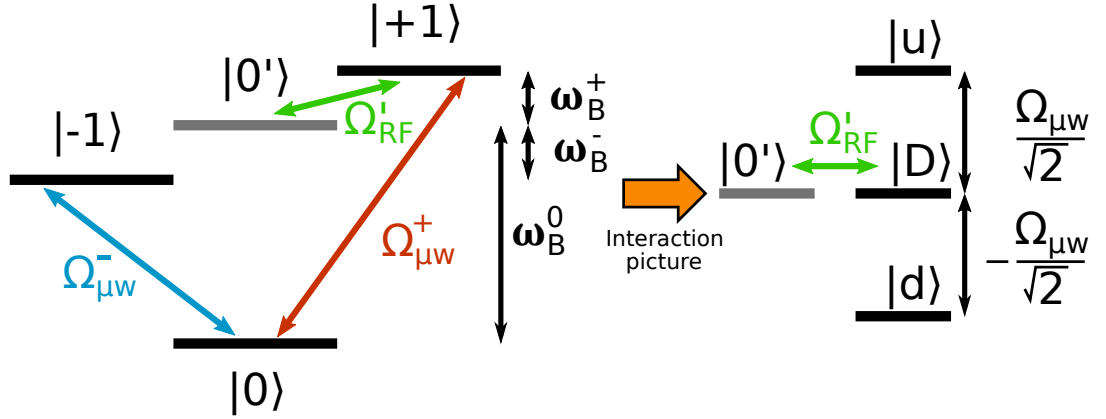


Fig. 2.12 (Left) Energy level diagram of the $2S_{1/2}$ ground state hyperfine manifold of $^{171}\text{Yb}^+$ where the degeneracy of the Zeeman states has been lifted by a static magnetic field. Here the transitions $|0\rangle \leftrightarrow |-1\rangle$ and $|0\rangle \leftrightarrow |+1\rangle$ are coupled with resonant microwave radiation dressing fields, when the Rabi frequencies of the dressing fields are set to be equal ($\Omega_{\mu w}^+ = \Omega_{\mu w}^- = \Omega_{\mu w}$) the dressed state energy levels $|d\rangle$, $|D\rangle$ and $|u\rangle$ are produced. (Right) Energy level diagram showing the dressed state basis and energy splittings $\pm\hbar\Omega_{\mu w}/\sqrt{2}$. Rabi oscillations at Rabi frequency Ω'_{RF} are driven via the $|0'\rangle \leftrightarrow |D\rangle$ transition.

The Hamiltonian describing the dressed states is derived in the same manor as Eq. 2.13, by moving to the interaction picture and performing the rotating wave approximation, with the two microwave fields phases equal to zero ($\phi_+ = \phi_- = 0$), on resonance ($\delta_+ = \delta_- = 0$) and at equal Rabi frequencies ($\Omega_{\mu w}^+ = \Omega_{\mu w}^- = \Omega_{\mu w}$); it takes the form

$$H_{\mu w} = \frac{\hbar\Omega_{\mu w}}{2} (|+1\rangle \langle 0| + |-1\rangle \langle 0| + |0\rangle \langle +1| + |0\rangle \langle -1|). \quad (2.19)$$

The resulting eigenstates of this Hamiltonian are the dressed states of the system and are given as

$$\begin{aligned} |D\rangle &= \frac{1}{\sqrt{2}} (|+1\rangle - |-1\rangle), \\ |u\rangle &= \frac{1}{2} |+1\rangle + \frac{1}{2} |-1\rangle + \frac{1}{\sqrt{2}} |0\rangle, \\ |d\rangle &= \frac{1}{2} |+1\rangle + \frac{1}{2} |-1\rangle - \frac{1}{\sqrt{2}} |0\rangle. \end{aligned} \quad (2.20)$$

The Hamiltonian can be re-written in terms of the dressed states as

$$H_{\mu w} = \frac{\hbar\Omega_{\mu w}}{\sqrt{2}} (|u\rangle \langle u| - |d\rangle \langle d|). \quad (2.21)$$

The dressed states $|u\rangle$ and $|d\rangle$ are separated from the dressed state $|D\rangle$ by an energy of $\hbar\Omega_{\mu w}/\sqrt{2}$ and $-\hbar\Omega_{\mu w}/\sqrt{2}$ respectively (Fig. 2.12). When in the dressed state basis, rotations between $|0'\rangle$ and any of the three dressed states can be induced using a single RF magnetic field near resonance with either the $|0'\rangle \leftrightarrow |+1\rangle$ or $|0'\rangle \leftrightarrow |-1\rangle$ transitions.

These two transitions at low magnetic fields are relatively close in frequency, the slight difference arises from the 2nd order Zeeman shift $\Delta\omega_{2nd} = (\omega_B^0 - \omega_{hf}) = (\omega_B^+ - \omega_B^-)$ shown in Fig. 2.8.

Now we want to define the Hamiltonian describing a RF field driving the $|0'\rangle \leftrightarrow |D\rangle$ transition. By defining δ_{RF} as the RF field detuning from the $|0'\rangle \leftrightarrow |+1\rangle$ transition, and ϕ_{RF} as its phase, we get the Hamiltonian describing rotations between the $|0'\rangle$ and $|D\rangle$ states as

$$H_{RF} = \frac{\hbar\Omega_{RF}}{2} \left(|+1\rangle \langle 0'| e^{-i\delta_{RF}t} e^{i\phi_{RF}} + |-1\rangle \langle 0'| e^{i(\delta_{RF} - \Delta\omega_{2nd})t} e^{-i\phi_{RF}} + H.c. \right), \quad (2.22)$$

where $H.c.$ is the Hermitian conjugate and Ω_{RF} is the Rabi frequency of the $|0'\rangle \leftrightarrow |+1\rangle$ transition. By using dressed state equations (Eq. 2.20) to describe H_{RF} and then transforming to the interaction picture with respect to the dressing Hamiltonian (Eq. 2.21), the Hamiltonian describing the possible transitions is

$$\begin{aligned} H'_{RF} = & \frac{\hbar\Omega_{RF}}{2\sqrt{2}} \left(|D\rangle \langle 0'| \left(e^{-i\delta_{RF}t} e^{i\phi_{RF}} - e^{i(\delta_{RF} - \Delta\omega_{2nd})t} e^{-i\phi_{RF}} \right) + H.c. \right) \\ & + \frac{\hbar\Omega_{RF}}{4} \left(|u\rangle \langle 0'| \left(e^{-i(\delta_{RF} - \frac{\Omega_{\mu w}}{\sqrt{2}})t} e^{i\phi_{RF}} - e^{i(\delta_{RF} - \Delta\omega_{2nd} + \frac{\Omega_{\mu w}}{\sqrt{2}})t} e^{-i\phi_{RF}} \right) \right. \\ & \left. + |d\rangle \langle 0'| \left(e^{-i(\delta_{RF} + \frac{\Omega_{\mu w}}{\sqrt{2}})t} e^{i\phi_{RF}} + e^{i(\delta_{RF} - \Delta\omega_{2nd} - \frac{\Omega_{\mu w}}{\sqrt{2}})t} e^{-i\phi_{RF}} \right) + H.c. \right). \end{aligned} \quad (2.23)$$

From this it can be seen that there are two transitions from $|0'\rangle$ to each of the three dressed states, totalling six transitions with each dressed state pair being separated by $\Delta\omega_{2nd}$. This means there are a few conditions to ensure only a single $|0'\rangle \leftrightarrow |D\rangle$ transition is driven. One is that the Rabi frequency of the $|0'\rangle \leftrightarrow |+1\rangle$ transition should be much less than the Rabi frequency of the dressing fields $\Omega_{RF} \ll \Omega_{\mu w}$, this is because a large Rabi frequency associated with the $|0'\rangle \leftrightarrow |+1\rangle$ transition, corresponds to a higher strength magnetic field driving the transition. This means the field on resonance with the $|0'\rangle \leftrightarrow |D\rangle$ transition also drives the off resonant transitions $|0'\rangle \leftrightarrow |d\rangle$ and $|0'\rangle \leftrightarrow |u\rangle$ with a Rabi frequency $\Omega \gg 1/t$ (t is the experiment time). Another condition is that $\Omega_{RF} \ll \Delta\omega_{2nd}$, this is to ensure that none of the dressed state pairs are driven simultaneously. Furthermore it should be ensured that none of the transitions overlap, for example if $\Delta\omega_{2nd} \approx \Omega_{\mu w}/\sqrt{2}$, transitions from $|0'\rangle$ to $|u\rangle$ and $|D\rangle$ would have similar transition frequencies.

With these conditions met, we can neglect the terms containing the 2nd order Zeeman shift terms $\Delta\omega_{2nd}$ as these transitions are far from resonance. From this we can reduce the Hamiltonian to a form analogous to Eq. 2.6 describing rotations $|0'\rangle$ and a single $|D\rangle$ state as

$$H'_{RF} = \frac{\hbar\Omega'_{RF}}{2} \left(|D\rangle \langle 0'| e^{-i\delta_{RF}t} e^{i\phi_{RF}} + |0'\rangle \langle D| e^{i\delta_{RF}t} e^{-i\phi_{RF}} \right), \quad (2.24)$$

where $\Omega'_{RF} = \Omega_{RF}/\sqrt{2}$ is the Rabi frequency of the $|0'\rangle \leftrightarrow |D\rangle$ transition. Note that

either $|D\rangle$ state can be driven with the same solution by setting the detuning δ_{RF} to $\delta_{RF} + \Delta\omega_{2nd}$ and neglecting the off-resonant terms in the same way.

An interesting and useful feature of the $\{|0'\rangle, |D\rangle\}$ states is that the RF transition frequency is insensitive to magnetic field fluctuations to the first order. This can be understood by considering that a drift in magnetic field gives an equal and opposite energy shift to the 1st order component of the $|+1\rangle$ and $|-1\rangle$ states (Eq. 2.1), we assume that the drift caused by the second order Zeeman shift is negligible. If the dressing fields and RF field are initially set on resonance, a magnetic field drift causing them to be off resonance is equivalent to detuning the dressing fields equally in opposite directions by an amount $\delta_+ = -\delta_- = \delta$. The RF field is also detuned from the $|+1\rangle$ state by this drift, giving it the same detuning $\delta_{RF} = \delta$. But this detuning is also prevalent on the $|0'\rangle \leftrightarrow |D\rangle$ transition in the opposite direction to the detuning on the bare states (See [42] for numerical simulations showing this), meaning that if we neglect the second order shifts on the $|0'\rangle$ and $|D\rangle$ states, the RF field will always be on resonance for small magnetic field drifts.

By setting $\phi_{RF} = 0$ in the Hamiltonian Eq. 2.24, the equation describing the population transfer between $|0'\rangle$ and $|D\rangle$ can be derived in the same manor as Eq. 2.6 and can be written as

$$P(\delta_{RF}, t) = \frac{\Omega_{RF}'^2}{2(\Omega_{RF}'^2 + \delta_{RF}^2)} \left(1 - \cos\left(\sqrt{\Omega_{RF}'^2 + \delta_{RF}^2} t\right) \right). \quad (2.25)$$

With appropriate symbol changes this is identical to Eq. 2.12. It is a useful tool for describing the state population transfer in dressed state experiments that involve sweeping the RF field frequency or time the ion is exposed to.

2.2.4 RF dressed states for microwave frequency sensing

Analogous to the microwave dressed states, RF dressed states can be utilized to measure microwave frequency magnetic fields. In this case two RF fields are used for preparing the ion in the dressed state basis. The signal to be sensed is the transition frequency of the $|0\rangle \leftrightarrow |D'\rangle$ transition where $|D'\rangle$ is the hyperfine dressed state comprised of the 1st order magnetic field sensitive states $|-1\rangle$ and $|+1\rangle$, and $|0\rangle$ is an 1st order magnetic field insensitive bare state that is not part of the dressed states. An energy level diagram can be seen in Fig. 2.13, this corresponds to the ”/” configuration in Fig. 2.11.

The Hamiltonian describing the dressed states is derived in the same manor as Eq. 2.13, by moving to the interaction picture and performing the rotating wave approximation, with the two RF fields phases equal to zero ($\phi_+ = \phi_- = 0$), on resonance ($\delta_+ = \delta_- = 0$) and equal Rabi frequencies ($\Omega_{rf}^+ = \Omega_{rf}^- = \Omega_{rf}$); it takes the form

$$H_{rf} = \frac{\hbar\Omega_{rf}}{2} (|+1\rangle \langle 0'| + |-1\rangle \langle 0'| + |0'\rangle \langle +1| + |0'\rangle \langle -1|). \quad (2.26)$$

The resulting eigenstates of this Hamiltonian are the dressed states of this system and are given as follows

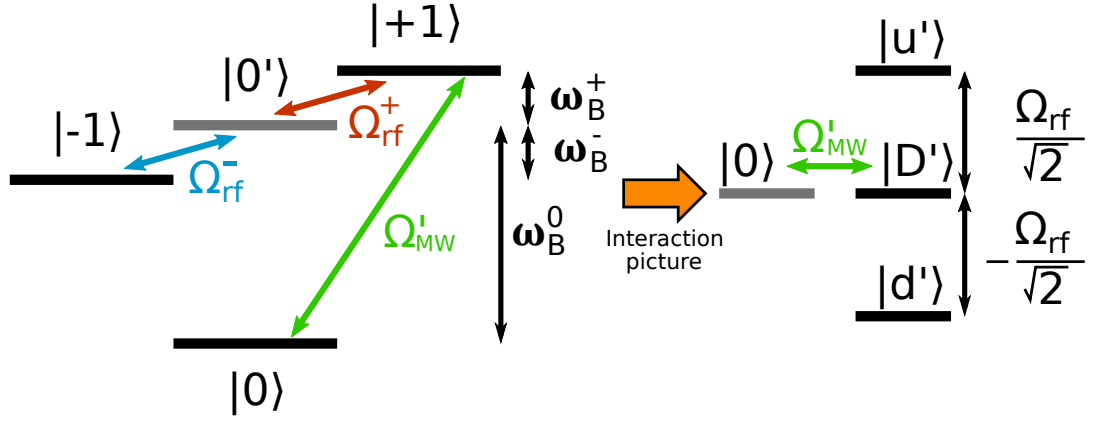


Fig. 2.13 (Left) Energy level diagram of the $^2S_{1/2}$ ground state hyperfine manifold of $^{171}\text{Yb}^+$ where the degeneracy of the Zeeman states has been lifted by a static magnetic field. Here the transitions $|0'\rangle \leftrightarrow |+1\rangle$ and $|0'\rangle \leftrightarrow |-1\rangle$ are coupled with resonant radio-frequency dressing fields. When the Rabi frequencies of the dressing fields are set to be equal ($\Omega_{rf}^+ = \Omega_{rf}^- = \Omega_{rf}$) the dressed state energy levels $|d'\rangle$, $|D'\rangle$ and $|u'\rangle$ are produced. (Right) Energy level diagram showing the dressed state basis and energy splittings $\pm\hbar\Omega_{rf}/\sqrt{2}$. Rabi oscillations at Rabi frequency Ω_{MW}' are driven via the $|0\rangle \leftrightarrow |D'\rangle$ transition.

$$\begin{aligned}
 |D'\rangle &= \frac{1}{\sqrt{2}}(|+1\rangle - |-1\rangle), \\
 |u'\rangle &= \frac{1}{2}|+1\rangle + \frac{1}{2}|-1\rangle + \frac{1}{\sqrt{2}}|0'\rangle, \\
 |d'\rangle &= \frac{1}{2}|+1\rangle + \frac{1}{2}|-1\rangle - \frac{1}{\sqrt{2}}|0'\rangle.
 \end{aligned} \tag{2.27}$$

The Hamiltonian can be re-written in terms of the dressed states as

$$H_{rf} = \frac{\hbar\Omega_{rf}}{\sqrt{2}}(|u'\rangle\langle u'| - |d'\rangle\langle d'|). \tag{2.28}$$

The dressed states $|u'\rangle$ and $|d'\rangle$ are separated from the dressed state $|D'\rangle$ by an energy of $\hbar\Omega_{rf}/\sqrt{2}$ and $-\hbar\Omega_{rf}/\sqrt{2}$ respectively (Fig. 2.13). When in the dressed state basis, rotations between $|0\rangle$ and any of the three dressed states can be induced using a single microwave magnetic field near resonance with either the $|0\rangle \leftrightarrow |+1\rangle$ or $|0\rangle \leftrightarrow |-1\rangle$ transitions. Unlike the microwave dressed states, these two transitions have a larger separation between them equal to the splitting between the 1st order sensitive states $\Delta\omega_{1st} = (\omega_B^+ + \omega_B^-)$.

Now we want to define the Hamiltonian describing a microwave field driving the $|0\rangle \leftrightarrow |D'\rangle$ transition. By defining δ_{MW} as the microwave field detuning from the $|0\rangle \leftrightarrow |+1\rangle$ transition, and ϕ_{MW} as its phase, we get the Hamiltonian describing rotations between the $|0\rangle$ and $|D'\rangle$ states as

$$H_{MW} = \frac{\hbar\Omega_{MW}}{2} \left(| +1 \rangle \langle 0' | e^{-i\delta_{MW}t} e^{i\phi_{MW}} + | -1 \rangle \langle 0' | e^{i(\delta_{MW} - \Delta\omega_{2nd})t} e^{-i\phi_{MW}} + H.c. \right), \quad (2.29)$$

where $H.c.$ is the Hermitian conjugate and Ω_{MW} is the Rabi frequency of the $|0'\rangle \leftrightarrow | +1 \rangle$ transition. By using dressed state equations (Eq. 2.27) to describe H_{MW} and then transforming to the interaction picture with respect to the dressing Hamiltonian (Eq. 2.28), the Hamiltonian describing the possible transitions is

$$\begin{aligned} H'_{MW} = & \frac{\hbar\Omega_{MW}}{2\sqrt{2}} \left(|D\rangle \langle 0' | (e^{-i\delta_{MW}t} e^{i\phi_{MW}} - e^{i(\delta_{MW} - \Delta\omega_{1st})t} e^{-i\phi_{MW}}) + H.c. \right) \\ & + \frac{\hbar\Omega_{MW}}{4} \left(|u\rangle \langle 0' | (e^{-i(\delta_{MW} - \frac{\Omega_{\mu w}}{\sqrt{2}})t} e^{i\phi_{MW}} - e^{i(\delta_{MW} - \Delta\omega_{1st} + \frac{\Omega_{rf}}{\sqrt{2}})t} e^{-i\phi_{MW}}) \right. \\ & \left. + |d\rangle \langle 0' | (e^{-i(\delta_{MW} + \frac{\Omega_{rf}}{\sqrt{2}})t} e^{i\phi_{MW}} + e^{i(\delta_{MW} - \Delta\omega_{1st} - \frac{\Omega_{rf}}{\sqrt{2}})t} e^{-i\phi_{MW}}) + H.c. \right). \end{aligned} \quad (2.30)$$

From this it can be seen that there are two transitions from $|0\rangle$ to each of the three dressed states, totalling six transitions with each dressed state pair being separated by $\Delta\omega_{1st}$. This means there are a few conditions to ensure only a single $|0\rangle \leftrightarrow |D'\rangle$ transition is driven. A condition analogous to the microwave dressed state scheme in Sec. 2.2.3 is that the Rabi frequency of the microwave transition $|0\rangle \leftrightarrow | +1 \rangle$ should be much less than the Rabi frequency of the RF dressing fields $\Omega_{MW} \ll \Omega_{rf}$. Another condition is that $\Omega_{MW} \ll \Delta\omega_{1st}$. The reasoning for these two conditions is the same as the microwave dressed states scenario.

Unlike the microwave dressed state system, transitions between the bare state and dressed states overlapping is not a significant concern for RF dressed state system, it should only be a concern if very high power dressing fields are used. This would only happen if $\Delta\omega_{1st} \approx \Omega_{rf}/\sqrt{2}$, which is unlikely as Ω_{rf} is typically much smaller than ω_{1st} . Unlike the microwave dressed states though, the two RF dressing fields driving the $|0'\rangle \leftrightarrow | +1 \rangle$ and $|0'\rangle \leftrightarrow | -1 \rangle$ transitions only have a frequency separation equal to the second order Zeeman shift $\Delta\omega_{2nd}$. Therefore to maintain stable dressing field Rabi frequencies Ω_{rf}^+ and Ω_{rf}^- , it is advised to keep the field strengths of the two dressing fields small enough to avoid the frequency profile of the two fields from overlapping and off resonantly driving the other transition.

With these conditions met, we can neglect the terms containing the 1st order Zeeman shift terms $\Delta\omega_{1st}$ as these transitions are far from resonance. From this we can reduce the Hamiltonian to a form analogous to Eq. 2.6 describing rotations $|0\rangle$ and a single $|D'\rangle$ state as

$$H'_{MW} = \frac{\hbar\Omega'_{MW}}{2} \left(|D\rangle \langle 0' | e^{-i\delta_{MW}t} e^{i\phi_{MW}} + |0'\rangle \langle D | e^{i\delta_{MW}t} e^{-i\phi_{MW}} \right), \quad (2.31)$$

where $\Omega'_{MW} = \Omega_{MW}/\sqrt{2}$ is the Rabi frequency of the $|0\rangle \leftrightarrow |D'\rangle$ transition. Note that either $|D'\rangle$ state can be driven with the same solution by setting the detuning δ_{MW} to $\delta_{MW} + \Delta\omega_{1st}$ and neglecting the off-resonant terms in the same way.

An interesting and useful feature of the $\{|0\rangle, |D'\rangle\}$ states is that the RF transition frequency is insensitive to magnetic field fluctuations to the first order like the microwave dressed states, but due to a slightly different reason. This can be understood by considering magnetic field drift causing an equal energy shift to the 1st order component of the $|+1\rangle$ and $|-1\rangle$ states (Eq. 2.1), we assume that the drift caused by the second order Zeeman shift is negligible. If the RF dressing fields and microwave field are initially set on resonance, a magnetic field drift causing them to be off resonance is equivalent to detuning the dressing fields equally in the same direction by an amount $\delta_+ = \delta_- = \delta$. The microwave field is also detuned from the $|+1\rangle$ state by this drift, giving it the same detuning $\delta_{MW} = \delta$. But this detuning is also prevalent on the $|0\rangle \leftrightarrow |D'\rangle$ transition in the opposite direction to the detuning on the bare states [42]. Meaning that if we neglect the second order shifts on the $|0\rangle$ and $|D'\rangle$ states, the RF field will always be on resonance for small magnetic field drifts. The main difference to notice is that the detunings caused by the magnetic field drift are now equal, not equal and opposite, fortunately the solution is still the same. It's also interesting to note that unlike the microwave dressed states, this has no effect on the transitions between $|0\rangle$ and the other dressed states $|u'\rangle$ and $|d'\rangle$.

By setting $\phi_{MW} = 0$ in the Hamiltonian Eq. 2.24, the equation describing the population transfer between $|0\rangle$ and $|D'\rangle$ can be derived in the same manor as Eq. 2.6 and can be written as

$$P(\delta_{MW}, t) = \frac{\Omega_{MW}'^2}{2(\Omega_{MW}'^2 + \delta_{MW}^2)} \left(1 - \cos\left(\sqrt{\Omega_{MW}'^2 + \delta_{MW}^2} t\right) \right). \quad (2.32)$$

Like the microwave dressed states in Sec. 2.2.3, this equation is identical to Eq. 2.12 and can also be used to describe the state population transfer in dressed state experiments that involve sweeping the RF field frequency or time the ion is exposed to.

2.2.5 Dressed state sensitivity limits

As described in Sec. 1.1, the sensitivity S is one of the most important metrics for determining the capabilities of a magnetometer. It is typically defined as minimal change in Rabi frequency Ω_S' that can be discerned within a total experiment time of 1 sec and is in units of Hz/\sqrt{Hz} [34].

This section derives the maximum sensitivity attainable using the sensing protocols outlined in this thesis. To begin deriving the sensitivity we first need to look at the equation describing the evolution in time of the ion rotating between two energy levels in the $^2S_{1/2}$ hyperfine manifold. For the $|0'\rangle \leftrightarrow |D\rangle$ or $|0\rangle \leftrightarrow |D'\rangle$ transitions. The probability of an ion of being in the dressed state $|D\rangle$ or $|D'\rangle$ when initialised in the $|0'\rangle$ or $|0\rangle$ for the microwave dressed and RF dressed states respectively can be written as

$$P = \frac{\Omega_S'^2}{2(\Omega_S'^2 + \Delta^2)} (1 - e^{-t/T_2} \cos(\sqrt{\Omega_S'^2 + \Delta^2} t)), \quad (2.33)$$

where Ω'_S is the Rabi frequency of the dressed state transition, Δ is the frequency detuning of the signal from the atomic transition, T_2 is the coherence time of the system and t is the electromagnetic field pulse time. This equation is the same as Eq. 2.12 but with appropriate sign changes and the introduction of a decoherence term e^{-t/T_2} , which describes the slow decay towards $P = 0.5$ due to noise coupling to the ion.

To calculate the sensitivity, we initially need to find the frequency resolution of the Rabi frequency $\delta\Omega'_S$, from this a magnetic field amplitude sensitivity can be derived as the Rabi frequency and magnetic field strength are directly proportional $\Omega'_S \propto B$. We start with the definition for the standard deviation ΔP of a single population measurement as [34]

$$\frac{\Delta P}{\delta\Omega'_S} = \left| \frac{\partial P}{\partial\Omega'_S} \right|, \quad (2.34)$$

where $\left| \frac{\partial P}{\partial\Omega'_S} \right|$ is the derivative of P with respect to Ω'_S . Rearranging we find the the minimal change in Ω'_S that can be discerned to be

$$\delta\Omega'_S = \frac{\Delta P}{\left| \frac{\partial P}{\partial\Omega'_S} \right|}. \quad (2.35)$$

From this we now need to define our population standard deviation and derivative of a fitted Rabi function. Assuming the magnetic field is on resonance with the transition splitting ($\Delta = 0$), the derivative of the fitted Rabi function is found from Eq. 2.33 to be

$$\left| \frac{\partial P}{\partial\Omega'_S} \right| = \left| t e^{-t/T_2} \sin(\Omega'_S t) / 2 \right|. \quad (2.36)$$

The standard deviation of the population measurement has typically been defined as $\Delta P = \sqrt{P(1-P)/n}$ [34] where n is the number of repetitions per population measurement. This definition is adequate for describing the sensitivity when the state detection fidelity is 100%, but has issues when this is not the case. A method for calculating the population standard deviation using a maximum log-likelihood function based on a binomial distribution is used for experimental data. This is described in detail in appendix D. The sensitivity will be derived using the binomial standard deviation $\Delta P = \sqrt{P(1-P)/n}$ because in the ideal case this is perfectly valid. First, we insert Eq. 2.33 at zero detuning to get

$$\Delta P = \sqrt{\frac{1 - e^{-2t/T_2} \cos^2(\Omega'_S t)}{4n}}. \quad (2.37)$$

Inserting Eq. 2.37 and Eq. 2.36 into Eq. 2.35 we find $\delta\Omega'_S$ to be

$$\delta\Omega'_S = \frac{1}{t\sqrt{n}} \sqrt{\frac{1 - e^{-2t/T_2} \cos^2(\Omega'_S t)}{e^{-2t/T_2} \sin^2(\Omega'_S t)}}. \quad (2.38)$$

The oscillating term can be removed from this equation by finding the values of $\Omega'_S t$ that correspond to a minimum values of $\delta\Omega'_S$. This is found to any odd integer N of $\Omega'_S t = N\pi/2$ giving the simpler version

$$\delta\Omega'_S = \frac{e^{t/T_2}}{t\sqrt{n}}. \quad (2.39)$$

From this we can now calculate the shot-noise limited sensitivity for a measurement of $\delta\Omega'_S$. This is given by [17, 34, 46]

$$S = \delta\Omega'_S \sqrt{T_{tot}}, \quad (2.40)$$

where $T_{tot} = n(t + T_{add})/n_i$ is the total time needed for N repetitions of the measurement with t experiment time, n_i is the number of ions and T_{add} being the additional time needed for laser cooling, state preparation and detection. It is always preferable to keep T_{add} to a minimum to achieve the best possible sensitivities, the largest contribution to T_{add} for trapped ions is usually the cooling time, typically on the order of $\times 10$ ms, compared to the ≤ 1 ms detection time and $\approx 10\mu s$ state preparation time. Therefore it is advised to implement methods that yield less total anomalous heating on the ion to keep the cooling time to a minimum (Sec. 3.3.3). Unfortunately in our system there is excessive heating on the ion that causes it to eject at experiment times ≥ 400 ms (see Sec. 5.5.3 and 5.6.3) and a large cooling time of 75 ms is required per experiment. Fortunately T_{add} has a diminishing effect on the shot-noise limited sensitivity as $t \gg T_{add}$, which is realistic to expect from ion trap experiments. From Eq. 2.40 we can write the shot-noise limited sensitivity at $T_{add} = 0$ as

$$S = \frac{e^{t/T_2}}{\sqrt{n_i t}}. \quad (2.41)$$

With this we can now find what the optimum measurement time t , for a given T_2 coherence time, that would achieve the best possible sensitivity. This is found to be $t = T_2/2$, which can be found by differentiating S with respect to t and equating to zero. This is in contrast with the minimum value attainable for $\delta\Omega'_S$ which is found at $t = T_2$. This measurement is important as it represents the smallest magnetic field that can be distinguished. The difference in optimal measurement times t for S and $\delta\Omega'_S$ is due to the introduction of the $\sqrt{T_{tot}}$. This makes it so there is a point in which minimal observable change in Ω'_S doesn't correspond to minimal observable change in Ω'_S that can be discerned within a total experiment time of 1 sec. Plots of both minima can be seen in Fig. 2.14. For a system with a coherence time approaching infinity, the quantum limit sensitivity ($T_2 \rightarrow \infty$) is

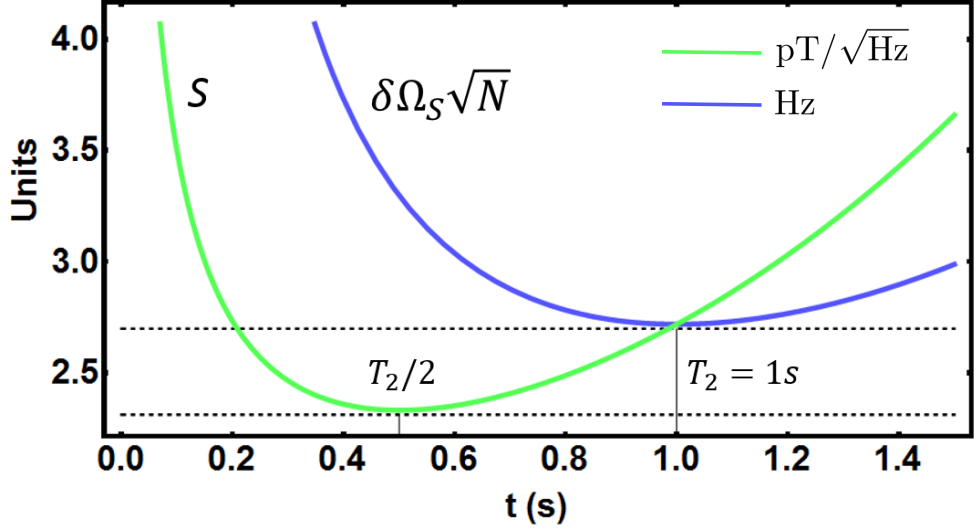


Fig. 2.14 The green line is the sensitivity function defined by Eq. 2.41 and the blue line is $\delta\Omega'_S\sqrt{n}$ defined by Eq. 2.39, both are plotted with $T_{add} = 0$ s, $n_i = 1$ and $T_2 = 1$ s. The experiment time that corresponds to the minimum sensitivity achievable is $t = T_2/2$ and the experiment time that corresponds to the smallest change in Rabi frequency, $\delta\Omega'_S$, that can be discerned is $t = T_2$.

$$S_{T_2 \rightarrow \infty} = \sqrt{\frac{1}{n_i t}}. \quad (2.42)$$

To calculate the magnetic field amplitude sensitivity we define the smallest distinguishable Rabi frequency change, $\delta\Omega'_S$ in terms of the smallest magnetic field amplitude distinguishable δB

$$\delta\Omega'_S = \frac{\delta\Omega_S}{\sqrt{2}} = \frac{\mu}{\hbar\sqrt{2}}\delta B. \quad (2.43)$$

This is taken from Sec. 2.2.1, where μ is the amplitude of the magnetic moment. For the hyperfine manifold $^2S_{1/2}$ in $^{171}\text{Yb}^+$, we have a spin projection quantum number $S = 1/2$ giving a total angular momentum, which we can use to calculate the magnetic moment $\mu = g\mu_B S$ where the electron gyromagnetic g factor ($g \approx 2$) and μ_B is the Bohr magneton. The $\sqrt{2}$ term comes from the bare state transition Rabi frequency being faster than the dressed state Rabi frequency, this is shown in Eq. 2.24 and Eq. 2.31 for both dressed state systems. This means that when converting a dressed state Rabi frequency into a magnetic field amplitude, the standard derivation from Sec. 2.2.1 for a bare two-level system needs to be scaled by $1/\sqrt{2}$ for either dressed state basis. With this, we can substitute Eq. 2.43 into Eq. 2.40 and define the magnetic field sensitivity to be

$$S_B = \frac{\hbar e^{t/T_2}}{\mu_B} \sqrt{\frac{2}{n_i t}} = \frac{\hbar\sqrt{2}}{\mu_B} S. \quad (2.44)$$

With Rabi oscillation data, this equation can be used with Eq. 2.40 to determine the measured sensitivity

2.2.6 Multi-ion sensitivity improvements

Based on the micro-fabricated chip design choices outlined in Sec. 3.3.1 ion traps can be specifically designed for magnetometry. Improvements on the sensitivity can be attained by increasing the number of ions n_i used for measuring a magnetic field, this will decrease the total experiment time T_{tot} and thus, improve the sensitivity as it scales as $S \propto 1/\sqrt{n_i}$. This is shown for increasing numbers of ions in Fig. 2.15 where the number of ions used are calculated from the sensor ion trap design in Sec. 3.3.1.

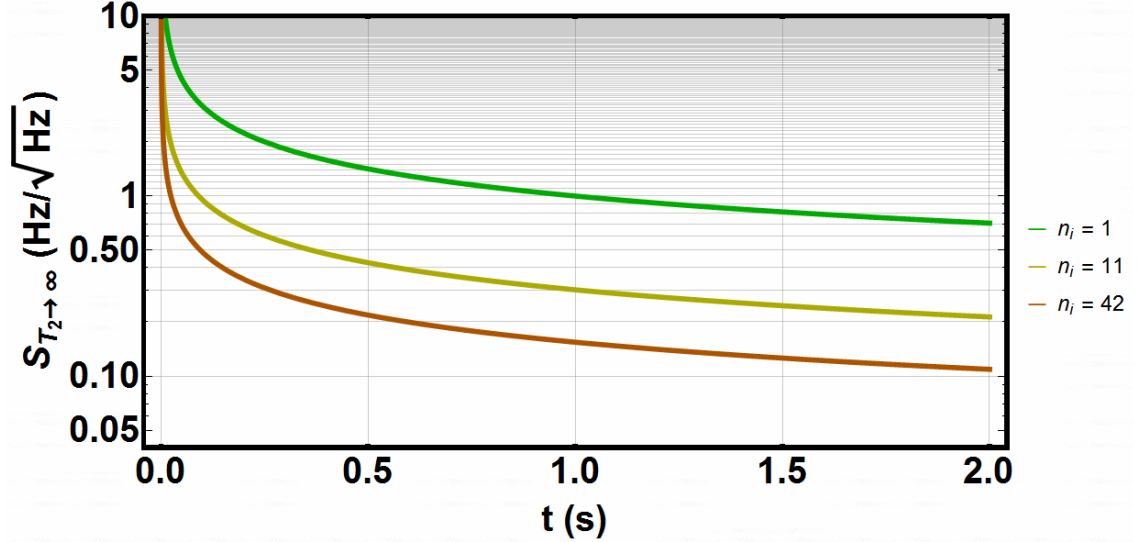


Fig. 2.15 Improvements on the standard quantum limit sensitivity from Eq. 2.42 for 1, 11 and 42 ions. 11 ions is the maximum number of ions that can be trapped in a string for a single trapping zone of the dual linear rail design outlined in Sec. 3.3.1. 42 ions is the maximum number of ions that can be trapped as strings across the four trapping regions of the dual linear rail chip outlined in Sec. 3.3.1.

This may be harder in practice as detection fidelities in current multi-ion systems typically decrease with number of ions being detected when using a PMT [47]. This would be detrimental for the sensitivity as it would increase the errors associated with population measurements (standard deviation ΔP). A proposed method is to use a CCD camera pixel or binned array of pixels as a photon detector for multi-ion sensing, this seems more reasonable than attempting to distinguish between many photons using a single PMT, although the dark count for a binned array of CCD pixels would have a much higher dark count than a PMT. This isn't ideal as the larger the dark count the lower the detection fidelity also, this is shown in Sec. 5.2.2.

2.3 Rabi oscillation numerical simulations for pulsed signals

It is likely that for some applications, like NMR and NQR sensing briefly mentioned in Sec. 1.4, that the magnetic field being detected will not have a constant magnetic field

amplitude over time and have a large signal linewidth relative to the strength of the signal. Both of these variables have an affect on how the ion population during Rabi oscillations and will change the way in which data is interpreted. NMR [48, 49, 50] and NQR [51, 52, 53, 54] sensing has been studied extensively due to the applications in biomedical and military industries. This section derives a numerical solution for these kinds of pulsed magnetic fields driving a two-level system. Note that the methods talked about in this section can be applied to any time dependent magnetic field amplitude and is not limited to NMR and NQR sensing.

2.3.1 Considerations for magnetic fields driving a two-level system

The derivation for a field driving a two-level system in Sec. 2.2.1 uses an ideal field of the form $\vec{B} = \vec{B}_0 \cos(\omega t - \vec{k} \cdot \vec{r} - \phi)$, this is a discrete, coherent signal with uniform polarisation and constant amplitude. There are four ways in which the field can deviate from this, it could:

- have a time varying amplitude
- have a large associated linewidth
- not be a coherent signal with a predictable phase
- not have uniform or predictable polarisation

If the field varies from the ideal case in any of these ways it will have an effect on the state population transfer. Because for most applications polarisation and phase can be predictable, only the effect of time varying amplitudes and large linewidth signals have on Rabi oscillations will be considered.

For time varying amplitudes driving a two-level system, like a pulse ramping up and down in time, it is preferable to have control over the time in which the pulse is created. This is because for Rabi oscillation experiments the time in which the ion is exposed to the signal needs to be reproduced many times to obtain a state population probability. This then needs to be repeated for a different duration of time to get another state population probability and so on; this is described in Sec. 5.3.2. It is also preferable to know the rate in which the pulse ramps up and down in time. This is because the Rabi frequency is dependent on the amplitude of the magnetic field (Sec. 2.2.1), meaning that the Rabi frequency will be dependent on time.

A large signal linewidth will have an effect on the state population transfer data by increasing the probability of a detuned photon driving the two-level system. The effects of a detuned field on a Rabi oscillation can be seen in Fig. 2.10. It is understood that to attain a Rabi oscillation resembling a discrete, on resonant field driving a two-level system, the Rabi frequency should be greater than the linewidth of the signal driving it [55]. This means that the magnetic field amplitude driving the system should be large relative to its linewidth.

2.3.2 Numerical simulation method for magnetic field sensing

Unlike the ideal field used to analytically derive the state population transfer in Sec. 2.2.1, there is no concise solution for fields that deviate from this; instead it is easier to derive the solution numerically. To do this we can start with the Hamiltonian solution after moving to the interaction picture and applying the rotating wave approximation similar to Eq. 2.6

$$H' = \frac{\hbar\Omega(t)}{2} \left(|\uparrow\rangle\langle\downarrow| e^{-i\delta t} e^{i\phi} + |\downarrow\rangle\langle\uparrow| e^{i\delta t} e^{-i\phi} \right), \quad (2.45)$$

except the Rabi frequency term Ω_0 has been replaced with a time dependent Rabi frequency term $\Omega(t)$ used to describe the shape of the pulse amplitude in time. From this a numerical solution can be found by solving the Schrödinger equation $i\hbar\frac{\partial}{\partial t} |\psi(t)\rangle = H' |\psi(t)\rangle$ for the initial condition $|\psi(0)\rangle = |0\rangle$.

To model the linewidth onto the Hamiltonian in Eq. 2.45, the linewidth of the signal can be modelled onto an array of detunings describing a Gaussian shaped signal. The numerical solutions for each detuning in the array can be averaged to create an approximate solution for $|\psi(t)\rangle$. The detuning array is created by using a pseudo-random variate for a Gaussian profile with a defined linewidth. A histogram of a pseudo-random variate with 2000 detunings and probability density function for a Gaussian with an arbitrary linewidth of 1000 Hz can be seen in Fig. 2.16.

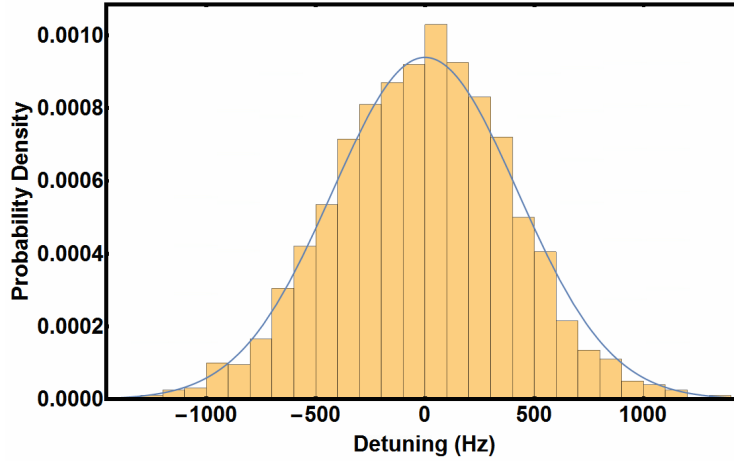


Fig. 2.16 The histogram of a pseudo-random variate of 2000 samples for a Gaussian distribution (blue line) with a linewidth of 1000 Hz.

For a static amplitude magnetic field driving the two-level system $\partial\Omega(t)/\partial t = 0$, Rabi frequencies approaching the linewidth of the field tends to cause suppression of the population measurement. This is shown in Fig. 2.17.

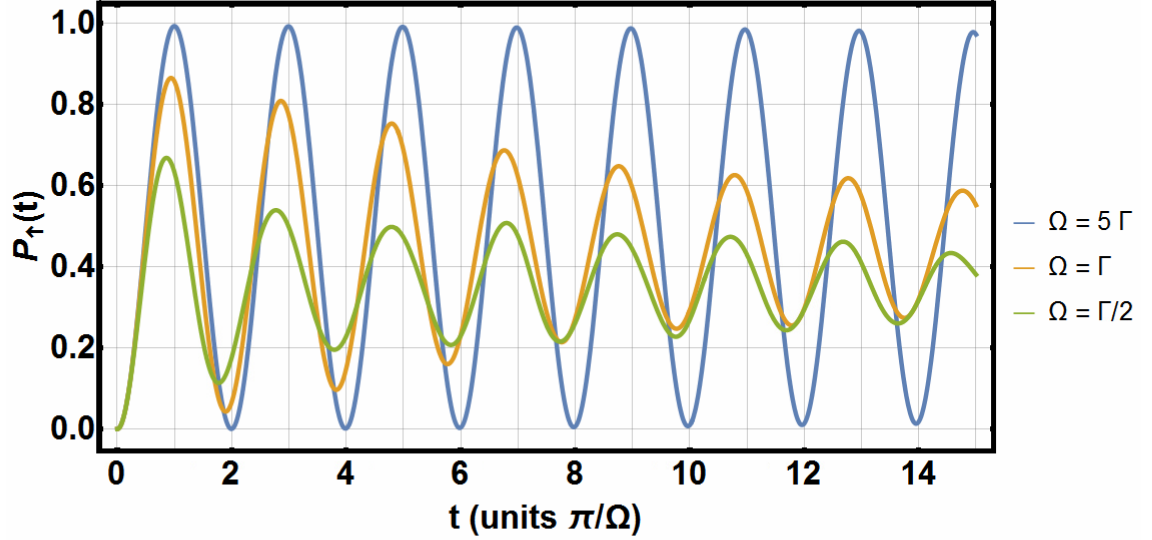


Fig. 2.17 Numerical simulation results for Rabi frequencies equal to linewidths $\Omega = 5\Gamma, \Gamma, \Gamma/2$. As the linewidth approaches and goes past the Rabi frequency the population transfer is suppressed. The suppression increases for longer measurement times due to the averaging of the separate numerical solutions for the Rabi frequency at different detunings.

2.3.3 Pulsed signal driving a two-level system

As mentioned in Sec. 1.4 NQR and NMR sensing is of interest for the medical and military industries. This means that modelling of pulsed signals driving a two-level system will be of use in the future when these applications are realised. Firstly, it is beneficial to gain a rough understanding of how these signals are typically created.

The following description for NMR signals is taken from [56, 57, 58] and the description for NQR signals is taken from [59, 51, 52, 53]. A brief description is beneficial for understanding the shape of different pulses, but a thorough introduction to NMR is beyond the scope of this thesis.

NMR signals are typically created by application of a large static magnetic field to the sample of interest containing atoms of a non-zero nuclear spin. The nuclear magnetic moment of the samples nuclei cannot align parallel to the static field due to the different energy states of the nucleus. This causes the nucleus to spin at the so-called Larmor frequency, a value directly proportional to the strength of the external magnetic field. Applying an RF pulse will tip the net magnetisation away from its equilibrium, the nuclei will then relax to its equilibrium in a process called free induction decay (FID). The properties of this signal are dependent on the physical and chemical composition of the sample, as well as the strength of the static magnetic field applied.

NQR can be induced on a quadrupolar nuclei with a spin quantum number $I > 1/2$ by application of a near resonant RF magnetic field [59]. Unlike NMR, there is no need for application of an external static magnetic field. The excited nuclei relax back to their equilibrium by a FID and produce an RF signal by doing so; the properties of this signal

are dependent on the chemical composition of the sample.

The FID signal from NMR and NQR are not coherent signals, the RF pulse they require also overlaps with the FID signal, meaning that the detector will likely detect the RF pulse used to drive the sample. A well studied method for circumnavigating this is by application of refocusing RF pulses after the FID of the sample (NMR [49, 50] and NQR [51, 52, 53]). This creates an echo from the sample that does not overlap with the RF driving resonance in a sample. A series of $m = 0, 1, 2, \dots$ refocusing pulses can be applied to create a train of pulses spaced $\mu = 2t_{sp}$ apart where t_{sp} is the time after the initial pulse that caused the FID. The individual echos slowly decay in amplitude, this can be seen in Fig. 2.18.

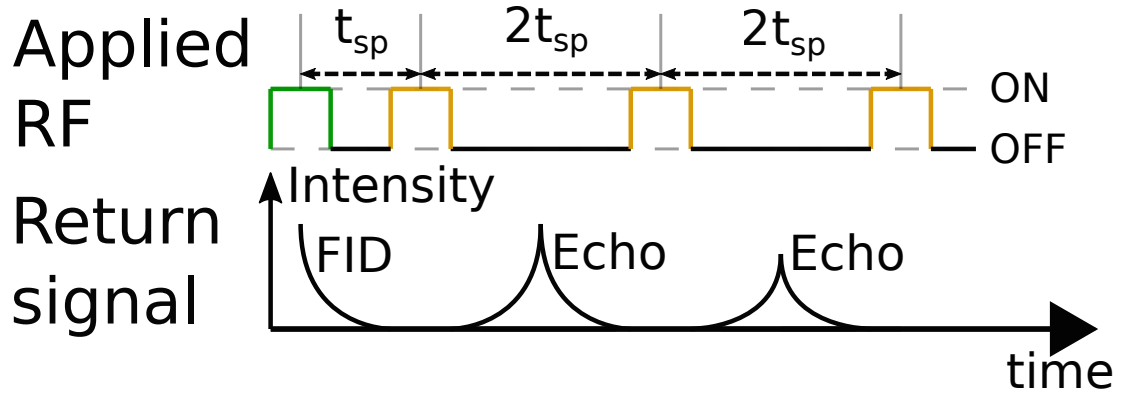


Fig. 2.18 Example pulse sequence for echo train. The preparatory pulse (green) allows the sample to FID. After some time t_{sp} , a refocusing pulse (orange) is applied to create an echo. This can be followed by a sequence of refocusing pulses spaced $\mu = 2t_{sp}$ apart to create more echos that decay in amplitude at a rate of $e^{-\eta_k(t+m\mu)}$. The timing of these pulses has been extensively studied, material on the timing and frequency of the pulses for example materials can be found in [60, 49, 50, 51, 52, 53].

The shape of the amplitude of these echoed signals has been modelled [60, 61] to have the form

$$y_m(t) = \sum_{k=1}^d \alpha_k e^{-\eta_k(t+m\mu)} e^{-\beta_k|t-t_{sp}|+i w_k(T)t}, \quad (2.46)$$

where $m = 0, \dots, M - 1$ is the echo number; $t = t_0, \dots, t_{N-1}$ denotes the sampling time, measured with respect to the center of the refocusing pulse and typically starting at $t_0 \neq 0$ to allow for the dead time between the pulse and the first measured sample; α_k is the complex amplitude, β_k is the damping constant and $w_k(T)$ is the temperature dependent frequency shifting function of the k th sinusoid. Like the frequency being detected, the values of these terms varies between samples and can be used to better determine the properties of sample being sensed. $w_k(T)$ can be removed as it is used for determining a temperature dependency of the samples echo pulses and isn't relevant for this numerical

simulation. Also the introduction of many pulses isn't of too much importance yet as averaging data over many pulses may not be necessary. For these reasons, the simulated single echo takes the form

$$y_0(t) = \alpha_k e^{-\eta_k t} e^{-\beta_k |t - t_{sp}|}. \quad (2.47)$$

From this a conversion to the time dependent Rabi frequency for a two-level system can be done in the same manor as Eq. 2.43 by

$$\Omega(t) = \frac{\mu_B}{\hbar} y_0(t). \quad (2.48)$$

Taking this general pulse waveform, we can use it as a tool for understanding how pulsed fields will effect population transfer in a two-level system. We start by assigning some arbitrary values, $\beta_1 = 500$, $\eta_1 = 0$ and $t_{sp} = 10$ ms, and giving the signal a linewidth of $\Gamma \approx 200$ Hz a reasonable value for the purpose of this simulation as it is roughly the same order of magnitude as typical Rabi frequency measurements. The decay of the signal amplitude can be plotted as shown in Fig. 2.19.

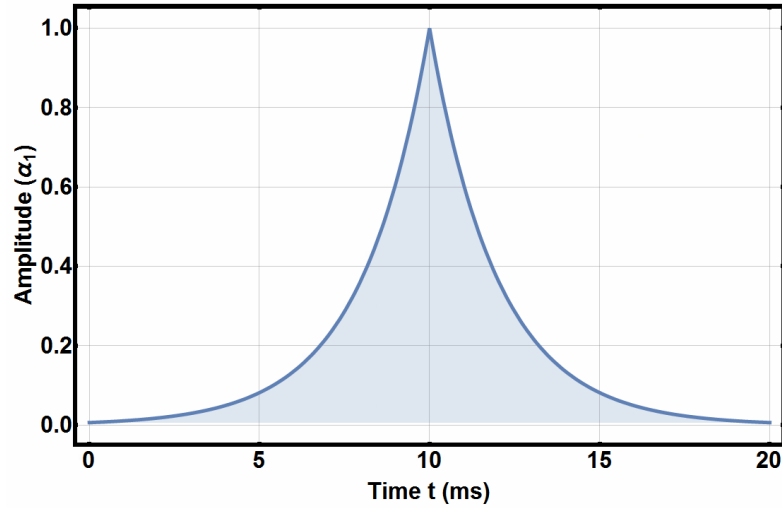


Fig. 2.19 Pulse amplitude example from Eq. 2.47 with values $\beta_1 = 500$, $\eta_1 = 0$ and $t_{sp} = 10$ ms.

For simulating the population transfer result the pulse needs a defined amplitude. The amplitude of the signal being detected is dependent on how close an emitter is to the ion, so the Rabi frequency will change depending on the distance between the sample and the ion. For this reason the amplitude Rabi frequency will be assigned to variable $\Omega_0 = (\alpha_1 \mu_B) / \hbar$. By fixing the peak Rabi frequency Ω_0 and changing the linewidth of the signal it can be seen in Fig. 2.20 that signal linewidths approaching the peak Rabi frequency causes suppression of the population transfer to a similar point as shown in Fig. 2.17. This is an undesirable situation for sensing pulses as attempting to decipher signal linewidth from a population suppression will likely give a result with a large error due to

the statistical fluctuations of the population measurements and non-ideal fidelities that are expected in state population readout measurements (Sec. 5.2.2).

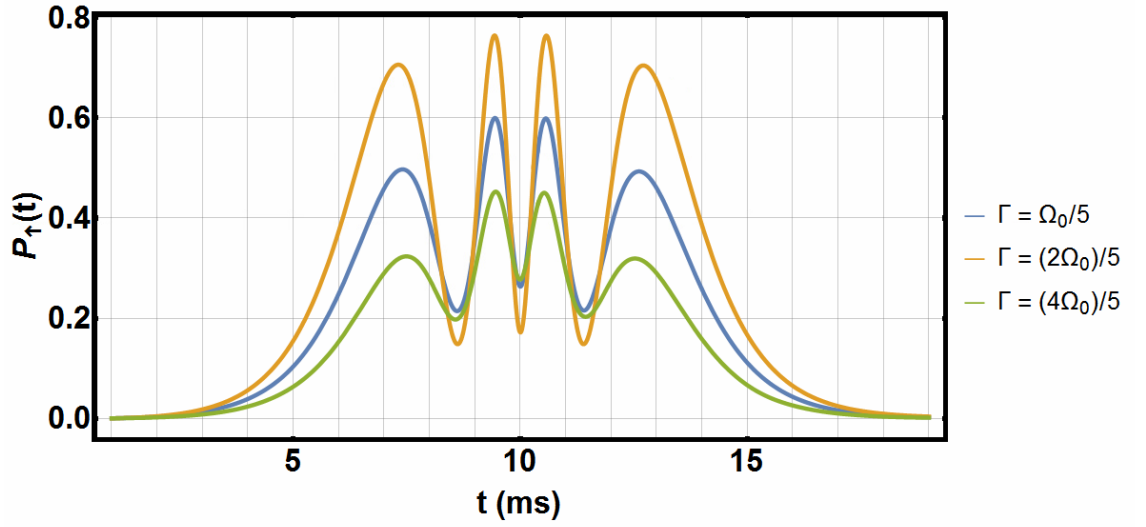


Fig. 2.20 Pulsed signal with coefficient values $\beta_1 = 500$, $\eta_1 = 0$ and $t_{sp} = 10$ ms driving a two-level system for different linewidths Γ at a fixed peak Rabi frequency $\Omega_0 = 2\pi \times 1000$ Hz.

A more likely scenario for detecting pulses would be for the signal to have a fixed linewidth and a variable peak Rabi frequency which would determine the distance between the detector and emitter. The numerical solution for this can be seen in Fig. 2.21, this result is very different to the result shown in Fig. 2.20. Potential valuable information could easily be deciphered from a measurement similar to this by counting the number of Rabi oscillations on the population and using that to determine the distance between the emitter and detector. Potentially other properties of the pulse could be measured by translating the rate of change in Rabi frequency to the coefficients describing the pulse waveform.

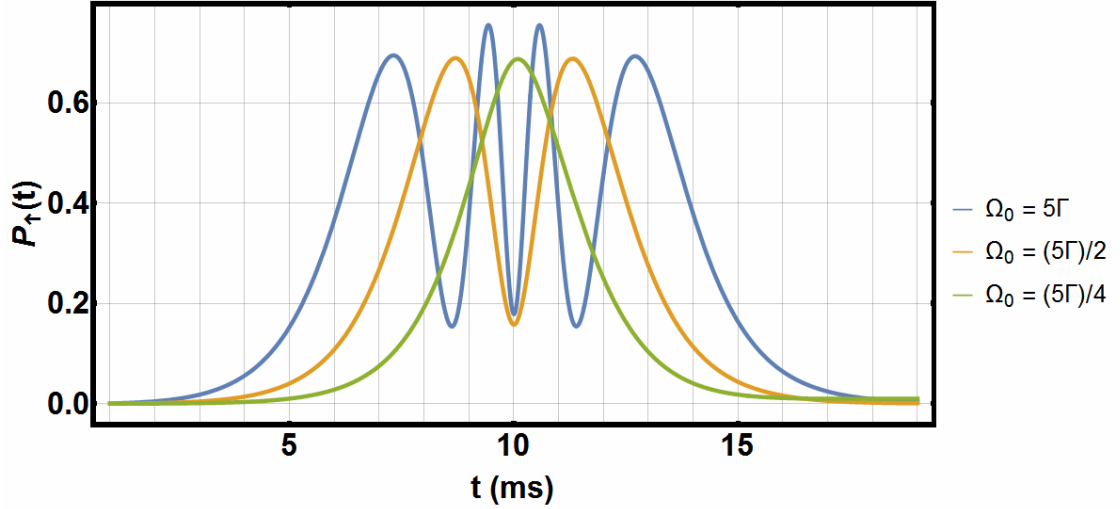


Fig. 2.21 Pulsed signal with coefficient values $\beta_1 = 500$, $\eta_1 = 0$, $t_{sp} = 10$ ms and linewidth $\Gamma = 200$ Hz driving a two-level system for different peak Rabi frequencies Ω_0 .

The feasibility for sensing pulsed signals similar to NQR or NMR signals seems prosperous. Not only could the properties of the sample be determined by measuring the fields resonance, a rough distance between the detector and the sample could also be deciphered. One short coming would likely be relatively long data acquisition time due to the nature of the experiment. A continued investigation on the potential for applications by this method is currently being conducted by Ph.D. student Harry Bostock.

3 Ion trapping for magnetometer applications

This chapter focuses on the fundamentals for trapping ions by application of RF and DC electric fields in Paul traps [62], optimizing geometries for magnetometer applications, analytical and numerical simulation results and fabrication techniques currently being implemented. The motivation for this is based on the improvements in magnetometer sensitivity that are achievable when sensing with multiple trapped ions (Sec. 2.2.6). There is also the need for minimising the space required for the ion trap as space will eventually become a concern when the device becomes portable (Sec. 7). Two trap designs are considered here, a simple linear design² and a dual linear design with a single electrode layer that has been optimized for sensing applications. This section will focus on the analytical and numerical solutions for the electric fields produced for each design, followed by the design considerations and fabrication process for the dual linear design.

3.1 Electric fields, ion motion and stability in ion traps

This section describes how to confine ions using only electric fields and how to select appropriate trapping parameters for any arbitrary trap geometry. Confining ions at a point in space requires a force to be acting on the ion in three dimensions so that it is constantly being pushed into a nil position where the force acting on the ion is equal in all directions. A common form of confinement is the Penning trap [63] which uses a strong magnetic field combined with static voltages to create a quadrupole electric potential to confine ions. The magnetic field confines the ion in two dimensions (radial confinement) by creating a zero field position at the central third axis of the trap due to magnetic repulsion, the electric fields repel the ions from the two sides of this axis (axial confinement) so that the ions are confined to a single nil position. This method boasts a significant advantages over Paul traps which is they confine ions with only static fields, this means that there is no heating of ions even in large ion crystals due to micro-motion (discussed in Sec. 3.1.2). A common configuration for this is the ring trap whose ideal geometry is shown in Fig. 3.1. However they do not possess the freedom to rotate the principal axis of the ion crystal (described in Sec. 3.2.2) and the presence of a large magnetic field means that the sensing protocols described in this thesis would not be valid as the static magnetic field required for sensing needs to have a high level of tuneability so that multiple Zeeman splittings can be used for sensing different frequencies (Described in Sec. 2.1.3).

²Developed by the National University of Defence Technology, Changsha, Hunan, China.

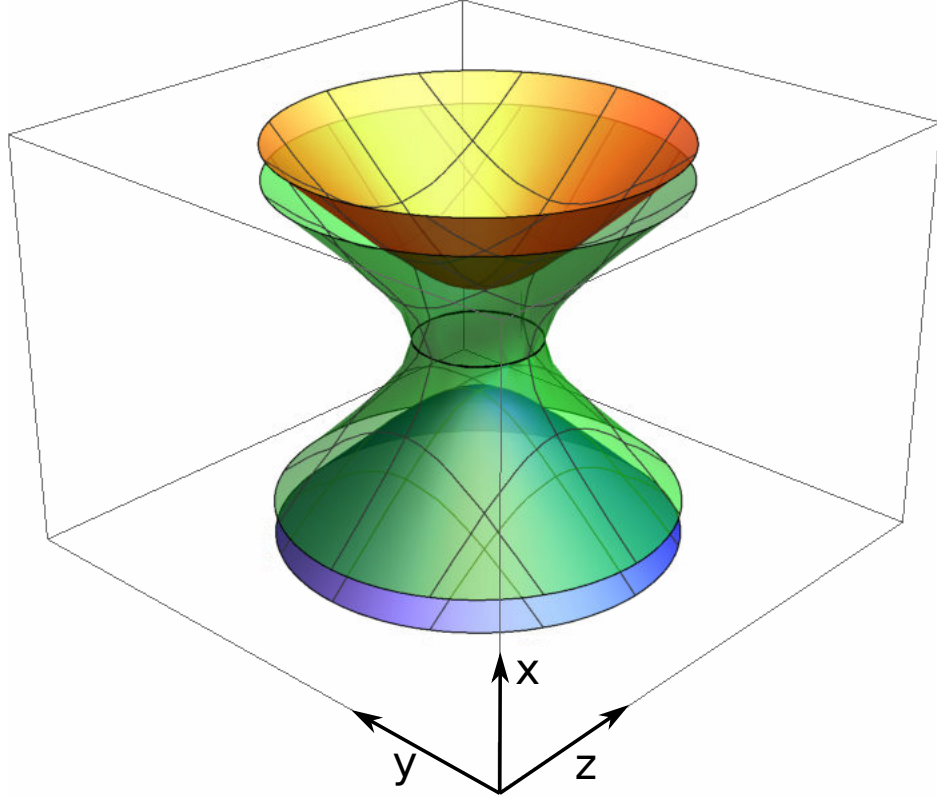


Fig. 3.1 Hyperbolic ring trap geometry ideal for Penning traps where the green electrode confines ions in the y - z plane via static magnetic fields and the end caps confine ions in the x axis via static electric fields.

Unlike a Penning trap, Paul traps use an RF electric field for radial confinement and DC electric fields for axial confinement to create a nil field trapping position. This is because of the incongruity between Gauss's Law and the resultant electrostatic force required for confining ions. Gauss's law states that the divergence of an electric field $E(z)$ in free space is equal to zero $\nabla \cdot E(z) = 0$, where $E(z) = -\nabla \cdot \Phi(z)$ which gives $\nabla \cdot^2 \Phi(z) = 0$, which is the Laplace equation and is also stated by Earnshaw's theorem [64]. A result of this (from Earnshaw's theorem) is that the electrostatic force acting on the ion $F(z)$ (stemming from $\Phi(z)$ as described above) cannot hold a charge in a stable equilibrium, meaning that confinement of ions using static electric fields is unattainable.

To circumvent this, an alternating potential $\phi(t) = V_{RF} \cos(\Omega t)$ is applied to the trap electrodes. This results in a rotating saddle potential that confines the ion radially, this can be imagined as the force on the ion constantly rotating around it so that the time averaged force creates stable confinement. This two dimensional radial confinement can be used with static electric fields for axial confinement producing three dimensional confinement of an ion. An ideal hyperbolic geometry for the RF electrodes is shown in Fig. 3.2. This produces a linear quadrupole RF potential when the electrode lengths extend to infinity.

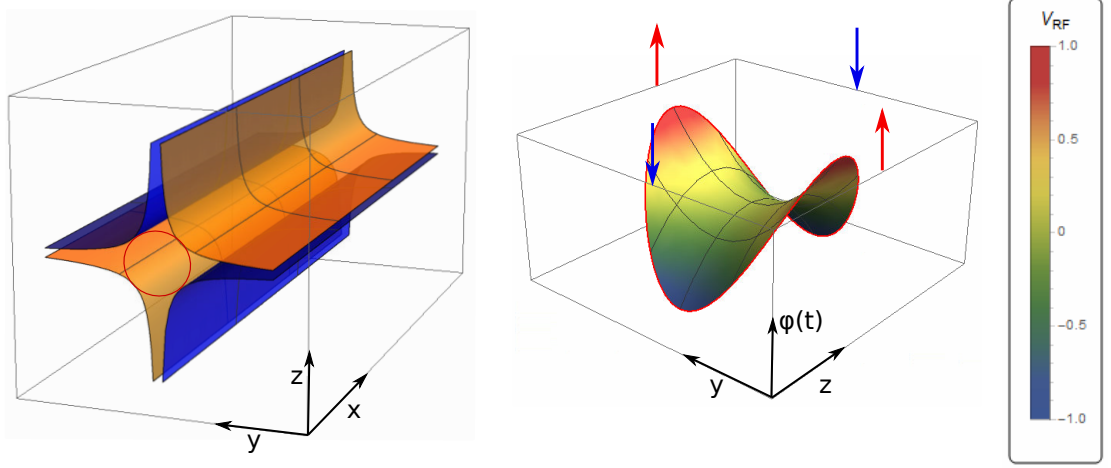


Fig. 3.2 (Left) Ideal hyperbolic geometry for the RF electrodes in a linear Paul trap when electrodes extend to infinity (not shown). Blue and orange electrodes have potentials $-(1/2)V_{RF} \cos(\Omega t)$ and $(1/2)V_{RF} \cos(\Omega t)$ applied to them respectively. The nil position would be at the centre of the four electrodes, the red circle on the y - z plane is a cross section, visual aid for the RF saddle potential. (Right) Saddle potential created by the RF electrodes within the red circle, the four arrows represent the sinusoidal amplitudes about the y - z plane that each oscillate at a frequency equal to Ω .

3.1.1 Pseudopotential approximation and ion secular motion

Most modern Paul traps [65, 66, 67] use a combination of two dimensional radial confinement via application of RF electric fields and one dimensional axial confinement via application of DC electric fields as described here; though the geometries are not equivalent to the ideal hyperbolic structures shown here as it is not possible to extend the geometries to infinity and the need for more complex systems trapping many ions in different locations and size constraints will limit the the geometries accessible.

The following analytical derivations for fields and forces acting upon an ion in a Paul trap are from Hughes *et al.* [65] and Olmschenk [68]. To calculate the time-averaged force induced on the ion from a rotating saddle potential, we can consider the spatial dependence of the electric field in one axis $E(z)$ and the time dependence of the field $\cos(\Omega t)$. For this case, the force acting on an ion of mass m and charge e is $F = -eE$, meaning the equation of motion can be written as

$$m \frac{d^2 z}{dt^2} = -eE(z) \cos(\Omega t), \quad (3.1)$$

which can be solved for an ion initially at position z_0

$$z(t) = \frac{e}{m\Omega^2} E(z) \cos(\Omega t) + z_0. \quad (3.2)$$

From this it can be seen that the ions motion for a homogeneous $E(z)$ will have a relatively simple motion and give a time averaged force induced on the ion equal to zero,

though this is not the case as $E(z)$ is slightly inhomogeneous near the centre of the trap. Typically the differential equations of motion for this cannot be solved analytically and require numerical simulations to calculate [69]. In the presence of a slightly inhomogeneous field an analytical solution can be calculated by Taylor expanding $E(z)$ around the position z_0 , this gives

$$\begin{aligned} E(z) &= E(z_0) + \left. \frac{\partial E(z)}{\partial z} \right|_{z_0} (z - z_0) + \dots \\ &\approx E(z_0) + \frac{\partial E(z_0)}{\partial z} \frac{e}{m\Omega^2} E(z_0) \cos(\Omega t), \end{aligned} \quad (3.3)$$

which allows the force induced on the ion to be expressed as

$$F(z) \approx -eE(z_0) \cos(\Omega t) - \frac{\partial E(z_0)}{\partial z} \frac{e^2}{m\Omega^2} E(z_0) \cos^2(\Omega t). \quad (3.4)$$

From this the time averaged force over one oscillation period can be calculated ($\langle \cos(\Omega t) \rangle = 0$ and $\langle \cos^2(\Omega t) \rangle = 1/2$) to be

$$\langle F(z) \rangle \approx -\frac{\partial E(z_0)}{\partial z} \frac{e^2}{m\Omega^2} E(z_0) = -e \frac{\partial \Psi(z_0)}{\partial z}, \quad (3.5)$$

where

$$\Psi(z_0) = \frac{e}{4m\Omega^2} E^2(z_0). \quad (3.6)$$

This is known as the pseudopotential or time averaged confining potential acting on the ion. In order to solve the equations of motion in all three axes, a general definition for the pseudopotential and time averaged force acting on the ion can be given as

$$\Psi(x, y, z) = \frac{e}{4m\Omega^2} |\vec{E}(x, y, z)|^2, \quad (3.7a)$$

$$\langle \vec{F}(x, y, z) \rangle = -e \nabla \cdot \Psi(x, y, z). \quad (3.7b)$$

Now to disentangle the RF and DC fields from each other, a general expression for the quadrupole potential from the RF electrodes can be expressed as

$$\phi_{RF}(x, y, z, t) = \eta_{RF} V_{RF} \left(\frac{\alpha x^2 + \beta y^2 + \gamma z^2}{2r_0^2} \right) \cos(\Omega t), \quad (3.8)$$

where r_0 is the distance from the centre of the trap to the RF electrodes and η_{RF} is a geometric factor that is unitary for the hyperbolic electrodes and decreases as the geometry deviates from perfect [70]. α , β and γ are dependent on the geometry of the RF electrode hyperboloids, following the derivations presented in [71]. For a linear trap geometry as shown in Fig. 3.2 they have the values $\beta = -\gamma = 1$ and $\alpha = 0$. This gives an expression for the RF potential in the y-z plane as

$$\phi_{RF}(y, z, t) = \eta_{RF} V_{RF} \left(\frac{y^2 - z^2}{2r_0^2} \right) \cos(\Omega t). \quad (3.9)$$

The resulting electric field from this potential is expressed as

$$\begin{aligned} \vec{E}(y, z, t) &= -\nabla \cdot \phi_{RF}(y, z, t) \\ &= -\frac{\eta_{RF} V_{RF}}{r_0^2} \cos(\Omega t) (y - z) \\ &= -\vec{E}(y, z) \cos(\Omega t). \end{aligned} \quad (3.10)$$

Now by inserting $\vec{E}(y, z)$ into Eq. 3.7a, we get

$$\Psi(y, z) = \left(\frac{e}{4m\Omega^2} \frac{\eta_{RF}^2 V_{RF}^2}{r_0^4} (y^2 + z^2) \right), \quad (3.11)$$

the pseudopotential approximation for this case is visually represented in Fig. 3.3.

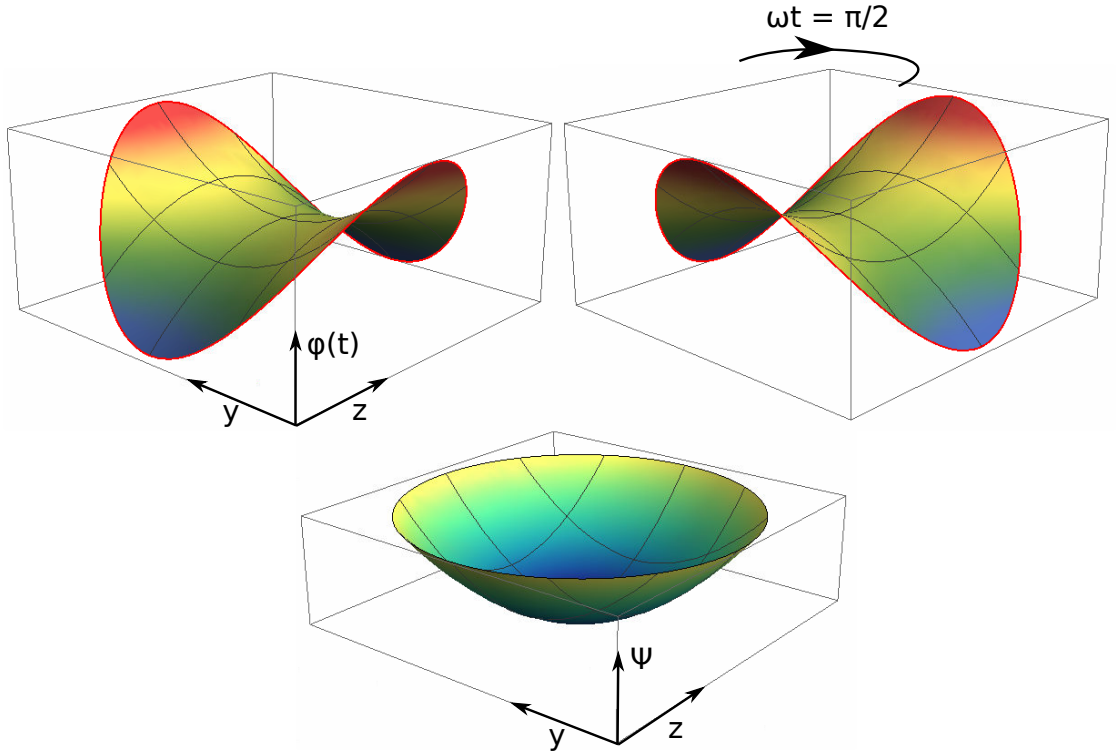


Fig. 3.3 (Top) Eq. 3.9 shown visually in the x - y plane for ideal electrode configuration in Fig. 3.2 with a $\pi/2$ rotation of the potential shown. (Bottom) Pseudopotential of the field averaged over one full rotation of the electric potential $\Phi(t)$.

From this, the time averaged force induced on the ion by the RF field in this plane can be expressed as

$$\begin{aligned}
\langle \vec{F}(y, z) \rangle &= -e \nabla \cdot \Psi(y, z) \\
&= -e \nabla \cdot \left(\frac{e}{4m\Omega^2} \frac{\eta_{RF}^2 V_{RF}^2}{r_0^4} (y^2 + z^2) \right) \\
&= -\frac{e^2 \eta_{RF}^2 V_{RF}^2}{2m^2 \Omega^2 r_0^4} (x + y),
\end{aligned} \tag{3.12}$$

which is also the force from a quantum harmonic oscillator potential in two dimensions. The characteristic secular frequency ω_r of the ion trap is

$$\omega_y = \omega_z = \omega_r = \frac{e\eta_{RF}V_{RF}}{2m\Omega r_0^2}. \tag{3.13}$$

Though both radial secular frequencies are equal for the ideal case, in reality any deviation from the ideal electrode geometry will result in asymmetrical secular frequencies. The trap's axial secular frequency induced from the DC endcap electrodes can be found in the same manor except there is no need for a time averaged force as the fields are static. The potential from which this can be solved is expressed as

$$\phi_{DC}(x, t) = \eta_{DC} V_{DC} \left(\frac{2x^2 - (y^2 + z^2)}{2x_0^2} \right), \tag{3.14}$$

where x_0 is the distance from the centre of the trap to the endcap electrodes and η_{DC} is a geometric factor that is unitary for hyperbolic geometries and deviates from this for non hyperboloids and the geometry offset from the RF electrodes [72]. The axial secular frequency ω_x for this type of quantum harmonic oscillator can be expressed as

$$\omega_x = \frac{\sqrt{2}e\eta_{DC}V_{DC}}{mx_0^2}. \tag{3.15}$$

3.1.2 Stability parameters and ion micro-motion

The above derivation is useful for finding general trap depths and secular frequencies by approximating the oscillating fields to a static pseudopotential, but it doesn't take into consideration ion motion that could result in unstable trajectories where the ion accumulates enough energy to leave the trap. The unstable trajectories are only a consideration in the y - z plane as this is the plane in which the RF pseudopotential approximation is made. The derivation that follows equates the ions motion in this plane to a set of Mathieu equations to determine the relationship between trapping parameters and stable ion trajectories [73].

By looking at the potential around the trap nil for a linear RF electrode configuration, the combined RF and DC potential can be expressed as a combination of Eq. 3.9 and Eq. 3.14

$$\Phi(x, y, z, t) = \eta_{RF} V_{RF} \left(\frac{y^2 - z^2}{2r_0^2} \right) \cos(\Omega t) + \eta_{DC} V_{DC} \left(\frac{2x^2 - (y^2 + z^2)}{2x_0^2} \right). \tag{3.16}$$

Assuming the ions motion in the three axes is uncoupled, the equations of motion for the ion in the y and z axes can be equated to each other with opposite signs. The equation of motion for the ion in the y and z axes are

$$\frac{d^2y}{dt^2} = -\frac{e}{m} \left(\frac{\eta_{RF} V_{RF}}{r_0^2} \cos(\Omega t) - \frac{\eta_{DC} V_{DC}}{x_0^2} \right) y, \quad (3.17a)$$

$$\frac{d^2z}{dt^2} = \frac{e}{m} \left(\frac{\eta_{RF} V_{RF}}{r_0^2} \cos(\Omega t) - \frac{\eta_{DC} V_{DC}}{x_0^2} \right) z. \quad (3.17b)$$

By making the following substitutions

$$\Omega t = 2\zeta, q_z = -q_y = \frac{2\sqrt{2}\omega_r}{\Omega} = \frac{2e\eta_{RF}V_{RF}}{m\Omega^2r_0^2} \text{ and } a_z = -a_y = -\frac{4e\eta_{DC}V_{DC}}{m\Omega^2x_0^2}, \quad (3.18)$$

the equations of motion can be expressed as a standard Mathieu differential equations

$$\frac{d^2i}{d\zeta^2} + (a_i - 2q_i \cos(2\zeta))i = 0 \text{ and } i = [y, z]. \quad (3.19)$$

The solutions to the Mathieu equations have an infinite number of solutions, but only stable periodic solutions will result in trapped ions. The Floquet theorem [73] can be used to obtain stable solutions; for the case of linear ion traps where $a_i < q_i^2 \ll 1$ a solution for y and z is given by [66]. The resulting plot in a and q space is well studied with numerical solutions [66] and works as a visual aid to see the stable solutions to the Mathieu equations. This allows for selection of trap DC voltages, RF voltages and RF frequencies that will result in a stable ion trajectory and thus, a stable ion trap.

A simpler solution can be produced where $a_i = 0$ and $q_i^2 \ll 1$ which is common in ion traps as this is attained when there is no DC offset at the ions position in the trap $V_{DC} = 0$. The result gives the ions motion in the z axis as [65]

$$z(t) = \left(1 + \frac{q_z}{2} \cos(\Omega t) \right) z_0 \cos(\omega_z t), \quad (3.20)$$

where ω_z is the secular frequency in the z axis as shown in Eq. 3.13. This solution is equivalent to the solution for the ion motion in the y axis. The q parameter can be substituted for a secular frequency term from the substitutions in Eq. 3.18 to give the solution

$$z(t) = \left(1 + \frac{\sqrt{2}\omega_z}{\Omega} \cos(\Omega t) \right) z_0 \cos(\omega_z t). \quad (3.21)$$

This solution describes the ions two types of motion; secular motion ω_z which is a result of the pseudopotential approximation and describes the larger motion of the ion, and micro-motion which is caused by the fast oscillating RF field Ω . From the solutions to the Mathieu equations [66], when $q = \frac{2\sqrt{2}\omega_z}{\Omega} < 0.9$ the ions trajectory would be stable,

or equivalently $\Omega/\omega_z \geq \alpha$ where $\alpha = 2\sqrt{2}/0.9 \approx 3.14$. The ions trajectory for different values of Ω/ω_z are shown in Fig. 3.4 with stable and unstable trajectories.

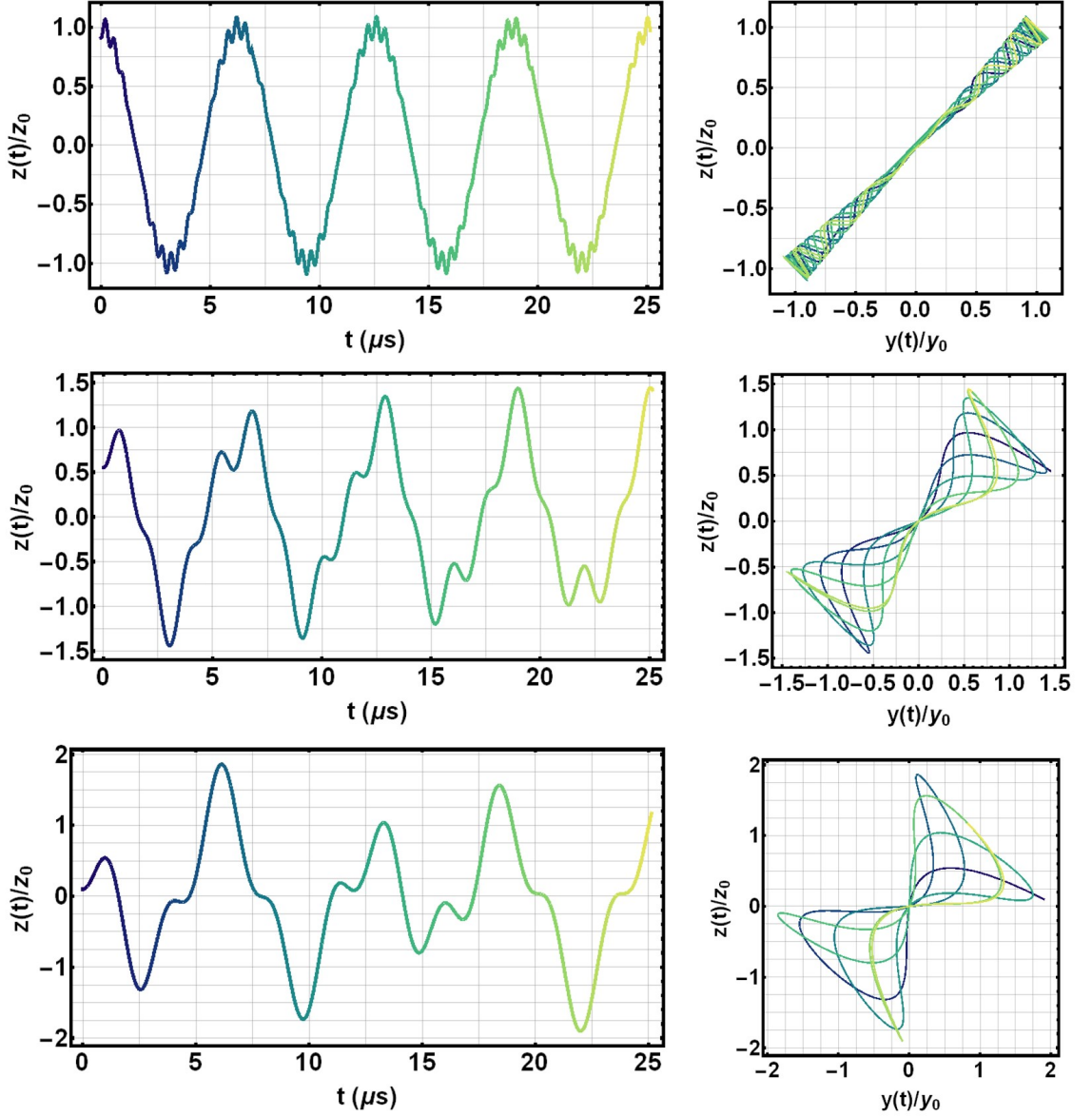


Fig. 3.4 Plots of ions combined secular and micro motion for different values of Ω/ω_r in a linear hyperbolic electrode configuration, where ω_r is fixed at 1 MHz and each graph displays four periods of ω_r . Ions motion in the z axis against time (left) and parametric plot of ions motion in the y - z plane (right) for the same length of time where a colour function maps this. Ω/ω_r ratios are $\Omega/\omega_r = 5\alpha$ for a stable trajectory (top), $\Omega/\omega_r = \alpha$ for an ion trajectory on the precipice of being unstable (middle) and $\Omega/\omega_r = 0.5\alpha$ where the ions trajectory has become unstable (bottom).

The previous section has given insight to how RF fields in ideal trap geometries create a pseudopotential. How the ions motion is affected by these fields and how to avoid unstable trajectories when choosing trapping voltages and trap frequencies for hyperbolic trap geometries, this is later used for optimising non-ideal geometries like the 2D surface

Paul trap.

3.2 Methods for simulating 2D linear paul traps

The analytical solutions mentioned in the previous section give a general idea of how Paul traps work for ideal geometries. Unfortunately the problem is not this simple when designing an ion trap for sensing, where many ions trapped in a small region of space across a 2D surface is ideal. When designing and testing 2D surface Paul traps for sensing, there were two methods in which designs were simulated. A combination of analytical and numerical simulations were carried out on multiple chip designs before the optimal designs were chosen. This section goes over the analytical and numerical methods used for simulating the simple linear trap used in Sec. 5.

3.2.1 Basis function technique

The following analytical model was derived in [74] and [75]. The derivation is for the electric fields produced from 2D rectangular electrodes with a gap-less approximation for adjacent electrodes, meaning we assume that the electrodes occupy an entire plane and extend to infinity with no gaps between electrodes. This provides an accurate model for trap chips where the gaps between electrodes are much smaller than the feature size of the electrodes. The model eventually described here is for a combination of RF electrodes and grounded electrodes. Axial confinement simulations from DC electrodes are explored in the numerical simulations in the next section.

We start with a basic definition for the electric potential $\Phi_i(\mathbf{x})$ generated from an arbitrary rectangular 2D electrode i in the x-y plane as shown in Fig. 3.5 is

$$\Phi_i(\mathbf{x}) = \frac{\phi_i}{2\pi} \left(\arctan \left[\frac{(x_{2,i} - x)(y_{2,i} - y)}{z\sqrt{z^2 + (x_{2,i} - x)^2 + (y_{2,i} - y)^2}} \right] - \arctan \left[\frac{(x_{1,i} - x)(y_{2,i} - y)}{z\sqrt{z^2 + (x_{1,i} - x)^2 + (y_{2,i} - y)^2}} \right] - \arctan \left[\frac{(x_{2,i} - x)(y_{1,i} - y)}{z\sqrt{z^2 + (x_{2,i} - x)^2 + (y_{1,i} - y)^2}} \right] - \arctan \left[\frac{(x_{1,i} - x)(y_{1,i} - y)}{z\sqrt{z^2 + (x_{1,i} - x)^2 + (y_{1,i} - y)^2}} \right] \right), \quad (3.22)$$

where $\mathbf{x} = (x, y, z)$. This is valid if the potential ϕ_i applied to the electrode is constant over the entire electrode surface.

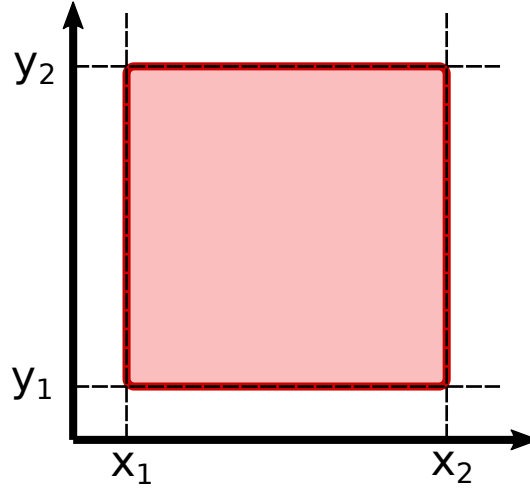


Fig. 3.5 Rectangular electrode geometry with co-ordinates x_1 , x_2 , y_1 and y_2 described by Eq. 3.22.

The solution for many electrodes with potentials $\Phi_i(\mathbf{x})$ is

$$\Phi(\mathbf{x}) = \sum_i \Phi_i(\mathbf{x}). \quad (3.23)$$

Summing electrode potentials in this way is better known as the basis function technique. A justification and proof for this technique is given by [76], in the context of this thesis the problem reduces to a more simple definition for electric fields based on the following constraint and assumptions:

- The geometries being used are all linear configurations of electrodes
- The linear electrodes extend to infinity in the x axis
- The RF trapping frequency applied to the electrodes has a much longer wavelength than the width of the RF electrodes

This is valid as linear-based geometries were considered to be optimal for sensing applications due to these geometries being capable of trapping the largest numbers of ions. The width of the electrodes in fabricated ion traps is typically much shorter than the length [65, 67, 77] of the RF frequencies used and typically have wavelengths of around $10^6 \mu\text{m}$ and the RF electrode widths are typically around $10^3 \mu\text{m}$.

Allowing the electrodes length in x to extend to infinity, $x_1 \rightarrow -\infty$ and $x_2 \rightarrow \infty$, Eq. 3.22 can be simplified to

$$\Phi_i(y, z) = \frac{\phi_i}{\pi} \left(\arctan \left[\frac{(y_2 - y)}{z} \right] - \arctan \left[\frac{(y_1 - y)}{z} \right] \right). \quad (3.24)$$

From here, multiple linear-based geometries can be considered for trapped ion magnetometry.

3.2.2 Analytical method and solution for simple linear chip design

The simple linear chip design consists of two RF electrodes and three grounded electrodes as shown in Fig. 3.6, for the analytical simulation all of the electrode lengths extend to infinity in the x axis as mentioned before. The more complex dual linear design that was fabricated initially exhibited glow and as a result could not trap ions which is explained in appendix B. Using Eq. 3.24 for individual RF electrodes and putting them into Eq. 3.23 an expression for the potential generated by the two electrodes with equal potentials ϕ applied to them can be given as

$$\begin{aligned} \Phi(y, z) = \frac{\phi}{\pi} & \left(\arctan \left[\frac{(a_2 - y)}{z} \right] - \arctan \left[\frac{(a_1 - y)}{z} \right] \right. \\ & \left. + \arctan \left[\frac{(b_2 - y)}{z} \right] - \arctan \left[\frac{(b_1 - y)}{z} \right] \right). \end{aligned} \quad (3.25)$$

From this, the pseudopotential approximation can be made by using the relation $\mathbf{E}(y, z) = -\nabla \cdot \Phi(y, z)$ and inserting the electric field into Eq. 3.7a to give

$$\Psi(y, z) = \frac{e^2}{4m\Omega^2} (\nabla \cdot \Phi(y, z))^2, \quad (3.26)$$

which allows us to find some initial features of the simple linear chip such as:

- Trap depth Ξ
- Ion height h
- Principal axis of rotation α
- Radial secular frequencies ω_z and ω_y
- In-homogeneously mapped q parameter

All of which are necessary when designing an ion trap geometry and selecting trapping parameters such as RF voltage V_{RF} and frequency Ω . The rest of this section will focus on selecting the correct trapping parameters.

Trap depth and ion height

By plotting Eq. 3.26 the trap depth Ξ and ion height h of the simple linear trap can be found, this is shown in Fig. 3.6.

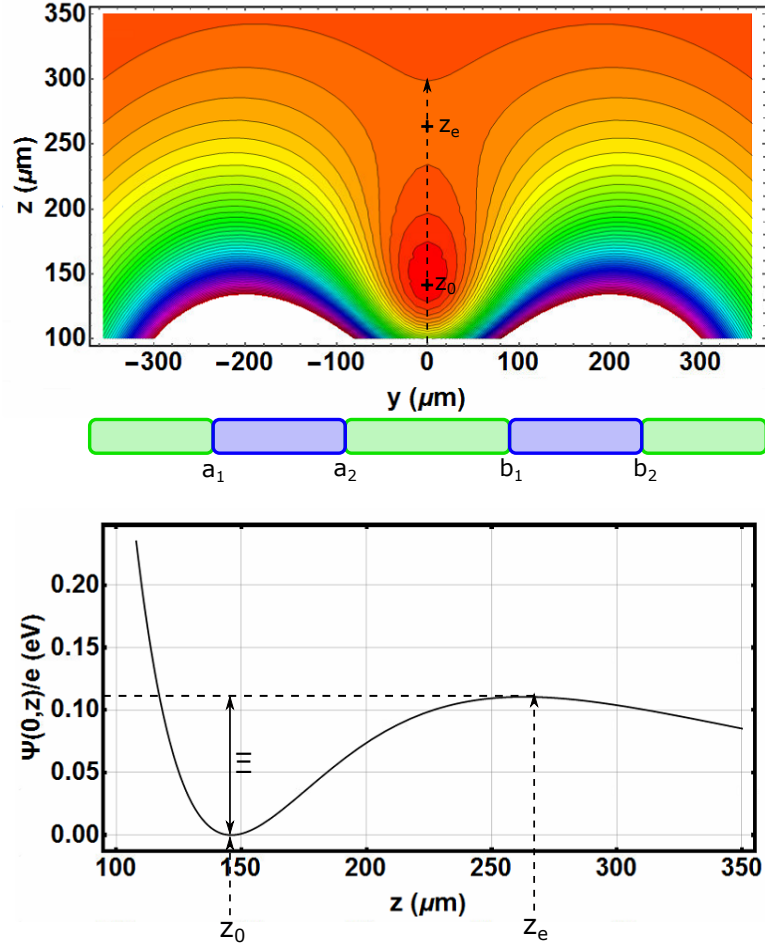


Fig. 3.6 Analytical simulation for simple linear Paul trap. (Top) Contour plots of the traps potential with the traps ion height $z_0 = 147\mu\text{m}$ and escape position $z_e = 268\mu\text{m}$ marked and electrode geometries in the y plane drawn below with $a_1 = -237\mu\text{m}$, $a_2 = -90\mu\text{m}$, $b_1 = 90\mu\text{m}$ and $b_2 = 237\mu\text{m}$. (Bottom) Pseudopotential at $y = 0$ showing the ions height, escape position and trap depth $\Xi = 0.11$ eV for a trapping frequency of $\Omega = 2\pi \times 16.61$ MHz and trapping voltages $V_{RF} = 200$ V.

These values for different linear electrode geometries have been studied in [78], where it was shown that the values can be calculated as

$$\Xi = \frac{e^2 V_{RF}^2}{\pi^2 m \Omega_{RF}^2 \hbar^2} \kappa_{RF}, \text{ with } h = \frac{\sqrt{abc(a+b+c)}}{b+c}. \quad (3.27)$$

Here, κ_{RF} is a geometric factor that takes the form

$$\kappa_{RF} = \left[\frac{2\sqrt{abc(a+b+c)}}{(2a+b+c)(2a+b+c+2\sqrt{a(a+b+c)})} \right]^2, \quad (3.28)$$

where $a = b_1 - a_2 = 180 \mu\text{m}$, $b = a_2 - a_1 = 147 \mu\text{m}$ and $c = b_2 - b_1 = 147 \mu\text{m}$. Optimization of these values to maximize trap depth for a given ion height have been studied [78] and are discussed in Sec. 3.3.1 for the dual linear chip design. The ion height

is found to be $h = z_0 = 147 \mu\text{m}$ with a trap depth of $\Xi = 0.11 \text{ eV}$ for an arbitrarily applied RF peak voltage of $V_{RF} = 200 \text{ V}$ and trap frequency of $\Omega = 2\pi \times 16.61 \text{ MHz}$ (same as the frequency of the resonant circuit in Sec. 4.3.1).

Principal axis and secular frequency

Cooling ions with a laser requires the laser light to be incident upon the ion at an angle that allows the ions motion to be suppressed in all dimensions. As discussed for the ideal hyperbolic trap in Sec. 3.1.2, the ions exhibits secular motion in all three axis, this means that the cooling laser needs to be directed at an angle that can cool motion in all these dimensions. The principal axis of the trap is defined by the eigenvector solutions to the Hessian matrix which describes the curvature of the potential confining the ion in space at the nil position. One eigenvector solution for the simple linear chip design is shown by the dashed black line in Fig. 3.6 (left) passing through the trap nil position z_0 and the escape position z_e . Note the worked through solution for these eigenvectors as shown below would not result in an ion cooled in all three dimensions when the cooling laser is parallel to the chip surface. This is because the cooling laser and secular motion in the z axis ω_z are orthogonal meaning that motion in this axis isn't suppressed. To get around this, DC voltages used to trap ions in the axial direction x are used to rotate the principal axis.

The Hessian matrix [79] for ion traps is a matrix comprised of the second order derivatives of the pseudopotential calculated from the trapping potential at the traps nil position, for the 2D analytical solution it can be written as

$$\mathcal{H}(\Psi(y, z)) = \begin{pmatrix} \frac{\partial^2 \Psi}{\partial y^2}(y_0, z_0) & \frac{\partial^2 \Psi}{\partial y \partial z}(y_0, z_0) \\ \frac{\partial^2 \Psi}{\partial z \partial y}(y_0, z_0) & \frac{\partial^2 \Psi}{\partial z^2}(y_0, z_0) \end{pmatrix}. \quad (3.29)$$

From which the eigenvector solutions $\mathbf{e}_i = \{y, z\}$ for Fig. 3.6 are $\mathbf{e}_1 = \{1, 0\}$ and $\mathbf{e}_2 = \{0, 1\}$ with associated eigenvalues λ_i which give the curvature of the field in the direction of the eigenvector. Notice that the eigenvectors are orthogonal, this is the same for all eigenvector solutions to the Hessian matrix. For this solution the principal axis (defined by the eigenvectors) rotation from the trap normal $\mathbf{n} = \{0, 1\}$ is $\alpha = 0^\circ$, a calculation of the angle between any eigenvector solution and trap normal can be made by using

$$\cos(\alpha) = \frac{\mathbf{n} \cdot \mathbf{e}_i}{\|\mathbf{n}\| \|\mathbf{e}_i\|}, \quad (3.30)$$

where $\|\mathbf{e}_i\| = \sqrt{\mathbf{e}_i \cdot \mathbf{e}_i}$. The eigenvalue solutions to this can also be used to calculate the ions secular frequency in the direction of the eigenvectors corresponding to the principal axis [80]

$$\omega_i = \sqrt{\frac{m}{\lambda_i}}. \quad (3.31)$$

The radial secular frequencies for Fig. 3.6 are $\omega_1 = \omega_2 = 2\pi \times 1.457$ MHz corresponding to the y and z axis secular frequencies respectively due to the eigenvectors being parallel to the trap axis in this case, the symmetry arises due to the principal axis of rotation being zero ($\alpha = 0$). This solution for calculating the secular frequencies is the preferred method over Eq. 3.13 as the geometric factor η_{RF} is unknown. The value of this can be found as the ratio of the hyperbolic secular frequency and the secular frequency described in this section $\omega_{i,hyp}/\omega_i$.

Inhomogeneously mapped q parameter

Due to the large difference between the quantum harmonic oscillator potential derived for hyperbolic electrodes in Sec. 3.1 and the asymmetrical potential derived in this section and for other 2D linear based designs, the q parameter from Eq. 3.18 needs to be mapped to the inhomogeneity of the field on a 2D linear trap so that the correct RF trapping voltage and frequency can be selected. This is due to there being evidence presented in [81] showing that ion trajectories can become unstable if the trapping potential deviates too far from a perfect quadrupole potential. The inhomogeneity of the trapping field $E(y, z)$ can be quantified by an adiabaticity parameter $\theta(y, z)$ [82] as

$$\theta(y, z) = \frac{2e|\nabla \cdot E(y, z)|}{m\Omega^2} = \frac{2e|\nabla \cdot (-\nabla \cdot \Phi(y, z))|}{m\Omega^2}. \quad (3.32)$$

This parameter can then be normalised against the field seen at the nil position (y_0, z_0) which is equivalent to the nil position of a perfect quadrupole field. The normalised value for the adiabaticity parameter can then be used to map the homogeneous field q parameter $q_i = \frac{2\sqrt{2}\omega_i}{\Omega}$ to an in-homogeneously mapped q parameter as

$$q_\theta(y, z) = q_i \times \theta(y, z)_{norm} = q_i \times \frac{\theta(y, z)}{\theta(y_0, z_0)}. \quad (3.33)$$

To define the q parameter at any position in the inhomogeneous field. It has been shown experimentally [83, 81] that values of $q_\theta(y, z) > 0.4$ and $a_i = 0$ result in unstable ion trajectories, this is in conflict with the quadrupole potential limit of $q_i < 0.9$ when $a_i = 0$ even after in-homogeneously mapping the q parameter. This is due to a different effect where strong deviations from the quadrupole field result in perturbations and instabilities of the ion motion at certain frequencies. These perturbations have been shown to create unstable trajectories when $q_\theta(y, z) > 0.4$ and $a_i = 0$, which is the limiting factor for deciding RF trapping voltages and frequencies.

From now only $q_\theta(0, z)$ will be considered as deviations from the quadrupole trapping potential are most prevalent in this dimension. Ideally $q_\theta(0, z) < 0.4$ for all values of z in

trap depth, this is shown in Fig. 3.7 where the introduction of z_{min} is shown. $q_\theta(0, z)$ is typically larger as $z < z_0$, the minimum value of z that needs to be taken into consideration then is z_{min} as if the ions energy was larger than the potential at this value it would simply be ejected from the trap at z_e . This gives the final condition that $q_\theta(0, z_{min}) < 0.4$ when $a = 0$; stable and unstable trapping voltages, and their effect on the in-homogeneously mapped q parameter are shown in Fig. 3.7.

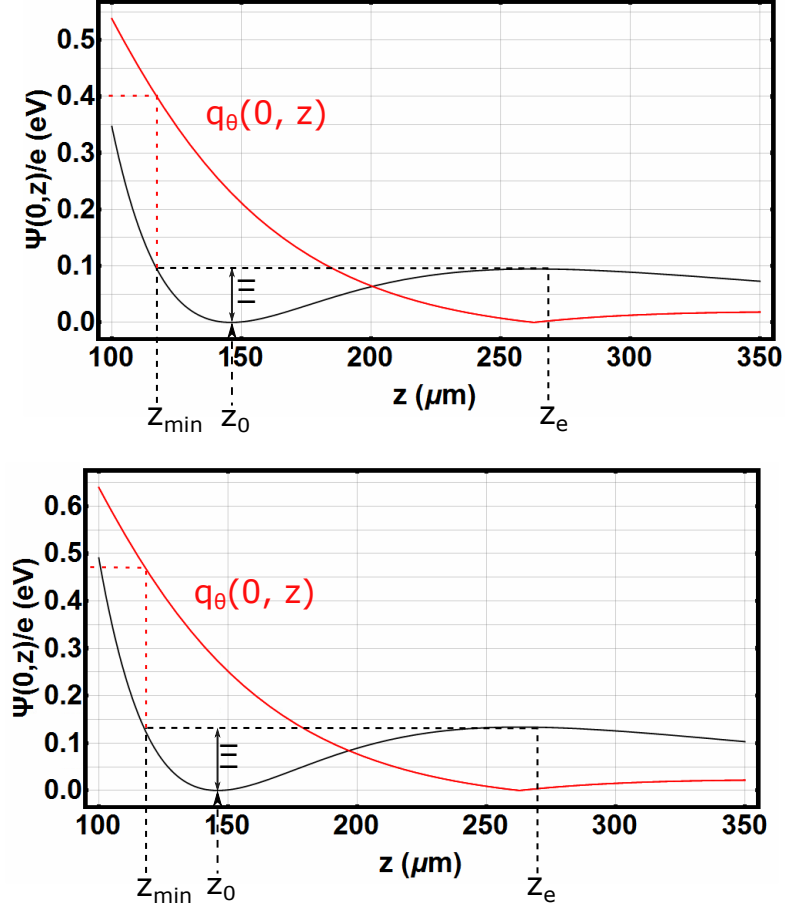


Fig. 3.7 (Top) Stable trapping parameters $V_{RF} = 185$ V and $\Omega = 2\pi \times 16.61$ MHz, as $q_\theta(0, z_{min}) = 0.40$, resulting trap depth is $\Xi = 0.095$ eV. (Bottom) Unstable trapping parameters $V_{RF} = 220$ V and $\Omega = 2\pi \times 16.61$ MHz, as $q_\theta(0, z_{min}) = 0.48$; though the resulting trap depth at a higher voltage is $\Xi = 0.134$ eV, the instability of the ions trajectories make this option less preferential.

The analytical method gives trapping parameters for a stable trap, a trapping frequency of $\Omega = 2\pi \times 16.61$ MHz (more dependent on the capacitance of the chip and resonator can, can be altered with hardware changes as described in Sec. 4.3.1), a peak trapping voltage of $V_{RF} = 185$; with $q_z = q_y = 0.23$ giving secular frequencies at (y_0, z_0) of $\omega_z = \omega_y = 2\pi \times 1.348$ MHz.

3.2.3 Numerical method and solution for simple linear chip design and experimental results with numerical model

For more complex electrode structures, electrodes that have a finite limit in space and have distinct gaps between electrodes, numerically generated potentials can be beneficial. Numerically simulating electrode potentials also allows for an understanding of a three dimensional potential, which is required for choosing axial trapping potentials generated via DC electrode voltages. A commonly used numerical method for ion traps is a boundary element method (BEM) [84, 85], where a two dimensional surface is meshed and the Laplace equation is solved for each mesh point. The solution for the sum of each mesh point can then be used to express the electric field at any point inside the simulated volume for an applied potential on each surface. The BEM is chosen over a finite element method (FEM) as the BEM has been shown to produce more accurate results for electric fields and shows no discontinuities in field strength by laying the mesh over the volume of interest for chip electrode structures; Additionally BEM is a lot faster to simulate than the FEM [85].

Numerical and analytical comparison

The meshed model for the simple linear chip design can be seen in Fig. A.1. The total potential $\Phi(x, y, z)$ generated by the individually generated potentials for different electrodes $\phi_i(x, y, z)$ where $i = \{RF, DC1, DC2, DC3...\}$, can be expressed as the sum of the RF electrode pseudopotential approximation and the individual DC electrode potentials

$$\begin{aligned}\Phi(x, y, z) &= \Psi(x, y, z) + \sum_{j=DC1,..} \phi_j(x, y, z) \\ &= \frac{e^2}{4m\Omega^2} (\nabla \cdot \phi_{RF}(x, y, z))^2 + \sum_{j=DC1..} \phi_j(x, y, z).\end{aligned}\tag{3.34}$$

From this, the trapping parameters in list 3.2.2 can be found. For an applied RF field with no DC voltages, the optimized trapping parameters for $q_\theta(0, 0, z_{min}) \leq 0.4$ are shown in Table 3.1 with associated contour plot and potential in the z axis in Fig. 3.8. The only difference in calculation is that the Hessian matrix and in-homogeneously mapped q parameter are solved in three dimensions for the numerical result instead of two for the analytical result. The numerical simulation CAD file can be found in Fig. A.1.

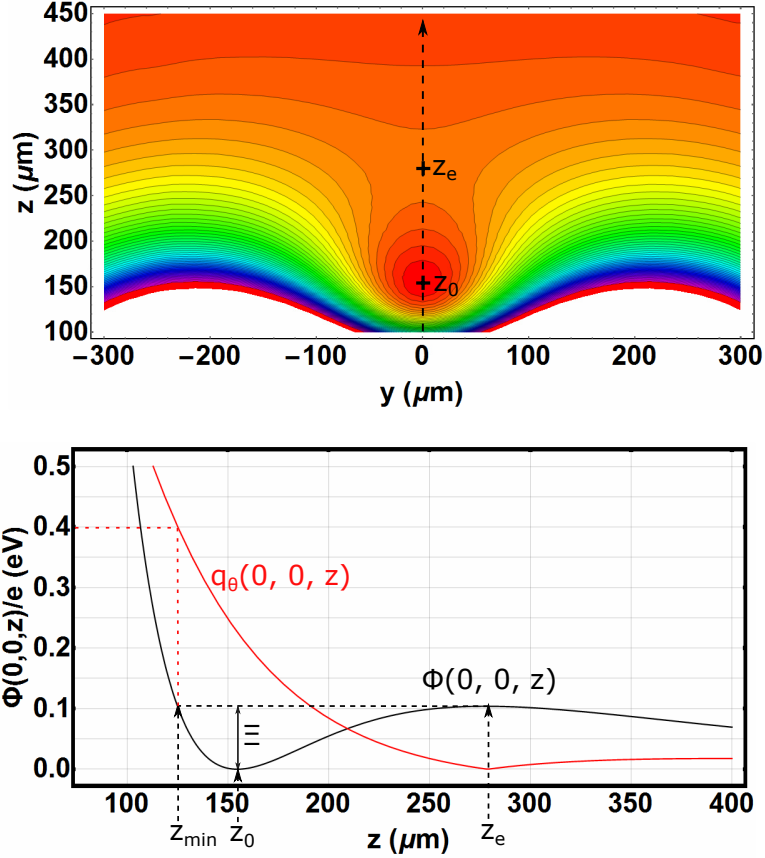


Fig. 3.8 (Top) Contour plot of numerically simulated potential $\Phi(0, y, z)$ for simple linear chip with no DC voltages applied, CAD design is in Fig. A.1. (Bottom) Stable trapping parameters $V_{RF} = 200$ V and $\Omega = 2\pi \times 16.61$ MHz, as $q_\theta(0, z_{min}) = 0.40$, resulting trap depth is $\Xi = 0.103$ eV with $z_{min} = 125$ μm , $z_0 = 154$ μm and $z_e = 271$ μm .

Trapping parameter	Numerical result	Analytical result
Trap depth Ξ (eV)	0.103	0.095
Ion height z_0 (μm)	154	147
Trapping frequency $\Omega/2\pi$ (MHz)	16.61	16.61
Optimal trapping voltage V_{RF} (V)	200	185
Radial secular frequency $\omega_y/2\pi$ (MHz)	1.414	1.348
Radial secular frequency $\omega_z/2\pi$ (MHz)	1.362	1.348

Table 3.1 Comparison of analytical and numerical simulation trapping parameters for just RF voltage applied.

As it can be seen in table 3.1 the numerical simulation has higher values for all trapping parameters, the increase in ion height can be attributed to the 10 μm gaps between the electrodes, this is typical for electrodes spaced further apart in a linear ion trap. This has likely had a knock on effect for other values like q_θ , making it so that a higher trapping

voltage can be applied before $q_\theta = 0.4$, this has likely the reason for the higher trap depth value as well as typically increased ion height means decreased trap depth. The radial secular frequencies are slightly higher for the numerical simulation which could also be attributed to the higher trapping voltage, though the numerical result gives different values in the y and z directions, this is likely because of the field at the trap nil position for the numerical simulation not being analogous to a perfect quadrupole potential. It makes sense that this would arise as the electrode lengths in the numerical simulation are not extended to infinity. Though slightly different most of the results are relatively similar and can easily be attributed to differences in the simulation techniques, this gives confidence in the numerically simulated results even though just the local trap geometry was simulated and not the entire chip. For this reason, the more complex chip designs later mentioned will only focus on the numerical result as analytically simulating these structures will have in-concise solutions.

Applied DC potentials for axial confinement and principal axis rotation

The application of DC voltages in the case of this chip is to produce axial confinement and principal axis rotation, a few values can be derived from the application of DC voltages like the axial secular frequency ω_x , the principal axis rotation and axial secular frequency are calculated from a three dimensional Hessian matrix, analogous to the two dimensional case in Sec. 3.2.2. Effects on previous values like the ion height and radial secular frequency can be calculated, ideally the deviations on these values from applying DC voltages should be minimised, this can be done through careful selection of DC voltages so that the total field that they induce on the RF nil position is close to, if not zero. This is typically done by application of positive and negative DC voltages, in the case of this chip eight DC electrodes, four on each side of the RF electrode facing each other were used to create axial confinement, labelled DC2, DC3, DC4, DC5, DC10, DC11, DC12 and DC13 in Fig. A.1 in Appendix A.

Axial confinement is produced by applying +5.5 V onto the outer four electrodes (DC2, DC5, DC10 and DC13) and -4.07 V on the inner four electrodes (DC2, DC3, DC11 and DC12), from this principal axis rotation can be induced by applying anti sign offsets equal to +1.1 V and -1.1 V to the two diagonally facing electrodes (DC13 and DC5), this is all done while minimising the potential offset at RF nil position and keeping the axial confinement above the RF trap depth, values can be adjusted slightly to ensure this. The voltages are chosen The resulting trapping parameters are:

Trapping parameter	Numerical result with DC voltages
Axial confinement Ξ_{ax} (eV)	0.104
Ion height z_0 (μm)	152
Principal axis rotation α ($^\circ$)	9.0
Radial secular frequency $\omega_y/2\pi$ (MHz)	1.346
Radial secular frequency $\omega_z/2\pi$ (MHz)	1.473
Axial secular frequency $\omega_x/2\pi$ (kHz)	326.3

Table 3.2 Numerical results with DC voltages applied for simple linear chip design.

with contour plot and axial confinement shown in Fig. 3.9.

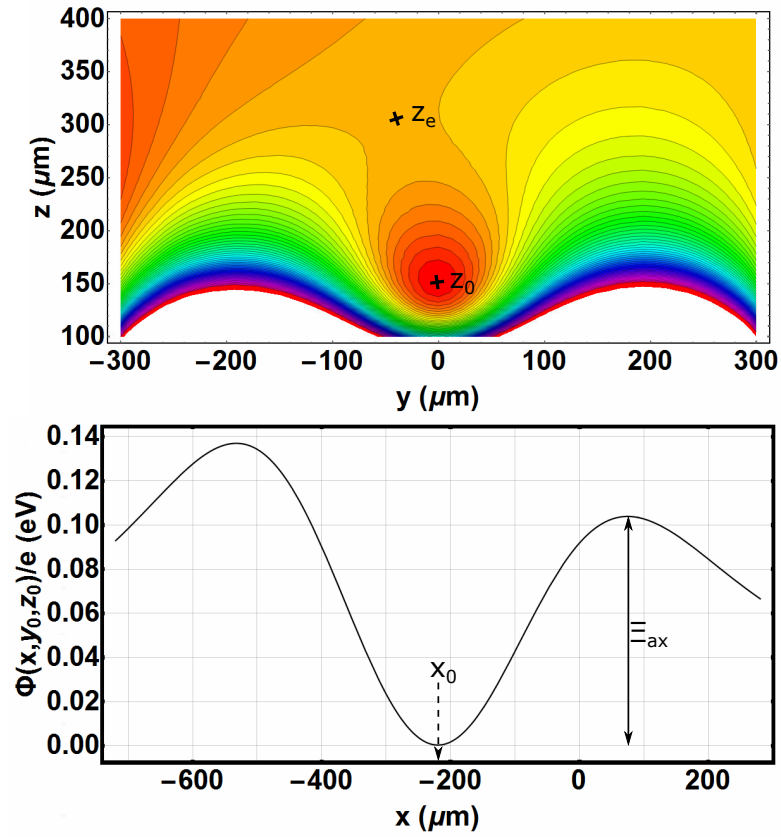


Fig. 3.9 (Top) Contour plot of numerically simulated potential $\Phi(x_0, y, z)$ for simple linear chip with DC voltages applied for principal axis rotation angle of $\alpha = 9.0^\circ$, CAD design is in Fig. A.1. (Bottom) Potential along $\Phi(x, y_0, z_0)$ showing an axial confinement of $\Xi_{ax} = 0.104$ eV, the lower axial confinement peak corresponds to negative offset voltage applied to DC electrode DC5.

Trapping strings of ions for improved sensing capabilities

On the topic of improving trapped ion magnetometry sensitivity (theoretically described in Sec. 2.2.6), it is beneficial to trap many ions to sense with so to speed up sensing experiments which results in improved sensitivity. One option for this is to trap multiple ions in the same axial confining potential forming a Coulomb crystal, the name Coulomb crystal comes from the Coulomb repulsion between ions in the crystal structure which forms the crystals shape. Typically Coulomb crystals form around the trap nil position, the crystal shapes depending on the how steep the confining potentials are around the nil position, creating string, zig-zag or ellipse structures. The type of crystal formed can also be understood from the secular frequencies in each direction, typically the steeper a potential in one axis the higher the secular frequency. Strings for example are more likely to form in the axis with the lowest secular frequency which is typically the axial direction for linear Paul traps [86, 87].

Strings of ions would be ideal for sensing as not only do the particles in the crystal structure have less motional energy, there is minimal verticality between ion positions for imaging and state readout and it is easier to distinguish different ions due to increased separation. The phase transition of the crystal structure for Paul traps from string to zig-zag mode has been observed in [87] to be when the squared ratio of the two secular frequencies $\alpha_{c1} = \omega_x^2/\omega_y^2$ reaches above a certain threshold value for different numbers of trapped ions N . The threshold for the phase transition between string to zig-zag mode was would to obey the power scaling law

$$\alpha_{c1} = c_1 N^{\beta_1}, \quad (3.35)$$

where the experimental results for the coefficients are $c_1 = 2.53$ and $\beta_1 = -1.71$. This can be rearranged to give the maximum number of ions that can be trapped for given secular frequencies ω_x and ω_y before the crystal transitions into a zig-zag mode

$$N = \left\lfloor 1.72 \left(\frac{\omega_x}{\omega_y} \right)^{-1.17} \right\rfloor, \quad (3.36)$$

giving $N = 9$ for the case in Table 3.2. Nine ions trapped using these confining potentials can be seen in Fig. 3.10.

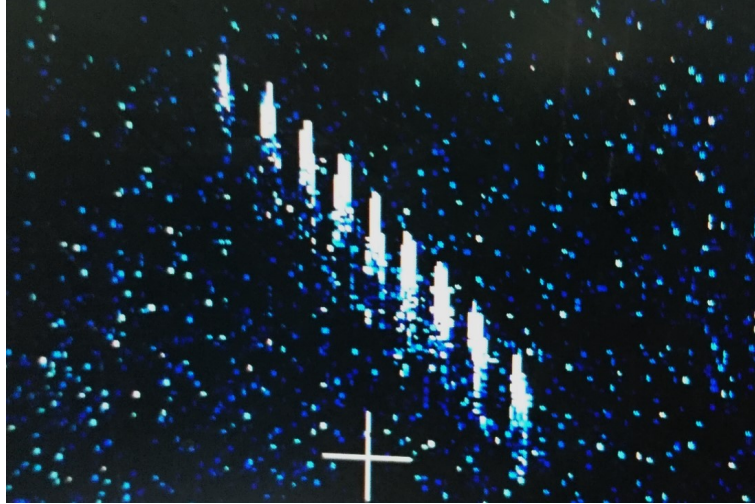


Fig. 3.10 String of nine ions trapped with the trapping parameters in Table 3.2. The fluorescence tail from the ions extending towards the bottom of the screen is due to a camera issue and not representative of the ions motion.

When imaging strings of ions the separation between them is another concern, this is because the resolution of the imaging optics may not be sufficient for imaging multiple ions over a large surface area. Typically the minimum distance between ions in a string is at the centre of the string, this makes intuitive sense as the Coulomb force on the ions in the centre of the string is larger than the ions on the ends of the string. Numerical simulations from [88] have shown that for strings of trapped ions in Paul traps, the smallest separation between ions in a string of N ions follows the relation

$$x_{min}(N) = \left(\frac{Z^2 e^2}{4\pi\epsilon_0 m\omega_x^2} \right)^{1/3} \frac{2.018}{N^{0.559}}, \quad (3.37)$$

where $Z = 1$ is the degree of ionisation and ϵ_0 is the permittivity of free space. For the nine ion case in the simple linear trap this gives a minimal separation between ions as $x_{min}(9) = 3.4 \mu\text{m}$, which is fine for the imaging optics in Sec. 4.4 where the resolution of the camera combined with the collection optics is $1.8 \mu\text{m}$.

3.3 Dual rail linear chip for trapped ion magnetometry

This section will focus on optimal trap geometries for trapped ion magnetometry. Ideally a trap capable of trapping many ions trapped in a small region of space (like in a string as mentioned in the previous section) would be beneficial for performing scalar magnetometry with improved sensitivity. Trapping strings of ions at multiple regions of space would also be beneficial for performing vector magnetometry as in magnetic field gradient measurements. A constraint of performing sensing experiments with many trapped ions is the resolution and field of focus of the imaging system, the designs outlined in this section were optimized for the imaging optics outlined in Sec. 4.4 where all trapping zones must

be in a 1x1 mm region. A simple chip structure with one electrode layer, one dielectric layer, a grounded under layer and a substrate was considered; fabrication of this structure is outlined in greater detail in Sec. 3.3.3. The design choices are based of the derivations for the linear Paul trap in the previous section with appropriate geometry optimizations and adjustments.

3.3.1 Dual linear chip geometry optimization

The design choice for the single electrode layer trap is equivalent to two linear Paul traps in close proximity, the four RF electrodes that are required for this are connected to the same RF source and the two linear designs are separated by a distance that allows for DC electrode access on either side of the of the two linear traps, the chip mask design can be found in Fig. A.3 with trap geometries used for the numerical simulation in Fig. A.2.

The first consideration for the dual linear chip design that wasn't taken into account for the simple linear chip in the previous section is the optimization of RF electrode widths b and spacing a , which determine the ion height and trap depth. Using the equations for trap depth, ion height and the geometric factor of the RF electrodes, Eq. 3.27 and 3.28, near optimal trap depths for a given ion height can be calculated [78]. By setting $b = c$ and $\zeta = b/a$, the equations for ion height and the geometric factor can be rewritten as

$$h = \frac{\sqrt{a(a+2b)}}{2}, \quad (3.38a)$$

$$\kappa_{RF} = \frac{\zeta^2(1+2\zeta)}{4(1+\zeta)^2(1+\zeta+\sqrt{1+2\zeta})^2}. \quad (3.38b)$$

As the trap depth is directly proportional to the geometric factor $\Xi \propto \kappa_{RF}$, it is preferable to maximize κ_{RF} , the plot for this in Fig. 3.11 shows that for equal RF electrode widths the optimal value is when $\zeta = 3.68$. It is also preferable to select a small ion height to maximize trap depth, an ion height of $h \approx 130 \mu\text{m}$ was chosen for this design, the reason for this choice was to minimise laser light scattering off the chip. Using the maximum spot size of the 935 nm laser in table 4.1, $89 \mu\text{m}$, an ion height of $h \approx 130 \mu\text{m}$ would allow for a large trap depth while allowing for a large $41 \mu\text{m}$ margin of error in the beam alignment. Unfortunately the electrode widths that come with selection of this ion height and drastically reduces axial confinement and principal axis rotation capabilities from the DC electrodes due to the large distance between them and the trapping position. To improve the effects of the DC potential on the trapping position the ratio was brought down to $\zeta = 2$, this allowed for a higher DC confinement and principal axis rotation without reducing κ_{RF} that significantly from its maximum value.

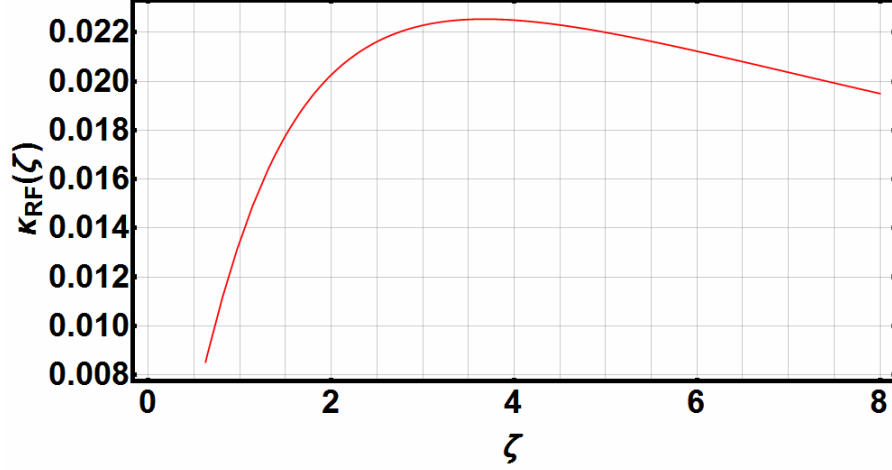


Fig. 3.11 Geometric factor κ_{RF} expressed as a function of the RF electrode width over the spacing between them $\zeta = b/a$ for equal RF electrode widths. The largest value of $\kappa_{RF} = 0.0225$ is found when $\zeta = 3.68$.

Note that increasing the value of ζ can have other effects on trapping parameters, it will increase radial secular frequencies which can be beneficial for trapping larger numbers of ions in a string as seen in Eq. 3.36, but this comes at the expense of an increased q parameter, which would result in an increased value of $q\theta$, meaning stable traps with a large ζ would result in a decrease in the trap voltage that could be applied, meaning a lower trap depth. Due to the multiple benefits and costs of changing the value of ζ , its best to prioritise what is desired out of the chip. The top priorities for this design in each separate trapping zone were:

- Ion height of $\approx 130 \mu\text{m}$
- Trap depth of at least 0.1 eV at each trapping zone
- Capable of creating sufficient axial confinement and principal axis rotation
- Four separate trapping zones capable of trapping long ion strings
- All four trapping regions being within a $1 \times 1 \text{ mm}$ area for imaging purposes

Though the trap depth value may seem arbitrary, this is generally considered to be a reasonable value to aim for in surface Paul traps [89] and has been demonstrated within this thesis to allow for prolonged trapping of ions. Another design choice for this chip was to stagger the widths of the DC electrodes as seen in Fig. A.2 to allow for a shallower axial confinement potential. This would result in a decreased axial secular frequency ω_x , meaning that a larger number of ions could be trapped in a string before phase changing into a zig-zag mode as seen in Eq. 3.36. It would also mean that the minimum space between ions in a string would decrease as shown by Eq. 3.37, meaning that camera

resolution and optical resolution of the collection optics don't need to be as good; this would allow for optimization of other parameters like binning rates of the camera or field of focus of the objective lens.

The result of these optimizations can be expressed numerically. For this chip at each trapping region (shown in Fig. A.2), the resulting trap parameters are shown in table 3.3, the way in which these values were calculated are the same as the methods derived in Sec. 3.2. The DC voltages applied for axial confinement are DC1 = DC6 = 5.075 V, DC2 = DC7 = -7.224 V, DC3 = 12.11 V, DC4 = DC9 = -7.245 V, DC5 = 5.607 V, DC8 = -13.321 V, DC10 = 6.23 V; the asymmetry of these voltages occurs due to the thin DC rails coming in from the $-x$ direction between the two linear traps and the slight differences in DC electrode surface area.

Trapping parameter	zone 1	zone 2
Trapping frequency $\Omega/2\pi$ (MHz)	16.61	16.61
Optimal trapping voltage V_{RF} (V)	167	167
Ion height z_0 (μm)	141	141
Trap depth Ξ (eV)	0.109	0.109
Axial confinement Ξ_{ax} (eV)	0.119	0.115
Principal axis rotation α ($^\circ$)	12.1	9.3
Radial secular frequency $\omega_y/2\pi$ (MHz)	1.401	1.372
Radial secular frequency $\omega_z/2\pi$ (MHz)	1.602	1.595
Axial secular frequency $\omega_x/2\pi$ (kHz)	282.5	281.5
Max. No. of trapped ions in a string n	11	10
Min. distance between ions $x_{min}(n)$ (μm)	3.4	3.6

Table 3.3 Dual rail chip numerical simulation results.

One noticeable change is the difference between the ion height in the simulated results and the one previously calculated, this can be attributed to the two linear traps not having sufficient space between them, making the RF fields from the opposite linear trap change the ion height. Fortunately there isn't too much asymmetry in the simulation results due to the careful selection of the DC voltages to mitigate the asymmetry of the chip in the x direction. All the ions would be able to be imaged by the collection optics outlined in Sec. 4.4. The maximum number of ions that could be trapped on this chip would be 42 and The cross sectional area that they cover ($x \times y$) would be approximately 0.65×1.00 mm. The relevant plots for the simulation results can be seen in Fig. 3.12.

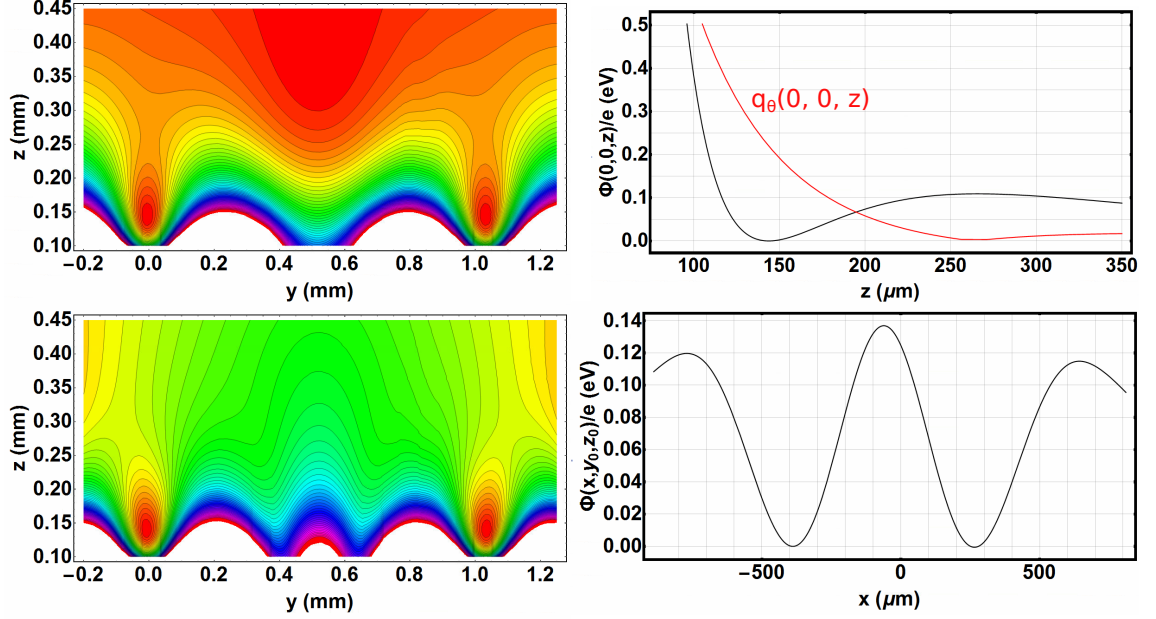


Fig. 3.12 Plots of numerically simulated dual rail chip. (Left) Contour Plots of the electric field taken at x_0 for no DC voltages applied (Top) and DC voltages applied (Bottom). (Right) Electric potential plots for the radial confinement with no DC voltages applied (Top) and axial confinement with DC voltages applied (Bottom).

3.3.2 Linear trap vs dual rail trap

Due to the dual rail chip having a broader scope in terms of experiments and tangible results, the chip used in the experiments conducted in this thesis were using the linear design described in 3.2.3. This is due to a plague of problems encountered during fabrication of the dual linear chips highlighted in Appendix B. A direct comparison of the two chips can be seen in table 3.4.

Trapping parameter	zone 1 (dual)	zone 2 (dual)	linear
Trapping frequency $\Omega/2\pi$ (MHz)	16.61	16.61	16.61
Optimal trapping voltage V_{RF} (V)	167	167	200
Ion height z_0 (μm)	141	141	152
Trap depth Ξ (eV)	0.109	0.109	0.103
Axial confinement Ξ_{ax} (eV)	0.119	0.115	0.103
Principal axis rotation α ($^\circ$)	12.1	9.3	9.0
Radial secular frequency $\omega_y/2\pi$ (MHz)	1.401	1.372	1.346
Radial secular frequency $\omega_z/2\pi$ (MHz)	1.602	1.595	1.473
Axial secular frequency $\omega_x/2\pi$ (kHz)	282.5	281.5	326.3
Max. No. of trapped ions in a string n	11	10	12
Min. distance between ions $x_{min}(n)$ (μm)	3.4	3.6	3.0

Table 3.4 Dual rail chip and linear chip numerical simulation results.

3.3.3 Chip fabrication and design considerations

With large contributions from Ph.D. students Weikang Fan and Zak Romaszko, attempts were made to fabricate ion traps within the confines of the quantum hubs our group is affiliated with. This section will briefly outline the fabrication and geometry considerations for creating ion traps, and, the ion trap fabrication techniques and process for single electrode layer ion trap with a grounded under-layer, all on top of a substrate. A general representation of the ion trap structure developed for the chip described in the previous section can be seen in Fig. 3.13.

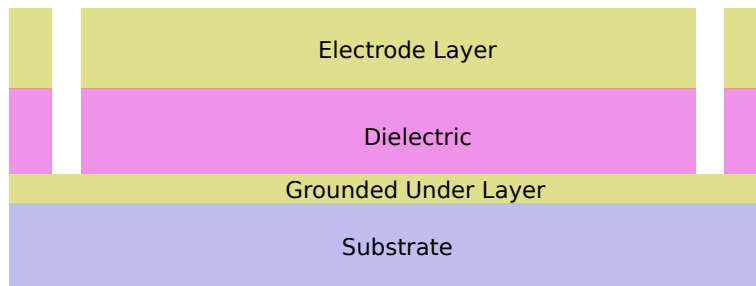


Fig. 3.13 Basic cross section diagram of the four major chip fabrication layers.

Geometry Considerations for the Dual Rail Linear Chip Design

Major chip property considerations when fabricating ion traps are as follows:

- Low power dissipation from the chip
- Low resistance
- Low capacitance
- Minimal dielectric exposure to the ion trapping position

Heating of an ions secular motion (Sec. 3.1.2) is induced from the power spectrum of the electromagnetic field noise [90]. This can typically be suppressed through design considerations by minimizing the dielectric exposure to on ion. This can sometimes happen when electrode trenches are too wide relative to electrode widths. It can be evaded by ensuring that the top electrode layer is thick enough relative to the trench width to not have a line of sight between the ion and the dielectric. This is generally undesirable as exposed dielectrics can create excessive electric field noise at the ions position resulting in unwanted secular motion, this is also the reason for the grounded mesh over the front viewport of the vacuum system in Sec. 4.1.4 as it reduces the total dielectric exposure to the ion.

Though electric field noise can be minimised, exposure to electrode surfaces with large RF voltages applied will inevitably induce secular heating on the ion. This is expected to scale with $\approx d^{-4}$ [90], where d is the shortest distance from the ion to the electrode surface.

Thermal heating of the ion trap can induce unwanted heating on the trapped ions that can cause the ion to eject from the trap as well, this is typically associated with the power dissipated from the trap and should be taken into heavy consideration when designing an ion trap. Power dissipation from the chip surface and potentially other sources can induce heating of the ion. Detailed descriptions of the influence the electric field noise has on the heating rates of the ion based on the perturbation theory are given in [91, 92]

High power dissipation from the chip is typically seen when the real part of the chips impedance is high, this is undesired as it induces unwanted motional heating on trapped ions. This may not be an issue when Doppler cooling the ion, but can result in the ion being ejected from the trap if this value is too high, this was the major limitation of the trap used in this thesis as motional heating of the ion would cause the ion to regularly eject from the trap after experiment times > 300 ms, this drastically limited the potential sensitivity results that could have been attained. Impedance of the simple linear chip at the resonant frequency of $\omega_0/2\pi = 16.61$ gave $Z = (16.85 - 296.5j)\Omega$ which gives a capacitance of 32.3 pF. The power dissipation P_d can be calculated as [89]

$$P_d = \frac{V_p^2 \omega_0 C_T}{2} (\omega_0 C_T R_T + \tan \delta), \quad (3.39)$$

where C_T is the capacitance of the trap, R_T is the resistance of the trap, ω_0 is the RF frequency applied and $\tan \delta$ is the loss tangent of the dielectric in the chip. The loss tangent can be expressed as $\tan \delta = G/C_T \omega_0$ by making approximating the chip to a parallel plate capacitor where G is the conductance of the dielectric layer. The loss tangent is approximated to $\tan \delta \approx 0.01$ for silicon dioxide at room temperature [89], At a peak trap voltage of s , this gives a power dissipation of ≈ 4.50 W for the simple linear chip used in this thesis. From Eq. 3.39 it can be seen that reductions in the chip resistance and capacitance will result in a lower power dissipation. Lowering the trapping frequency can also result in a lower power dissipation but this will increase the q parameters that are paramount for minimising for stable ion trapping as described in Sec. 3.2.2. For the chips developed using the fabrication process outlined in the next section the impedance for the dual rail chip has a value of approximately $Z = (5 - 279.1j)\Omega$ giving a capacitance of 20 pF at a resonant frequency of $\omega_0/2\pi = 16.61$ MHz, this gives a power dissipation of 0.145 W at the optimized trapping voltage $V_p = 167$ V. Being over an order of magnitude lower than the simple linear chip design suggests that excessive heating during experiments would unlikely result in a loss of the ion of the for this chip design.

Another reason for lowering the capacitance and resistance of the chip is because of the benefits it will have on the Q value of the resonant circuit and minimise the total

power required for attaining trapping voltages as described in Sec. 4.3.1. The resistance can typically be lowered by increasing the thickness of the electrodes, this can be hard to fabricate though as a larger thickness will make etching electrode trenches difficult. The capacitance of the chip can be changed by lowering the thickness of the dielectric layer below the electrodes, this can sometimes be problematic though as it has been seen in previous fabrications that the dielectric can contain pinholes that would short the top electrode layer to the grounded layer below. This is more likely to happen when the dielectric thickness is low.

This has been shown experimentally to scale with $\approx d^{-3.5\pm 0.1}$ [90], where d is the shortest distance from the ion to the electrode surface. This suggests that it would be preferential to increase ion height, unfortunately this typically increases electrode widths making the density of ions that can be trapped in a region of space increase, and it also decreases trap depth as described in Sec. 3.2.2.

Single electrode layer ion trap fabrication

The most recent fabrication process predominantly developed by Ph.D. student Weikang Fan is briefly outlined in this section. There were major issues with chip glow on previously micro-fabricated batches of chips. The chip glow caused major breakdown in the chip surfaces as described in Appendix B.

This section contains micro-fabrication terminology for different processes whose meanings can be found in [89, 93], individually discussing each term or process cannot be done concisely. The following terms used are:

- Thermal oxidation
- Sputter gun
- Thermal evaporation
- Plasma enhanced vapour deposition
- Photo-lithography
- Spin coated photo-resist
- Electroplated
- Reactive ion etch

The substrate chosen was a high resistivity ($10k\Omega$ cm) silicon substrate, the high resistivity was chosen to minimise electrical conductivity, the silicon was chosen as it was a relatively cheap solution to previous adhesion problems with diamond substrates. A

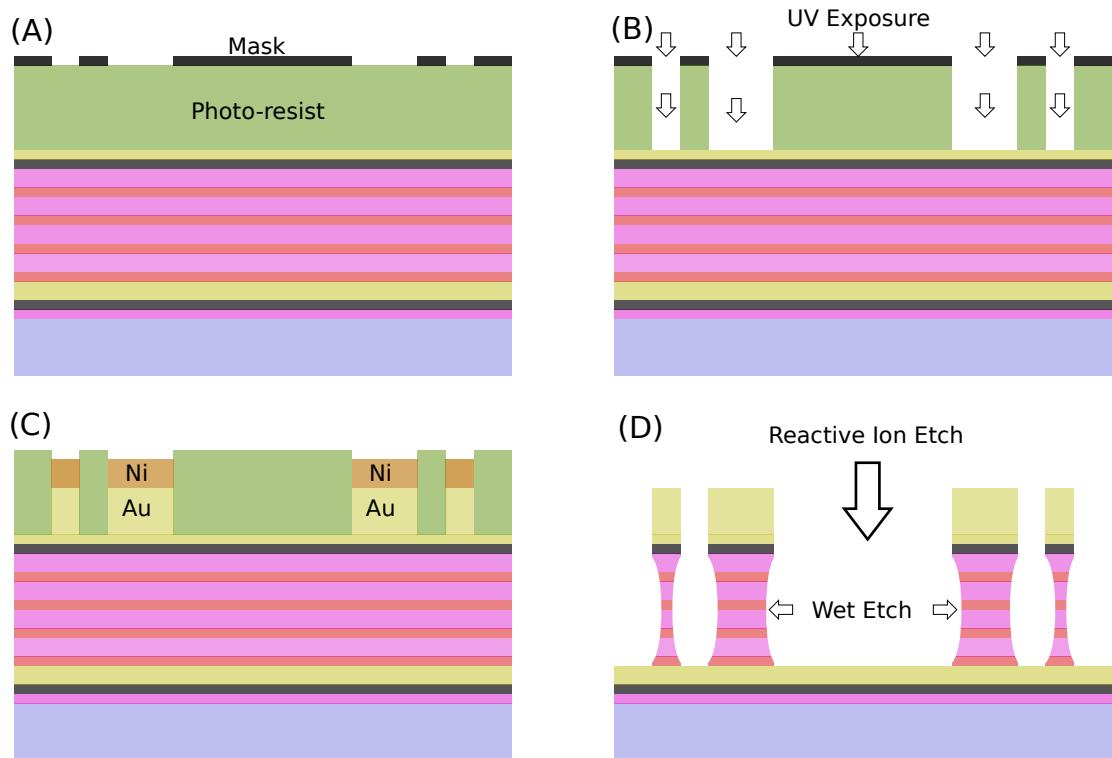


Fig. 3.15 (A) Positive photo-resist and electrode mask applied. (B) UV exposure removing all parts of the photo-resist not covered by the mask. (C) Gold and nickel layers deposited into removed photo-resist areas. (D) Reactive ion etch to etch to the grounded gold under layer followed by a wet etch to create an undercut on the silicon dioxide and silicon nitride stack and a wet etch to remove the nickel.

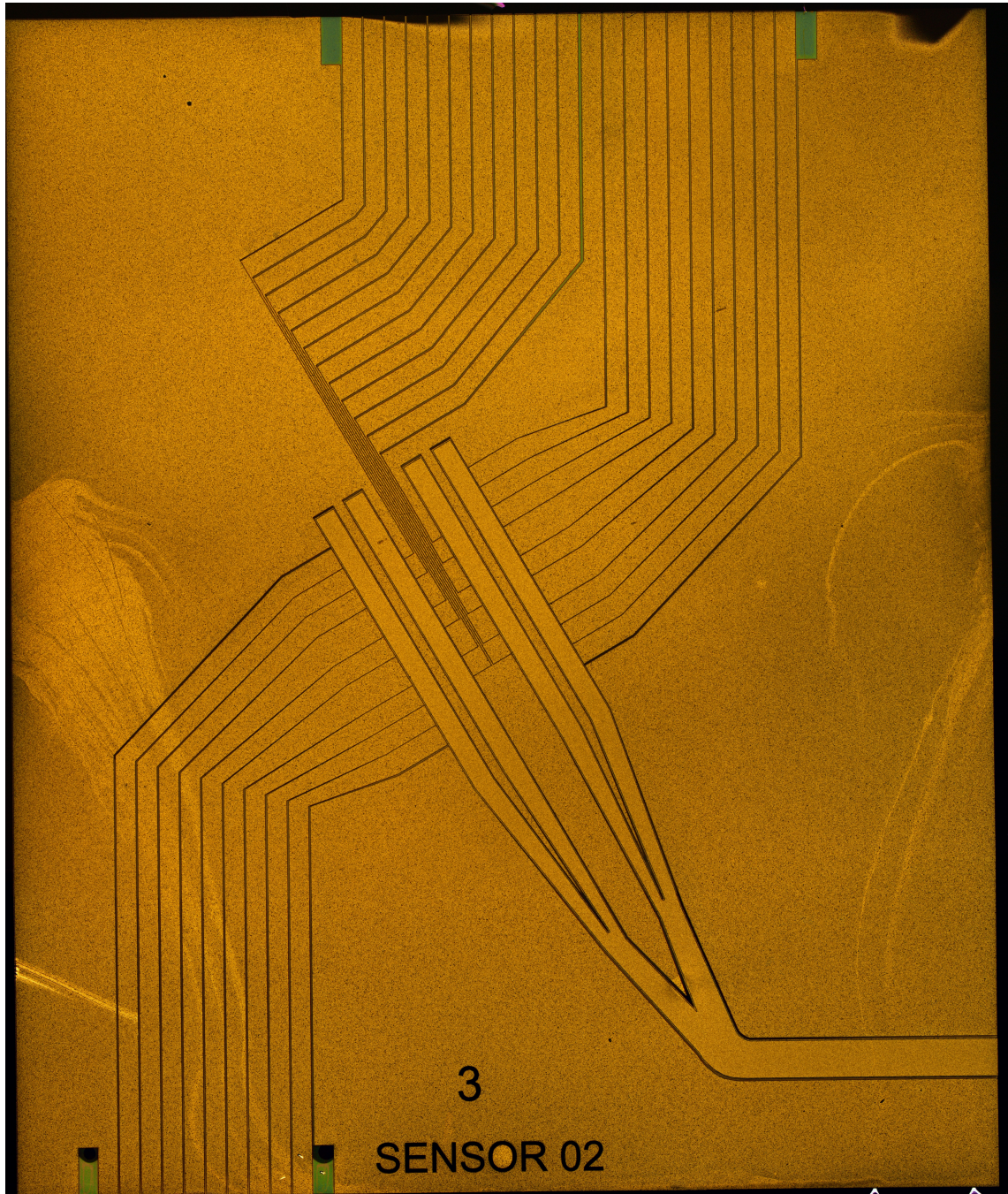


Fig. 3.16 The resulting dual rail chip fabricated using the above process.

4 Demonstrator device setup

Developing an experiment capable of trapping ions and coherently manipulating their quantum states requires systems engineering and knowledge of multiple physics and engineering fields. To gain an overall picture of the experiment, Fig. 4.2 shows a systems information flow of all the sub-systems described in this chapter, each of which was developed over the period of research within this thesis.

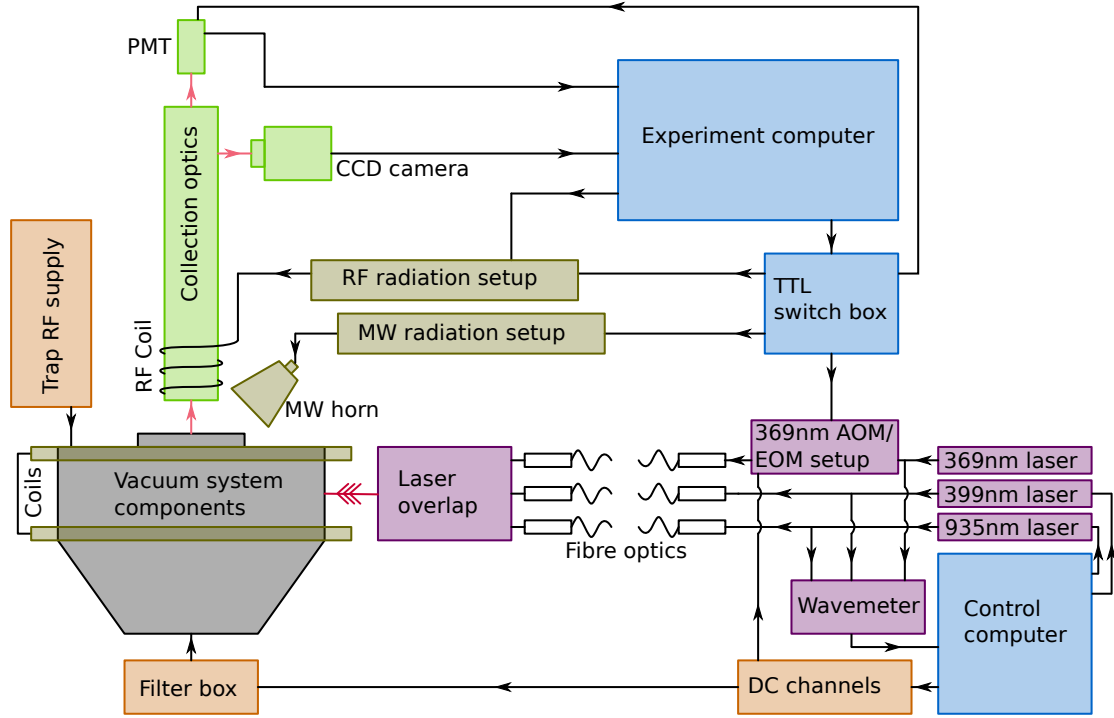


Fig. 4.1 System information flow diagram of the demonstrator quantum magnetometer, arrows show the flow of information between different components. Separate sub-systems are coloured based on primary functions; grey for vacuum system, purple for laser setup, orange for trapping voltages, green for ion imaging, dark yellow for coherent manipulation radiation and blue for computer control setup.

4.1 Vacuum system components

The vacuum system components include the vacuum system chamber with all feedthroughs, optical access viewports, gauges and pumps; as well as the internal structures of the vacuum system, excluding the micro-fabricated ion trap (see Sec. 3 for more details). A diagram of the separate components within the vacuum system and this section can be seen in Fig. 4.2.

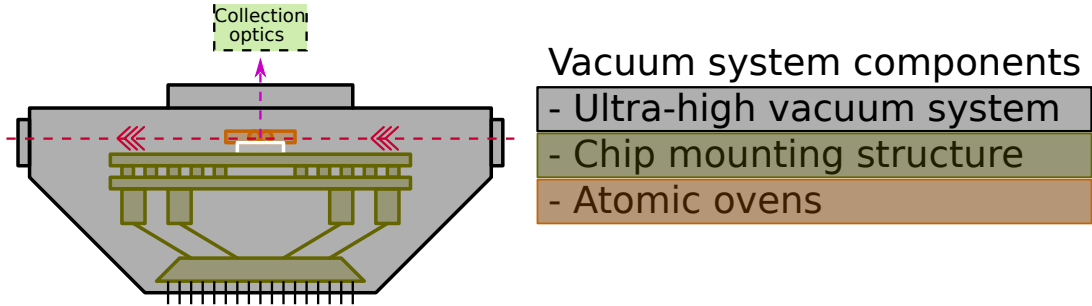


Fig. 4.2 Diagram of the vacuum system and internal components. Each set of components, which are described in the following subsections, are colour-coded and labelled in the legend of the diagram.

The materials used for the vacuum system and internal structures are checked if they are in the ultra-high vacuum (UHV) compatible materials list for Laser Interferometer Gravitational-Wave Observatory (LIGO) experiment [94]. The vacuum chamber is made from type 304 stainless steel, the chamber components are attached to the main octagon structure using silver plated screws and annealed copper gaskets. Some components not on the LIGO materials list have been tested in house [95] for out-gassing such as the PCB-based chip mount resistors, capacitors, D-sub connectors and spring-loaded connectors (all described in Sec. 4.1.2), as well as the solder, DC cable assemblies and in-house built SMA-SMP connector. All components have also been tested to withstand the 200°C bakeout procedure described in Sec. 4.1.4.

4.1.1 Ultra-high vacuum system

The vacuum system houses the micro-fabricated ion trap required for trapping ions with electric fields as described in Sec. 3. For the demonstrator setup vacuum system described in this section, the ultra-high vacuum (UHV) pressures reduce the likelihood of gas collisions with the trapped ion. The chamber walls also shield the ions from stray electromagnetic fields while providing access for all the other components required for trapping and coherently manipulating the ions quantum states as described in the later sections of this chapter. An image of the fully constructed vacuum system can be seen in Fig. 4.3. The vacuum system used in this thesis provides the following:

- Internal vacuum pressure of 2.8×10^{-10} mbar
- Shielding from stray electromagnetic fields
- Internal mount for chip carrier
- Internal mount and feedthrough for ^{174}Yb and ^{171}Yb atomic ovens
- High density feedthrough for 100 analog voltages used for application of DC trapping voltages to ion trap

- 50 Ω SMA feedthrough for application of RF trapping voltages to ion trap
- Optical access for laser beams
- Optical access for ion imaging
- Line of sight to main chamber for ion and getter pump
- Line of sight to main chamber for ion gauge
- Valve for turbo pump during baking process

From this list, each item can be elaborated upon to understand why they are necessary and how they could be improved upon. The internal vacuum pressure is within the desirable range for ion trapping, typically gas collisions with the trapped ion cause the ion to enter the $^2D_{5/2}$ state (see Sec. 2.1.2) or eject the ion from the trap, that rate of which this occurs in this experiment is approximately once per day. A lower pressure is always desirable though, so cleaning of the system is recommended during construction, see Sec. 4.1.4 for the method in which this vacuum system was prepared to achieve this pressure.

Shielding from low magnetic field noise is not provided for this experiment, low frequency noise is usually the largest source of decoherence as numerically described in Sec. 2.2. This would typically be provided by a mu metal Faraday cage, mu metal is a nickel-iron soft ferromagnetic alloy with very high permeability. Adding this would be ideal for a high frequency sensor but wasn't included in this experiment due to the nature of this experiment being demonstration.

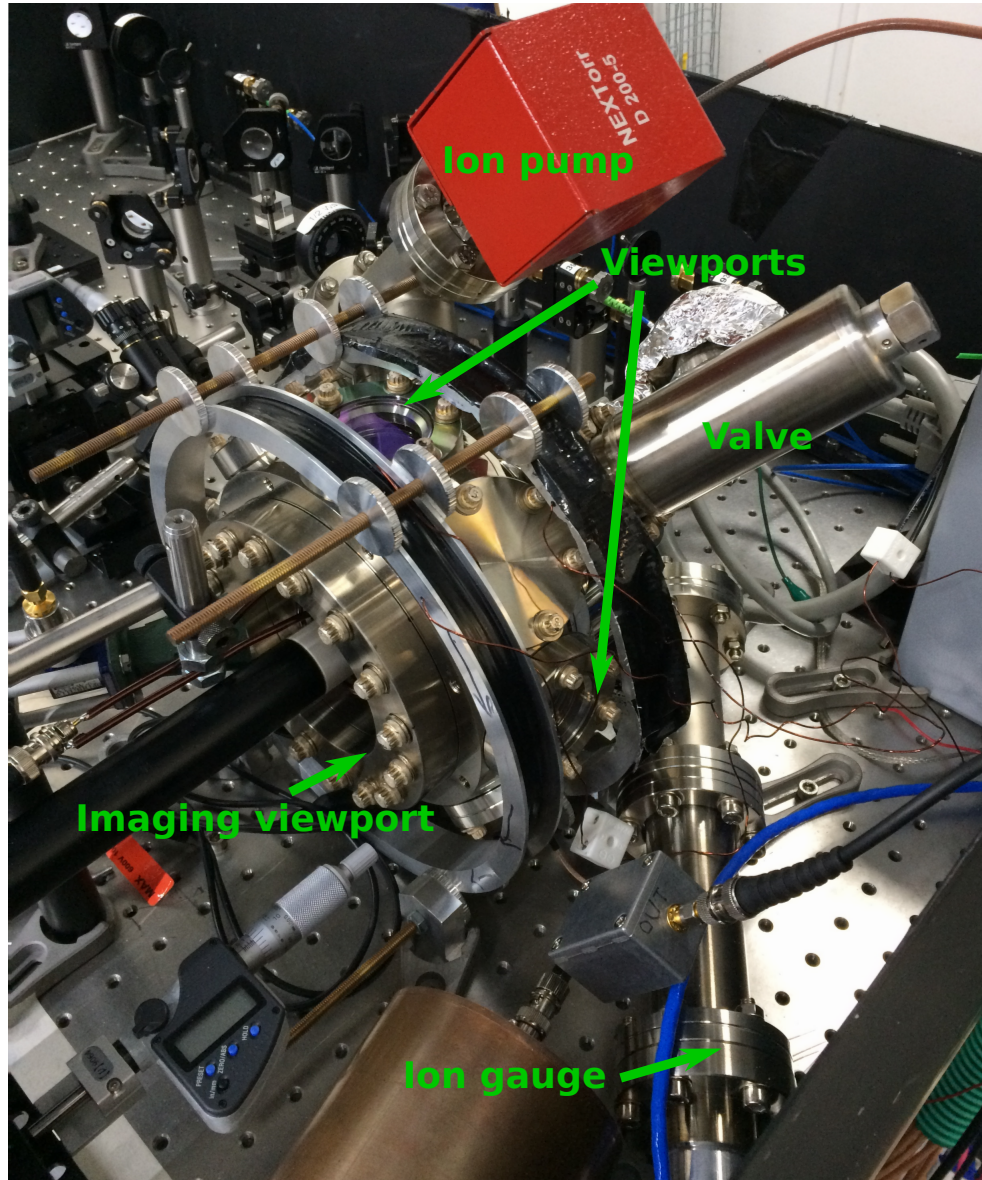


Fig. 4.3 Picture of the fully assembled vacuum system with the parts in view labelled.

The main chamber of the vacuum system is a spherical octagon and a weldable cluster³ welded together to form a single chamber. The chamber is comprised of twelve DN40CF flanges, eight of which make up the octagon each perpendicular to the trap surface, the other four are located behind the octagon on the cluster. There are also two larger flanges, one DN100CF flange on the octagon side parallel to the chip surface and one DN63CF flange at the rear face of the cluster. The structure of the main chamber can be seen in Fig. 4.3.

The internal mount for the chip carrier is to provide a stable, stationary support for the chip carrier while giving the carrier of 360° rotation to aid the principal axis rotation required for Doppler cooling the ion (Sec. 3.2.2); the mount attaches the back PCB structure of the chip carrier (described in Sec. 4.1.2) to the internal structure of the

³Kimball Physics MCF600-SphOct-F2C8 and MCF450-WeldClstr-E1C4

vacuum system. This is so that different chip designs with different principal axis can be used in the system without having to change the position of the viewports or the direction of the lasers when three laser polarisations are required for 369 nm Doppler cooling (see Sec. 5.1.3).

The internal mount for the atomic ovens are to provide alignment of the ovens to the chip surface. It is preferable to align the ovens in such a way that the atomic flux incident on the micro-fabricated ion trap surface is minimised, this is done by placing the mount in a position where the flux is parallel to the chip surface (See Sec. 4.1.3). The mount for the atomic ovens attaches the oven to the internal structure of the vacuum system near the oven feedthrough. The oven feedthrough⁴ is attached to the bottom DN40CF flange of the octagon. The feedthrough allows for 16 A of current to be supplied to up to four atomic ovens (Vacuum system is used as a common ground) and has bare pins on the vacuum side, which are attached to the wires⁵ on the atomic ovens using barrel connectors⁶.

The rear DN63CF flange of the cluster hosts the 100 pin high density feedthrough⁷ for application of the DC trapping voltages. On the outside, the feedthrough consists of one 78-pin D-sub connector and one 26-pin D-sub connector (4 pins of which are grounded), from which the filter box described in Sec. 4.3.3 is connected directly with a short cable with compatible connectors to reduce noise pick-up. On the vacuum side, custom multi-core, Kapton insulated cable assemblies⁸ connect the feedthrough D-sub to four, 25-pin connectors located on the back of the chip carrier described in Sec. 4.1.2.

The 50 Ω SMA feedthrough⁹ for application of RF trapping voltages should preferably be as close to the SMP connector on the chip carrier as possible, for our system this is the bottom right DN40CF flange of the octagon. Longer distances will add to the total impedance of the wire connecting the feedthrough to the chip carrier which is undesirable for the high Q resonant circuit comprised of the external helical can transformer, capacitive divider, RF feedthrough, micro-fabricated ion trap and cables connecting these components (see Sec. 4.3.1). The feedthrough is a double sided female SMA connector, from which the helical can and capacitive divider are connected on the outside, and a custom made SMA-SMP connector is attached on the vacuum side constructed from male SMA¹⁰ and SMP¹¹ connectors crimped onto a coax RG316 cable¹².

All the glass viewports are anti-reflection coated for high transmission at UV wavelengths (above 99% at 369 nm). The optical access for the lasers are provided by fused-

⁴EFT0243032

⁵LewVac KAPW1X061

⁶Kurt J. Lesker FTAIBC094

⁷Kurt J. Lesker IFDGG501056AX

⁸Allectra 211-FS50-PK, 212-PINF-25, 211-MS25-PK and 212-PINM-25, 311-KAP-RIB25-1000

⁹Allectra 242-SMAD50-C40

¹⁰TE Connectivity 1056456-1

¹¹Rosenberger19K201-302L5

¹²RS Pro 794-7206

silica viewports¹³ placed on the side DN40CF flanges of the vacuum system octagon. There is one on each side to minimise internal scattering of the laser within the vacuum system and to help with laser alignment. The top flange of the vacuum system octagon is the same as the side viewports, this is to give an un-obstructed vantage point for looking into the vacuum system.

The optical access for ion imaging is a large central viewport on the front of the vacuum system octagon. It and the chip carrier are placed close together to minimise the ion and collection optics objective distance. The viewport is also recessed towards the chip surface; this is done to improve the collection efficiency of the collection objective (see Sec. 4.4). The viewport also has a wire mesh attached to the vacuum side of it to reduce the total dielectric exposure of the window to the ion as described in [96], the reasoning for minimising dielectric exposure is also described in Sec. 3.3.3). A small hole is left in the centre of the mesh to not obstruct the photons being collected by the imaging objective. A negative effect the mesh can have on the system is obstruction of the microwave and RF delivery systems for manipulating the ions internal states. Experimentally this did not appear to present any issues but has been shown to have an effect in simulations for a similar system in [97].

Two T-pieces¹⁴ are attached to the two bottom DN40CF flanges of the cluster and oriented to support and keep the vacuum system upright, another T-piece is attached to one of the top DN40CF flanges of the cluster. The ion gauge¹⁵ is attached to one of the T-pieces and the ion pump¹⁶ is attached to one of the top DN40CF flanges of the cluster. This so that the chip carrier is roughly centred in-between the ion pump and ion gauge. Due to pressure gradients within the chamber the actual pressure at the ions position is unknown, by centring the ions position between the ion pump and gauge, a better estimate of the pressure at the ions position can be made. Additionally the ion pump is attached to a T-piece so that the getter material surrounding the ion pump has the largest amount of surface area exposed to the main chamber, this is speculated to improve vacuum pressure inside the main chamber.

The valve¹⁷ used during the baking process in Sec. 4.1.4 is attached to the last remaining DN40CF flange of the cluster. All other flanges of the main chamber are housed with blank flanges¹⁸.

¹³Kurt J. Lesker VPZL-275Q

¹⁴Kurt J. Lesker T-0275

¹⁵EPIMAX PVCX Gauge

¹⁶NexTorr D200-5

¹⁷Kurt J. Lesker VZCR40R

¹⁸Kurt J. Lesker F0275X000N

4.1.2 Chip carrier

The chip carrier consists of two custom designed PCBs, a front PCB which hosts the micro-fabricated ion trap which is epoxied¹⁹ to a copper block heat sink, and a back PCB which hosts a low-pass filter on each channel, mounts for the chip carrier to the vacuum system and four, 25 pin connectors to attach the D-sub feedthrough to the chip.

The front and back PCBs are made from 1.6 mm thick Rogers RO4350B material, 44 μm of copper is deposited onto both sides of the Rodgers from which an electroless nickel electroless palladium immersion gold (ENEPIG) finish; this gives $\approx 70 \mu\text{m}$ of gold, which is suitable for soldering components and wirebonding. Components are soldered with lead-free solder²⁰ and cleaned with flux remover²¹ before the chip carrier is assembled, as solder flux and leaded solder out-gas a considerable amount, this would raise the vacuum pressure.

It is important to have a filter near the chip to attenuate noise picked up by the cables and feedthrough after the first DC voltage filters (Sec. 4.3.3), because of this a low pass filter is soldered to the back PCB after the 25 pin connectors. The low-pass filter consists of a 1 k Ω resistor²² in series with the DC electrode, followed by a 620 pF capacitor²³ in parallel to the channel, both of which were tested to be vacuum compatible. The single stage filter has a cut-off frequency of ≈ 260 kHz, this is higher than the filters on the filter box but low enough to attenuate noise picked up by the RF and microwave frequencies used during experiments. The reasons for only a single stage filter located near the trap is simply due to the size constraints of the PCB. The back PCB is connected to the front PCB via a spring loaded pogo pins²⁴ that are soldered to through-holes on the back PCB. The spring loaded end of the pogo connectors are then compressed to the front PCB during assembly. Both sides of the back PCB can be seen in Fig. 4.4.

¹⁹Epoxy Technology EPO-TEK H21D

²⁰Multicore 96SCLF320AGS88

²¹Chemtronics Flux-Off Aqueous

²²KOA Speer RK73N2ATTD102M

²³Presidio Components VP0505NP0621K150V4M1R6

²⁴Mill Max 0852-0-15-20-83-14-11-0

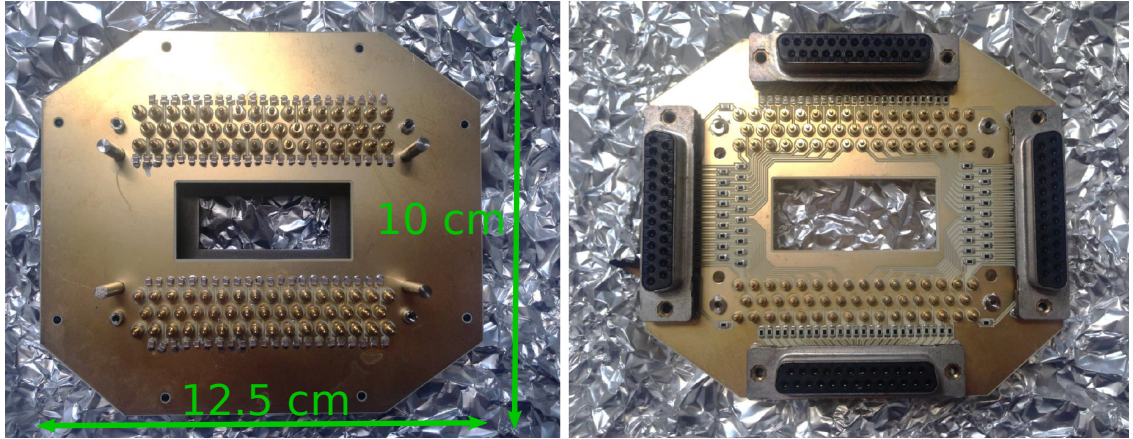


Fig. 4.4 Front (left) and rear (right) views of the back PCB, showing the pogo connectors, low-pass filters (capacitors and resistors) and D-sub connectors. Also visible are the mounting holes and threaded inserts for the front PCB.

The front PCB has a surface mount SMP connector²⁵ soldered to it for the trap RF delivery via the custom RF cable described in the previous section. The copper block that hosts the micro-fabricated ion trap is secured to the front PCB with M2 nuts and bolts and the chip electrodes are wire bonded to the front PCB electrode rails. Each DC electrode of the chip is double bonded, the RF electrode is sextuple bonded and the ground of the chip is bonded to the front PCB ground using $30\ \mu\text{m}$ aluminum wire. The multiple wire-bonds are to reduce the resistance added by the wire bond and reduce the probability of the electrodes detaching from the front PCB during the baking process. Aluminium wire was chosen because of the ease in which it is wire-bonded when compared to gold, which requires a constant heat supplied to both surfaces being wire-bonded. This was found to be troublesome on this copper block and PCB design as an even temperature on both bonding surfaces could not be easily attained due to the geometry of the structure. The front PCB and the connected copper block with wire-bonded chip attached can be seen in Fig. 4.5. The bolts connecting the front PCB to the back PCB (described in Sec. 4.1.4) and the mounting structure attached to the back PCB ground the chip and chip carrier to the common ground vacuum system.

²⁵Rosenberger 19S101-40ML5

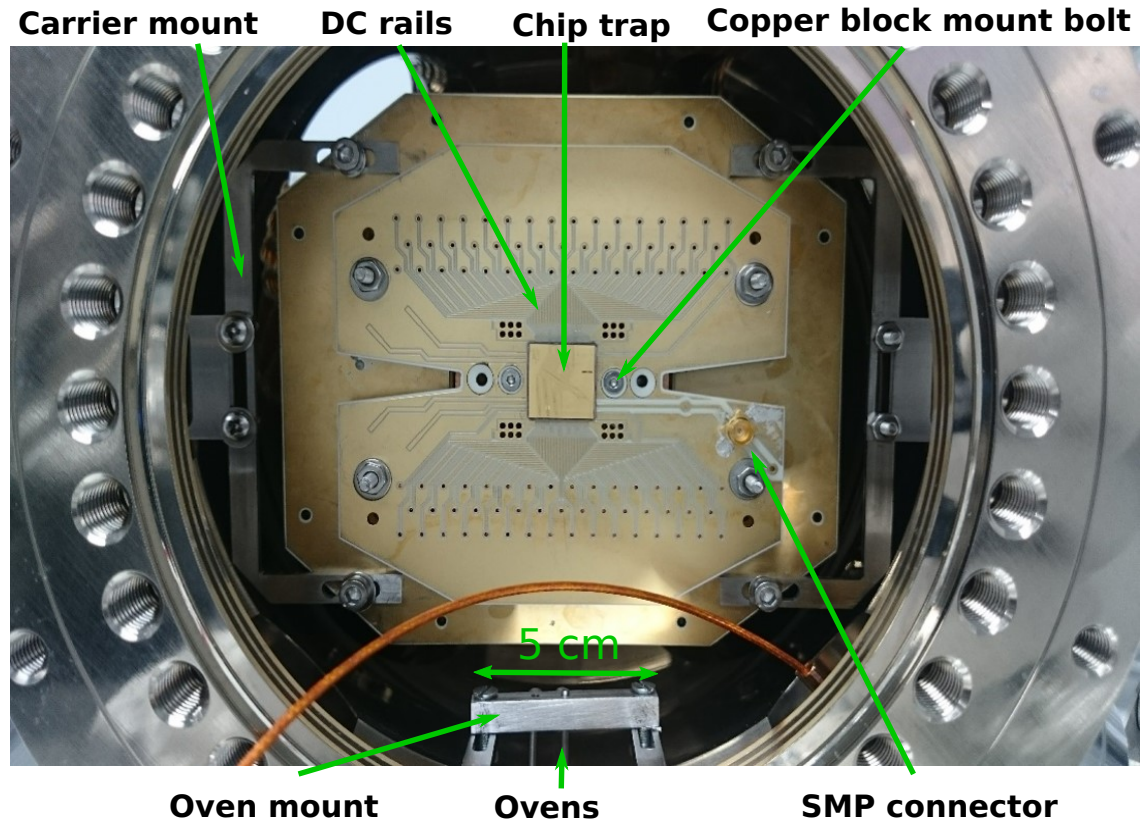


Fig. 4.5 The front PCB with an attached wire bonded chip inside the vacuum system with the front viewport detached and all visible components labelled. The four corner bolts are tightened until all pogo connectors are in contact with the DC rails.

4.1.3 Atomic ovens

The atomic ovens used in this setup are relatively simple in design, yet effective for loading ions on a surface trap. The main issue that could arise from using these ovens is coating the surface of the chip with ytterbium atoms as ytterbium adheres to most surfaces, including gold. The ovens for this experimental setup provide the following:

- Loading of natural or enriched ytterbium
- Limited atomic flux incident on the ion trap surface
- Low thermal dissipation and good thermal isolation of the atomic sample from the vacuum system
- Operable for a high number of loading runs

The ovens used are long, small diameter, stainless steel tube²⁶ ovens with dimensions 16 mm long, 1.2 mm inner diameter and 1.5 mm outer diameter. The oven tubes are spot

²⁶Stainless Tube and Needle Co. 17G Thin Wall 304/316

welded to a piece of wire²⁷ via constantan foil at the closed end. The tube is attached to the oven mount with minimal surface area contact to avoid sinking too much heat to the mount. The wire is attached to the feedthrough via a barrel connector, these parts are described in Sec. 4.1.1. The ytterbium samples are packed in the open ended side of the tube so it is in close proximity to the heating source and produces a narrow atomic beam. Similar oven designs have been used before in our laboratory for macroscopic blade traps [98], and micro-fabricated ion traps [95, 99]. The atomic ovens in this experiment are aligned near parallel to the surface of the chip, the centre of the ovens tube is not in direct line of sight with the ion position, instead they are aligned slightly below to avoid excessive ytterbium coating on the trap surface.

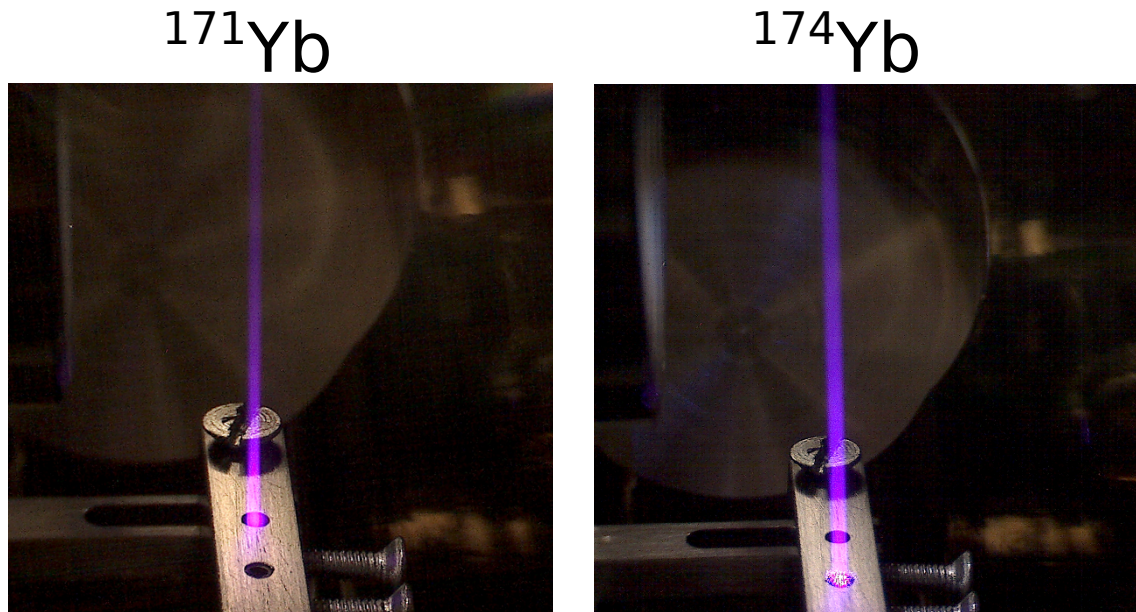


Fig. 4.6 Natural (^{174}Yb atomic flux) and enriched (^{171}Yb atomic flux) ovens tests for ionisation fluorescence with 399 nm laser pointed directly into the oven tube. The wavelengths used for each of the tests is the same as those in Table 2.1.

These ovens need to reach a temperature of 420 K to generate a ytterbium atomic flux, the calculated current for these ovens to create an internal temperature [95] is ≈ 0.8 A, an order of magnitude below the observed currents required for creating an atomic flux. It is speculated that the reason for the extra required current is due to thermal dissipation through the clamp on the outside of the vacuum chamber, the feedthroughs and the mount holding the oven tube. The oven test shown in Fig. 4.6 shows an observable fluorescence of the neutral atomic oven at 6.4 A and the enriched atomic oven at 6.8 A, these values are slightly higher than the values observed in Sec. 5.1. It is likely because the fluorescence was observed with a naked eye as shown in Fig. 4.6 instead of a CCD camera.

²⁷LewVac KAPW1X061

4.1.4 Assembly, pumping and baking process

Before the vacuum system and its internal components can be assembled, all parts must be cleaned of contaminants that would prevent the vacuum from achieving UHV pressures. A finger print for example would out-gas at a rate that would make UHV pressures unachievable without ever truly being removed. Every part pre-assembly is cleaned in an acetone ultra-sonic bath in a class 1000 clean room to get rid of any deposits of grease or dirt. They are then rinsed with isopropyl alcohol to remove any remaining traces of acetone and sprayed with nitrogen gas to evaporate all remaining isopropyl alcohol. The micro-fabricated ion trap and viewports are simply rinsed in acetone, followed by isopropyl alcohol and nitrogen gas, this is because the chip and the viewport coating is too fragile to be submerged in an ultra-sonic bath.

After these solvent cleans, all vacuum chamber parts are wrapped in aluminium foil to keep the pieces clean during transport from the clean room to the oven²⁸ and baked at 200°C for two weeks. This is to form an oxide layer on the surfaces of the stainless steel components which reduces the rate that gases diffuse through the bulk of the metal chamber, as noble gasses and hydrogen diffusing through the chamber walls are typically a limiting factor at UHV pressures. After the bake the vacuum chamber parts are cleaned in the same manor as before and kept in the clean room until further baking is required.

After this the chamber with its internal parts are assembled. Initially the chip carrier and atomic ovens are mounted in the main body for ease of access before the flanges are closed up. The components of the vacuum system all have industry standard conflat (CF) flange, which have protruding knife edges that cut into a copper gasket placed between them. Each flange contains bolt holes that allow for the knife to cut into the gasket with the required compression for UHV pressures. The correct mating force is achieved with a torque wrench, each bolt is tightened in a specific pattern to achieve uniform compression on the gasket. If assembled correctly, CF flanges can maintain pressures down to 10^{-13} mbar [101]. Before any flanges and gaskets are connected they should be checked for imperfections as this could prevent a seal from being formed, any parts with defects should be replaced. Note that for all tapped holes on the chamber silver plated bolts are used to lubricate the threads and prevent the bolts from seizing, a common occurrence for non-silver plated bolts after a second bakeout.

Once assembled, the valve opening is attached to a turbo-pump²⁹, pumped to $\approx 10^{-7}$ mbar and the entire system is leak tested with an argon gas needle gun. This is made possible by attaching a residual gas analyser to the pump and looking for spikes in argon when the gun is on and pointed into a flange. Any leaks found can be fixed by checking the torque on all the bolts around the flange, if this fails the gasket may need replacing, otherwise it is likely an issue with the flange. Once no leaks are present, the system

²⁸designed by Dr. James Siverns [100]

²⁹Leybold Turbolab

is transported to the oven, pumped back to pressure using the turbo-pump and slowly ramped to 180°C over the course of 24 hours. Once this temperature is achieved, the system is left to bake until the pressure remains stable for a few days, this was found to be $\approx 10^{-7}$ mbar at 180°C. The slow reduction in pressure can be attributed to the out-gassing of the vacuum chamber walls and components inside the chamber.

From this, the ion gauge is activated according to the instructions provided with the ion gauge controller³⁰. The ion pump getter material is activated after this, which is done by following the instructions provided with the ion pump controller³¹. Note that the ion pump part has two modes of pumping, passive pumping from the getter material and active pumping from the ion pump. Activating either of these causes extra out-gassing to occur due to the high currents passed through the pumps during activation. Pressure stabilisation after activation of either the getter or ion pump is required, this typically took 12 to 24 hours. Once the pumps have been activated and the pressure is stable, the valve is closed and ion pump turned on. This causes the pressure to decline rapidly, for this system it plateaus at $\approx 10^{-9}$ mbar at 180°C. From this the oven temperature is slowly reduced over the course of a day, this is done to avoid damaging the viewports of the vacuum system as a fast temperature ramp would create a large temperature gradient, meaning cracking of the viewports could occur due to the thermal expansion of the material. The pressure stabilised around 10^{-10} mbar at room temperature; after a three days at room temperature the final pressure attained from this process was 2.8×10^{-10} mbar. This could arguably be lower and is likely high due to dirt mistakenly placed inside the chamber as no leaks could be detected; this is also suspected because of the many iterations of glowing and broken microchips (see Sec. 3.3.3) that went through this system before a working microchip was used, the glowing effect caused excessive breakdown on the chips and likely caused the materials of the chip to coat the chamber walls.

4.2 Laser setup

As described in Sec. 2.1, this experiment uses two lasers for Doppler cooling of ytterbium ions and one additional laser for ionisation. The 369 nm cooling laser is a MSquared system, comprising a Ti:sapphire laser (SOLSTIS CW) for the 739 nm light and a bow cavity with a SHG crystal (ECD-X) to double the frequency, with a 369 nm output power of ≈ 1.3 W. the 399 nm laser is a Toptica DL pro with an output power of ≈ 110 mW and the 935 nm laser is a Toptica DL pro with an output power of ≈ 90 mW. All the lasers are located on different tables within the lab, powers are split at the laser outputs to reach multiple experiments and a fraction of the total laser power is fibre coupled to this experimental setup by using single-mode, polarisation maintaining fibres³². Part of

³⁰EPIMAX PVCX Controller

³¹NexTorr N10PS-03

³²Thorlabs PM780-HP-CUSTOM

the laser output for each laser is coupled to a wavemeter³³ and monitored by a Labview program developed by Ph.D. student Anton Grounds, the Labview program is connected to the Toptica laser controllers³⁴ and adjusts the grating voltage over the laser diode for the laser to lock the wavelength to a specific value given to the program. The 935 and 399 nm laser can be fixed at a the required wavelengths for multiple experiments when the same ytterbium isotope is used, the Toptica lasers provide relatively good stabilisation over the wavelengths but still require both wavelengths to be locked. The 369 nm laser requires better stability than the 399 and 935 nm lasers, a locking system developed by group member Tomas Navickas [102] locks the 369 nm laser using a passive cavity.

4.2.1 369 nm laser setup

Additional control is also needed over the 369 nm laser for each experiment for Doppler cooling, state preparation and state detection. This is achieved by introducing an acousto-optic modulator³⁵ (AOM) and an electro-optic modulator³⁶ (EOM) in the path of the laser. This is introduced after laser light for the 369 nm laser has been split into the wavemeter and other experiments, therefore the frequency shifts induced on the laser will not be shown on any wavemeter reading. This setup is also placed before the 369 nm light is fibre coupled to the experiment. This is because of space constraints on the experiment table, it is preferable to place the AOM/EOM setup closer to the experiment control computer (Sec. 4.6) to avoid potential delays when sending TTL pulses over long distances to the AOM and EOM. The function of the AOM is to have fine control over the power and wavelength when bringing the ion to its saturation point for Doppler cooling and state detection while also switching the 369 nm laser on and off for experiments (see Sec. 5.1). The function of the EOM is to put side-bands on the 369 nm light when preparing the ion in its ground state for experiments (see Sec. 5.2.1).

³³HighFinesse WS-7

³⁴Toptica SYS DC 110

³⁵Isomet AOM 1206C-833

³⁶QUBIG EO-T2100M3

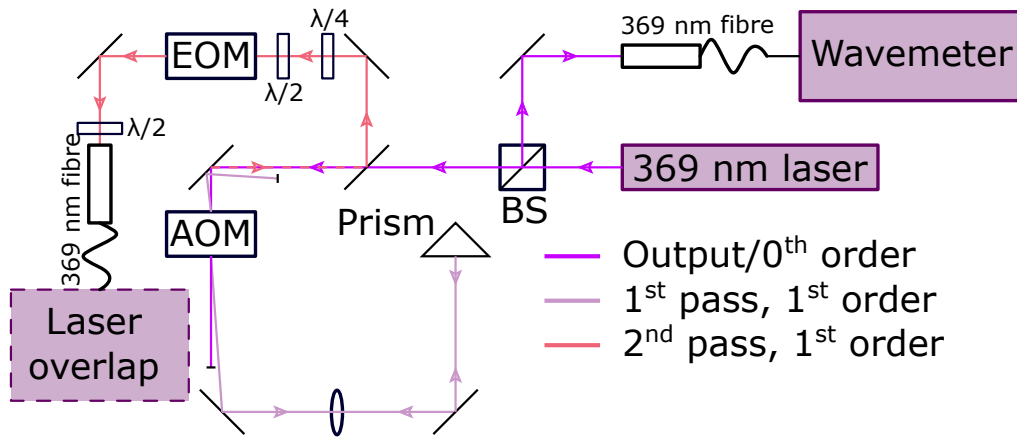


Fig. 4.7 AOM/EOM setup used for experimental control of the 369 nm laser light. The beam initially goes through a beam splitter (BS) cube where a fraction of the laser power is sent to a wavemeter. The other path goes through a double pass AOM setup followed by $\lambda/4$ (0th order quarter waveplate) and $\lambda/2$ (half waveplate) waveplates to linearly polarise the light travelling into the EOM, from which it goes through another $\lambda/2$ waveplate polarisation maintain the light going through the fibre.

The AOM setup shown in Fig. 4.7 is setup in a double pass configuration, this doubles the frequency shift induced on the 369 nm light and minimises laser beam movement when applying a range of frequency shifts. This is done to stop the laser beam position decoupling the fibre coupler and is achieved by overlapping the second pass, 1st order beam with the initial output of the 369 nm laser. This works because any variation of Bragg angle of the 1st order beam on the first AOM pass (that changes depending on the induced frequency shift of the light) will equal the angle between the input beam for the AOM (laser output/0th order) and the 0th order beam of the second pass. Note that the 2nd pass 1st order and 369 nm laser output are not overlapped vertically, this is fine because the AOM produces nth order beams horizontally, it is also necessary so that the two beams can be distinguished between and separated in the laser setup. The way the double pass setup achieves this is by creating vertical separation between the 1st pass, 1st order output of the AOM and the return path of this beam back into the AOM by introducing a prism to create vertical separation between the output and return of the 1st pass 1st order and a bi-convex lens to refocus the return path back into the AOM. The focal length of the bi-convex lens is equal to the distance between the AOM and the lens, and the prism and the lens.

The AOM is controlled by the AOM controller³⁷, two of the DC channels from the DC channel box in Sec. 4.3.3 are connected to the controller for tuning the power and frequency shift of the 369 nm light coming out of the AOM. A TTL pulse from the TTL

³⁷Isomet 630C-110-G AO Driver

switch box in Sec. 4.6 connected to the AOM controller turns the AOM on or off. The switch of the AOM controller does not have a good extinction ratio (meaning when in the off state, some 369 nm photons still reach the experiment), so an additional switch³⁸ is placed in the path between the AOM and the AOM controller.

After the AOM, the laser passes through the EOM which does nothing to the laser light when in the off state and applies ≈ 2.1 GHz side-bands when in the on state. The EOM is controlled by an EOM controller³⁹ that has a TTL input connected to the TTL switch box (Sec. 4.6) to control its on and off states during experiments. The EOM has a minor polarisation dependence, hence the $\lambda/4$ (0th order quarter waveplate) and $\lambda/2$ (half waveplate) waveplates are placed before the input so that the power output of the EOM can be optimised. The output polarisation of the EOM is controlled by the second $\lambda/2$ waveplate to maintain polarisation through the fibre.

4.2.2 Laser overlap

Once all three lasers are coupled to the table hosting the vacuum system, they are combined and manipulated as shown in Fig. 4.8 to provide the following:

- Overlap of all three lasers outside and inside the vacuum system
- Power control of the 369 and 399 nm lasers
- Polarisation control of the 369 nm laser entering the vacuum system
- Removal of spherical aberrations on the 369 nm beam
- Three axis control of the beam focal point at the ions position
- Small beam waist focused to the ion position above the trap with minimal laser light reflecting off the surface of the trap

³⁸Mini Circuits ZASW- 2-50DR+

³⁹QUBIG RF generator + amplifier

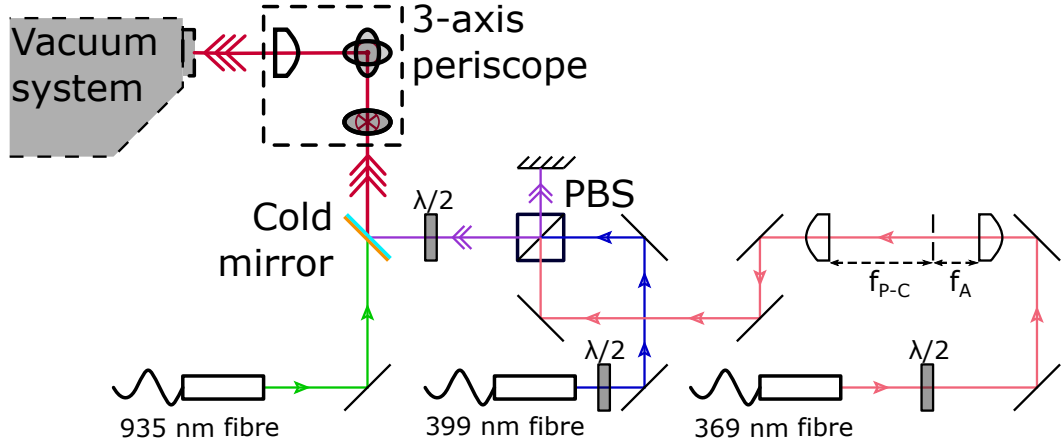


Fig. 4.8 Laser overlap setup next to the vacuum system, the purple beam arrow is the combined 369 and 399 nm lasers coming out of the UV polarisation beam-splitter cube (PBS), the red beam arrow represents all three lasers combined that enter the vacuum system through one of the side viewports and can be aligned parallel to the microchip surface via the 3-axis periscope.

The overlap of the three lasers is achieved by overlapping the 369 and 399 nm beams using a UV polarisation beam-splitter cube (PBS), the combined UV beams are then directed to a cold mirror that reflects UV light and transmits IR light, this allows for the 935 nm beam to be combined with the UV beams. The power of the 369 and 399 nm beams can be adjusted by changing the polarisation of each before they are combined in the PBS by using the $\lambda/2$ waveplates at the fibre outputs. The $\lambda/2$ waveplate for the 369 nm beam is useful for polarisation maintaining the beam through the fibre and lowering the power incident on the ion when bringing the Doppler cooling transition to its saturation limit (Sec. 5.1.3). The $\lambda/2$ waveplate for the 399 nm beam is useful for day to day adjustments of the 399 nm power incident on the trap but is not necessary. The $\lambda/2$ waveplate after the PBS is adjusted to address all hyperfine transitions in the $^2S_{1/2} |F = 1\rangle \leftrightarrow ^2P_{1/2} |F = 0\rangle$ transition for $^{171}\text{Yb}^+$ ions that the 369 nm laser is driving (see Sec. 5.2.1).

The 369 nm beam coming out of the fibre is a collimated beam with a beam width of ≈ 1.2 mm, the profile of the beam also contains some spherical aberrations from the fibre coupler lens. It is preferable to increase the beam width and remove these spherical aberrations before the beam reaches the focusing lens on the 3-axis periscope, this is to make the spot size of the beam at the ions position smaller and to make it easier to align the beams peak power to the ions position. To achieve this, a telescope with a pinhole is put in the path of the 369 nm beam, the tutorial followed is found in [103]. Ideally the spot size of the 369 nm beam should be as small as possible so that minimal 369 nm power is used for the ion trap experiments. This is preferable because of potential power limitations

in the portable device under development (Sec. 7), it also helps to minimise scatter that could come from the 369 nm beam reflecting off the chip surface. The telescope consists of an aspherical lens at the beam input side and a plano-convex lens at the output side separated by a distance equal to the sum of their focal lengths as seen in Fig. 4.8. The increase in beam diameter is attained from the ration of focal lengths in the telescope $f_{P-C}/f_A = r_{desired}/r_{source}$ ($r_{source} = 0.6$ mm at $1/e^2$, $r_{desired} = 1.8$ mm at $1/e^2$), the focal lengths for both lenses chosen were $f_{P-C} = 150$ mm and $f_A = 50$ mm. To remove spherical aberrations, a pinhole is placed near the focal point of the two lenses in the telescope, the diameter of the pinhole, D , to let only the TEM₀₀ laser mode through is calculated by

$$D = 1.3 \frac{\lambda f_A}{r_{source}}, \quad (4.1)$$

where λ is the laser wavelength (369 nm). this gives a value of $D = 39.975$ μm , because this isn't a common manufactured pinhole, the actual pinhole diameter that was used was 40 μm .

Once all three beams are overlapped, they beams are focused at the ions position, this is achieved by construction of a periscope made from miscellaneous parts and micrometer stages. The micrometer stages⁴⁰ are setup in a way that allows the beam path to remain parallel to the surface of the chip while allowing the beam path to move freely in the y and z axis as shown in Fig. 4.9. The periscope has a plano-convex lens with focal length $f = 200$ mm for focusing the light to the ions position and prevent scattered light coming off the chip surface. The focusing lens is also attached to a micrometer so that the focal point of the lens can be moved along the beam path; the input and spot size beam diameters after focusing are listed in Table 4.1.

⁴⁰Mitutoyo Digital Micrometer 350-351-30

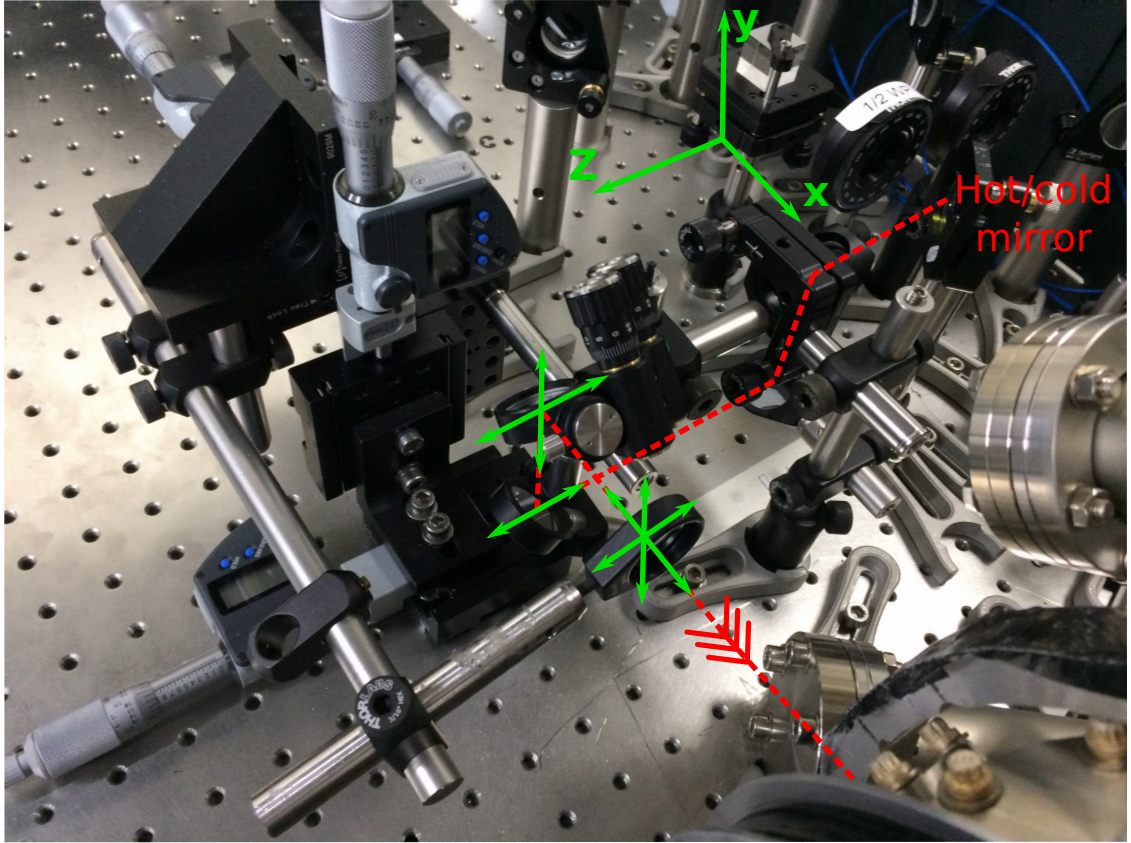


Fig. 4.9 3-axis periscope used for aligning the laser beams parallel to the chip surface. Red dashed line indicates the overlapped beam path, axis degrees of freedom are indicated by green arrows. The bottom mirror, top mirror (on gimbal mount) and focusing lens are all moved by the z axis micrometer stage, the top mirror and focusing lens are moved by the y axis micrometer stage and the focusing lens can be moved in the x axis for moving the focus point along the beam path.

	Input beam diameter $1/e^2$ (mm)	Spot size diameter $1/e^2$ (μm)
369 nm	3.6	21
399 nm	1.8	44
935 nm	2.1	89

Table 4.1 Collimated beam diameters at beam overlap with associated beam spot size diameters once focused to the ions position. All beams have a small enough diameter as to not reflect off the chip surface when parallel with the chip and focused at the ions position $152 \mu\text{m}$ above the chip surface.

4.3 Trapping voltages

To trap ions on a micro-fabricated Paul trap, a minimum of two voltage types are required to confine ions in all three dimensions, high voltage RF voltages to trap the ion in the radial

dimensions of the chip and DC voltages to trap the ion in the axial dimensions of the chip (see Sec. 3 for more details). The simulated voltages in the BEM solvers described in Sec. 3.2.3 are applied. The applied RF voltage, frequency and amplitude should be resistant to voltage fluctuations. The resonant circuit should have a Q value as high as possible to filter out unwanted noise that may otherwise couple to the circuit. The DC voltages should also be as free from voltage noise as possible, to filter out noise a DC filter system on all the analogue DC voltages is implemented outside and inside the vacuum system (in vacuo filter described in Sec. 4.1.2). The main sources of noise that can couple to either the RF or DC voltages is from mains 50 Hz noise, the RF and microwave emitters for coherent manipulation of the ion (Sec. 4.5) and other miscellaneous lab equipment located around the experiment.

4.3.1 RF resonant circuit design and optimization

This section describes how to apply RF fields to the micro-fabricated chip inside the UHV system. For simplicity the micro-fabricated ion trap, inner vacuum system cable and vacuum feedthrough described in Sec. 4.1.1 will be seen as a singular component with its own complex impedance, as disentangling each individual component is not useful for optimizing the Q of the resonant circuit. The general setup can be seen in Fig. 4.10 where the signal generator⁴¹ and RF amplifier⁴² were chosen for their frequency and amplitude stability, and to generate a high voltage RF signal to drive the resonant circuit.

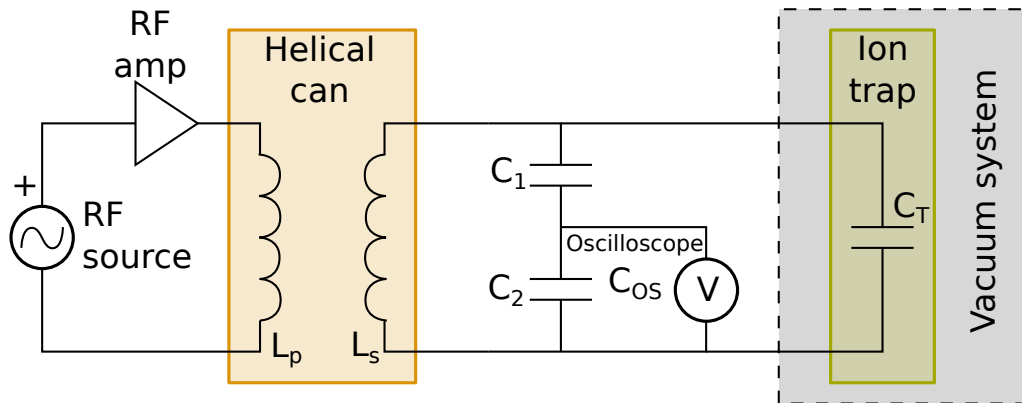


Fig. 4.10 Circuit for applying and probing RF voltages to an ion trap.

The resonant circuit is comprised of three parts, the helical can, the capacitive voltage probe and the ion trap in vacuo. The function of the helical can is to further amplify the RF voltage by stepping a low impedance source (primary coil L_p) to a high impedance load (secondary coil L_s and the other components). The capacitive probes function is to step the voltage of the circuit down to voltage that can be measured on an oscilloscope.

⁴¹Rigol DG4062

⁴²MiniCircuits ZHL-5W-1+

The chip in vacuo completes the resonant circuit by acting as the primary contribution to the circuits capacitance. By grouping the capacitive probe and chip in vacuo together, and viewing the helical can as a single inductor to ground, the components can be seen as a parallel LCR resonant circuit. This would give a resonant frequency and circuit Q factor of

$$\begin{aligned}\omega_0 &= \frac{1}{\sqrt{LC}}, \\ Q &= \frac{1}{R}\sqrt{\frac{L}{C}},\end{aligned}\tag{4.2}$$

where ω_0 is the resonant frequency of the circuit, and R , L and C are the effective resistance, inductance and capacitance of the components. The inductance and capacitance can be written as

$$L = k\sqrt{L_p L_s},\tag{4.3a}$$

$$C = C_T + \left(\frac{1}{C_1} + \frac{1}{C_2 + C_{OS}} \right)^{-1},\tag{4.3b}$$

where k is the coupling coefficient between the two helical can coils. By viewing the circuit in this simple way, decisions on what components to use becomes a lot easier. The first priority is protecting the chip from being subject to a high RF power that would cause excessive heating, or worse, breakdown. Though the chip itself needs relatively high voltages applied to it for trapping to occur, so some values need to be carefully selected in order to minimise the total power across the chip and maximize the voltage. The peak voltage V_p for a parallel LCR circuit can be written as

$$V_p = \sqrt{2PQ} \left(\frac{L}{C} \right)^{1/4},\tag{4.4}$$

where P is the input power to the circuit. From Eq. 4.4 we can extrapolate what needs to be done to maximize V_p and minimise P . We can see that maximizing L and Q , while minimising C will maximise V_p . There are some constraints to consider first, usually the ion trap micro-fabrication process attempts to minimise the chips total capacitance and effective resistance in order to maximize the Q of the circuit, though this is not a controllable variable once the chips have been fabricated so adjustments of the capacitance of the chip is not feasible. It could be proposed that maximizing the inductance of the helical can is the best route to optimize the circuit, but this does have an upper limit as resonant frequency of the circuit $\omega_0/2\pi$ needs to be a roughly 10 to 50 MHz for stable trapping with large trap depths; this is better understood by looking at the stable trapping parameters outlined in Sec. 3.2.2. The helical can was designed with these constraints in mind and the dimensions of the helical can were analytically calculated from [104], the dimensions are shown in Fig. 4.11.

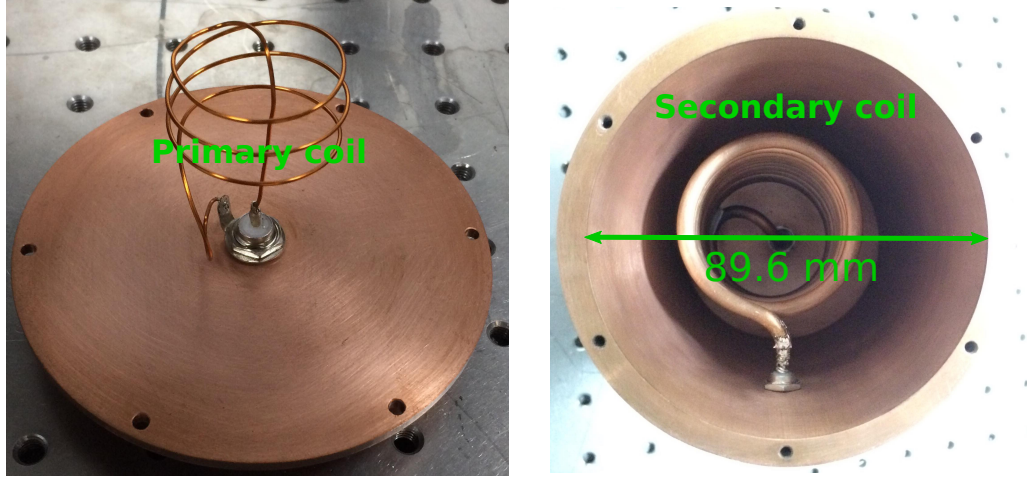


Fig. 4.11 Resonator can dimensions, the can is built from copper and has a 6 mm thick wall with 3 mm thick lids; it has an outer diameter of 101.6 mm (4 inches) and a height of 150 mm. The primary coil has 3 turns, a coil diameter of 35 mm, a coil height of 25 mm and a wire diameter of 0.71 mm; the secondary coil has 10 turns, a coil diameter of 70 mm, a coil height of 65 mm and a wire diameter of 5 mm. The distance (or coupling) between the two coils can be adjusted by moving the primary coil turns closer to or further away from the secondary.

There are three things that can be done to optimize the circuit once the helical can has been designed. Firstly the capacitive probes total capacitance can be minimised, this is done by selecting a small value for C_1 relative to the ion trap in vacuo capacitance C_T , the rest of the capacitance components of the probe are effectively invisible to the resonant circuit as described in Sec. 4.3.2. Secondly, the inner walls of the can can be cleaned of any dirt and imperfections to raise the Q of the resonator, this is done by hand with a micro-fibre metallic polish cloth; this is because the skin depth of copper for 1 MHz signals or higher is typically < 0.1 mm. Thirdly, Q factor can be increased by making the entire circuit from the input be matched to 50Ω real impedance. To understand why this is important we need to consider the total impedance, Z , of the parallel RLC circuit

$$\frac{1}{Z} = \sqrt{R^{-2} + (X_L^{-1} - X_C^{-1})^2}, \quad (4.5)$$

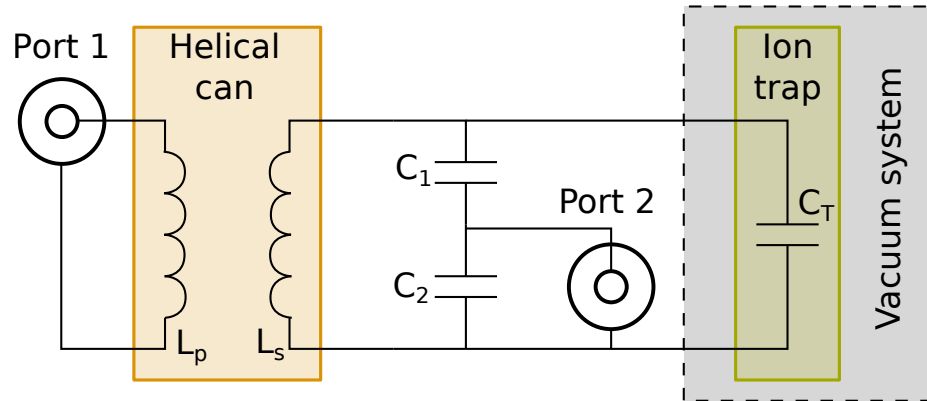


Fig. 4.12 VNA port configuration for testing resonant circuit s-parameters, cables connecting VNA ports are de-embedded so that only the resonant circuit is seen in the S parameters. Port 1 is at the input for the circuit, it is predominately used to measure the load of the entire resonant circuit when driving it with RF frequencies. Port 2 is connected in place of the oscilloscope for the capacitive divider, this port in uni sync with port 1 is predominantly used to measure the Q of the resonant circuit, this placement is sufficient as the power drop from the capacitive divider should be relatively uniform for frequencies around the resonant frequency, this can be seen from the low decibel reading for S_{21} in Fig. 4.13. Port 2 is placed here for convenience above all as probing the resonant circuit on the other side of C_1 would disrupt the already setup system and require extra hardware.

where X_L and X_C are the inductive and capacitive reactance respectively. When $X_L = X_C$ the impedance is completely resistive ($Z = R$), this is when the circuit is on resonating, meaning the RF voltage and current are both in phase. To ensure maximum power transfer from the amplifier, the impedance must be equal to the impedance of the cables connecting it, which is a $50\ \Omega$ SMA cable. This ensures minimal power is reflected to the amplifier making the circuit as power efficient as possible, this will also help when experimental power is a constraint like for the portable system in Sec. 6.2. To match the impedance of the circuit to $50\ \Omega$, a VNA⁴³ with ports attached to the system as shown in Fig. 4.12 is used. Once attached, the shape of primary coil inside the helical can is adjusted to change the coupling between the two coils and primary coil inductance, this changes the mutual inductance of the two coils. As the capacitance of the rest of the circuit is fixed, it is relatively easy to match the reactances, the results of this can be seen in the Smith chart in Fig. 4.13 where Q of the circuit is found to be 83 from the S_{21} or S_{12} parameters, which is similar to other helical can setups previously tested.

⁴³Rohde and Schwarz ZNB20 Vector Signal Analyser

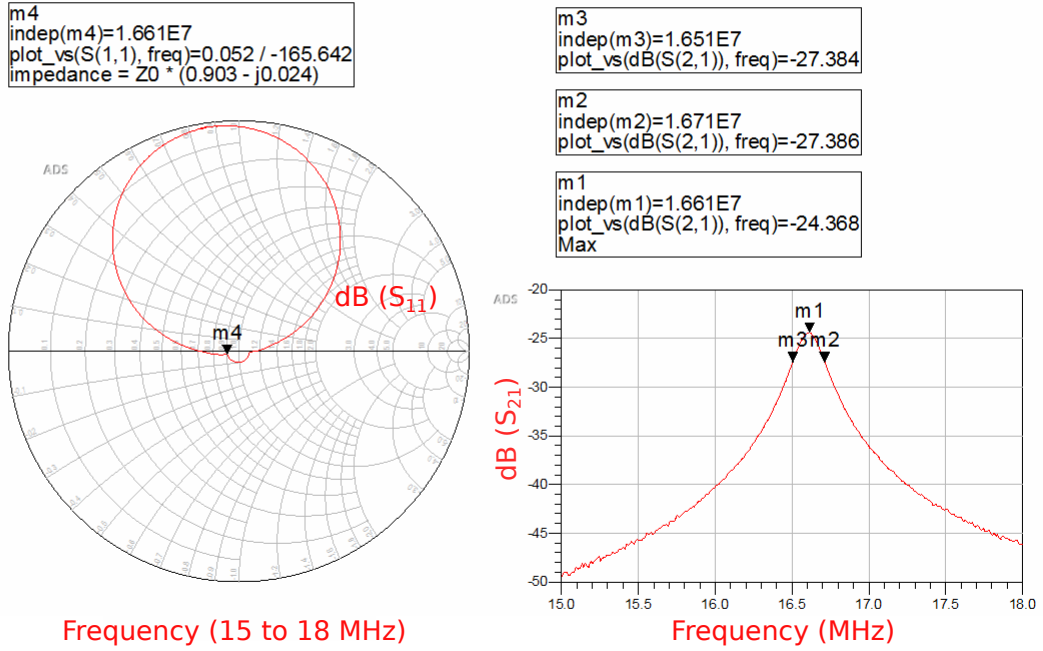


Fig. 4.13 S_{11} (left) and S_{21} (right) parameters for VNA-resonant circuit configuration shown in Fig. 4.12, using the simple linear chip from Sec. 3.2, with connecting cables de-embedded, primary coil geometry adjusted to match impedance roughly to 50Ω and compiled in Advance Design System (ADS). Markers $m1$ and $m4$ show the resonant frequency of the circuit at $\omega_0/2\pi = 16.61$ MHz, markers $m2$ and $m3$ show the -3 dB point (roughly, values aren't exact due to step size of data set) and are used to calculate the Q parameter of the circuit at $Q = 83$. Note the small dimple around $m4$, this isn't a real result and just a fault in the compiled data set as ADS predicts data between two data points as a circle with diameter equal to the spacing of the two data points.

4.3.2 RF voltage capacitive probe

The capacitive probe used to monitor the trap voltage is similar to the one found in [105]. It is important to know the voltage being applied to the chip so that the chip can be kept below its breakdown voltage and to apply the correct voltage regarding the inhomogeneity parameter described in Sec. 3.2.2. As described in the previous section, it is preferable to keep the capacitance of the probe relatively low compared to the chip capacitance, the capacitors chosen are specially for high voltages and were chosen to have values of $C_1 = 0.2$ pF and $C_2 = 20$ pF. From Eq. 4.3b and with the oscilloscope⁴⁴ having a capacitance of $C_{OS} = 16$ pF, the contribution that the probe has towards the total capacitance C is ≈ 0.2 pF; this is small relative to the chip in vacuo capacitance, which was measured to be 35 pF.

⁴⁴GW Instek GDS-2072E

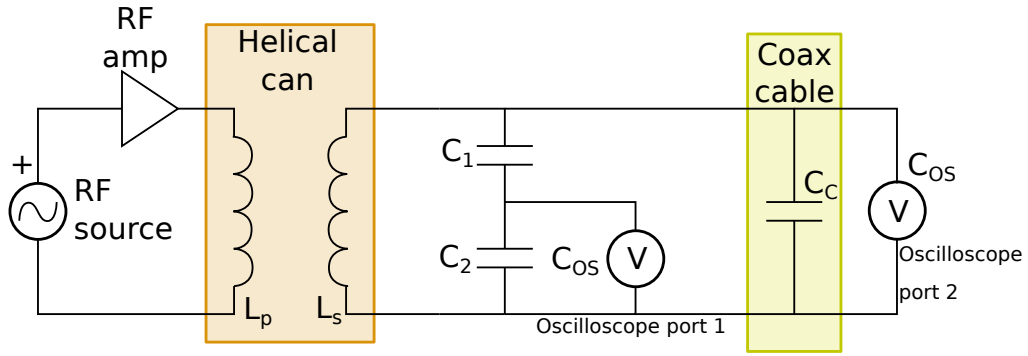


Fig. 4.14 Circuit diagram of the setup used to find the value in which the capacitive divider steps down the voltage across the chip.

The capacitive divider works in the same way as a resistive divider for DC circuitry, the ratio of the two impedances that arise from C_1 and $C_2 + C_{OS}$ defines the fraction in which the RF voltage is stepped down when probed by the oscilloscope, simply put $(C_2 + C_{OS})/C_1$ is the fraction of the trap voltage that the oscilloscope should read. Note that the cable that is used to connect the two capacitors to the oscilloscope will also contribute to the ratio, this is hard to measure though so its better to expect that the measured ratio will always differ from the calculated ratio.

To measure the ratio, the resonant frequency of the entire circuit is required, and can be measured on the VNA as shown in Fig. 4.13. From this, the helical can and capacitive probe can be disconnected from the chip in vacuo and attached to another port on the oscilloscope with a short length of coax cable. The length of cable should be chosen to give the circuit the same resonant frequency as measured when connected to the chip in vacuo, this can be imagined as the sum of the oscilloscope capacitance and the cable capacitance being equal the the trap capacitance at the resonant frequency $C_{OS} + C_C = C_T$; a circuit diagram of this setup can be seen in Fig. 4.14. Once this length of cable gives a resonant frequency value close to the value taken from the VNA setup in Fig. 4.12, the ratio of the two measured voltages on the oscilloscope can be measured in incremental steps up to the oscilloscopes voltage threshold, all the values should be relatively equal.

The average of all these ratios for different applied voltages gives a ratio used when calculating the voltage across the chip. For this system it was found to be $1/730.6$ at a resonant frequency of 17.20 MHz (with cable) which is relatively close to the trap in vacuo resonant frequency 16.61 MHz, meaning that a reading of 273.7 mV on the oscilloscope would correlate to the desired voltage of 200 V across the chip, calculated in Sec. 3.2.3.

4.3.3 Trap DC voltage application

To generate DC voltages for trapping ions, voltages are produced from a DC channel box constructed by Ph.D. student Harry Bostock. There are 16 channels total meaning

16 unique voltages can be created. It is comprised of four, four channel voltage cards⁴⁵ connected to a 16 SMA channel output box. Note that two of the channels are used in the AOM setup as mentioned in Sec. 4.2.1 for frequency and amplitude control of the 369 nm beam.

Before the voltages from the DC channels enter the vacuum system, it is important to filter out any unwanted noise that can couple to the cables. Though noise can couple to the DC electrodes post filter, the feedthrough and cable connecting the filter box are kept as short as possible to mitigate this effect. An additional filter inside the vacuum system is implemented as mentioned in Sec. 4.1.2. The main source of noise that couples to or comes from the DC channels is predominantly from 50 Hz mains noise, switching power supplies located around the lab and, RF and microwave radiation used for coherent manipulation of the ion. High levels of attenuation for this noise is important as it will result in less total micro-motion on the ion.

The filter box designed by group member Dr. Bjoern Lekitsch, the box totals 100 channels and is comprised of a four stage low-pass filter on each channel as shown in Fig. 4.15. The filter is comprised of four $1\text{ k}\Omega$ resistors⁴⁶ and capacitors with a range of values⁴⁷ from 200 pF to $2.2\ \mu\text{F}$ for each channel to cover a wide range of frequencies; the components are all capable of handling 100 V. An LTSpice simulation of the filter gives a -3 dB suppression at a frequency at 32 Hz, a -5 dB at 50 Hz and -10 dB at 100 Hz. The output of the filter box is comprised of compatible D-sub connectors for the vacuum system feedthrough in this thesis.

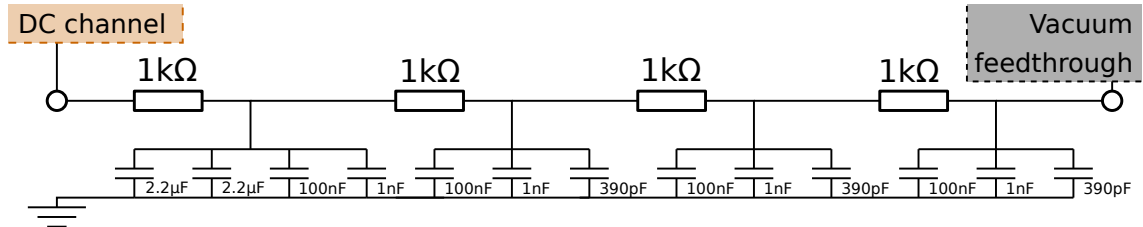


Fig. 4.15 Circuit diagram of the four stage low-pass filter used for a single channel in the DC filter box.

4.4 Ion imaging

The system used for imaging ions has two purposes, the first is to image the chip and ion when initially trapping to attain precise alignment on the ions position and reduce any potential laser scatter off the surface of the chip; the second is to minimise background photon scatter and count the number of photons collected for the ion for performing

⁴⁵Analog Devices AD9959/PCB

⁴⁶Panasonic ERJ-1TNF1001U

⁴⁷Murata GCM1885C2A102JA16D, GCM1885C2A221JA16D, GRM1885C2A391JA01D, Kemet C0603C104K4RACTU and TDK C3216X7S2A225K160AB

coherent experiments. This is done by implementation of a collection optic tube comprised of a telescopic arrangement of lenses focused to a charge coupled device (CCD) camera⁴⁸ and photo-multiplier tube⁴⁹ (PMT). The collected photons from the ion can be directed to either device via a flipper mirror box as shown in Fig. 4.16. There is also a narrow bandpass filter⁵⁰ for 369 nm light placed before the filter box that can easily be placed or removed depending on what wavelength is of interest. For example all experiments are only concerned with 369 nm light for state detection so the filter is in place; for oven testing 399 nm light is of interest so the filter is removed.

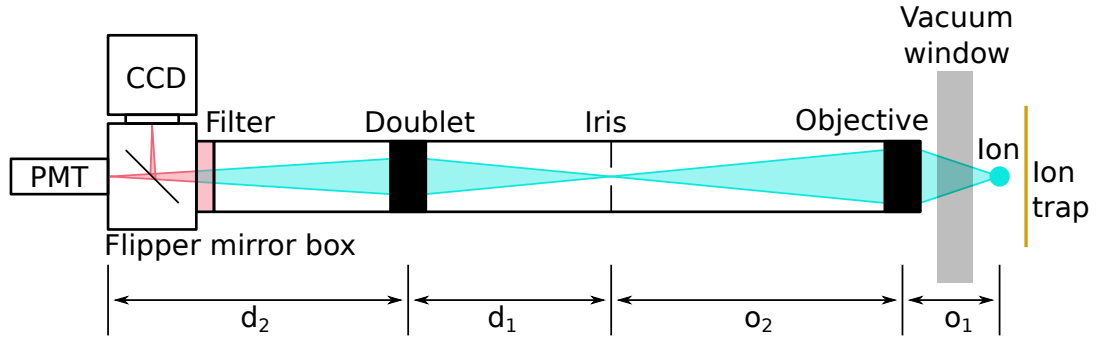


Fig. 4.16 Ion imaging setup, distances and focal lengths are not to scale. The light collected from the ion is shown in turquoise and the filtered 369 nm light is shown in pink.

The collection optics design is similar to the design outlined in [100] comprised of a doublet, iris and triplet, except instead of a triplet used as the objective. The objective of custom build⁵¹ comprised of 5 lenses with anti-reflection (AR) coating for 369 nm and specialised for sensing experiments specifically. It was designed to have a high numerical aperture ($NA = 0.2$, F number = 2.3) for a wide field of view (1.018×1.018 mm), meaning it has a collection efficiency of 1.01%. Simulations in Zeemax reveal that it can distinguish between particles at a distance of at least $2 \mu\text{m}$ apart across its field of focus and has a diffraction limit of . It has a front object distance of $o_1 = 18.3$ mm which allows ions to be imaged through the viewport where the ion-viewport distance is ≈ 11 mm and the viewport thickness is 6.35 mm. The rear focal length is $o_2 = 300$ mm, it is hard to minimise the rear focal length while maintaining the mentioned specifications without the introduction of more lenses in the objective which raises the cost exponentially. The objective is housed in a plastic⁵² tube instead of metallic components so that RF and microwave radiation from the emitters (Sec. 4.5.2 and 4.5.3) located close to the objective aren't reflected off the objective.

⁴⁸Andor iXon+

⁴⁹Hamamatsu H11870-01

⁵⁰Semrock FF01-370/36-25

⁵¹EKSMA Optics PLCA1

⁵²Ketron 1000PEEK

The magnification of the objective was chosen to be $M_o = 11\times$ which when paired with the doublet in a position that gives $M_d = 1\times$ magnification, an image of 0.86×0.86 mm area (chip in Sec. 3.3) to a region of 9.49×9.49 mm, which fits on to most CCD camera cell sizes. The cell size of the CCD being used in this experiment is 13.29×13.29 mm, meaning that a total magnification of $M_{tot} = M_o M_d = 15.46$ is required for this setup. To achieve this the doublet must be placed in a position that gives an extra 1.41 times magnification. This can be calculated from the distances d_1 and d_2 shown in Fig. 4.16, this is given by the equations

$$\begin{aligned} M_d &= \frac{d_2}{d_1}, \\ \frac{1}{f_d} &= \frac{1}{d_1} + \frac{1}{d_2}, \end{aligned} \tag{4.6}$$

which can be rearranged to find the distances to use for a known magnification and doublet focal length

$$\begin{aligned} d_1 &= f_d \left(1 + \frac{1}{M_d} \right), \\ d_2 &= \frac{1}{1/f_d - 1/d_1}. \end{aligned} \tag{4.7}$$

The focal lengths of the two single bi-convex lenses that are comprised within the doublet are chosen to both be 150 mm to give a single doublet focal length of $f_d = (f_1 f_2)/(f_1 + f_2) = 75$ mm, this is assuming the double lens formula for two single bi-convex lenses in close proximity. This gives distances of $d_1 = 128$ mm and $d_2 = 181$ mm. The entire optical tube is attached to a 3-axis micrometer stage for moving to different positions on the chip and adjusting the focus of the setup.

If the resolution of the telescope is sufficient for imaging ions with a distance of $2 \mu\text{m}$ apart, the next constraint that will make it difficult to image multiple ions in a string is the CCD camera pixel size, image area and resolution, which are $13 \times 13 \mu\text{m}$, 13.3×13.3 mm and 1024×1024 respectively. This means that if the imaging area of 0.86×0.86 mm is mapped onto the image area of 13.3×13.3 mm with a 15.46 total magnification, the ions must be at least $1.8 \mu\text{m}$ apart to distinguish between them on two separate CCD pixels (this is assuming an ion can be imaged on 1 pixel, if the ion fluorescence occupies 2×2 pixels then this value doubles). This is an important consideration for developments on multi-ion sensing that will be done in the future. This is of course dependent on the choice in detection scheme; although a PMT with an iris is far better for minimising dark counts and background scatter which results in an improved detection fidelity (Sec. 5.2.2), it is unlikely for PMT detection schemes to be applicable when using many ions for sensing due to the increasing difficulty that comes with distinguishing between many ions on a single photon detector [47].

4.5 Coherent manipulation magnetic fields

To coherently manipulate the energy states within the $^2S_{1/2}$ manifold of $^{171}\text{Yb}^+$ ions (as described in Sec. 2 and shown in Sec. 5) to demonstrate magnetometry, three types of magnetic fields are required, a relatively homogeneous static B-field, RF radiation and microwave radiation. This chapter describes the delivery mechanisms for each and considerations that are taken into account when designing them.

4.5.1 Static B-field coils

A homogeneous static B-field across all potential trapping regions in a 1×1 mm region of space is necessary for sensing with multiple ions on the dual rail chip described in Sec. 3.3. The B-field also needs to generate large enough static fields to lift the degeneracy of the Zeeman states by an amount that corresponds to the desired frequency to be sensed. To create large, homogeneous magnetic fields two 125 mm radius coils, each comprised of 200 turns of insulated copper wire with a diameter of 0.8 mm and wound in an aluminium housing (design in Appendix C) are placed a distance of 75 mm apart around the vacuum system as shown in Fig. 4.17 with the ion position being at the centre position between the two coils. The ideal configuration for creating a homogeneous magnetic field at the ions position is the Helmholtz configuration where the centre of each coil diameter is separated from the other coil by a distance equal to the coils radius, this was not done on this system due to obstructions from the vacuum system. The coils are connected to a stable current supply⁵³ that supplies current in the same direction in each coil.

⁵³Delta elektronika ES015-10

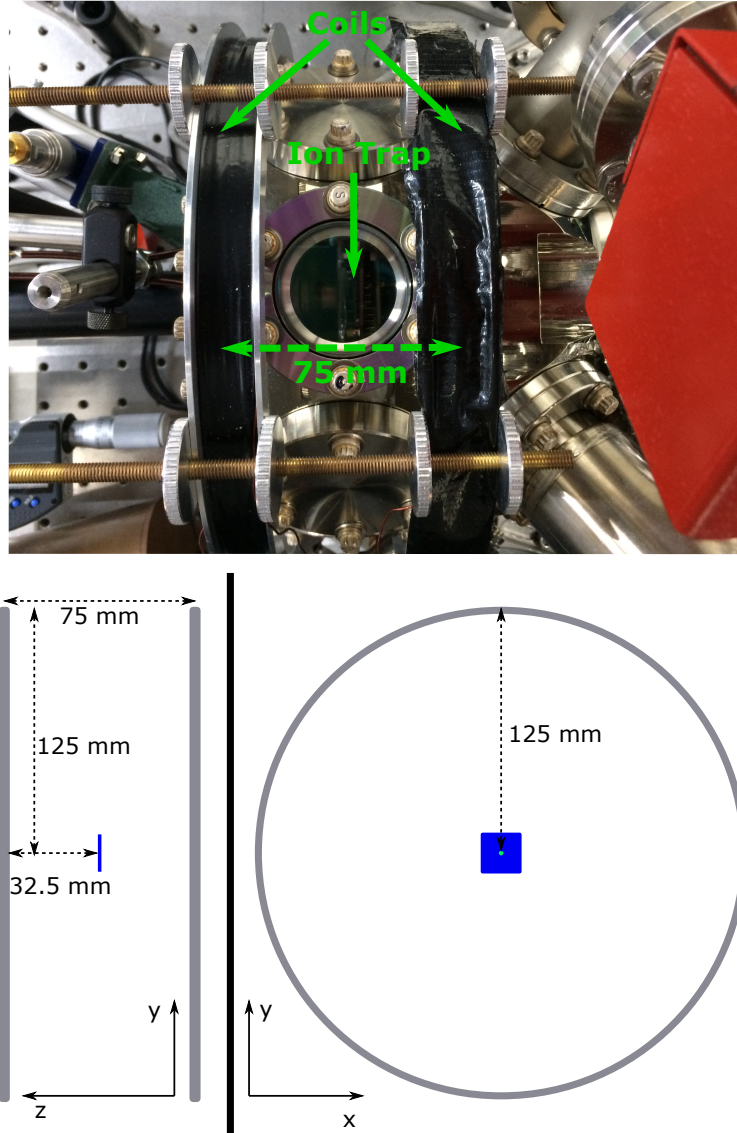


Fig. 4.17 (Top) Top viewport and coils separation around the vacuum system. (Bottom) Side view and front view of current loop geometries, grey indicates the current loops geometry, blue indicates the 2D cross sectional area associated with potential trapping regions and green indicates the centre trapping region used for Fig. 4.18.

An analytical solution to the free space magnetic field amplitude at the ions position can be calculated using the Biot-Savart law for a current loop. This can be extrapolated to two coils with $N = 200$ turns each to give a magnetic field amplitude at the centre position (ion position) of the two coils as

$$B_z = N\mu_0 I R^2 (R^2 + (s/2)^2)^{-3/2}, \quad (4.8)$$

where B_z is the magnetic field in the z direction, $\mu_0 = 4\pi \times 10^{-7} \text{ H.m}^{-1}$ is the permeability of a vacuum, I is the current applied to the coils, R is the radius of the coils and s is the separation between the two coils. The other components in the x and y axis

cancel out due to the geometry of the setup. The magnetic field amplitude induced on the ion for a range of applied currents can be seen in Fig. 4.18, this is a fairly good estimation for finding transition frequency gaps when performing frequency scans like in Sec. 5.4.1.

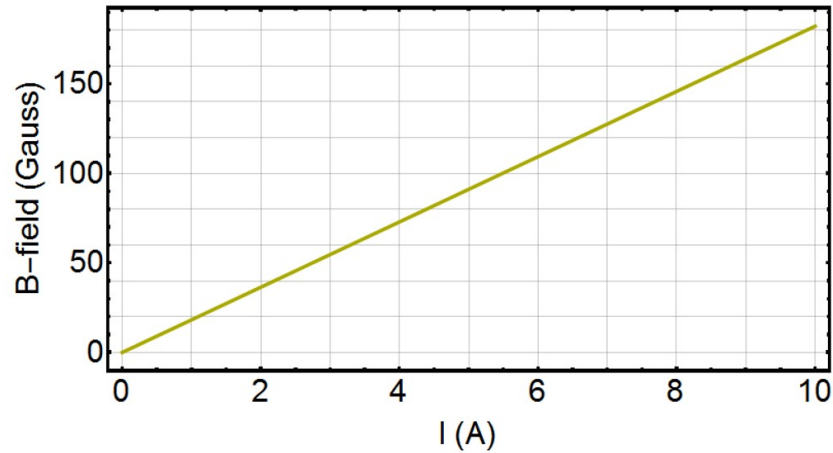


Fig. 4.18 Induced B-field at the ions position for coil geometry as shown in Fig. 4.17, this is generally used for calculating transition frequencies when performing initial frequency scans.

The off-axis analytical solutions would be useful for calculating the change in magnetic field amplitude for different trapping regions within a 2D space near the centre of the two coils but the solution becomes very complex as finding an analytical solution involves finding complete elliptic integrals of the first and second kind whose solutions become hypergeometric functions [106]. A more practical solution would be simulating the solution with finite element method (FEM) software, this way the spacing of the coil turns and vacuum system structure effects on the magnetic field can be taken into account as these factors are likely to effect the homogeneity of the field over a 2D region of space in which the ions are being trapped more than the free space solution. When moving to multi-ion sensing over separate trapping regions, this would be a useful solution.

4.5.2 RF radiation

For driving the Zeeman sub-levels in the $^2S_{1/2} |F = 1\rangle$ hyperfine manifold RF radiation needs to be applied to the ion. It is desirable to have a wide range of powers in which these fields can be applied so that control over Rabi frequencies for dressing fields can be easily chosen to be optimal and the effects of low power RF radiation on the ions can be tested to demonstrate the possibility for detecting weak magnetic fields. Additionally these frequencies should be easily controllable for the demonstrator device so that the frequency can be matched to the Zeeman splitting rather than matching the Zeeman splitting to the frequency being sensed. This is expected to happen for certain applications where there isn't experimental control over the frequency being sensed.

To generate the RF fields, a four channel RF source based on a direct digital synthesizer

(DDS) evaluation board⁵⁴ developed by Dr. David Murgia [95] is used. The device uses a single 25 MHz input signal⁵⁵ that is converted to a 500 MHz clock signal using a phase-locked loop to generate the four outputs with frequencies ranging from 1 MHz to 250 MHz with powers up to 0 dBm. This produces frequency (32 bit precision), power (10 bit precision) and phase control (14 bit precision) of all the RF fields with a rise time of around 10 ns, ideal for experimental protocols. The DDS board is controlled by a Python code developed for the Advanced Real-Time Infrastructure for Quantum physics (ARTIQ) (Sec. 4.6) over a USB connection.

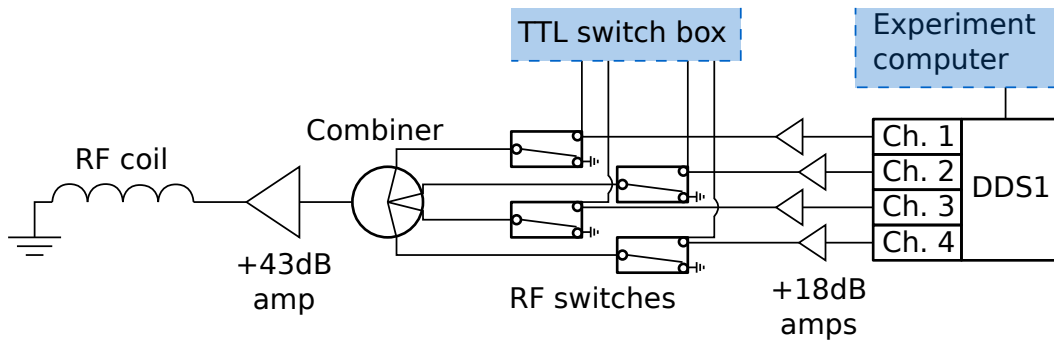


Fig. 4.19 Circuit diagram for the RF radiation setup.

Each output of the DDS board is amplified by an +18 dB amplifier⁵⁶ and passes through an RF switch⁵⁷ which is controlled by a TTL pulse from the switch box in Sec. 4.6. The four signals are then passed into a four way combiner⁵⁸ and go through further amplification via a +43 dB amplifier⁵⁹ which was chosen to have a high reflection tolerance and flat response over RF frequencies. The high reflection tolerance is so that the amplifier can be loaded with a low impedance coil which acts as an emitter for the RF radiation, the entire setup is shown in Fig. 4.19. The RF coil is three turns of copper wire⁶⁰ placed around the collection optics and close to the front viewport as shown in Fig. 4.20.

⁵⁴Analog Devices AD9959

⁵⁵Stanford Research Systems DS345

⁵⁶Mini Circuits ZFL-750+

⁵⁷Mini Circuits ZASW- 2-50DR+

⁵⁸Mini Circuits ZMSC-4-3+

⁵⁹Mini Circuits LZY-22+

⁶⁰Scientific Wire Company TX3350D-001

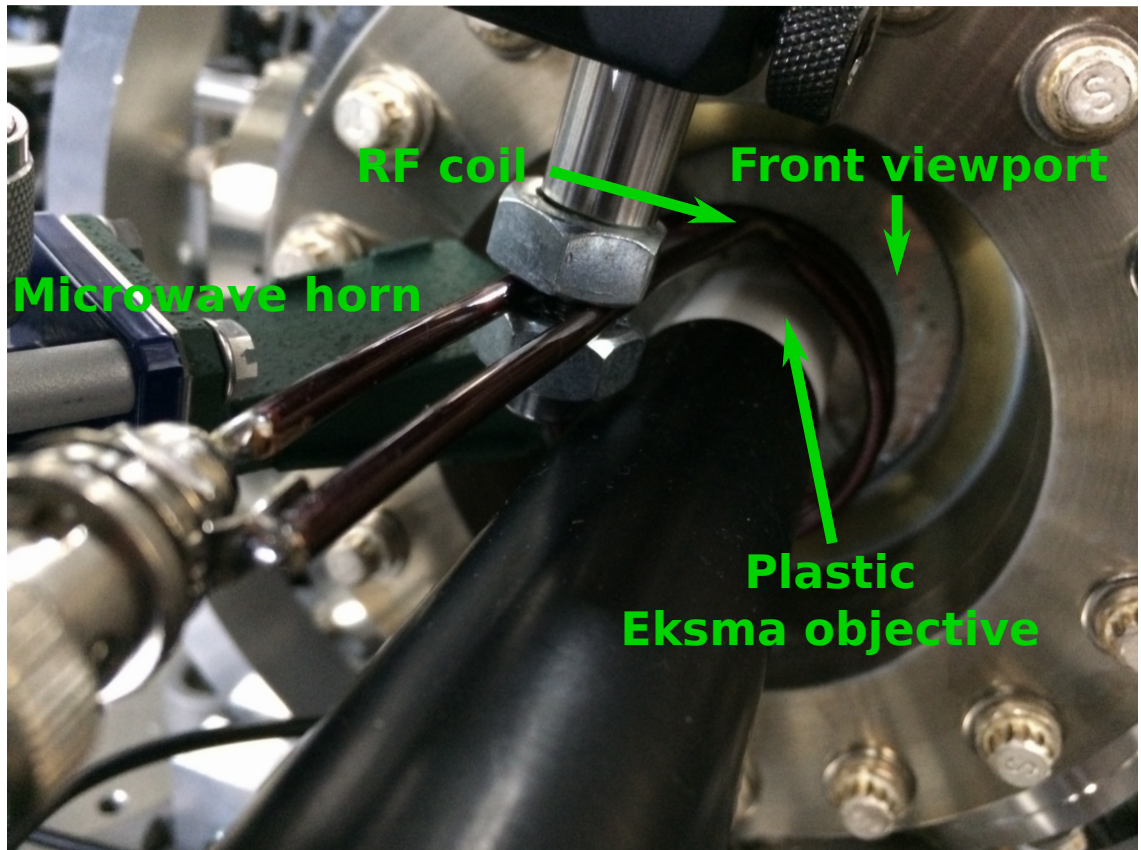


Fig. 4.20 Close up picture of the front viewport with the Eksma objective, RF coil and microwave horn in sight.

4.5.3 Microwave radiation

For driving the ground state of the $^2S_{1/2}$ manifold, microwave radiation needs to be applied to the ion near the clock transition at ≈ 12.64 GHz. It is generally quite difficult or expensive to individually create multiple microwave frequencies with fast experimental control. For this reason, this system produces multiple microwave signals by mixing⁶¹ multiple RF signals created from a DDS board (the same design mentioned in the previous section) with a local oscillator signal of 12.54 GHz produced by a vector signal generator⁶². This can produce up to four microwave signals around 12.64 GHz as shown in Fig. 4.21. The combined signal is amplified by a +43 dB microwave amplifier⁶³ with a flat gain over microwave frequencies near 12.64 GHz. This goes to a microwave horn⁶⁴ located near the front viewport as shown in Fig. 4.20 which is placed on a rotation mount for control over the microwave fields polarisation. This is necessary for addressing all the hyperfine states of the $^2S_{1/2}$ ground state of $^{171}\text{Yb}^+$ for Doppler cooling as mentioned in Sec. 5.1.3.

⁶¹Marki Microwave T3-03-16M

⁶²Hewlett Packard HP-83712B Synthesized CW Generator

⁶³Microwave Amps AM51-12-6S-43-43

⁶⁴Flann Microwave 18240-10

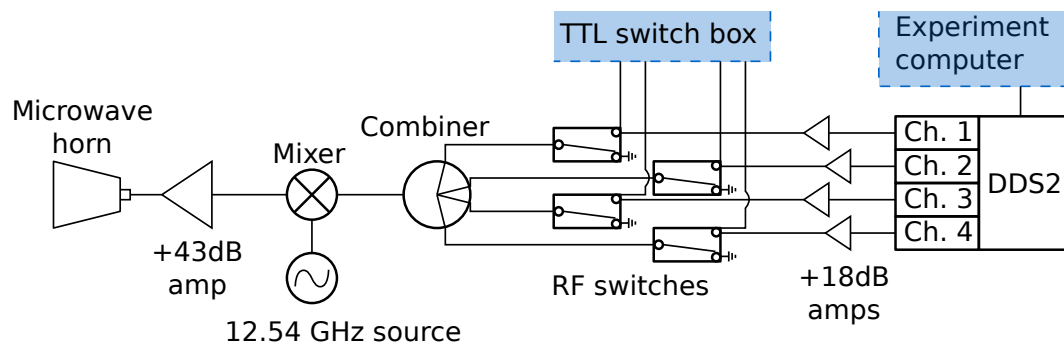


Fig. 4.21 Circuit diagram for the microwave radiation setup.

4.6 Master control setup

The control setup for the experiment is comprised of two computers running Windows 7 and one field-programmable gate array⁶⁵ (FPGA). One of the computers is used for real time user control of trapping and laser parameters, and the other is used for fast experiment protocols when manipulating the internal states of the ion.

The control computer has a DC output card⁶⁶, capable of 16 DC voltage outputs that can range from from -10 V to +10 V, that connects to a DC channel box where the 16 outputs of the DC card are separated into 16 female SMA connectors. The connectors are connected to the 369 nm laser AOM and EOM driver (Sec. 4.2.1) and the filter box (Sec. 4.3.3). A Labview program made by previous group member Dr. Altaf Nizamani is used to give the user precise control the voltage outputs of the DC card. Control of these voltages are needed for bringing the 369 nm beam wavelength and power to its cooling and saturation point (described in Sec. 5.1.3); and for control of the trap axial trapping voltages when compensating for ion micro-motion (described in Sec. 5.1.2). The second function of the control computer is to read the laser output wavelengths of each of the lasers and lock each individually. A Labview program developed by Ph.D. student Anton Grounds allows for a real time reading of the wavemeter wavelengths and allows for locking of the 399 and 935 nm lasers (described in Sec 4.2).

The experiment computer is connected to the CCD camera for viewing the trap and ion during trapping runs and micro-motion compensation. It is responsible for all coherent experiments involving manipulation of the ions internal states and for state readout (Sec. 5). The experiments are run in ARTIQ, a Python based experimental infrastructure developed by S. Bourdeauducq et al. [107] of which the Python scripts were modified by Ph.D. student Harry Bostock and Dr. Simon Webster. ARTIQ uses the FPGA hardware to perform tasks with nano-second timing. The FPGA's function is to provide TTL pulses to switch on/off the 369 nm laser, PMT, microwave and RF radiation when performing experiments. It is housed in a switch box that has 32 female BNC connectors directly

⁶⁵Xilinx FPGA KC705

⁶⁶ADLINK Technology cPCI 6216V-GL

connected to the FPGA's TTL outputs. After each experiment ARTIQ reads a photon number collected by turning on the PMT for the detection time (described in Sec. 5.2.1) which is stored in a .h5 file format that can be later read in Mathematica or other data processing software. The Python script running in ARTIQ can be coded to output any variable or constant values of the experiment, such as the RF pulse time associated with a collected photon number. For a more visual form of the information flowing between these components see Fig. 4.1 at the start of this section.

It should also be noted, though not included in this experiment the experiment control sequence can include a 50 Hz trigger that would minimise the 50 Hz mains noise attributing to decoherence of the ion as mentioned in Sec. 4.3.

5 Initial experiments and magnetometer results

5.1 Initial trapping and cooling procedure

This section will focus on the procedures carried out to initially trap Ytterbium ions on a 2-dimensional Paul trap, it is intended to work as a guide for newly developed ion trap systems. Due to the system being constructed during the course of this thesis, hence being a new system with no prior characterisation, initial trapping with Ytterbium on a new setup involves trapping of $^{174}\text{Yb}^+$ ions followed by trapping $^{171}\text{Yb}^+$ ions. This is because the levels of complexity in trapping $^{174}\text{Yb}^+$ are fewer making system characterisation initially simpler. Trapping $^{174}\text{Yb}^+$ first allows for a pragmatic confirmation of the trapping capabilities, laser alignment, alignment of the Ytterbium ovens and detection optics before introducing higher levels of complexity for trapping $^{171}\text{Yb}^+$, like laser and microwave polarisation. Ion micro-motion can be compensated for and secular frequencies can be measured for $^{174}\text{Yb}^+$ before trapping $^{171}\text{Yb}^+$ as well. The energy level structure of both isotopes with appropriate wavelengths and microwave frequency can be found in figures 2.5 and 2.6, and table 2.1.

5.1.1 Initial trapping of $^{174}\text{Yb}^+$

Once the vacuum system is at a stable and ultra-high vacuum (UHV) pressure, the imaging optics mentioned in sec. 4.4 are focused to the trap surface then zoomed out to the trapping position that corresponds to the trap RF and DC minima. The overlapped laser beams are aligned parallel to the chip surface and focused at the trapping region, $\approx 152 \mu\text{m}$ above the chip surface, this value is taken from table 3.2. The 369 nm laser is focused to a beam waist of $\approx 50 \mu\text{m}$ at a power of $150 \mu\text{W}$, for this laser it is important to focus the beam to a small waist to reduce scatter coming off the trap electrodes as this affects the state readout fidelity. Scattered light from the other lasers is significantly reduced during detection because of the 370 nm filter in the collection optics setup (Sec. 4.4), but should still be minimised to avoid unnecessary charge and heating build up on the chip (discussed in Sec. 3.3.3). The power of the 369 nm laser is later reduced when bringing the ion to its saturation point, but a higher power is beneficial for initial trapping as it allows for trapping despite small misalignments. The 399 nm laser has a power of $200 \mu\text{W}$ and the 935 nm laser has a power of 8 mW, the large 935 nm power is required to power broaden over the hyperfine structure in the $^2D_{3/2}$ and $^3[3/2]_{1/2}$ manifolds in $^{171}\text{Yb}^+$.

After initial alignment of the lasers and camera optics, the natural oven current is ramped up to 8 A to get rid of any residue in the oven and to tune the $^{174}\text{Yb}^+$ ionisation wavelength. This is done by removing the 370 nm filter and tweaking the wavelength until a 399 nm glow is observed across the chip surface. Once ionisation is observed from the scatter of 399 nm light, the oven current is reduced until ionisation is barely visible, which is at 6 A for the ovens used in Sec. 4.1.3. Now the 370 nm filter is placed in the path of

the CCD camera, trapping runs can begin. For trapping runs it takes ≈ 45 s for the ovens to heat up and produce an atomic flux. The time for each trapping run is kept short to avoid coating the ion trap with Ytterbium which can cause unwanted charge to build up on the chip surface. During trapping runs the 369 nm laser is red detuned by ≈ 50 MHz by using the AOM (Sec. 4.2.1) to keep the laser in the cooling regime and the laser position is swept as seen in Fig. 5.1. After a full iteration of spatial sweeps, the laser frequency is adjusted by further 10 MHz red detuning. If no ion appears after a satisfactory number of red detuning steps, blue detuning steps should be conducted as well in case the initial wavelength used was too far red detuned. Camera focus is swept during trapping runs in case an ion is trapped but out of focus. This process can be arduous, but the clinical approach will drastically speed up initial characterisation of a system assuming the initial alignment was done well.

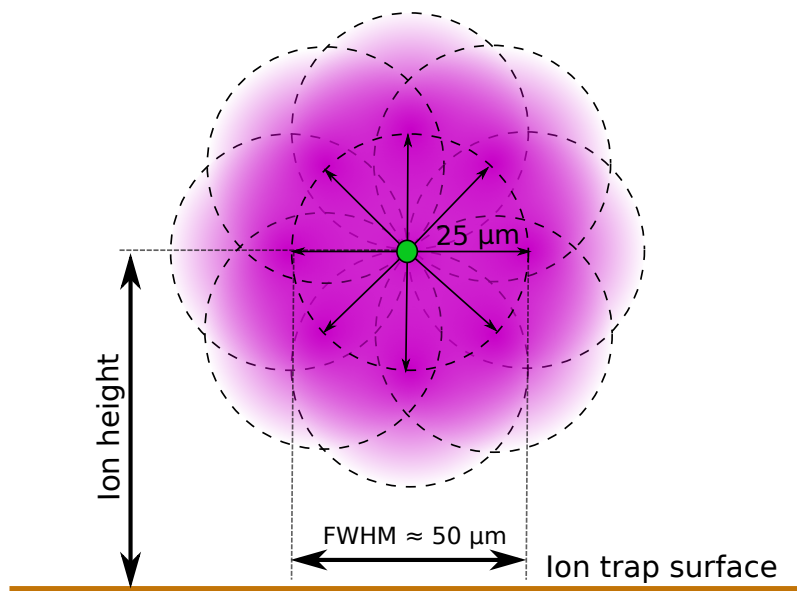


Fig. 5.1 Graphical representation of the laser position sweep. Green dot is the estimated trap RF nil position, each circle represents a FWHM of the 369 nm laser. There are a total of 9 steps, one with its center about the estimated trap RF nil position and eight with their centers $25 \mu\text{m}$ from the estimated trap RF nil position. It is likely that the laser is initially misaligned, this process or one similar is recommended if laser misalignment is a concern when conducting initial trapping experiments.

5.1.2 Micro-motion compensation and secular frequency measurements

Once a $^{174}\text{Yb}^+$ ion has been trapped, the imaging tube iris is reduced in size until only the ion is visible on the camera, this is to further reduce unwanted background scatter from the surface of the chip. It should look identical to the image shown in Fig. 5.3. The CCD camera is then switched for the PMT, the ion count that appears is predominantly from the ion, this is checked by temporarily blocking the 935 nm laser to put the ion into

a dark state and observing a corresponding reduction in photon count. Slight positional adjustments of the optical tube and laser are carried out to maximise the photon count from the ion and minimise the background photon scatter. The signal to noise ratio of the ions photon count compared to the background scatter is ≈ 50 .

Micro-motion compensation

Once the ion count is maximized, the ion is micro-motion compensated as stray electric fields may be pushing it away from its intended zero field position, the effects of a non-zero field at the ions position are described in Sec. 3.1.2 and the effects of excessive micro-motion from electromagnetic noise is described in Sec. 3.3.3. Micro-motion is compensated for by reducing the RF trapping field by $\approx 30\%$, which causes the ion to move in the direction the stray electric fields are pointing. This reduces the photon count by obscuring the ion partially behind the imaging tube iris. The DC voltages trapping the ion in the axial direction are adjusted until the photon count returns, the RF trapping field is then returned to its original voltage causing another reduction in photon count; this is due to the trap nil position being located in a different position due to the newly applied DC voltages. The photon count is then re-optimized by moving the optical tube position and focus to the new micro-motion compensated ion position, followed by slight adjustments to the laser position to maximise photon count. This process is repeated until changes in the RF trapping voltage does not exhibit any change in photon count, this means that the ion is sitting at or near a zero field position.

This method for micro-motion compensation was later confirmed to be sufficient for $^{171}\text{Yb}^+$, a method in which the effectiveness of micro-motion compensation can be measured is by measuring the linewidth of the cooling laser transition when the ion is at or below its saturation limit [108]. This was done for $^{171}\text{Yb}^+$ after the saturation limit was found and is described in Sec. 5.1.4.

Secular frequency measurement

To measure the ion secular frequency, an RF signal is applied to the RF coil (normally used to manipulate the ions internal states, see Sec. 4.5.2). This induces motion on the ion when resonant with the traps secular frequencies. The effect of the resonant driving field on the ion is visible on the CCD camera. RF frequency scans around the numerically simulated secular frequency values in Table 3.2 are applied, the measured secular frequencies of the trap are found to be $\omega_x/2\pi = 214$ kHz in the axial direction and $\omega_{\{z,y\}}/2\pi = \{950, 1091\}$ kHz in the radial directions. The difference from the simulated

values are likely due to a combination of stray electric fields from floating electrodes and the difference in zero field position that arises from the DC fields compensating for micro-motion in the experiment that are not present in the simulation. The floating electrodes were observed by probing the capacitance of the DC pins in the back of the D-sub described in Sec. 4.1.1 after baking. It is believed that the electrodes are floating due to either the wire-bonds connecting the front PCB (Sec. 4.1.2) to the micro-fabricated ion trap disconnecting; or it is due to the one of the back PCB resistors breaking, both are most likely to happen during the baking process in Sec. 4.1.4.

5.1.3 Initial trapping of $^{171}\text{Yb}^+$

After $^{174}\text{Yb}^+$ has been trapped and initial characterisation of the laser position, ion micro-motion and secular frequencies have been measured, attempts to trap $^{171}\text{Yb}^+$ can be made with a lower chance of error. The correct 399 nm wavelength can be found for $^{171}\text{Yb}^+$ the same way as $^{174}\text{Yb}^+$, the oven current for getting rid of residue was found to be higher at 8.5 A, the minimum current for a visible flux shown in the CCD camera was found to be 6.3 A. Trapping runs are performed in the same way but without the need for position adjustments on the laser, the 369 nm laser is red detuned and the AOM frequency is swept between trapping runs in the same manner as $^{174}\text{Yb}^+$. The 369 nm laser polarisation with respect to the quantization axis (z) is adjusted using the $\lambda/2$ waveplate before the vacuum system (Fig. 4.8) to have roughly equal parts σ_- (right circular), σ_+ (left circular) and π (linear) to drive all the Zeeman sub levels in $^2S_{1/2} |F = 1\rangle$. A current of 0.5 A is applied to the coils from Sec. 4.5.1 to produce a static magnetic field equal to ≈ 9.114 G, corresponding to $\approx 2\pi \times 12.7$ MHz splitting for the $^2S_{1/2} |F = 1, m_f = 0\rangle \leftrightarrow ^2S_{1/2} |F = 1, m_f = +1, -1\rangle$ transitions.

Three microwave field at frequencies of $\{12.6428, 12.6555, 12.6301\}$ GHz equal to the three hyperfine transitions in the $^2S_{1/2}$ manifold. A microwave power of 10W is used to account for slight errors in the calculated microwave frequencies. The microwave horn is placed on a rotational mount (Fig. 4.20) to provide equal parts σ_- , σ_+ and π polarisation to drive all the $^2S_{1/2} |F = 0\rangle \leftrightarrow ^2S_{1/2} |F = 1, m_f = 0, +1, -1\rangle$ transitions. This and the 369 nm polarisation works to strongly couple all the states into the cooling cycle to maximize fluorescence, this is shown in Fig. 5.2. The laser and microwave polarisations are tweaked over the duration of each trapping run as it is likely that they are not fully optimized at this point. Once $^{171}\text{Yb}^+$ has been trapped the PMT ion count is maximised by adjusting the 369 nm wavelength and polarisation, followed by adjustments on the microwave field polarisation and frequency.

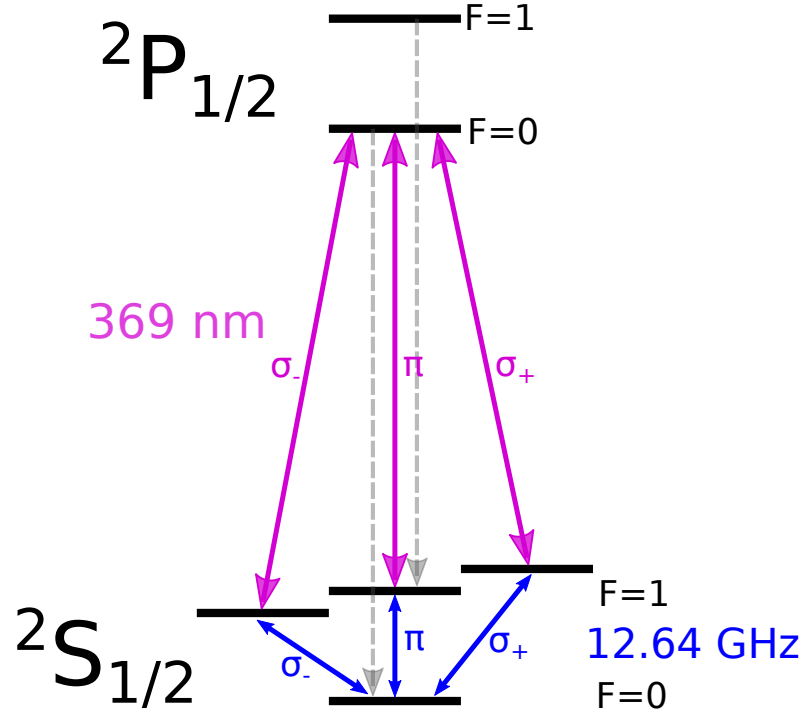


Fig. 5.2 σ_- , σ_+ and π polarisations and their associated transitions for the 369 nm laser and 12.64 GHz microwave field. The magnitude of each polarisation are quantified in reference to the ions quantization axis. If any of the polarisations are weakly coupled to the ion the ion fluorescence will be relatively low, to avoid this it is advised to avoid any parallel or normal polarisations of the laser or microwave fields relative to the ions quantisation axis.

5.1.4 Ion saturation limit and confirmation of micro-motion compensation effectiveness

Once $^{174}\text{Yb}^+$ has been trapped, the 369nm cooling laser intensity needs to be reduced until the ion is at or below its saturation limit. If the laser intensity is too high (past saturation) the laser power broadens over the hyperfine structure in the $^2S_{1/2}$ and $^2P_{1/2}$ manifolds shown in Fig. 5.2, this is undesirable for when performing state detection as described in Sec. 5.2.1. From [109], it is calculated that the saturation limit for $^{171}\text{Yb}^+$ is at 41.5% of its maximum photon fluorescence. The maximum number of photons collected from the ion by the imaging optics is ≈ 18000 photons/s above the background scatter when the cooling laser is red detuned by the natural linewidth of the transition $((\Gamma/2\pi)/2 = 19.6$ MHz), meaning that the ion will be roughly at its saturation limit when 7470 photons/s are collected. The 369nm cooling laser power is reduced to $\approx 6 \mu\text{W}$ to achieve this. A quick check to see if the ion is at its saturation limit is by turning off the microwave fields, this should cause the ion to quickly fall into the $^2S_{1/2} |F=0\rangle$ ground state and fluoresce an un-noticeable number of photons.

The effectiveness of the micro-motion compensation technique in Sec. 5.1.2 can be

checked by sweeping the AOM frequency applied to the 369nm laser and measuring the linewidth of the ions fluorescence γ ; this should be comparable to the linewidth of the cooling transition which is $\Gamma/2\pi = 19.6$ MHz when the ion is at its saturation limit [108]; a semi-classical description of the laser cooling process at the ions saturation limit is given by [110]. The measured linewidth was $\gamma/2\pi \approx 24$ MHz which is relatively close to the natural linewidth of the cooling transition not expected to induce excessive micro-motion on the ion [108].

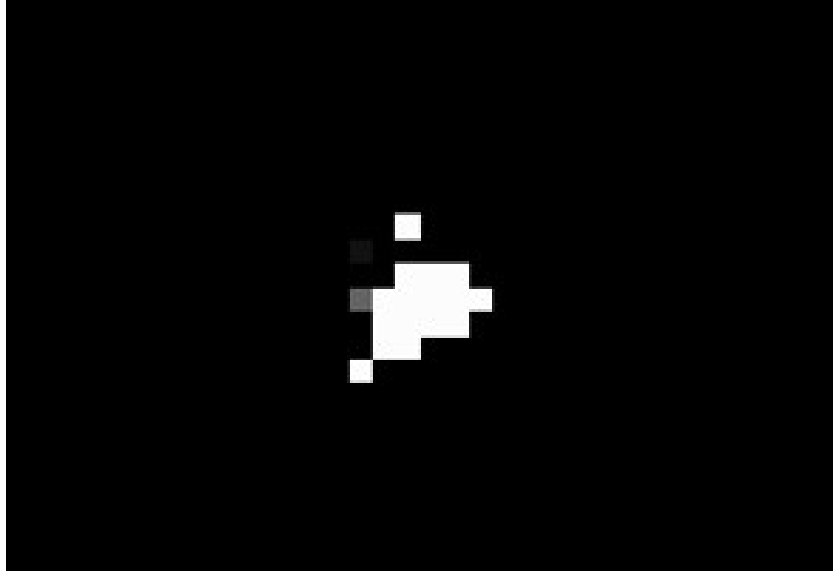


Fig. 5.3 Successfully trapped single $^{171}\text{Yb}^+$ ion scattering 369 nm photons.

5.2 Initial experiments

5.2.1 State preparation and detection

In order to create a high sensitivity quantum magnetometer it is desirable to prepare and detect our ion with high fidelity, this in turn reduces errors on state population measurements which results in a better sensitivity as mentioned in Sec. 2.40. During the processes mentioned here, the ion is constantly exposed to 935 nm light in order to keep the ion population in the cooling cycle, as described in Sec. 2.1.2. To prepare $^{171}\text{Yb}^+$ into its $^2S_{1/2} |F=0\rangle$ ground state, the 12.64 GHz microwave field is turned off to avoid repopulating the $^2S_{1/2} |F=1\rangle$ states, and the 369 nm cooling laser resonant with the $^2S_{1/2} |F=1\rangle \leftrightarrow ^2P_{1/2} |F=0\rangle$ has ≈ 2.1 GHz side-bands applied to it by switching on the electro-optic modulator shown in Sec. 4.2.1. This drives the $^2S_{1/2} |F=1\rangle \leftrightarrow ^2P_{1/2} |F=1\rangle$ transition, which in turn causes the ion population to decay into the $^2S_{1/2} |F=0\rangle$ ground state (due to the conservation of total angular momentum) which is not directly coupled to any laser when the 369 nm laser intensity is near the ions saturation limit. The power of the signal sent to the EOM is adjusted so that the carrier frequency, corresponding to the $^2S_{1/2} |F=1\rangle \leftrightarrow ^2P_{1/2} |F=0\rangle$ transition is strongly suppressed. The minimum

state preparation time to the EOM required for populating the ${}^2S_{1/2} |F=0\rangle$ state is then found by scanning the pulse time and performing a state readout, results for this can be seen in Fig. 5.4. The experimental procedure for cooling, state preparation, an arbitrary experiment and state readout can be seen in Fig. 5.5.

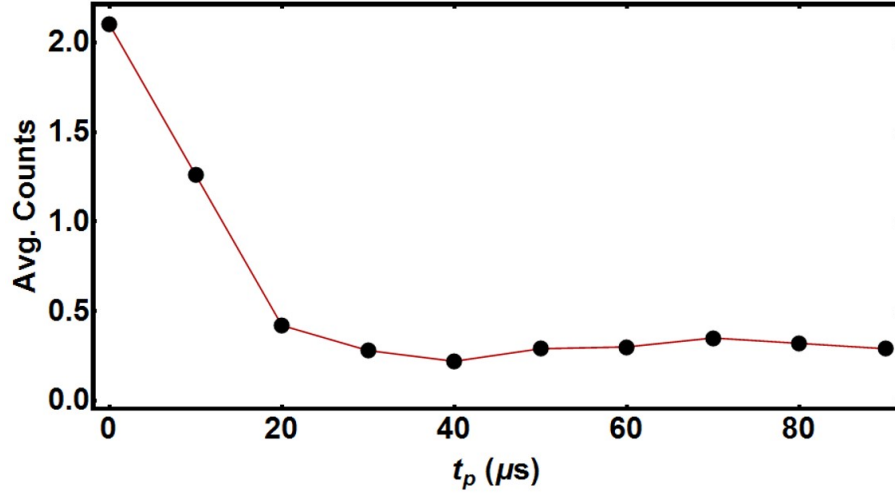


Fig. 5.4 Average photon counts detected after applying the 369 nm laser to a single ion with the EOM switched on for a time t_p , with detection time $t_d = 1$ ms. Each point is the result of 100 repetitions. The modulated 369 nm laser should cause population to be optically pumped into the $|0\rangle$ state, in which case the ion should not scatter any photons during the detection period. The average number of counts detected on the PMT can be seen to reach a steady state of ≈ 0.3 average photons after approximately $30 \mu\text{s}$. The excess photons are attributed mainly to background scatter of the 369 nm laser on the trap electrodes, which agrees with the result of a similar experiment performed when no ion is in the trap.

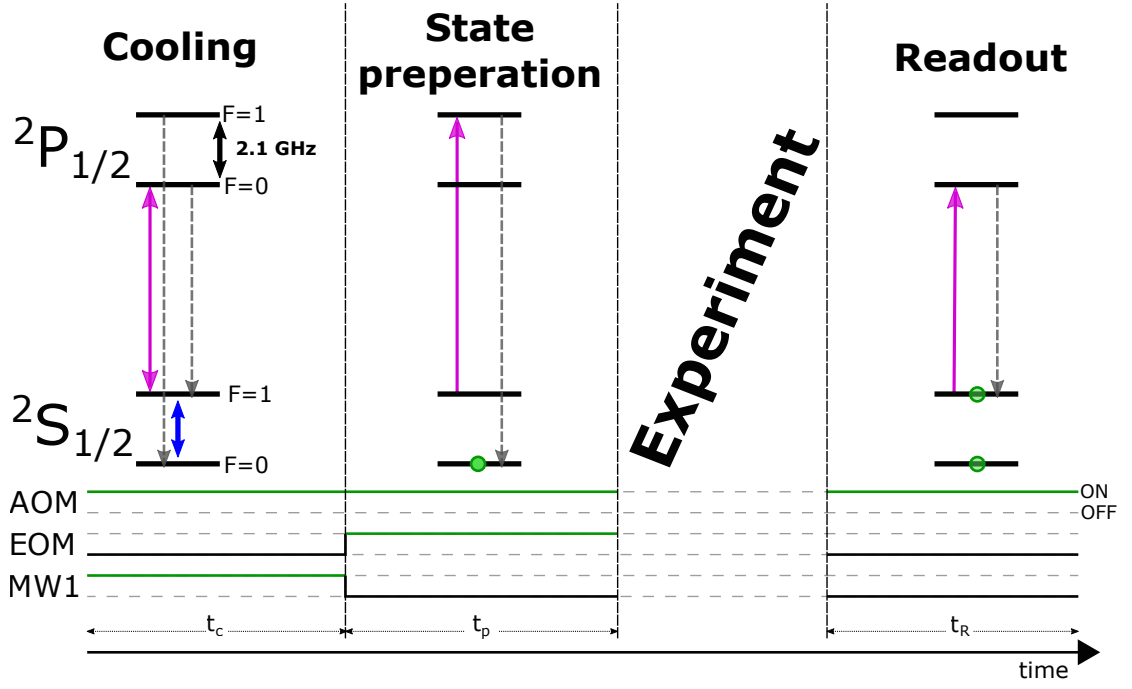


Fig. 5.5 Cooling, state preparation and readout procedure. (Top) Energy level diagram shows the transitions being driven for each step. (Bottom) Devices switched on or off for each step, switching the AOM off removes all 369 nm light going to the trap, MW1 is the microwave field driving the clock transition at 12.64 GHz in the $2S_{1/2}$ manifold. Blanked out step after state preparation can be any experiment that requires the ion to start in the ground state, all experimental procedures described in this thesis are within this segment. Cooling, preparation and detection times are indicated by t_c , t_p and t_R respectively.

State preparation fidelity is hard to disentangle from state detection fidelity so the two are normally combined into a single infidelity known as SPAM (state preparation and measurement) error [111]. A rate equations simulation of $^{171}\text{Yb}^+$ predicts that a state preparation infidelity of $< 10^{-4}$ should be achievable for a system similar to ours [111], meaning that most of the infidelity is likely to come from off resonant coupling from the cooling laser as mentioned in the previous section. For state detection the 369 nm laser and PMT are turned on for a brief amount of time and fluorescence is observed if the ion is in the $2S_{1/2} |F = 1, m_f = +1, -1, 0\rangle$ states (called bright states), and no fluorescence is observed if the ion is in the $2S_{1/2} |F = 0\rangle$ state (called the dark state); this is because the laser should be predominantly coupled to the $2S_{1/2} |F = 1\rangle \leftrightarrow 2P_{1/2} |F = 0\rangle$ transition, and the coupling to the $2S_{1/2} |F = 0\rangle \leftrightarrow 2P_{1/2} |F = 1\rangle$ and $2S_{1/2} |F = 1\rangle \leftrightarrow 2P_{1/2} |F = 1\rangle$ transitions should be heavily suppressed. Though it is difficult to completely remove off-resonant coupling, the laser is off-resonant by ≈ 14.7 GHz from the $2S_{1/2} |F = 0\rangle \leftrightarrow 2P_{1/2} |F = 1\rangle$ transition, giving a small chance for a dark state to be measured as a bright state. A more likely event is the laser off-resonantly coupling to the $2S_{1/2} |F = 1\rangle \leftrightarrow 2P_{1/2} |F = 1\rangle$ transition, which is only off-resonant by 2.1 GHz, giving a chance for a bright state to be measured the dark state. Background photons being scattered off the

chip surface and dark counts inherent on any PMT will also contribute to a loss in fidelity.

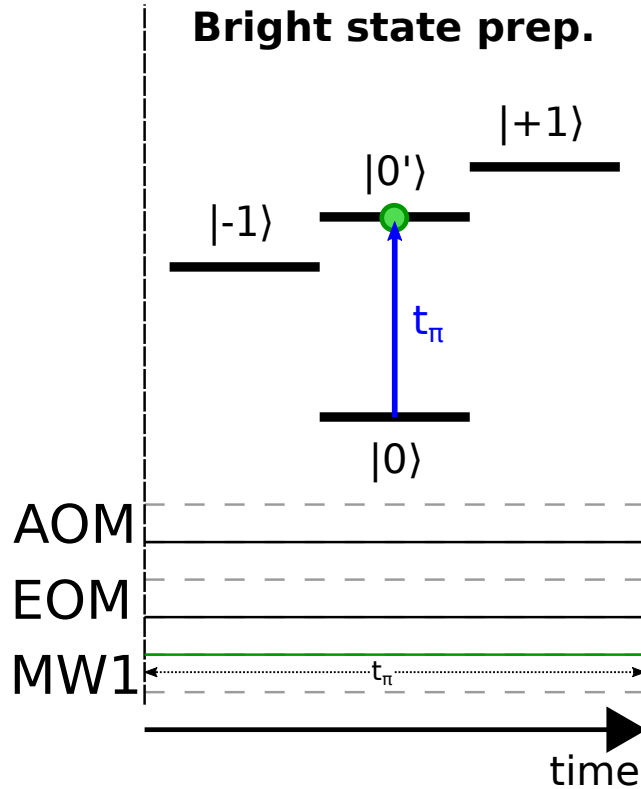


Fig. 5.6 Experiment to prepare the ion in the bright state. A microwave pulse is applied on resonance with the $|0\rangle \leftrightarrow |0'\rangle$ transition for a time t_π , this induces a π rotation about the Bloch sphere, meaning population has been transferred from the $|0\rangle$ state to the $|0'\rangle$ state. The π time t_π can be determined by inducing Rabi oscillations between the $|0\rangle \leftrightarrow |0'\rangle$ transition and measuring the experiment time required to transfer population, more on this in Sec. 5.4.

5.2.2 State detection fidelity

The state detection fidelity for any given experiment needs to be characterised as it plays directly into determining state population probability measurements and their associated errors. For state detection we assume the state preparation errors are negligible relative to the state detection errors. When determining whether an ion is in its bright or dark state during state readout, the output photon count number n is compared to a threshold photon count t_1 , so that values of $n \leq t_1$ give a dark reading and values of $n > t_1$ give a bright reading. To determine the value for t_1 that gives the highest fidelity, a state detection experiment is conducted where the ion is prepared in the dark state and the photon number is recorded during state readout, this is done multiple times to produce a dark state photon count histogram. The same is done for the bright state, where a microwave π pulse transfers population in the ${}^2S_{1/2} |F = 0, m_f = 0\rangle$ ground state to the ${}^2S_{1/2} |F = 1, m_f = 0\rangle$ state (Fig. 5.6). The two photon count histograms produced are

shown in Fig. 5.7, the histograms should approximately follow Poissonian statistics if off resonant coupling effects are neglected, the fitted function is the Poissonian function

$$f_{Poisson}(n) = \frac{\mu^n}{n!} e^{-\mu}, \quad (5.1)$$

where n is the photon number and μ is the mean photon number. The overlap of the two histograms is problematic, it means sometimes a bright readout will occur when the ion is in the ${}^2S_{1/2} |F = 0\rangle$ state and sometimes a dark readout will occur when the ion is in the ${}^2S_{1/2} |F = 1\rangle$ state, the reasons for this were described in the previous section. Because of this, conditional probabilities $P(B|1)$, $P(B|0)$, $P(D|0)$ and $P(D|1)$ are required to describe the state detection where $P(a|b)$ is defined as the probability of measuring a, given that b occurred; B and D correspond to bright and dark readouts, and 0 and 1 correspond to the ion being in the ${}^2S_{1/2} |F = 0\rangle$ and ${}^2S_{1/2} |F = 1\rangle$ states respectively. These values are the fraction of dark state preparation readouts $\leq t_1$ and $> t_1$ for $P(D|0)$ and $P(D|1)$ respectively, and the fraction of bright state preparation readouts $> t_1$ and $\leq t_1$ for $P(B|1)$ and $P(B|0)$ respectively. The threshold photon count t_1 that gives the highest state detection fidelity is chosen to be a value that maximizes $P(B|1)$ and $P(D|0)$, and minimises $P(B|0)$ and $P(D|1)$, the detection fidelity is then given as the average of $P(B|1)$ and $P(D|0)$.

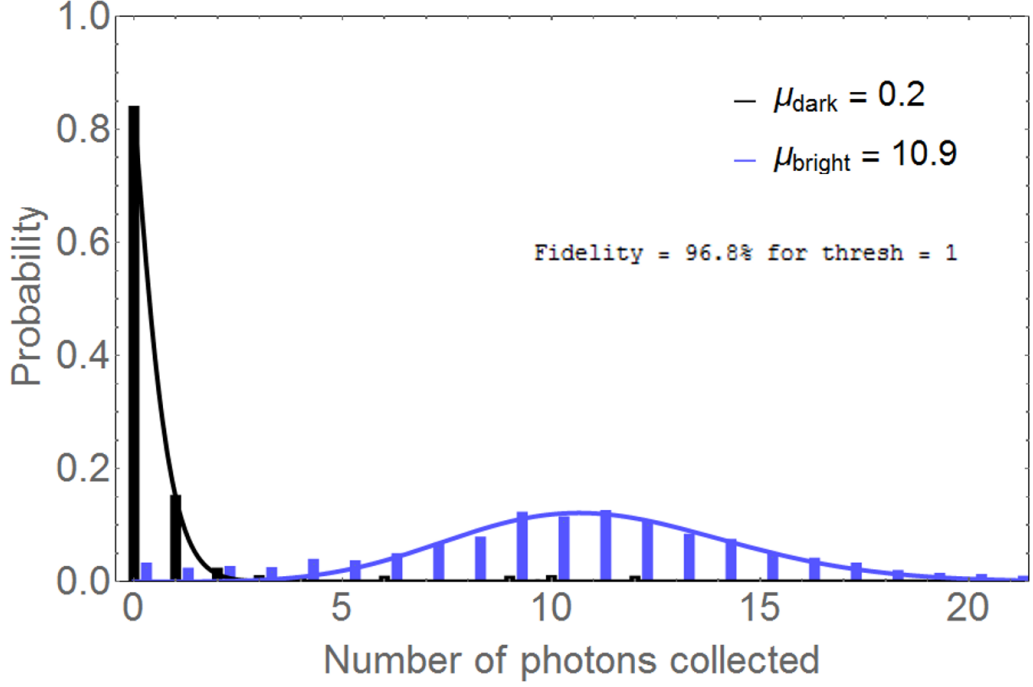


Fig. 5.7 State preparation histogram data, the black/blue histograms represent the dark/bright measurements respectively. 1000 repetitions for each experiment are performed to create the data set, the best detection fidelity of 96.8% is found when $t_1 = 1$. The conditional probabilities $P(D|0)$, $P(D|1)$, $P(B|1)$ and $P(B|0)$ are the fraction of data points below and above the threshold for their respective histogram plots. The fitted function is a Poissonian function described by Eq. 5.1 with mean bright and dark photon numbers $\mu_{\text{bright}} = 10.9$ and $\mu_{\text{dark}} = 0.2$ respectively.

Through multiple fidelity measurements for different detection time windows, the highest fidelity was measured to be at ≈ 1 ms detection time. The fidelity can also be increased by increasing the total number of photons from the ion being collected by the detection optics (known as the collection efficiency) to create a larger discrepancy between the mean photon count for the bright and dark state detections, meaning the histograms shown in Fig. 5.7 would overlap less due to a higher mean photon count on the bright state detection experiment. A detection fidelity of 99.915% was achieved for the $^{171}\text{Yb}^+$ hyperfine levels in [112] by using a specially designed optic that demonstrated a collection efficiency of 10% could be achieved. Any increase in state detection fidelity is preferable as it will bring the sensitivity of this magnetometer closer to the quantum limit by minimising the errors of any state population measurement. An in depth mathematical derivation of how the state population measurement errors are calculated can be found in Appendix D. The ideal case ($P(B|1) = P(D|0) = 1, P(B|0) = P(D|1) = 0$) sensitivity calculation for AC magnetic fields using dressed states can be found in Sec. 2.40.

5.3 Experimental procedures

It is beneficial to outline the experimental procedures utilized for bare state, microwave dressed state and RF dressed state experiments so to not repeat the similar protocols for each section. This section aims to give an idea of the procedures utilized for the remaining experiments conducted in this thesis. Note that the state detection threshold and fidelity measurements cannot be performed without knowing the $|0\rangle \leftrightarrow |0'\rangle$ clock transition frequency or π time, but accurate frequency scans or Rabi oscillations on this clock transition cannot be performed without a decent state detection experiment. What should be done to assure accurate results for both is a few cycles of frequency scan \rightarrow Rabi oscillation \rightarrow state detection \rightarrow frequency scan \rightarrow Rabi oscillation \rightarrow etc. to ensure that the correct values are being used. This iterative process converged in around four cycles initially, but in proceeding days the need for this cycle diminished.

5.3.1 Frequency scans

To perform a frequency scan, a frequency near the calculated transition frequency found from Eq. 2.1 for a given magnetic field calculated from Eq. 4.8 is applied for the π time of that transition. If the frequency is on resonance it will populate the bright state for state readout, conversely if it is off resonance the population will remain in the dark state for state readout. Each population measurement consists of numerous repetitions to attain a state transfer probability. The frequency applied to the ion is swept around the calculated value for multiple detunings δ . A function is then fitted to the data using a maximum log-likelihood method as described in Appendix D, the function is described by

$$P_{F=1}(\delta) = \frac{A}{2} \frac{\Omega^2}{\Omega^2 + \delta^2} \left(1 - \cos(t_\pi \sqrt{\Omega^2 + \delta^2}) \right), \quad (5.2)$$

where Ω is the Rabi frequency which is related to the π time as $t_\pi = \pi/\Omega$, both of which are measured by performing Rabi oscillations; δ is the detuning of the applied field from the peak frequency ($\delta = \omega_p - \omega$ where ω is the applied field frequency and ω_p is the frequency associated with peak population transfer into $|F = 1\rangle$) and A is the contrast of the function at $\delta = 0$. For short experiment times, a measurement of $A < 0.9$ would suggest that the measured π time t_π is not the correct value. Eq. 5.2 is very similar to Eq. 2.12, except with appropriate sign changes to produce a graph that is intuitive. Once the correct frequency has been found the true static magnetic field can be calculated from this value by reversing Eq. 2.1 to have magnetic field strength in terms of frequency splitting. This can be used to calculate better estimates of other transition frequencies that may need to be found for an experiment.

5.3.2 Rabi oscillations

Rabi oscillations are used to determine the t_π and Rabi frequency of a transition. For instance, the t_π time of the clock transition must be known for population transfer between the two states for state readout measurements, the more accurate this value is, the higher the state readout fidelity will be. The Rabi frequency of any transition has to be measured accurately in order to match the Rabi frequencies when performing dressed state experiments, as a mismatch in Rabi frequencies can have adverse effects on reliable population transfer between a dressed state and an axillary state as described in Sec. 2.2.2. It also describes the strength of the AC magnetic field applied, meaning an accurate measurement of the Rabi frequency, is an accurate measurement of the magnetic field strength.

To induce Rabi oscillations on a transition, the ion is prepared into its desired initial state, from which a magnetic field on resonance with the transition in which Rabi oscillations will be induced is applied for a time t_0 . The time the ion is exposed to the magnetic field is then swept across n , t_s sized steps as $t_n = t_0 + nt_s$. Each time t_n is repeated numerous times in order to get a state population probability at each time step. This induces a continuous rotation about the phase axis on the Bloch sphere while the ion is exposed to an on resonant magnetic field. A function is then fitted to the data using a maximum log-likelihood method as described in Appendix D, this function is described by

$$P_{F=1}(t) = \frac{(1 - A \cos(\Omega t))}{2}, \quad (5.3)$$

where A is the contrast of the Rabi oscillation, Ω is the Rabi frequency and t is the experiment time. This is very similar to Eq. 2.33, except we assume the transition is on resonance and replace the e^{-t/T_2} term with an amplitude term, this is assuming that the length of the Rabi oscillation experiment is short enough relative to the T_2 time (discussed in Sec. 5.3.3), meaning no significant amplitude change should be observed due to decoherence on the ion.

5.3.3 Ramsey T_2^* and T_2 spin-echo coherence time

The Ramsey T_2^* time is a measurement of the time in which the phase coherence remains between the two states $\{|\uparrow\rangle, |\downarrow\rangle\}$ in question. To measure this, a Ramsey-type experiment is performed, this involves preparing the ion in the $|\downarrow\rangle$ state, followed by application of a $\pi/2$ pulse to put the system into an equally weighted superposition state. It is then left for some delay time t_{delay} in which the ion is subject to no applied RF or microwave magnetic fields or lasers, followed by another $\pi/2$ pulse with an added phase relative to the first pulse, and finally a state readout. This is repeated 100 times for each phase measurement to attain a state population probability, this is repeated for multiple phase differences between the two pulses spanning from $0 \rightarrow 2\pi$. This can be imagined as the Bloch vector rotating on the x-y plane at a phase angle ϕ , a representation of this for an

arbitrary two-level system can be seen in Fig. 5.8, The unitary operator describing these Bloch sphere rotations with appropriate pulse times and phase changes can be seen in Eq. 2.11. The phase scan data for some delay time t_{delay} is then fitted with a function using a maximum log-likelihood method as described in Appendix D, the function is described by

$$P_{F=1}(\phi) = p_{off} + \frac{a}{2} \sin(\phi + \phi_{off}), \quad (5.4)$$

where a is the fringe contrast, p_{off} is the population offset, ϕ is the phase and ϕ_{off} is the phase offset. The entire experiment is repeated with increasing delay times, until a suppression of the fringe contrast towards $P_{\uparrow} = 0.5$ occurs. From this, an exponential decay function, e^{-t/T_2^*} , is fitted to the fringe contrast for each delay time to determine the T_2^* time.

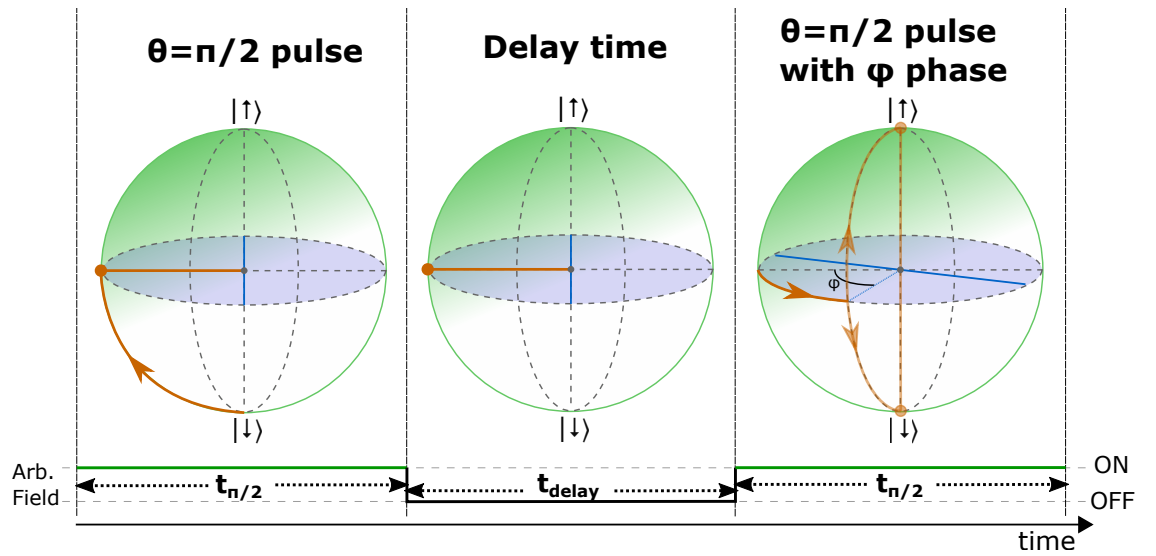


Fig. 5.8 Experimental procedure for T_2^* Ramsey experiment on a two-level system being driven by an arbitrary on resonance magnetic field. The system initialised in the $|\downarrow\rangle$ state and exposed to resonant pulse for a time equal to $t_{\pi/2}\Omega = \pi/2$ (Ω is the Rabi frequency), it then is allowed to stay in its superposition state for a time t_{delay} . A second $t_{\pi/2}$ pulse with an added phase ϕ relative to the first pulse, causing the Bloch vector (orange line) to rotate about the x-y plane by an angle ϕ and then have a weighted probability to return to the $|\downarrow\rangle$ or $|\uparrow\rangle$ state depending on the phase added to the second $\pi/2$ pulse.

The T_2 spin-echo time measurement is performed in the same manor as the T_2^* Ramsey measurement, but with the introduction of an additional pulse. Instead the T_2 spin-echo time procedure is a $\pi/2$ pulse followed by half the delay time $t_{delay}/2$, followed by a π pulse with the same phase as the first pulse, then a second half delay time $t_{delay}/2$, followed by $\pi/2$ pulse with relative phase change from the first pulse and then state readout, this can be seen in Fig. 5.9. The additional π pulse causes a 180 degree rotation of the Bloch vector about the phase axis of the Bloch sphere, this helps to cancel out slowly oscillating magnetic field noise causing decoherence.

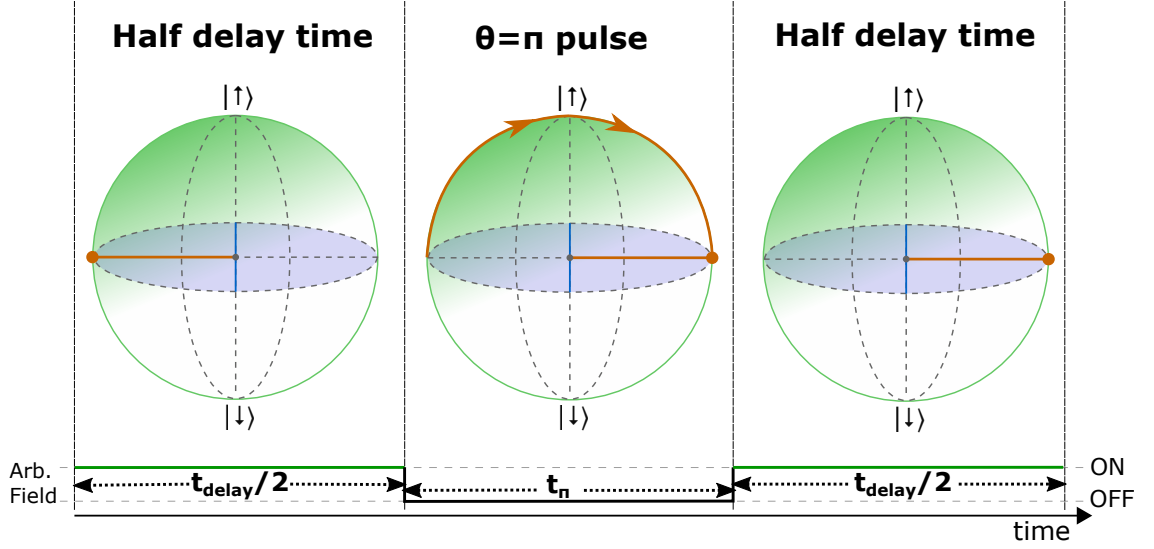


Fig. 5.9 Experimental procedure for T_2 spin-echo experiment on a two-level system being driven by an arbitrary on resonance magnetic field. A full view of the experiment can be seen by replacing the t_{delay} step in Fig. 5.8 with the three steps shown here. After half the t_{delay} time the system is exposed to a pulse for a time equal to $t_{\pi}\Omega = \pi$ which rotates the Bloch vector about the phase axis by 180 degrees (Fig. 2.9), from which the ion is left for an additional $t_{\text{delay}}/2$ time before the second phase shifted $\pi/2$ pulse.

Note that for the T_2^* and T_2 measurement times shown in this thesis, the variation in phase offset for different delay times is attributed to slow drifts in the phase of the microwave field. The sporadic nature of some of these data points and population offset is attributed to a sub-optimal state detection at the time this experiment was conducted.

5.4 Bare state experiments

It is beneficial to characterise an ion trap system by performing numerous bare state experiments. The bare state experiments are used for measuring the hyperfine transition frequencies, Rabi frequencies, π times and coherence times. Correct transition frequencies are paramount for driving transitions on resonance, Rabi oscillations are required for determining Rabi frequencies when matching field strengths for the dressed states (Sec. 2.2.2) and determining π and $\pi/2$ times for state preparation and Ramsey experiments, and T_2^* and T_2 coherence times are useful for determining potential sources of magnetic field noise.

Transition frequencies tend to drift from day to day due to slow ambient magnetic field drifts and temperature fluctuations in the lab, meaning that bare state frequency scan and Rabi oscillation experiments are always conducted prior to any dressed state sensing experiment.

5.4.1 Bare state frequency scans and Rabi oscillations

The frequency scans and Rabi oscillations are conducted as described in Sec. 5.3.1 and 5.3.2. It is important to understand how to correctly populate states for state readout measurements when performing bare state measurements as the experiment during state readout can only distinguish between the $\{|0'\rangle, |-1\rangle, |+1\rangle\}$ sub-levels and $|0\rangle$ ground state of the ${}^2S_{1/2}$ energy manifold as shown in Fig. 2.7. For the $|0\rangle \leftrightarrow \{|0'\rangle, |-1\rangle, |+1\rangle\}$ microwave transitions, the ion needs to only be prepared in the $|0\rangle$ ground state, followed by an experiment and state readout. For $|0'\rangle \leftrightarrow \{|-1\rangle, |+1\rangle\}$ measurements, the ion is prepared in the $|0'\rangle$ state via application of a π pulse on the $|0\rangle \leftrightarrow |0'\rangle$ clock transition, followed by the experiment, another π pulse on the $|0\rangle \leftrightarrow |0'\rangle$ clock transition and then state readout.

Clock Transition Measurements

A frequency scan on the clock transition measures the second order Zeeman shift that is induced on the ion from the applied B-field. A Rabi flop on the clock transition is used to attain a value for t_π , which is needed in every microwave dressed state experiment for state preparation and detection. Results of a standard clock frequency scan and Rabi oscillation can be seen in Fig. 5.10.

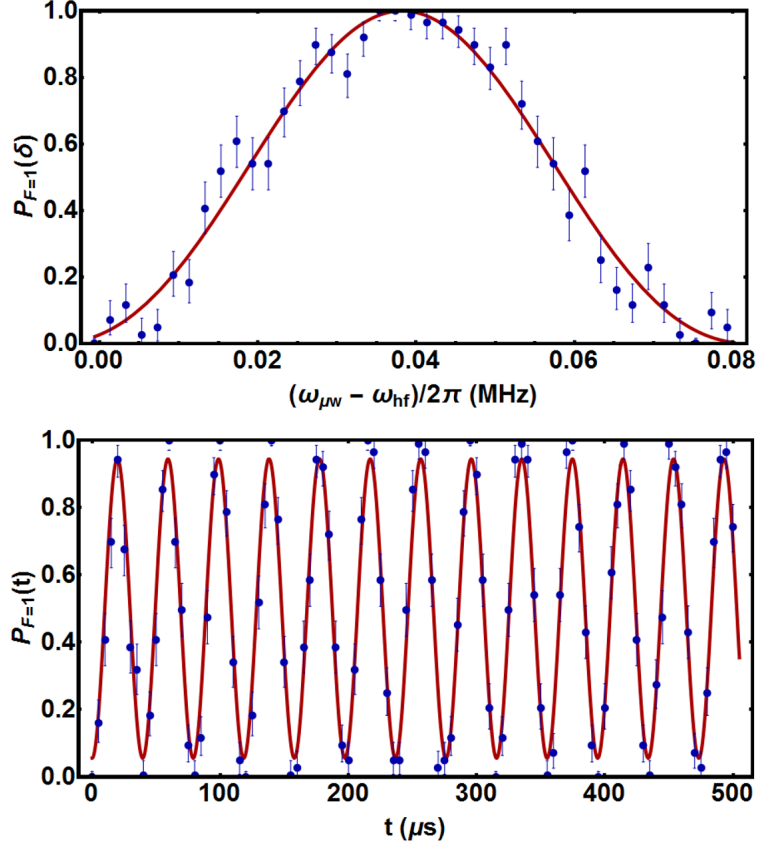


Fig. 5.10 Population in $F=1$ for a clock ($|0\rangle \leftrightarrow |0'\rangle$ transition) frequency scan (top) and Rabi oscillation (bottom). (Top) The red line is a fitted function described by Eq. 5.2 where $\omega = \omega_{\mu w}$, with contrast A and transition frequency ω_p set as free parameters. The second order Zeeman shift is found to be $(\omega_p - \omega_{hf})/2\pi = 39.1$ kHz where $\omega_{hf} = 12.6428121$ GHz is the zero-field hyperfine clock transition of $^{171}\text{Yb}^+$. (Bottom) The red line is a fitted function described by Eq. 5.3, with the contrast A and Rabi frequency Ω of the transition set as free parameters, the t_π time is found to be $19.72 \mu\text{s}$. This value is essential for high fidelity state preparation and detection so multiple oscillations are performed to get an accurate reading.

First order sensitive transitions

Frequency scans on any of the first order sensitive transitions measures the first order Zeeman shift that is induced from the externally applied static B-field. Rabi oscillations on the first order sensitive states are used to measure Rabi frequencies, the Rabi frequencies on these transitions are matched during dressed state experiments, the reason for this is described in Sec. 2.2.2.

The Rabi frequencies for two bare state transitions utilized in a dressed state experiments are measured separately, but by applying two fields simultaneously with one far

detuned from its transition frequency and one on resonance with the transition being measured. This is done due to a signal power change being present after the two signals have been mixed (as described in Sec. 4.5.3) as opposed to one single, unmixed frequency. This produces a different Rabi frequency when compared to an experiment with only one field applied during an experiment (ie: no detuned field applied). This allows for a better representation of what the Rabi frequencies would be when two fields are applied on resonance to put the ion into the dressed state basis. Matched dressing field Rabi frequencies for both the microwave and RF dressed states can be seen in Fig. 5.11 and 5.12 respectively. The two Rabi frequencies of the RF fields are matched by performing Rabi oscillations on each transition and adjusting the input power of each field until they are relatively close in Rabi frequency. The slight Rabi frequency mismatch shown in either Fig. 5.11 or 5.12 is expected due to statistical and experimental errors on the population measurements, which in turn have an effect on the maximum log-likelihood fitted function. This can be better accounted for by performing longer Rabi oscillations to attain a better reading on the Rabi frequency.

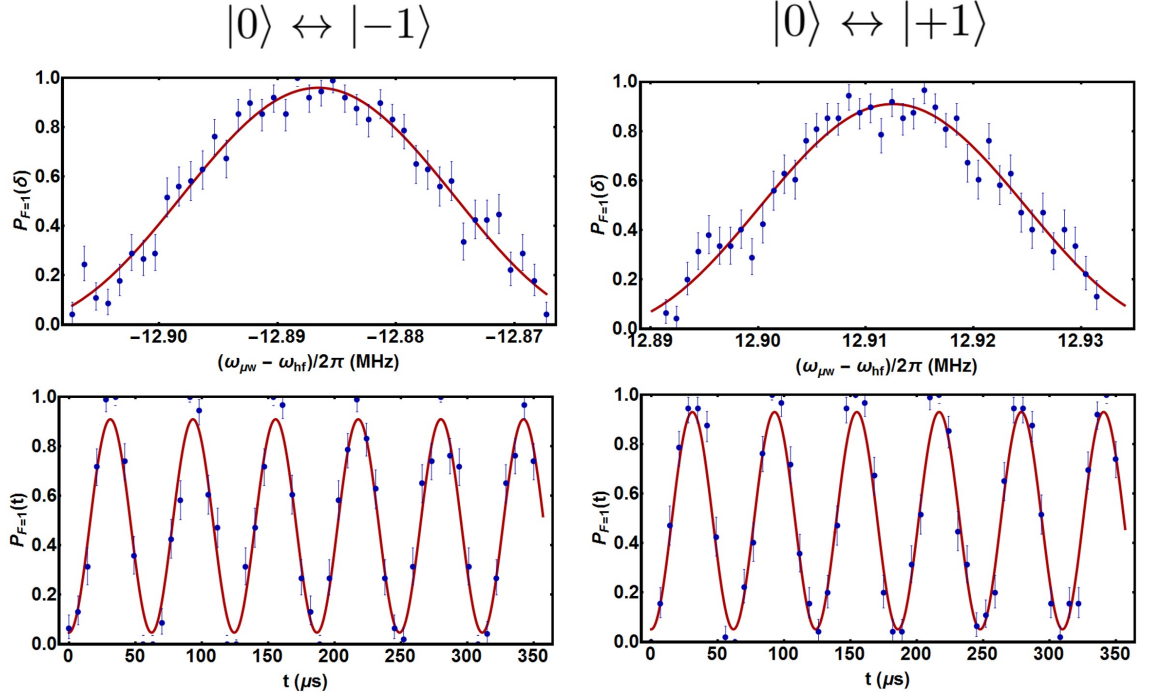


Fig. 5.11 Population in $F=1$ for $|0\rangle \leftrightarrow |-1\rangle$ (left) and $|0\rangle \leftrightarrow |+1\rangle$ (right) transition frequency scans (top) and Rabi oscillations (bottom). (Top) The red line is a fitted function described by Eq. 5.2 where $\omega = \omega_{\mu\nu}$, with contrast A and transition frequency ω_p set as free parameters. The $|0\rangle \leftrightarrow |-1\rangle$ and $|0\rangle \leftrightarrow |+1\rangle$ transitions are found to have transition frequencies of $(\omega_p - \omega_{hf})/2\pi = 12.8835$ MHz and $(\omega_p - \omega_{hf})/2\pi = 12.9112$ MHz. (Bottom) The red line is a fitted function described by Eq. 5.3, with the contrast A and Rabi frequency Ω of the transition set as free parameters. The two Rabi frequencies are $\Omega/2\pi = 16.065$ kHz and $\Omega/2\pi = 16.140$ kHz for the $|0\rangle \leftrightarrow |-1\rangle$ and $|0\rangle \leftrightarrow |+1\rangle$ transitions respectively.

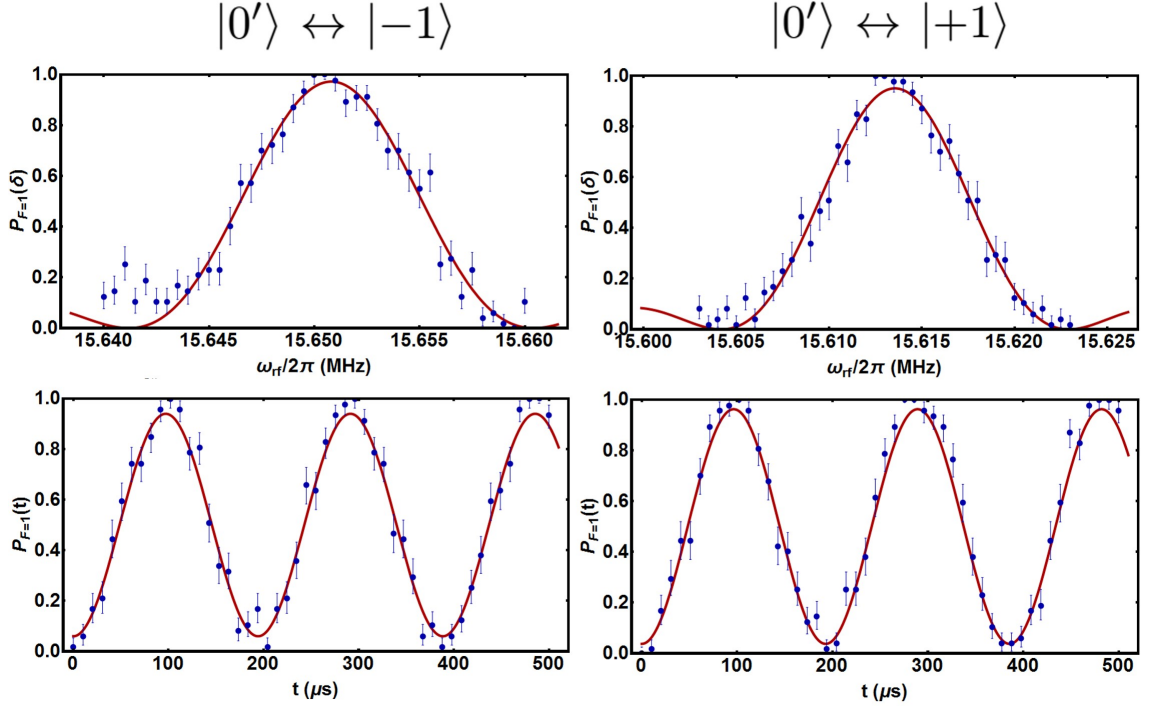


Fig. 5.12 Population in $F=1$ for $|0'\rangle \leftrightarrow |-1\rangle$ (left) and $|0'\rangle \leftrightarrow |+1\rangle$ (right) transitions, with frequency scans (top) and Rabi oscillations (bottom) induced by a single RF field. (Top) The red line is a fitted function described by Eq. 5.2 where $\omega = \omega_{rf}$, with contrast A and transition frequency ω_p set as free parameters. The $|0'\rangle \leftrightarrow |-1\rangle$ and $|0'\rangle \leftrightarrow |+1\rangle$ transitions are found to have transition frequencies of $\omega_p/2\pi = 15.6507$ MHz and $\omega_p/2\pi = 15.6136$ MHz. (Bottom) The red line is a fitted function described by Eq. 5.3, with the contrast A and Rabi frequency Ω of the transition set as free parameters. The two Rabi frequencies are $\Omega/2\pi = 5.149$ kHz and $\Omega/2\pi = 5.186$ kHz for the $|0\rangle \leftrightarrow |-1\rangle$ and $|0\rangle \leftrightarrow |+1\rangle$ transitions respectively.

The effect of off-resonant frequencies driving the bare states can be seen in Fig. 2.10. Off-resonant dressing fields driving the bare state transitions cause a reduction in coherence time of the dressed states as discussed in Sec 2.2.

5.4.2 Bare state T_2^* and T_2 coherence time measurements

The T_2^* and T_2 coherence times of the bare states reveal information about the magnetic field noise the ion is subjected to. This gives insight into the types of magnetic field noise the ion is subject to and can potentially be used to identify noise sources.

Clock transition measurements

The clock transition ($|0\rangle \leftrightarrow |0'\rangle$) has the longest T_2^* and T_2 coherence times due to

its states only being sensitive to the second order magnetic field sensitive states. Fast de-phasing of the clock state will mean that long coherence times will be hard to achieve for other two-level systems in the $^2S_{1/2}$ manifold. T_2^* and T_2 coherence times at a second order Zeeman shift of 7.9 kHz were measured to be 0.60(6) s and 3.81(3) s respectively, this can be seen in Fig. 5.13 and 5.14.

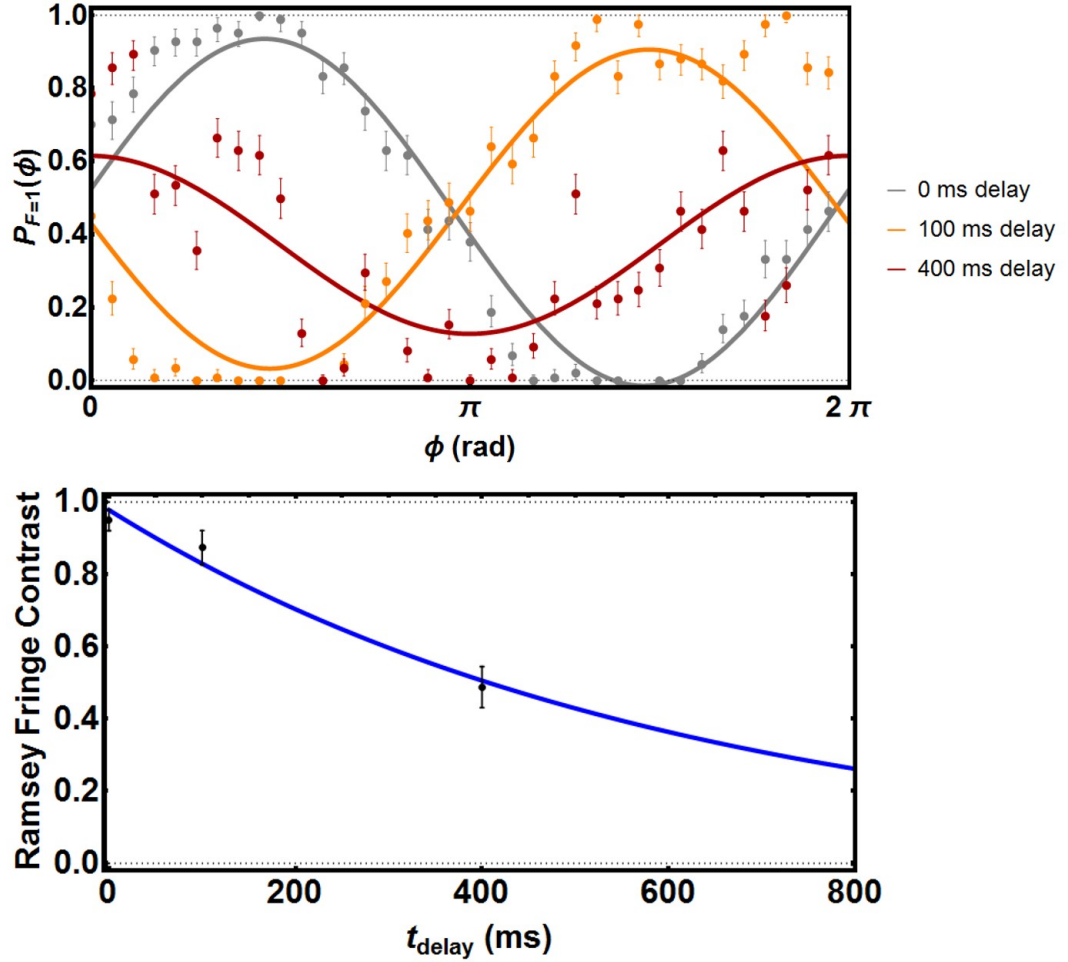


Fig. 5.13 (Top) Result of a Ramsey T_2^* experiment on the $|0\rangle \leftrightarrow |0'\rangle$ transition. The grey, orange and red data points each correspond to a different delay time t_{delay} as indicated on the legend. The corresponding lines are from a fitted function described by Eq. 5.4 with the fringe contrast a , population offset p_{off} and phase offset ϕ_{off} set as free parameters. (Bottom) Fitted Ramsey fringe contrast of the three delay times from the data in the top graph, where error bars are the standard errors extracted from the three fits. The blue line is an exponential decay fitted to the three data points, giving a T_2^* time of 0.60(6) s.

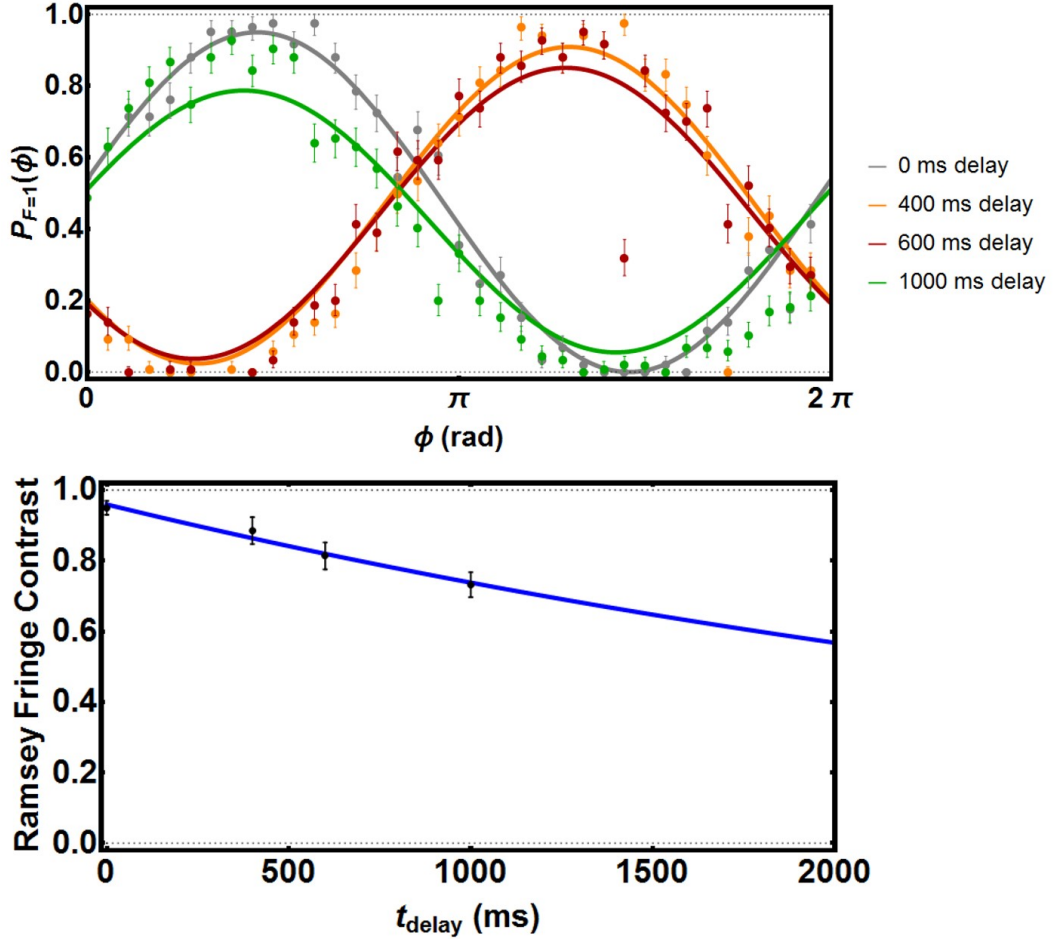


Fig. 5.14 (Top) Result of a Ramsey T_2 experiment on the $|0\rangle \leftrightarrow |0'\rangle$ transition. The grey, orange, red and green data points each correspond to a different delay time t_{delay} as indicated on the legend. The corresponding lines are from a fitted function described by Eq. 5.4 with the fringe contrast a , population offset p_{off} and phase offset ϕ_{off} set as free parameters. (Bottom) Fitted Ramsey fringe contrast of the four delay times from the data in the top graph, where error bars are the standard errors extracted from the four fits. The blue line is an exponential decay fitted to the four data points, giving a T_2 time of 3.81(3) s.

The large difference between T_2^* and T_2 on the clock transition suggests that slowly oscillating magnetic field fluctuations are the primary source of noise. This is because the extra π pulse on the T_2 time reduces the effect of slowly oscillating fields inducing decoherence on the ion [113]. The static B-field coils are likely the source of the slowly fluctuating magnetic fields (Sec. 4.5.1). The coils are built from a relatively small wire diameter which is wound tightly together; with a high current passing it, the temperature of the wire is likely to fluctuate. This would cause fluctuations of the wires resistance, normally the current supply would attempt to compensate for resistance changes to maintain a constant current but this is likely not a perfect compensation mechanism, this would mean the current would fluctuate slightly and cause the magnetic magnetic field to fluctuate.

tuate also. This can be compensated for in the future by using a larger diameter coil and heat sinking the coils with a heat conductive gel and larger housing to allow for a greater rate of heat dissipation. This speculation can be confirmed by measuring the resistance and current of the coils over a large period of time. This hasn't been conducted yet due to time constraints on this thesis.

First order sensitive transitions

The T_2^* and T_2 coherence times for the bare state transitions $|0\rangle \leftrightarrow |-1\rangle$ and $|0\rangle \leftrightarrow |+1\rangle$ have significantly lower values than the clock transition due to the first order sensitivity to magnetic fields. These tend to give more information about weaker, higher frequency magnetic field noise due to the sensitivity of the states and the relatively short experiment times. At a first order Zeeman shift of $\omega_B^+ = 6.901$ MHz (Fig. 2.7), the T_2^* times for the $|0\rangle \leftrightarrow |-1\rangle$ and $|0\rangle \leftrightarrow |+1\rangle$ transitions are 1.54(2) ms and 2.47(8) ms respectively, this is shown in Fig. 5.15. The T_2 times for the $|0\rangle \leftrightarrow |-1\rangle$ and $|0\rangle \leftrightarrow |+1\rangle$ transitions are 4.86(2) ms and 4.31(1) ms respectively, this is shown in Fig. 5.16.

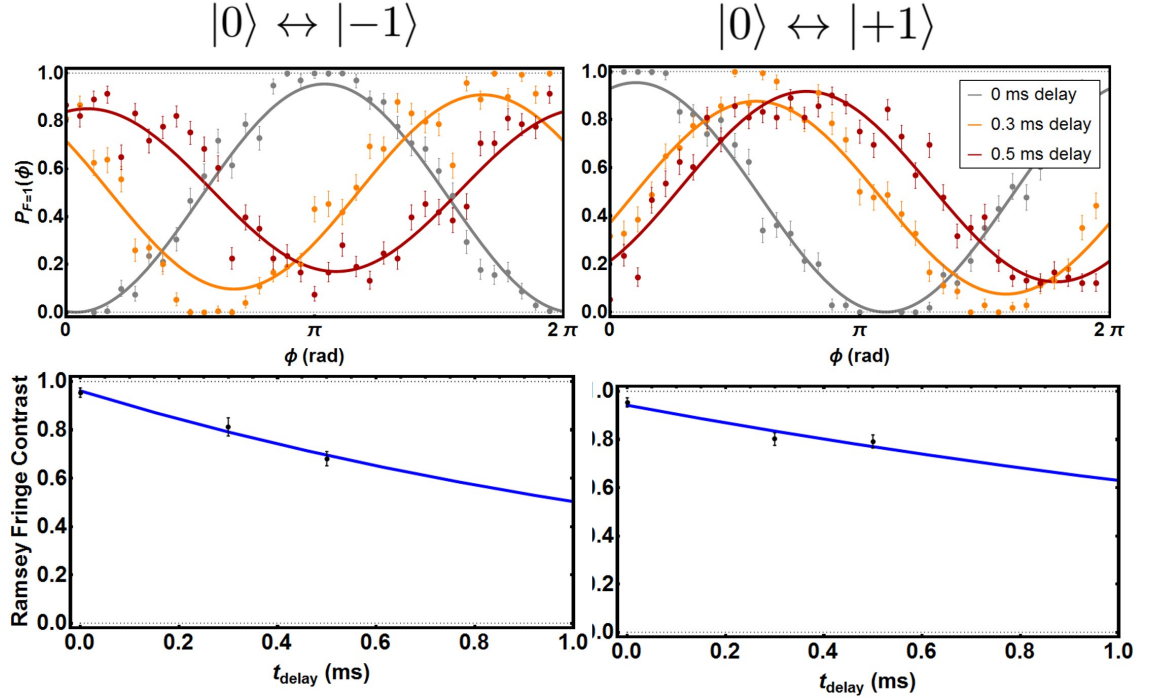


Fig. 5.15 (Top) Result of Ramsey T_2^* experiments on the $|0\rangle \leftrightarrow |-1\rangle$ transition (left) and $|0\rangle \leftrightarrow |+1\rangle$ transition (right). The grey, orange and red data points each correspond to a different delay time t_{delay} as indicated on the legend. The corresponding lines are from a fitted function described by Eq. 5.4 with the fringe contrast a , population offset p_{off} and phase offset ϕ_{off} set as free parameters. (Bottom) Fitted Ramsey fringe contrast of the three delay times from the data in the top graph, where error bars are the standard errors extracted from the three fits. The blue line is an exponential decay fitted to the three data points, giving T_2^* times of 1.54(2) ms and 2.47(8) ms for the $|0\rangle \leftrightarrow |-1\rangle$ and $|0\rangle \leftrightarrow |+1\rangle$ transitions respectively.

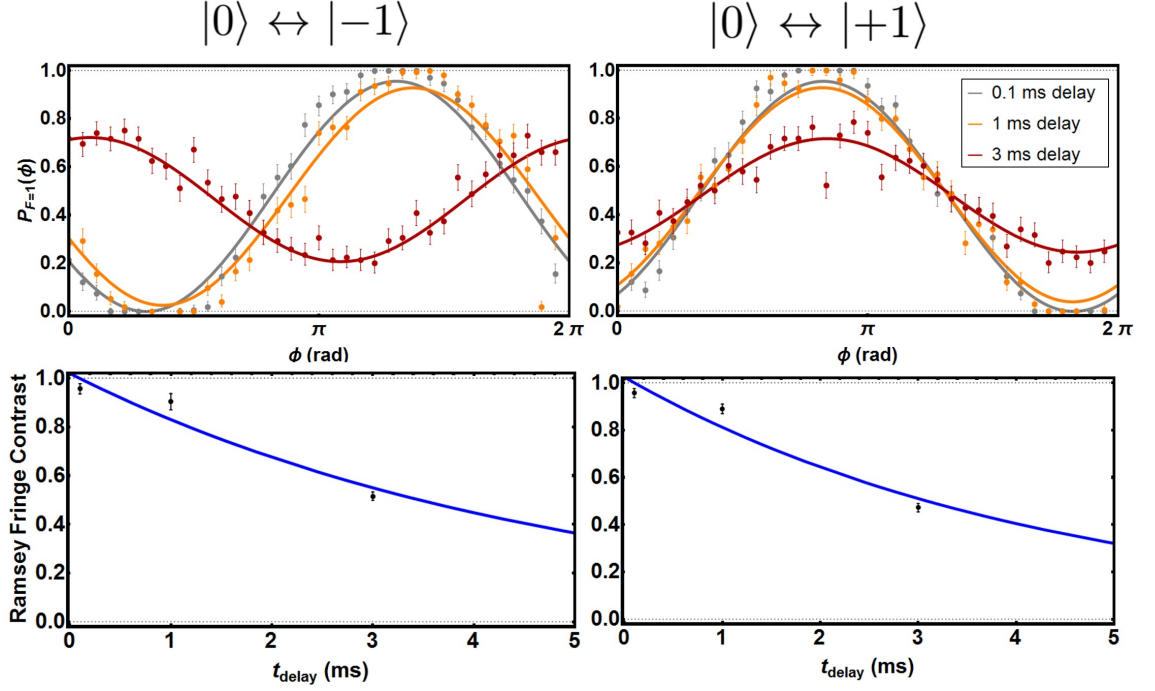


Fig. 5.16 (Top) Result of Ramsey T_2 experiments on the $|0\rangle \leftrightarrow |-1\rangle$ transition (left) and $|0\rangle \leftrightarrow |+1\rangle$ transition (right). The grey, orange and red data points each correspond to a different delay time t_{delay} as indicated on the legend. The corresponding lines are from a fitted function described by Eq. 5.4 with the fringe contrast a , population offset p_{off} and phase offset ϕ_{off} set as free parameters. (Bottom) Fitted Ramsey fringe contrast of the three delay times from the data in the top graph, where error bars are the standard errors extracted from the three fits. The blue line is an exponential decay fitted to the three data points, giving T_2 times of 4.86(2) ms and 4.31(1) ms for the $|0\rangle \leftrightarrow |-1\rangle$ and $|0\rangle \leftrightarrow |+1\rangle$ transitions respectively.

It would be expected that the coherence times for both transitions would be relatively close as they are both sensitive to magnetic field fluctuations to the same order. The differences can be attributed to measurement errors, this could be clarified by averaging over multiple Ramsey experiments. The improvement from the T_2^* to the T_2 measurements are less significant than the clock transition coherence time measurements. This might suggest that during the time scale of the experiment for the first-order sensitive measurements, slow magnetic field drifts are less of a source of decoherence than that of the higher frequency magnetic field drifts [113].

5.5 Microwave dressed states experiments

Utilising a dressed state system (as theoretically described in Sec. 2.2.2) is of great benefit for RF and microwave magnetic field sensing. The noise decoupling effects cause a large increase on T_2 coherence time which allows for smaller magnetic field amplitudes to be sensed. To prepare the ion in the dressed state basis using microwaves, two microwave

fields driving the $|0\rangle \leftrightarrow |-1\rangle$ and $|0\rangle \leftrightarrow |+1\rangle$ transitions on resonance with equal Rabi frequencies are applied (see Sec. 2.2). To select the correct field frequencies and powers, bare state experiments are performed as described in Sec. 5.4.1. Once the appropriate microwave field frequencies and transition Rabi frequencies are established, the experimental procedure for sensing RF magnetic fields via a resonant RF field driving the $|0'\rangle \leftrightarrow |D\rangle$ transition can be conducted.

The experimental procedure described here is taken from [114]. The procedure involves preparing the ion in the $|0'\rangle$ state (described in Sec. 5.2.2) followed by simultaneous application of the two microwave dressing fields and an RF field for dressed state manipulation. After the desired manipulation of the dressed state system has been conducted, an additional π pulse on the $|0\rangle \leftrightarrow |0'\rangle$ transition is used so that it can be determined whether the ion was in the $|D\rangle$ state or $|0'\rangle$ state during state readout; the procedure for this can be seen in Fig. 5.17. How this method compares to previously used STIRAP process for dressed state preparation can be found in [114].

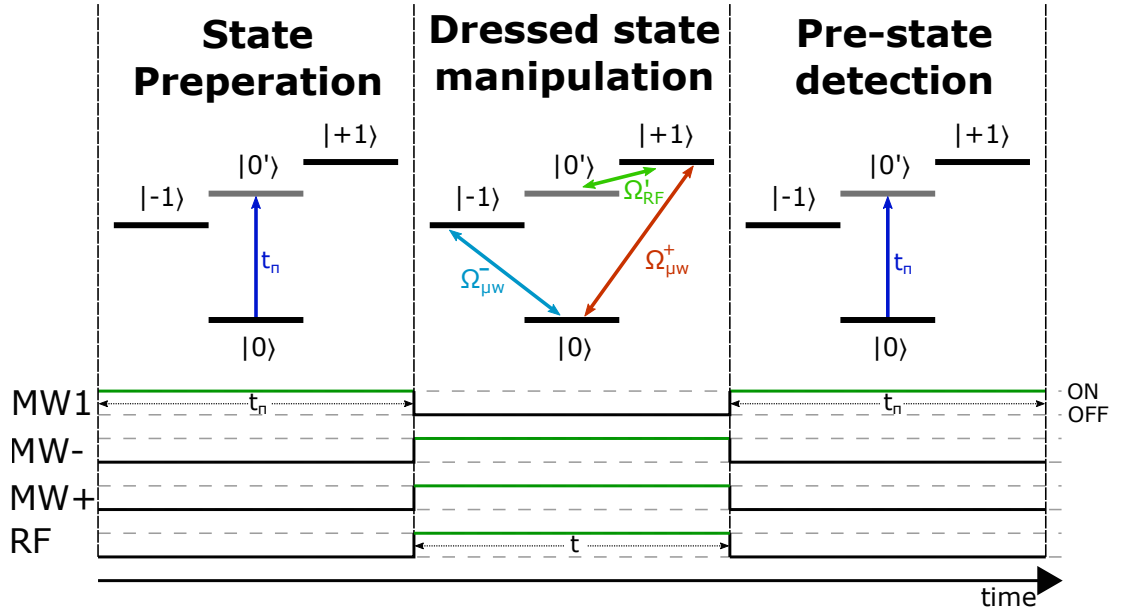


Fig. 5.17 The state preparation and detection protocol for using microwave dressed states. The ion is prepared in the $|0'\rangle$ state followed by simultaneous application of on resonant microwave dressing fields on the $|0\rangle \leftrightarrow |-1\rangle$ and $|0\rangle \leftrightarrow |+1\rangle$ transitions at equal Rabi frequencies ($\Omega_{\mu w}^- = \Omega_{\mu w}^+ = \Omega_{\mu w}$) and an on resonant RF field on the $|0'\rangle \leftrightarrow |D\rangle$ transition with Rabi frequency Ω'_{RF} (Eq. 2.25). This is done for an experiment time t , followed by a π pulse on the $|0\rangle \leftrightarrow |0'\rangle$ transition to distinguish between whether the ion was left in the $|D\rangle$ state or $|0'\rangle$ state before state readout.

5.5.1 Microwave dressed state frequency scans

To ensure the correct frequency is selected when performing Rabi oscillations on the $|0'\rangle \leftrightarrow |D\rangle$ transition, a frequency scan of the dressed states is performed. Dressed state frequency

scans are performed by preparing the ion in the $|0'\rangle$ state as shown in Fig. 5.17, from which a frequency scan (as described in Sec. 5.3.1) of the applied RF field is conducted during the dressed state manipulation window.

A frequency scan across all three dressed states (discussed in Sec. 2.2.3) $|u\rangle$, $|d\rangle$ and $|D\rangle$ will show the Rabi frequency of the dressing fields as the frequency difference between these dressed states is proportional to the dressing field Rabi frequency; this is shown in Fig. 5.18. A measurement across the six dressed states shows the second order Zeeman splitting, this is because the dressed state $|D\rangle$ pair is separated by the transition frequency difference of the $|0'\rangle \leftrightarrow |-1\rangle$ and $|0'\rangle \leftrightarrow |+1\rangle$ transitions; this is discussed in Sec. 2.2.3 and shown in Fig. 5.18.

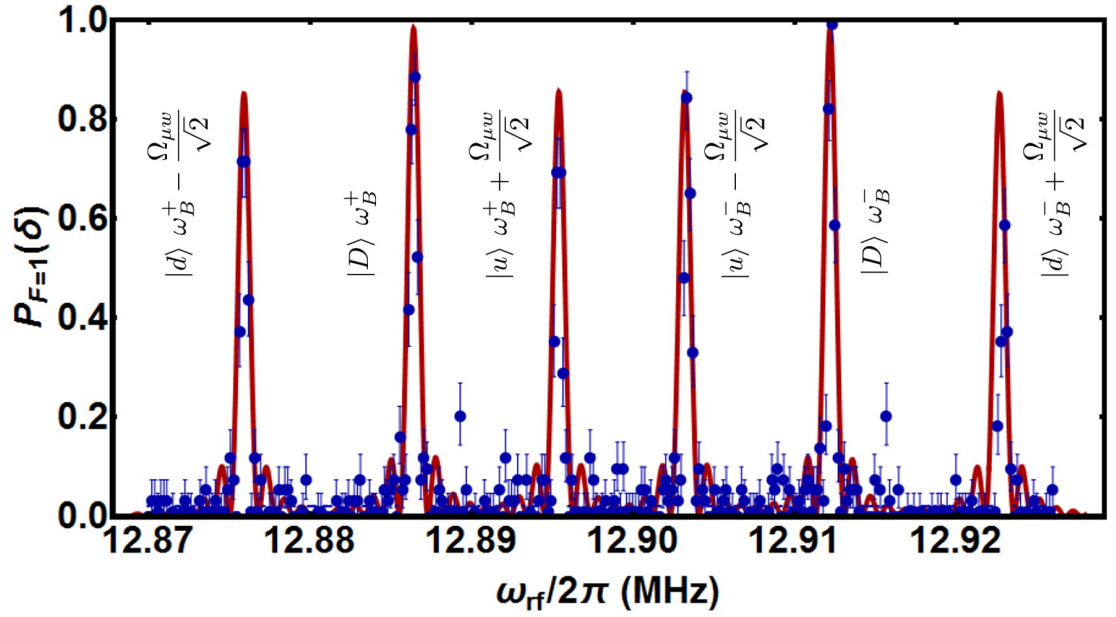


Fig. 5.18 Population in $F=1$ after a frequency scan of a single RF field applied for $975 \mu\text{s}$, after preparing the ion in the $|0'\rangle$ state and applying microwave dressing fields. The difference in peak height is due to the transitions having different t_π times. The red line is a fitted function of six transitions sum, individually described by Eq. 5.2 where $\omega = \omega_{rf}$, with individual contrasts A and transition frequencies ω_p set as free parameters. From the peak separation, the Rabi frequency of the dressing fields and the 2nd order Zeeman shift are determined to be $\Omega_{\mu w}/\sqrt{2} \approx 2\pi \times 9.8 \text{ kHz}$ and $(\omega_B^- - \omega_B^+)/2\pi = 25.8 \text{ kHz}$ (Fig. 2.12).

5.5.2 Microwave dressed state Rabi oscillations

Rabi oscillations on the $|0'\rangle \leftrightarrow |D\rangle$ transition are performed to deconstruct information about the RF magnetic field being sensed. The measurement can determine the Rabi frequency which can be used to determine the amplitude of the magnetic field driving the transition as described in Sec. 2.2.1. More importantly, the accuracy in which the field strength can be measured and the sensitivity of the ion can be determined from these

measurements.

To perform Rabi oscillations on the $|0'\rangle \leftrightarrow |D\rangle$ transition, the ion is prepared in the $|0'\rangle$ state and microwave dressing fields are applied as shown in Fig. 5.17, from which Rabi oscillations are induced by application of a single RF field as described in Sec. 5.3.2 during the dressed state manipulation window.

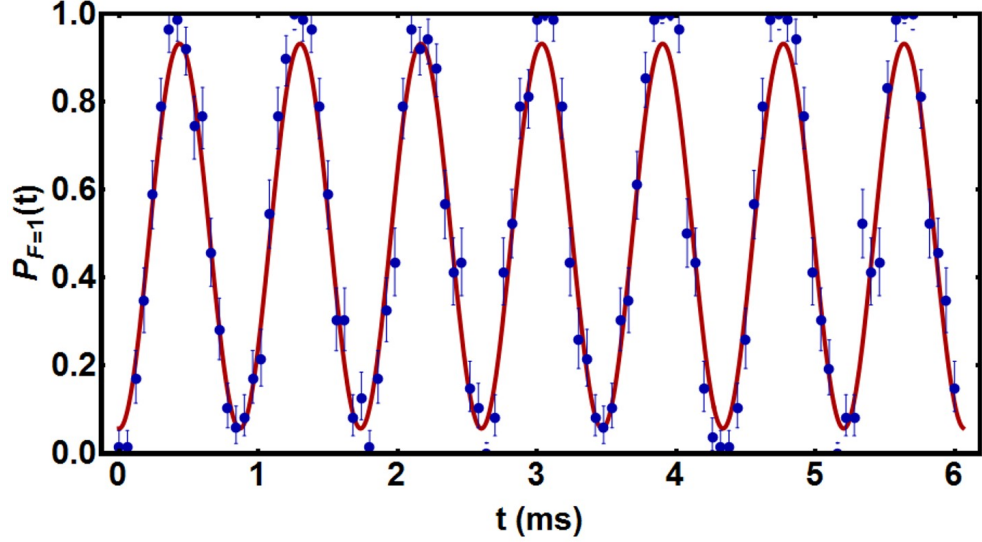


Fig. 5.19 Population in $F=1$ for a microwave dressed state Rabi oscillation ($|0'\rangle \leftrightarrow |D\rangle$) at a transition frequency of $\omega_{rf}/2\pi = 15.616$ MHz. Each data point consists of 50 repetitions. The red line is a fitted function described by Eq. 5.3, with the contrast A and Rabi frequency $\Omega = \Omega'_{RF}$ of the transition set as free parameters. The fitted function gives a Rabi frequency of $\Omega'_{RF}/2\pi = 1.153$ kHz.

Rabi oscillation data like that shown in Fig. 5.19 is used in Sec. 5.7 to determine the sensitivity of the magnetometer.

5.5.3 Microwave dressed state T_2^* and T_2 coherence time measurements

Measuring the T_2^* and T_2 coherence times on the microwave dressed states can be used to determine the theoretical limit of the Rabi frequency resolution and the shot-noise limited sensitivity of the trapped ion system for RF magnetic field sensing (Sec. 2.40).

To perform T_2^* and T_2 time measurements on the dressed states, the ion is prepared in the $|0'\rangle$ state and dressing fields are applied as shown in Fig. 5.17. From this, Ramsey experiments are conducted as described in Sec. 5.3.3 during the dressed state manipulation window. The $|0'\rangle \leftrightarrow |D\rangle$ transition associated with a first order Zeeman splitting of $\omega_B^+/2\pi = 15.616$ MHz (Fig. 2.12), and dressing field Rabi frequencies of $\Omega_{\mu w}^-/2\pi = 26.841$ kHz and $\Omega_{\mu w}^+/2\pi = 26.710$ kHz was found to have T_2^* and T_2 coherence times of 0.11(5) s and 0.64(5) s respectively, the results can be seen in Fig. 5.20 and Fig. 5.21.

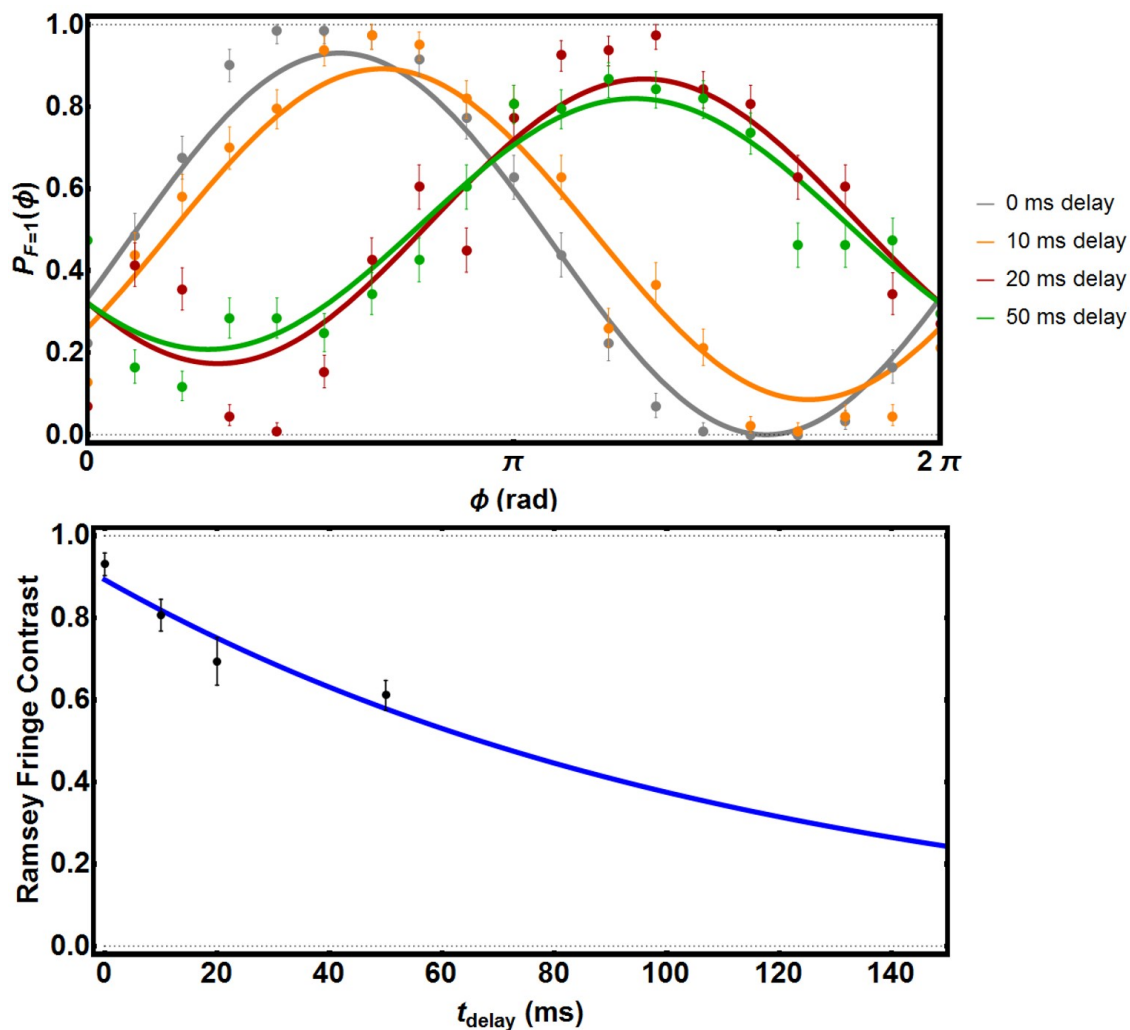


Fig. 5.20 (Top) Result of a Ramsey T_2^* experiment on the $|0'\rangle \leftrightarrow |D\rangle$ transition. The grey, orange red and green data points each correspond to a different delay time t_{delay} as indicated on the legend. The corresponding lines are from a fitted function described by Eq. 5.4 with the fringe contrast a , population offset p_{off} and phase offset ϕ_{off} set as free parameters. (Bottom) Fitted Ramsey fringe contrast of the four delay times from the data in the top graph, where error bars are the standard errors extracted from the four fits. The blue line is an exponential decay fitted to the four data points, giving a T_2^* time of 0.11(5) s.

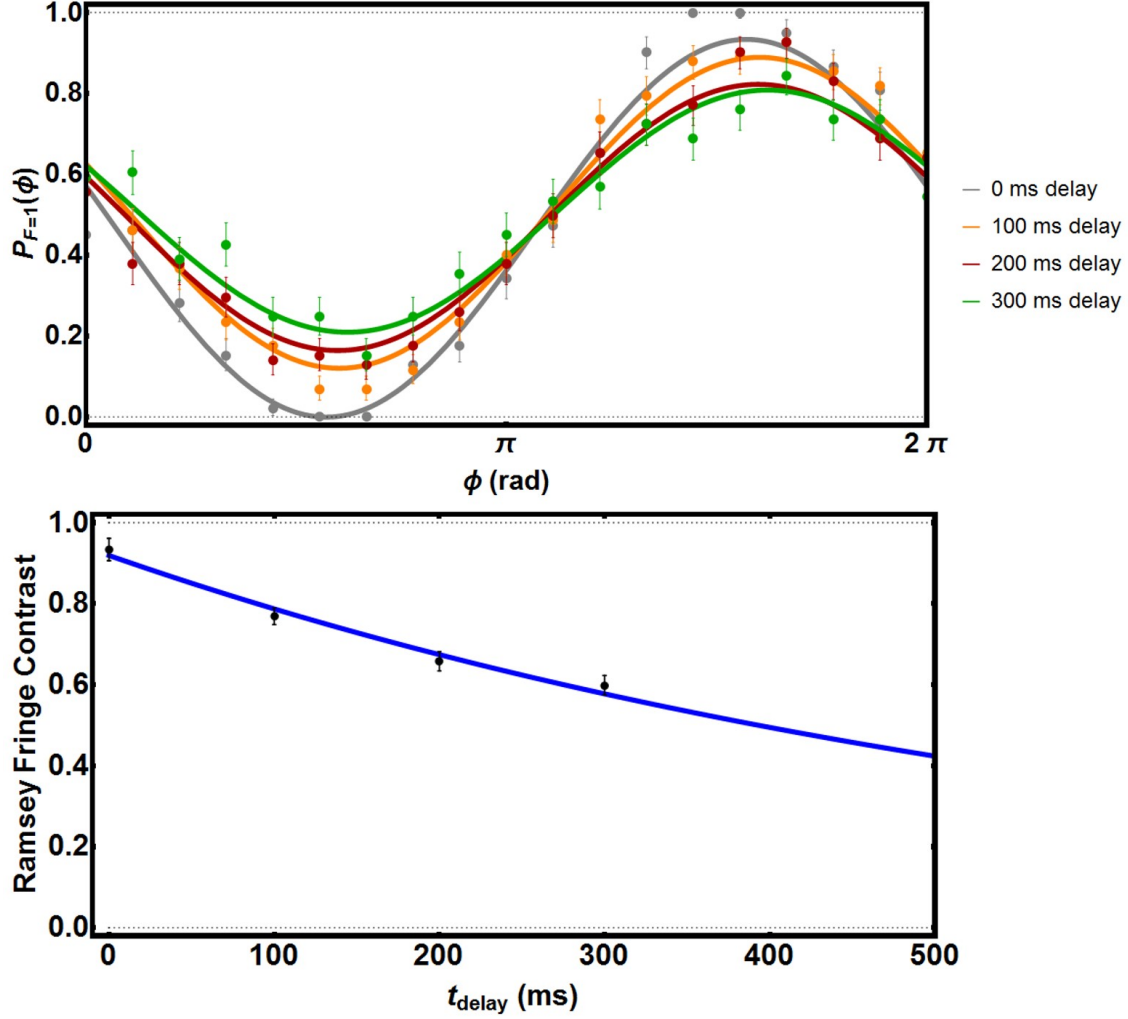


Fig. 5.21 (Top) Result of a Ramsey T_2 experiment on the $|0'\rangle \leftrightarrow |D\rangle$ transition. The grey, orange, red and green data points each correspond to a different delay time t_{delay} as indicated on the legend. The corresponding lines are from a fitted function described by Eq. 5.4 with the fringe contrast a , population offset p_{off} and phase offset ϕ_{off} set as free parameters. (Bottom) Fitted Ramsey fringe contrast of the four delay times from the data in the top graph, where error bars are the standard errors extracted from the four fits. The blue line is an exponential decay fitted to the four data points, giving a T_2 time of 0.64(5) s.

Though the relative difference between the T_2 time and the T_2^* time is not as significant as the clock transition difference in Sec. 5.4.2, the large improvement due to the added spin echo on the T_2 measurement is likely attributed to the cancelling out of the slow magnetic field drift induced by the coils as well. These results seem reasonable but not optimal when compared to other coherence times measured on $^{171}\text{Yb}^+$ in [34]. By comparison to the RF dressed states coherence time measurements in Sec. 5.6.3, a contributing factor could be that the mixing process for the microwave dressing fields (Sec. 4.5.3) would cause the Rabi frequency of the dressing fields to fluctuate. This was observed by connecting the

output of the mixer to a spectrum analyser and observing fluctuations in the microwaves peak power. The peak power of each microwave field at -5 dBm fluctuated rapidly by ± 0.1 dBm when both microwaves were switched on. This was not observed at the output of the combiner (Sec. 4.5.2) for the RF fields used for RF dressed state experiments (Sec. 5.6.3). A more in depth analysis of this could be conducted by recording the amplitude values of each independent microwave field in time by using a virtual network analyser (VNA). This wasn't conducted during the course of this thesis due to time constraints.

Another limiting factor for the T_2 time could be attributed to the ion being populated into the $|u\rangle$ or $|d\rangle$ states during experiments. Magnetic field noise at a frequency equal to the frequency separation of the $|D\rangle$ state and the $\{|u\rangle, |d\rangle\}$ states, $\Omega_{\mu w}/\sqrt{2}$, would cause this to happen. The rate in which this occurs is an exponential decay that decays at a rate equal to the T_1 time, of which the T_2 time cannot surpass. Measurements of the T_1 time would be carried out in the future work for this experiment, of which the methodology for such measurements can be found in [42].

5.6 RF dressed states experiments

The RF dressed states are utilised for sensing microwave field frequencies around the clock transition frequency. The RF dressed states are used for sensing instead of the stable clock transition itself because of the large level of frequency tuneability achievable when coupling a field to a first order sensitive state.

To prepare the ion in the dressed state basis using RF fields, two RF fields driving the $|0'\rangle \leftrightarrow |-1\rangle$ and $|0'\rangle \leftrightarrow |+1\rangle$ transitions with equal Rabi frequencies are applied (see Sec. 2.2). The correct transition frequency and Rabi frequency values are attained by performing bare state Rabi oscillations and frequency scans (as described in Sec. 5.4.1) on both transitions followed by appropriate adjustments in RF field strength to make the Rabi frequencies equal.

The experimental procedure for sensing with RF dressed states starts by preparing the ion in the $|0\rangle$ state (described in Sec. 5.2.2) followed by simultaneous application of the two RF dressing fields and a microwave field for dressed state manipulation. After the desired manipulation of the dressed state system has been conducted, the state readout can be initiated without the need for an extra clock π pulse (like the microwave dressed states). This is because the ion was rotating between two states that the state readout can distinguish between, this is simply shown in Fig. 5.22.

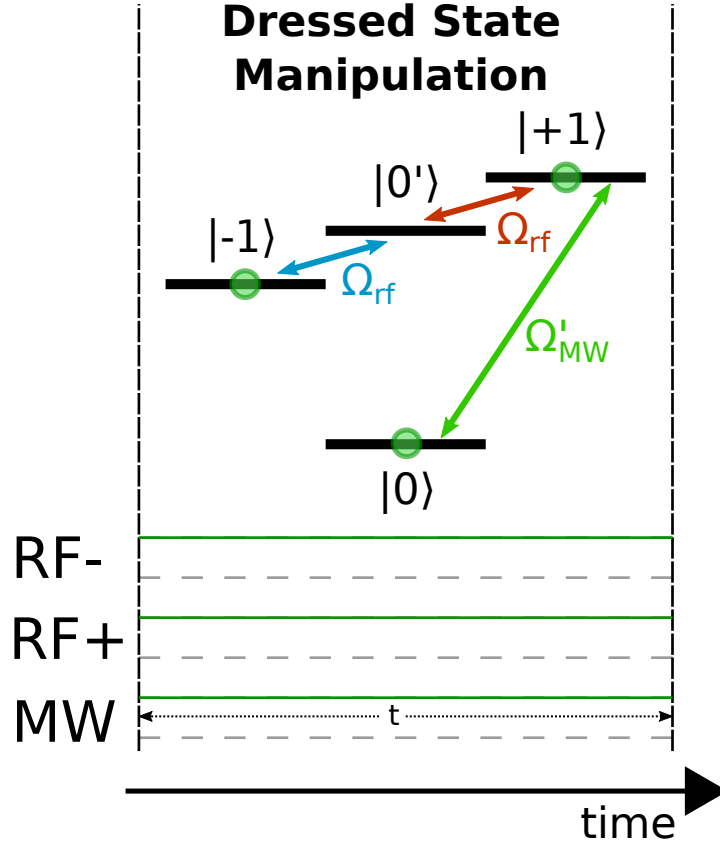


Fig. 5.22 The state preparation and detection protocol using RF dressed states. The ion is prepared in the $|0\rangle$ state (shown in Fig. 5.5) followed by simultaneous application of on resonant RF dressing fields applied to the $|0'\rangle \leftrightarrow |-1\rangle$ and $|0'\rangle \leftrightarrow |+1\rangle$ transitions at equal Rabi frequencies ($\Omega_{rf}^- = \Omega_{rf}^+ = \Omega_{rf}$), and a single on resonant microwave field driving the $|0\rangle \leftrightarrow |D\rangle$ transition with Rabi frequency Ω'_{MW} (Eq. 2.32). This is done for an experiment time t , followed by state readout.

5.6.1 RF dressed state frequency scans

To ensure the correct frequency is selected when performing Rabi oscillations on the $|0\rangle \leftrightarrow |D'\rangle$ transition, a frequency scan of the dressed states is performed. To perform a dressed state frequency scan the ion is prepared in the $|0\rangle$ state, from which a frequency scan on the applied microwave field is conducted (Sec. 5.3.1).

A frequency scan across all three dressed states (discussed in Sec. 2.2.4) $|u\rangle$, $|d\rangle$ and $|D\rangle$ will show the Rabi frequency of the dressing fields from the separation of the transitions as shown in Fig. 5.23. Unlike the microwave dressed states, the other three dressed states are separated by the first order splitting of the states $|-1\rangle$ and $|+1\rangle$, so conducting a frequency scan over all dressed states in a single experiment would require an exceptionally long total experiment time, for this reason only the three dressed states associated with the $|0\rangle \leftrightarrow |+1\rangle$ transition are shown in Fig. 5.23.

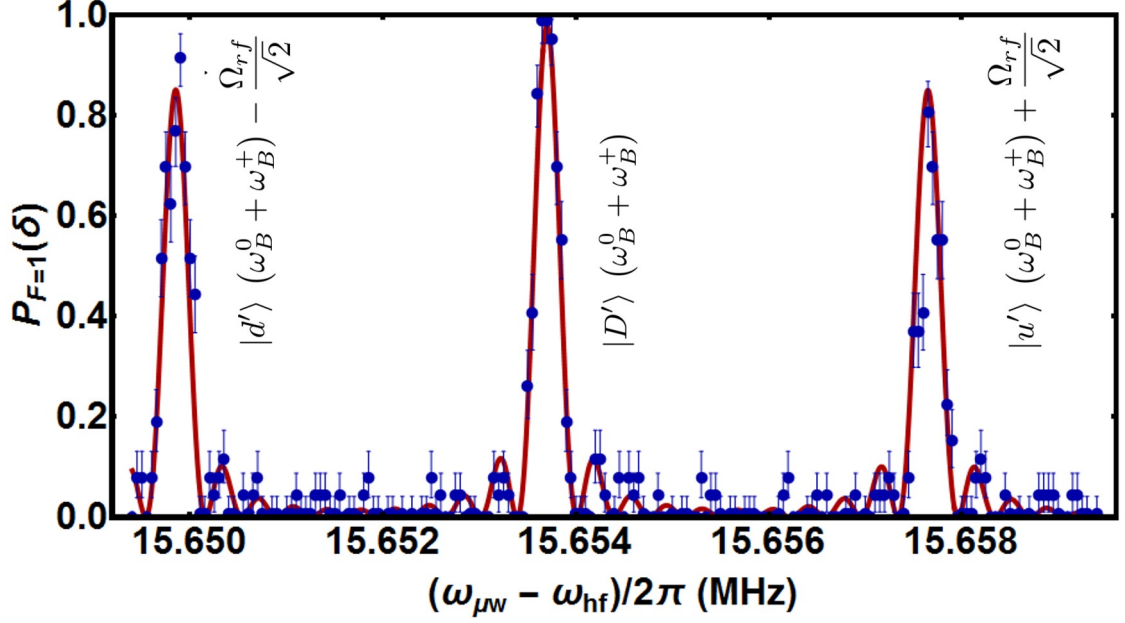


Fig. 5.23 Population in $F=1$ after a frequency scan of a single microwave field applied for 2.795 ms, after preparing the ion in the $|0\rangle$ state and applying RF dressing fields. The difference in peak height is due to the transitions having different t_π times. The red line is a fitted function of six transitions sum, individually described by Eq. 5.2 where $\omega = \omega_{\mu w}$, with individual contrasts A and transition frequencies ω_p set as free parameters. From the peak separation, the Rabi frequency of the dressing fields is found to be $\Omega_{rf}/\sqrt{2} = 2\pi \times 3.9$ kHz.

5.6.2 RF dressed state Rabi oscillations

Rabi oscillations on the $|0\rangle \leftrightarrow |D'\rangle$ transition are performed to deconstruct information about the microwave magnetic field being sensed. The Rabi frequency can be used to determine the amplitude of the magnetic field driving the transition, it is also a measurement of the sensitivity of the system.

To perform Rabi oscillations on the $|0\rangle \leftrightarrow |D'\rangle$ transition. The ion is prepared in the $|0'\rangle$ state and the RF dressing fields are applied, from which Rabi oscillations are induced as described in Sec. 5.3.2 by application of a single microwave field. Results of this can be seen in Fig. 5.24.

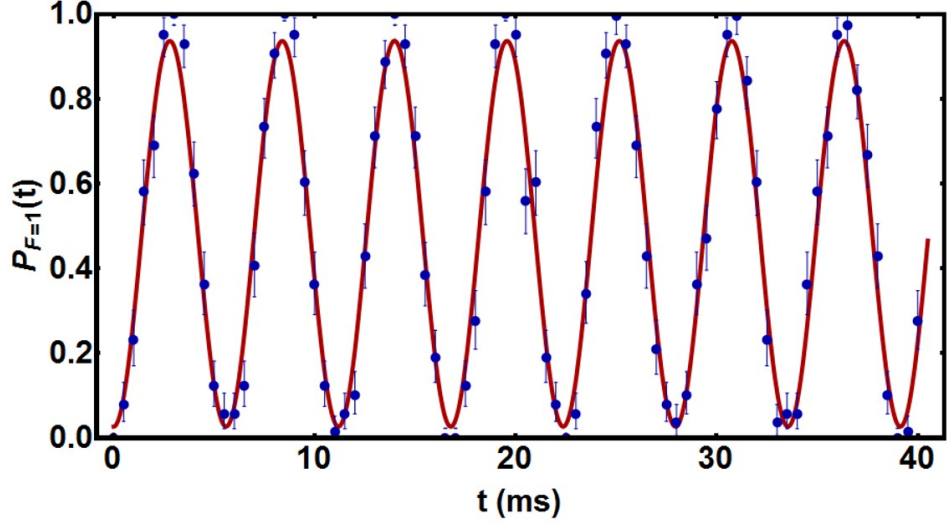


Fig. 5.24 Population in $F=1$ for a RF dressed state Rabi oscillation ($|0\rangle \leftrightarrow |D'\rangle$) at a frequency of $(\omega_{\mu w} - \omega_{hf})/2\pi = 15.654$ MHz. Each data point consists of 50 repetitions. The red line is a fitted function described by Eq. 5.3, with the contrast A and Rabi frequency $\Omega = \Omega'_{MW}$ of the transition set as free parameters. The fitted function gives a Rabi frequency of $\Omega'_{MW}/2\pi = 179$ Hz.

5.6.3 RF dressed state T_2^* and T_2 coherence time measurements

Measuring the T_2^* and T_2 coherence times on the RF dressed states can be used to determine the theoretical limit of the Rabi frequency resolution and the shot-noise limited sensitivity of the trapped ion system for microwave magnetic field sensing (Sec. 2.40).

To perform T_2^* and T_2 time measurements on the RF dressed states, the ion is prepared in the $|0\rangle$ state and RF dressing fields are applied as shown in Fig. 5.22, from which Ramsey experiments are conducted as described in Sec. 5.3.3 by application of a single microwave field during the dressed state manipulation window. The $|0\rangle \leftrightarrow |D'\rangle$ transition associated with a first order Zeeman splitting transition frequency of $(\omega_B^0 + \omega_B^+)/2\pi = 15.654$ MHz (Fig. 2.13), and dressing field Rabi frequencies of $\Omega_{\mu w}^-/2\pi = 5.030$ kHz and $\Omega_{\mu w}^+/2\pi = 5.120$ kHz was found to have T_2^* and T_2 coherence times of 0.35(8) s and 1.15(3) s respectively, the results can be seen in Fig. 5.25 and Fig. 5.26.

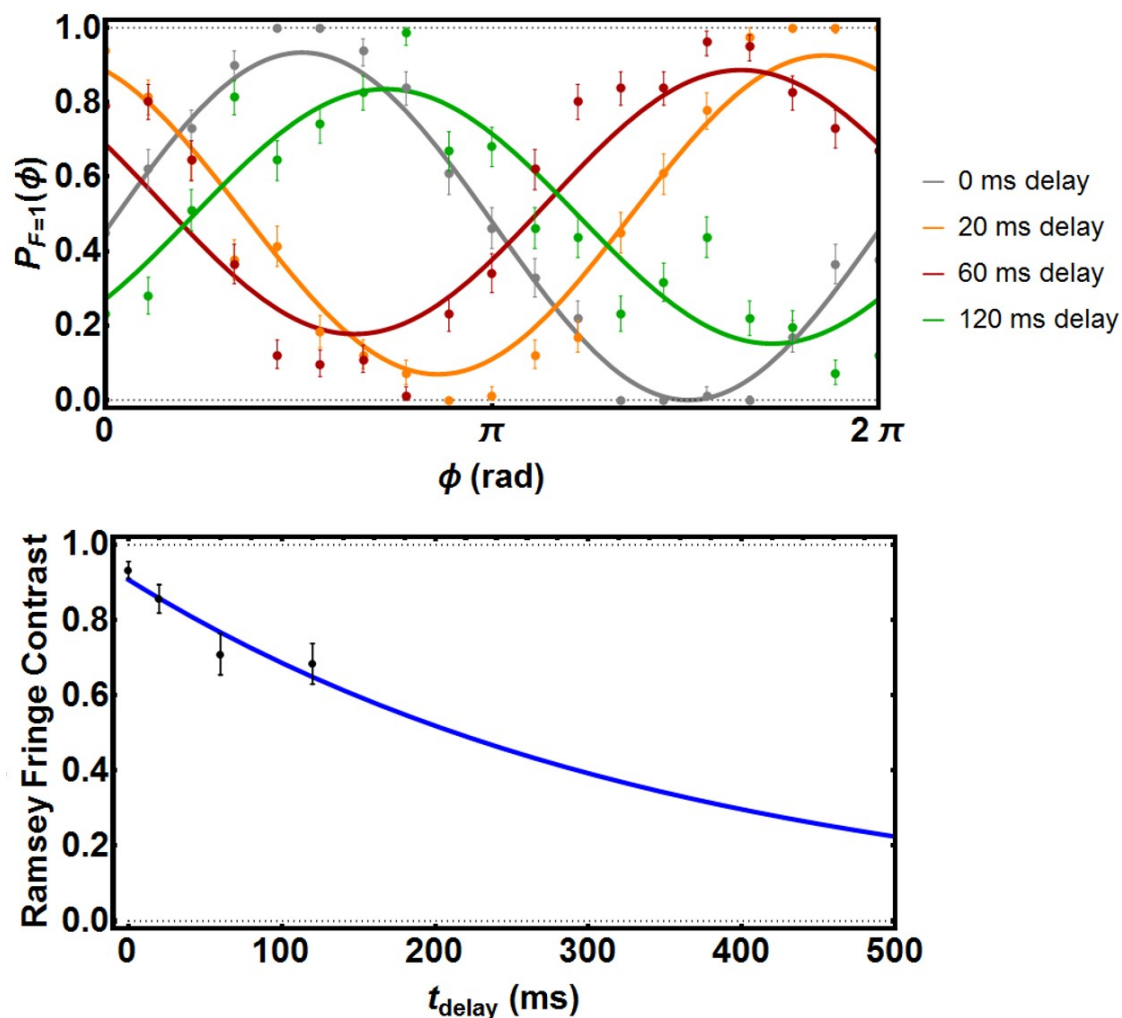


Fig. 5.25 (Top) Result of a Ramsey T_2^* experiment on the $|0\rangle \leftrightarrow |D'\rangle$ transition. The grey, orange, red and green data points each correspond to a different delay time t_{delay} as indicated on the legend. The corresponding lines are from a fitted function described by Eq. 5.4 with the fringe contrast a , population offset p_{off} and phase offset ϕ_{off} set as free parameters. (Bottom) Fitted Ramsey fringe contrast of the four delay times from the data in the top graph, where error bars are the standard errors extracted from the four fits. The blue line is an exponential decay fitted to the four data points, giving a T_2^* time of 0.35(8) s.

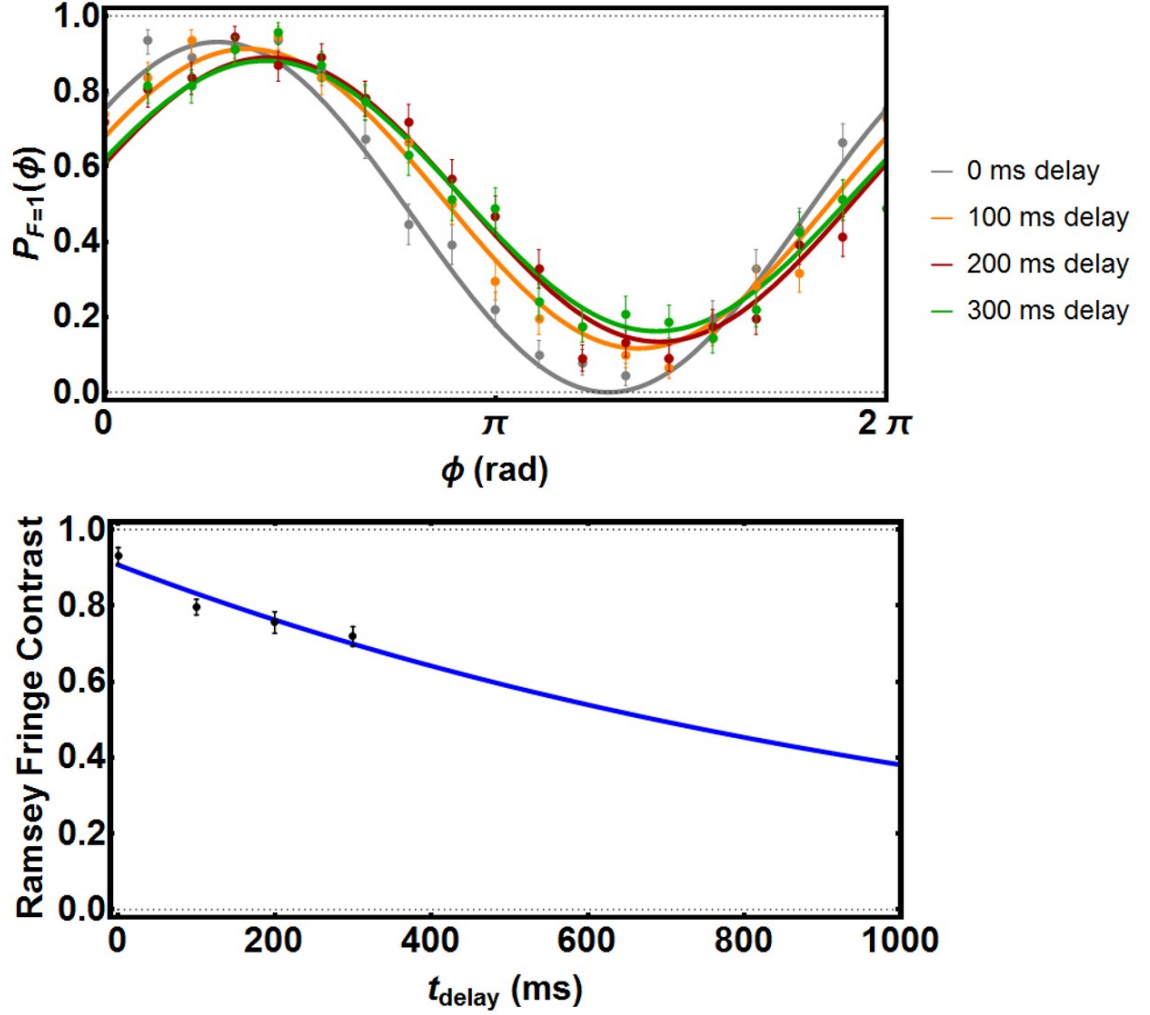


Fig. 5.26 (Top) Result of a Ramsey T_2 experiment on the $|0\rangle \leftrightarrow |D'\rangle$ transition. The grey, orange, red and green data points each correspond to a different delay time t_{delay} as indicated on the legend. The corresponding lines are from a fitted function described by Eq. 5.4 with the fringe contrast a , population offset p_{off} and phase offset ϕ_{off} set as free parameters. (Bottom) Fitted Ramsey fringe contrast of the four delay times from the data in the top graph, where error bars are the standard errors extracted from the four fits. The blue line is an exponential decay fitted to the four data points, giving a T_2 time of 1.15(3) s.

The states $|0\rangle$ and $|D'\rangle$ are insensitive to first order magnetic field fluctuations (Sec. 2.2.4). This may suggest that large, slowly drifting magnetic field fluctuations from the coils (like mentioned in Sec. 5.4.2 for the clock transition) are likely the main culprit for dephasing of the states.

Unlike the microwave dressed states, dressing field Rabi frequency fluctuations are less prevalent in the RF dressed state system, this may be attributing to the discrepancy in field combining methods for the RF and microwave fields (Sec. 4.5.2 and 4.5.3). It is expected that this is the reason for the improvement on coherence time in the RF dressed

state system because it is the only variable that has changed in the experimental setup, this is also discussed in Sec. 5.5.3. Though this needs a more thorough analysis involving a real time analysis of the field frequencies, this can be done with a VNA.

It was initially expected that the RF dressed states would exhibit lower coherence times due to the smaller dressing field Rabi frequencies the system is limited to. This is due to the close transition frequency gap between $|0'\rangle \leftrightarrow |+1\rangle$ and $|0'\rangle \leftrightarrow |-1\rangle$ (see Sec. 2.2.4 for more details). Because of the closer dressed state frequency gap $\Omega_{rf}/\sqrt{2} < \Omega_{\mu w}\sqrt{2}$ it is suspected that the RF dressed states would have a lower T_1 coherence time, but this still needs to be measured for confirmation. If the microwave dressed states have a higher T_1 time than the RF dressed states then it is likely that the discrepancy between the T_2 times in both dressed state systems is attributed either to signal mixing, amplification or delivery mechanisms for each system. Otherwise it would be beneficial to measure the T_2^* and T_2 coherence times for the microwave dressed states at a lower dressing field Rabi frequency comparable to the RF dressed states Rabi frequency $\Omega_{rf}/\sqrt{2} \approx 2\pi \times 3.59$ kHz. This would clarify if there is just a larger magnetic field noise amplitude at the $\Omega_{\mu w}/\sqrt{2} \approx 2\pi \times 18.933$ kHz frequency for the microwave dressed states.

5.7 Dressed state system magnetometer

5.7.1 Magnetic field resolution and sensitivity results

Like mentioned in Sec. 5.5.2 and Sec. 5.6.2, Rabi oscillations can be used to deconstruct information about the magnetic field being sensed. This section will focus on what information can be taken from a Rabi oscillation when viewed as a measurement of a magnetic field driving a two-level system. The results are for a magnetic field with a fixed frequency and amplitude. Both the sensitivity (Eq. 2.40) and smallest magnetic field that can be discerned (Eq. 2.35) improve by increasing the length of the Rabi oscillation to either the half the T_2 time or the T_2 time (Fig. 2.14). Rabi oscillations approaching the optimal experimental times were not conducted during this thesis due to time constraints and the heating induced on the ion (described in Sec. 3.3.3) causing the ion to be ejected from the trap too frequently for experiments to be conducted at experiments times roughly greater than $t > 300$ ms. The only exception to this was the Ramsey data taken in Fig. 5.14 where datasets taken from running the experiment on different ions were stitched together to attain the data shown. The longest Rabi oscillations recorded for the RF field sensing and microwave field sensing are shown in figures 5.27 and 5.28 respectively.

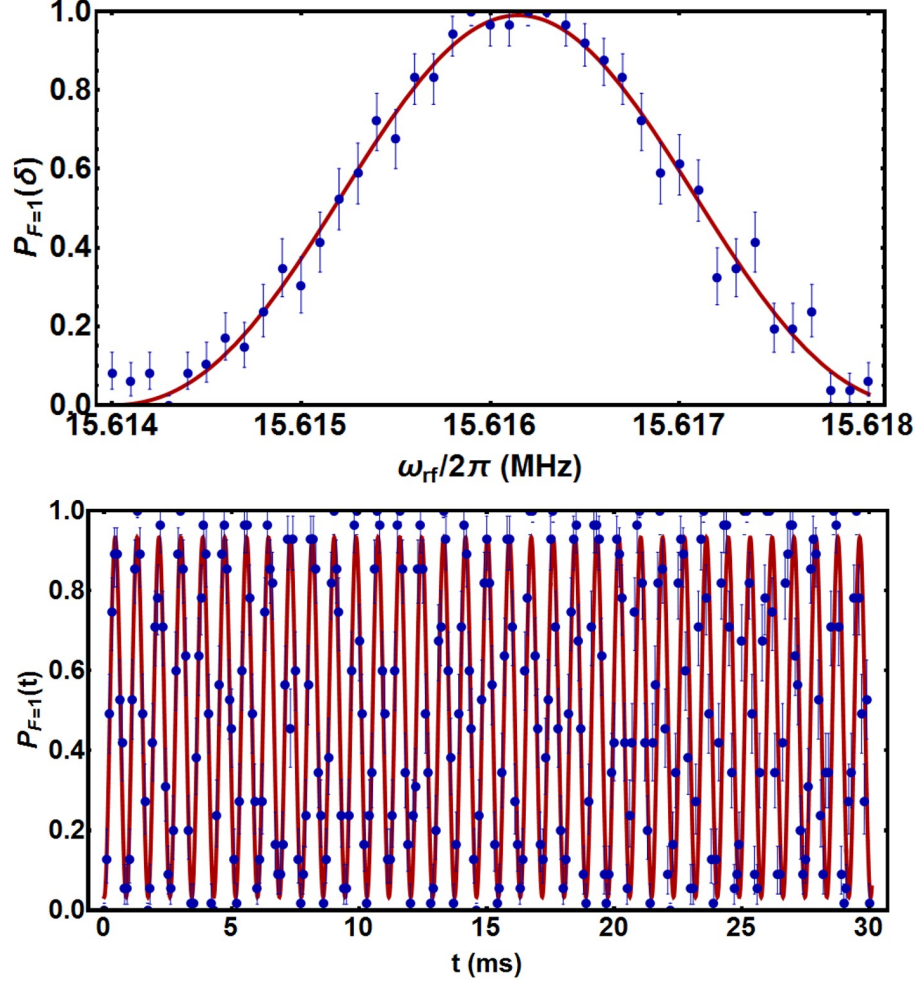


Fig. 5.27 Population in $F=1$ for a microwave dressed state frequency scan (top) and Rabi oscillation (bottom) on the $|0'\rangle \leftrightarrow |D\rangle$ transition at a frequency of $\omega_p/2\pi = 15.6161$ MHz. (Top) The π time of the applied RF field is $t_\pi = 429.36 \mu\text{s}$, each data point consists of 50 repetitions, the red line is a fitted function described by Eq. 5.2 where $\omega = \omega_{rf}$, with individual contrasts A and transition frequencies ω_p set as free parameters. (Bottom) Each data point consists of 50 repetitions, the red line is a fitted function described by Eq. 5.3, with the contrast A and Rabi frequency $\Omega = \Omega'_{RF}$ of the transition set as free parameters. The fitted function for the Rabi oscillation gives a Rabi frequency of $\Omega'_{RF}/2\pi = 1.165$ kHz which corresponds to a magnetic field amplitude of $B = 1.2 \times 10^{-7}$ T (Eq. 2.43).

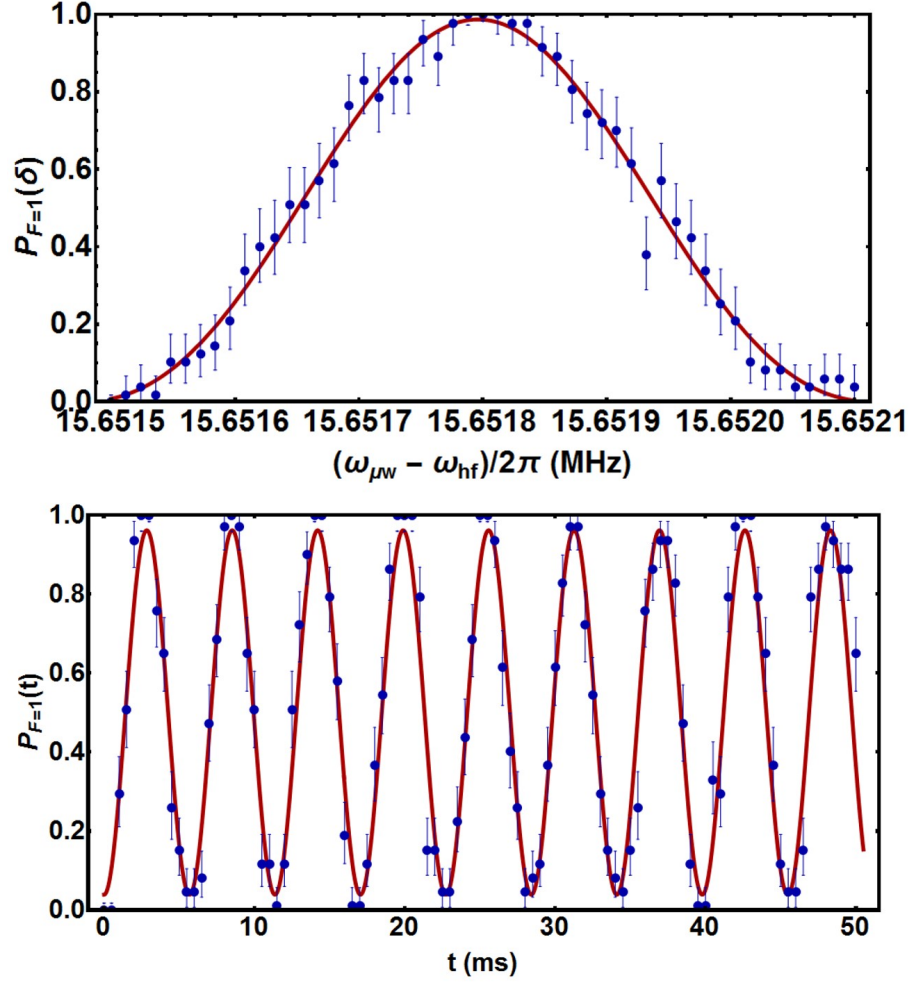


Fig. 5.28 Population in $F=1$ for a RF dressed state frequency scan (top) and Rabi oscillation (bottom) on the $|0\rangle \leftrightarrow |D'\rangle$ transition at a frequency of $(\omega_{\mu w} - \omega_{hf})/2\pi = 15.6518$ MHz. (Top) The π time of the applied RF field is $t_\pi = 2841.72 \mu\text{s}$, each data point consists of 50 repetitions, the red line is a fitted function described by Eq. 5.2 where $\omega = \omega_{\mu w}$, with individual contrasts A and transition frequencies ω_p set as free parameters. (Bottom) Each data point consists of 50 repetitions, the red line is a fitted function described by Eq. 5.3, with the contrast A and Rabi frequency $\Omega = \Omega'_{MW}$ of the transition set as free parameters. The fitted function for the Rabi oscillation gives a Rabi frequency of $\Omega'_{MW}/2\pi = 0.176$ kHz which corresponds to a magnetic field amplitude of $B = 1.2 \times 10^{-8}$ T (Eq. 2.43).

12.6584639

From the population errors and the derivative of the fitted function in Fig. 5.27 and Fig. 5.28, the minimal change in Rabi frequency that can be discerned from a population measurement is calculated using Eq. 2.39. This is then converted into the minimal magnetic field that can be discerned using Eq. 2.43. Results for the Rabi frequency resolution $\delta\Omega'_S = \{\delta\Omega'_{RF}, \delta\Omega'_{MW}\}$ for RF and microwave sensing is shown in figures 5.29 and 5.30.

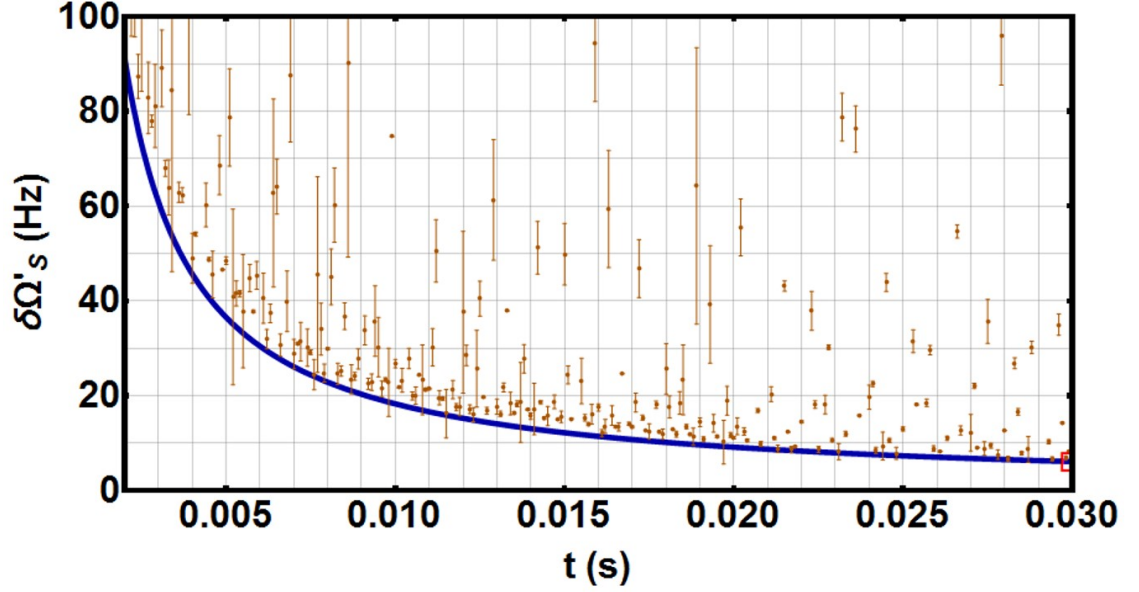


Fig. 5.29 Rabi frequency resolution $\delta\Omega'_s = \delta\Omega'_{RF}$ for the RF magnetic field sensing result shown in Fig. 5.27 where each data point in the Rabi oscillation with its associated error corresponds to a data point on this graph. The blue line is the minimal change in Ω'_s that is theoretically achievable, given by Eq. 2.39, the orange data points each represent the minimal change in Ω'_s that is attained by putting the values for the fitted equation and population measurement errors into Eq. 2.35. The best measurement (red square) in this experiment is attained at a measurement time of $t = 0.03$ s and is $\delta\Omega'_{RF} = 6.1$ Hz which corresponds to a minimal change in magnetic field $\delta B = 9.9 \times 10^{-11}$ T, where the errors are systematic errors due to the asymmetry of the population measurement errors as described in Appendix D.

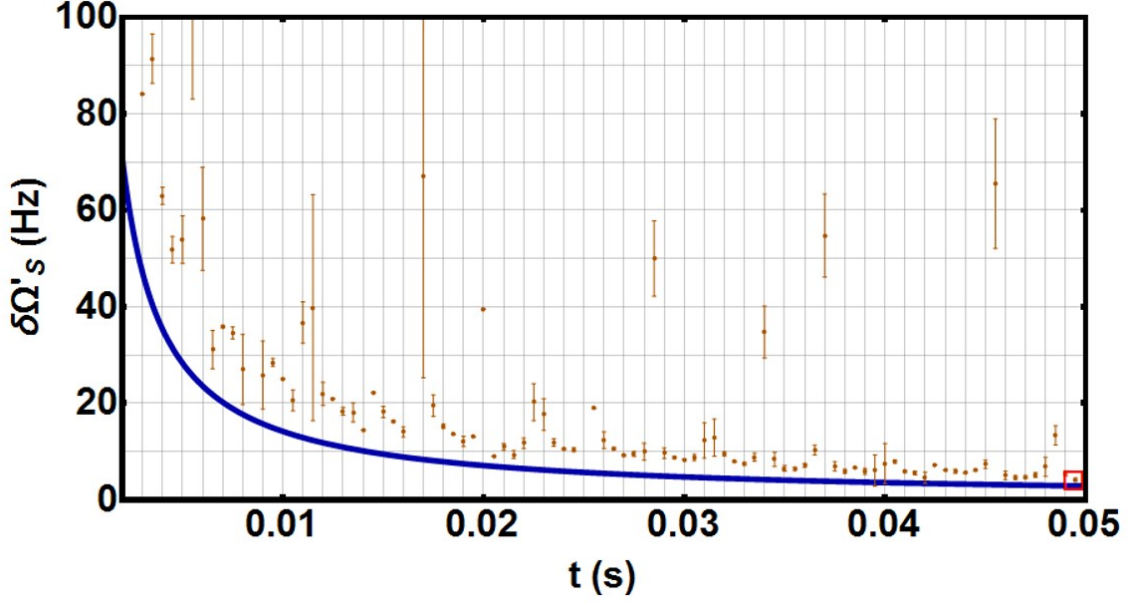


Fig. 5.30 Rabi frequency resolution $\delta\Omega'_S = \delta\Omega'_{MW}$ for the microwave magnetic field sensing result shown in Fig. 5.28 where each data point in the Rabi oscillation with its associated error corresponds to a data point on this graph. The blue line is the minimal change in Ω'_S that is theoretically attainable, which is given by Eq. 2.39. The orange data points each represent the minimal change in Ω'_S that is attained by putting the values for the fitted equation and population measurement errors into Eq. 2.35. The best measurement (red square) in this experiment is attained at a measurement time of $t = 0.0495$ s and is $\delta\Omega'_{MW} = 4.1$ Hz which corresponds to a minimal change in magnetic field $\delta B = 6.6 \times 10^{-11}$ T, where the errors are systematic errors due to the asymmetry of the population measurement errors as described in Appendix D.

The magnetic fields measured in figures 5.27 and 5.28 are converted into their associated sensitivities S by inserting the population measurement errors, derivative of the fitted Rabi function and experimental times into Eq. 2.35 to attain Ω'_S , from which the result is put into Eq. 2.40. Results for RF and microwave magnetic field sensing is shown in figures 5.31 and 5.32. Because the additional time for laser cooling, state preparation and state detection is larger than the experimental time $T_{add} > t$ in these results, it can be seen that the sensitivity of this measurement does not fit closely to the quantum limit sensitivity (Eq. 2.42). However as the experiment time increases, the negative effects on the sensitivity from T_{add} will diminish.

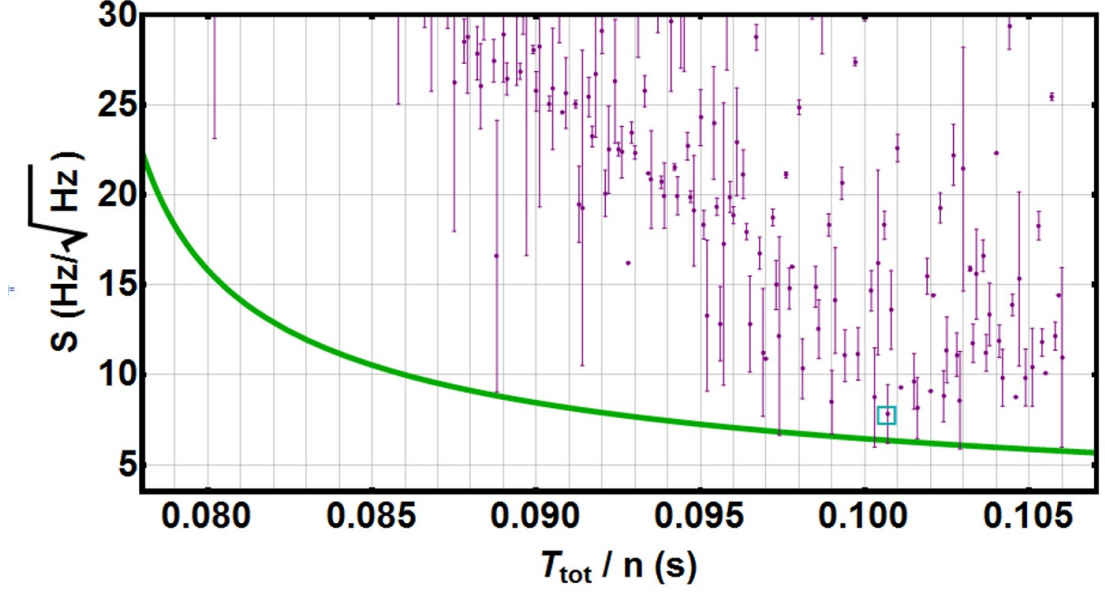


Fig. 5.31 Sensitivity graph for the RF magnetic field sensing result shown in Fig. 5.27 where each data point in the Rabi oscillation with its associated error corresponds to a data point on this graph. The green line is the quantum limit sensitivity given by Eq. 2.42. The purple data points each represent a sensitivity value that is attained by putting the values for the fitted equation population measurement errors and experimental times into Eq. 2.40 where the number of runs per measurement is $n = 30$ and the added time for cooling, state preparation and state detection is $T_{add} = 76$ ms. The best measurement (cyan square) in this experiment is attained at a measurement time of $T_{tot}/n = 0.1007$ s and is $S = 7.8$ Hz/ $\sqrt{\text{Hz}}$ which corresponds to a magnetic field sensitivity of $S_B = 125.9$ pT/ $\sqrt{\text{Hz}}$, where the errors are systematic errors due to the asymmetry of the population measurement errors as described in Appendix D.

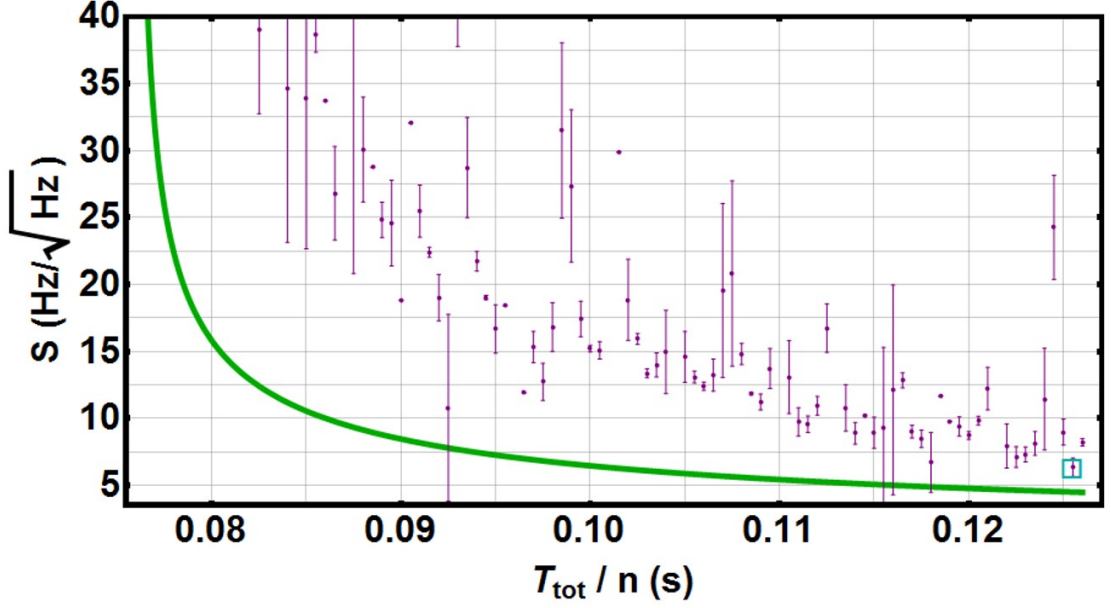


Fig. 5.32 Sensitivity graph for the microwave magnetic field sensing result shown in Fig. 5.28 where each data point in the Rabi oscillation with its associated error corresponds to a data point on this graph. The green line is the quantum limit sensitivity given by Eq. 2.42. The purple data points each represent a sensitivity value that is attained by putting the values for the fitted equation population measurement errors and experimental times into Eq. 2.40 where the number of runs per measurement is $n = 50$ and the added time for cooling, state preparation and state detection is $T_{add} = 76$ ms. The best measurement (cyan square) in this experiment is attained at a measurement time of $T_{tot}/n = 0.1255$ s and is $S = 6.3$ Hz/ $\sqrt{\text{Hz}}$ which corresponds to a magnetic field sensitivity of $S_B = 102.1$ pT/ $\sqrt{\text{Hz}}$, where the errors are systematic errors due to the asymmetry of the population measurement errors as described in Appendix D.

5.7.2 Magnetometer results and theoretical limits comparison

The true potential for this magnetometer scheme has not yet been fully realised, RF and microwave field sensing has only been performed for a narrow band of frequencies, and the magnetic field resolution δB and magnetic field sensitivity S_B results have only been performed on short experiment times $t < T_2$ in sections 5.7.1.

With the measured T_2 times for both setups recorded in sections 5.5.3 and 5.6.3, the potential of this trapped ion magnetometer system can be understood by using Eq. 2.39 and Eq. 2.43 for a theoretical estimation of δB at an experiment time of $t = T_2$, and a theoretical estimation of S and S_B by using Eq. 2.41 and Eq. 2.44 at an experiment time of $t = T_2/2$. The values measured and theoretical estimations can be seen for comparison in Table. 5.1.

	RF field sensing		Microwave field sensing	
	Measured	T_2 Theoretical	Measured	T_2 Theoretical
T_{add} (ms)	76		76	
n	30		50	
T_2 (s)	0.64		1.15	
$\delta\Omega'_S$ (Hz)	6.2	0.8	4.1	0.3
δB (pT)	99.0	12.4	65.9	5.4
S (Hz/ $\sqrt{\text{Hz}}$)	7.8	3.6	6.3	2.6
S_B (pT/ $\sqrt{\text{Hz}}$)	125.9	57.5	102.1	42.1

Table 5.1 Measured and theoretical values for all metrics in which this magnetometer can be measured in regards to magnetic field amplitude, errors on the measured values are systematic errors.

Though the RF sensitivity results for the single ion case on this experiment are not as competitive in terms of sensitivity as other quantum magnetometers outlined in Sec. 1.2, there are numerous improvements that can be made on this system. The results in table 5.1 are just preliminary results, and it is likely that the T_2 theoretical limits could be approached in the near future. Also, utilizing a multi-ion system will give improvements on the sensitivity values as described in Sec. 2.2.6. There are numerous advantages for trapped ions that can also be demonstrated, including spacial resolution, high levels of frequency tuneability, noise shielding from using the dressed states, and vector field sensing, all of which are discussed in Sec. 1.3. A table comparing the current state of the art quantum magnetometers with the system demonstrated can be seen in table 5.2.

	Sensitivity	Frequency
Trapped ion RF (demonstrator)	125.9 pT/ $\sqrt{\text{Hz}}$	16 MHz
Trapped ion MW (demonstrator)	102.1 pT/ $\sqrt{\text{Hz}}$	12.66 GHz
Trapped ion RF [34]	4.6 pT/ $\sqrt{\text{Hz}}$	14 MHz
NV center RF [16]	38 nT/ $\sqrt{\text{Hz}}$	1 MHz
NV center MW [12]	10 nT/ $\sqrt{\text{Hz}}$	2.88 GHz
SERF RF [22]	0.24 fT/ $\sqrt{\text{Hz}}$	0.423 MHz
SERF MW [23]	1 $\mu\text{T}/\sqrt{\text{Hz}}$	18 GHz
SQUID RF [30]	0.08 fT/ $\sqrt{\text{Hz}}$	0.425 MHz

Table 5.2 Sensitivity for a given frequency comparison between the current state of the art quantum magnetometers. It should be noted that each experiment comes with its own caveats specific only to that experiment. Discussion on some of these caveats are highlighted on Sec. 1.2.

Probably the most notable result from table 5.2 is the microwave field sensitivity value

of $102.054 \text{ pT}/\sqrt{\text{Hz}}$, which is an extremely good result when compared to other microwave quantum magnetometers that usually struggle to attain sensitivities better than $\text{nT}/\sqrt{\text{Hz}}$ [12, 23]. The tuneability of this is limited to a tuneable range frequencies around the clock microwave transition frequency of $\approx 12.64 \text{ GHz}$. Due to the long T_2 coherence time of the system and the scaling of the sensitivity $S \propto 1/\sqrt{T_2}$ with coherence time, it is suspected that sensitivities of $\text{pT}/\sqrt{\text{Hz}}$ could be maintained for large first order Zeeman shifts.

With more work, it is believed that this magnetometer will boast higher sensitivities for a wide range of frequencies. To demonstrate this, high values for T_2 measurements on both RF and microwave magnetic field sensing at different Zeeman splittings need to be demonstrated. Consistently high $\text{pT}/\sqrt{\text{Hz}}$ sensitivity across a wide range of RF and microwave frequencies with a very small spatial resolution is something other quantum magnetometers cannot attain as easily (Sec. 1.3). Further work from this would involve using n_i ion systems to improve sensitivity as described in Sec. 2.2.6, followed by application specific demonstrations (Sec. 1.4).

6 Towards a portable ion trap magnetometer technologies

Creating a portable ion trap magnetometer is the end goal of this entire project. For this reason, efforts to develop miniaturised technologies have been made. Contextually, portable means a device that can be battery powered and carried by a single person, for the applications outlined in Sec. 1.4 this would be beneficial. This is quite an ambitious task as it involves not only the miniaturisation of all the components in Sec. 4, but also a drastic power reduction for all the components as the final magnetometer device would ideally be battery powered. This chapter outlines the concept for a portable ion trap magnetometer and the development of a portable RF resonator that could be used for the RF voltage for a Paul trap.

6.1 Portable ion trap magnetometer concept

This section goes over the concept design and considerations that should be considered when developing each of the miniaturised components. The concept for the portable trapped ion magnetometer is still in its infancy, though design considerations are currently being taken into account to meet the "Quantum Technologies Hub for Sensors and Metrology" plan for a portable magnetometer device [2]. The concept for a complete portable ion trap sensor can be seen in Fig. 6.1.

There are some major considerations to be taken into account when creating the portable device:

1. The device should be easy to use for non-physicists.
2. The device should be small and light enough to be carried by a single individual or drone.
3. The total power consumption should be kept to a minimum in order to prolong battery life.

Ease of use for non-physicists would become a consideration after ion trapping for the device is fully automated. This would require automation of the laser wavelength locking, loading of the trap with the required number of ions and all experimental procedures in Sec. 5 to be carried out sequentially and output only the necessary information for the user.

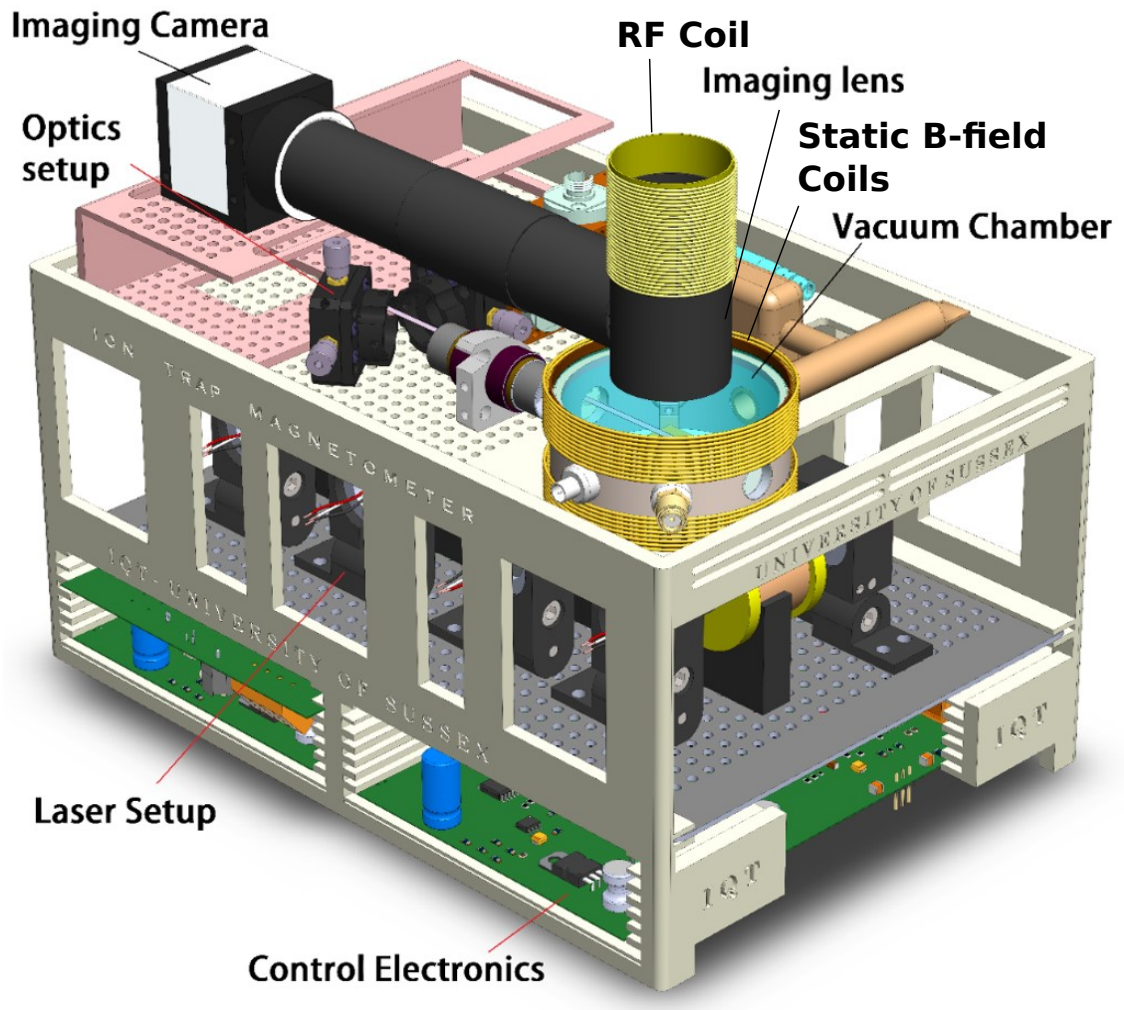


Fig. 6.1 Concept for a portable ion trap magnetometer. Predicted total dimensions are $30 \times 20 \times 20$ cm.

The concept for the design in Fig. 6.1 is a general design in which the total volume of space in which the device has been minimised. The design is a three layered structure in which the first layer contains all the required control electronics discussed in Sec. 4.6 and the components supplying the DC voltages for the axial ion confinement discussed in Sec. 4.3.3 would be located. Miniaturised computers are relatively easy and cheap to come by, so the miniaturisation of these components is of no concern. The second layer would house laser setup discussed in Sec. 4.2; these would be overlapped and coupled to the top layer. The top layer would house the resonator part of the trap RF supply as discussed in Sec. 4.3.1 (not shown in Fig. 6.1), the vacuum system (Sec. 4.1), the static B-field coils (Sec. 4.5.1), the RF and microwave radiation supplies (Sec. 4.5.2 and 4.5.3, microwave radiation supply not shown in Fig. 6.1) and the collection optics described in Sec. 4.4.

The power consumption and size of the device can be minimised by a case by case analysis of each component. To this date efforts to miniaturise the trapping voltage RF supply have been made; this is discussed in the next section.

6.2 Miniaturised RF resonator circuit

This section focuses on the development of a miniaturised, battery powered RF resonator, analogous to the table top resonator in Sec. 4.3.1. An RF circuit used for radial confinement of ions in Paul traps can be reduced to 6 components:

1. Power supply
2. Signal generator
3. RF amplifier
4. Transformer
5. Feedthrough on vacuum system
6. Ion trap

Typically, the table top system has the mains as its power supply, a large signal generator and RF amplifier, a bulky helical can resonator as the RF transformer, a $50\ \Omega$ RF feedthrough and an ion trap; in our case a micro-fabricated Paul trap. The ion trap itself cannot be miniaturised further and a miniaturised vacuum system could host either a $50\ \Omega$ SMA feedthrough or a direct connection to the chip, in either case a resonant circuit could still be developed. The challenge lies in miniaturising items 1-4, while being capable of producing large enough RF voltages to radially confine ions. The concept for the portable system is illustrated in Fig. 6.2 and consists of all the above components. The components consist of a lithium-ion battery connected to a voltage regulator circuit that generates all the required voltages, a crystal oscillator used for the frequency source, an operational amplifier (Op-amp) for the first RF amplification step, an auto-transformer for a secondary RF amplification and inductive component of the resonant circuit, a capacitive probe for reading the voltage across the chip and a capacitor PCB to represent an ion traps typical capacitance.

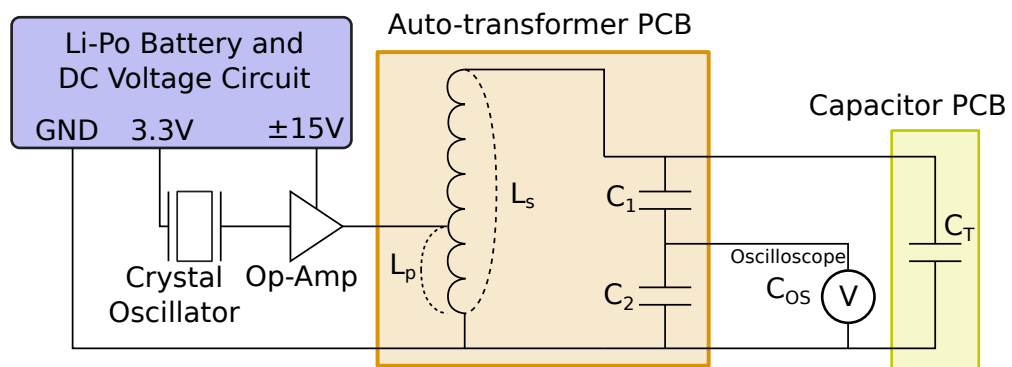


Fig. 6.2 An illustration of the portable RF device test circuit.

The components in Fig: 6.2 have been chosen to not only miniaturise the total system but also to allow the majority of the system fit onto one single printed circuit board (PCB). The reasons for choosing these components will become apparent in the next section.

6.2.1 miniaturised RF circuit design process

For this system, not all components have been tested together yet. The currently tested components consist of the voltage supply, op-amp circuit and the RF resonant circuit. The voltage supply has not yet been tested with a battery and the op-amp has not been tested with a crystal oscillator. This section will go over the design process of the developed components. Note that these components still need further optimisation if this device was to be used for a portable ion trap experiment, this is discussed in the following sections.

Voltage supply and voltage dependent components

If a battery was to be developed for this system, power for the crystal oscillator and Op-amp could be supplied from multiple Lithium-polymer (Li-po) battery cells stacked in series. Li-po cells are typically 3.7 V, making the maximum number of cells useful for this application 10 as the operational amplifier⁶⁷ has a maximum rail voltage of 40 V. Note that a protection circuit should be implemented in the series of Li-po cells to avoid over-discharging.

When trapping ions, it is ideal for the RF signal to be referenced to ground and have no positive or negative offset as this will make the a stability parameter not equal to zero (see Sec. 3.1). For this reason it is desirable to create a virtual ground for the Li-po battery so that positive and negative DC potentials can be pulled by the op-amp rails and keep the RF signal centred around a virtual ground. The virtual ground would be connected to the common ground of the entire system to ensure this. It is also desirable to create a voltage output for the crystal oscillator, as crystal oscillators typically have input voltages much lower than the supply rails of the op-amp. For this reason a circuit capable of creating virtual ground with appropriate op-amp voltages and a crystal oscillator voltage was designed and tested using a linear power supply in place of a Li-po battery, the circuit diagram used to achieve this can be seen in Fig. 6.3.

⁶⁷Analog Devices ADA4870

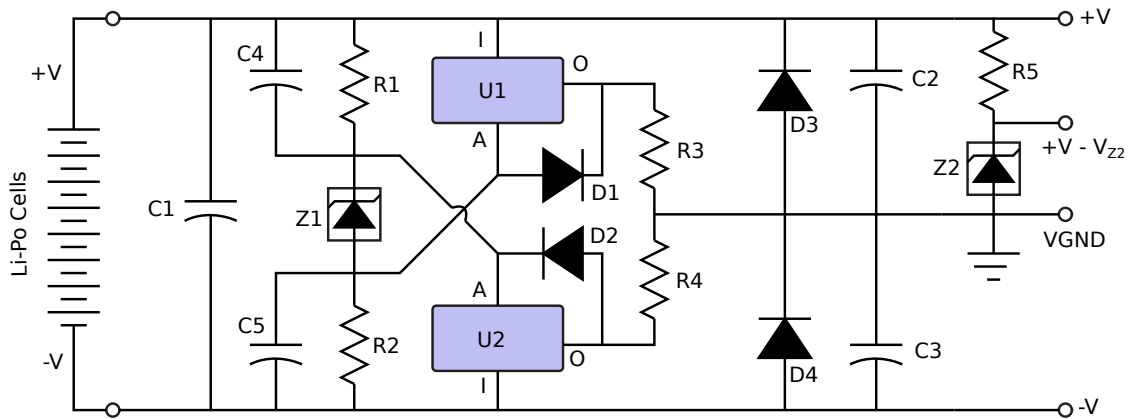


Fig. 6.3 Battery powered voltages sources for supplying the Op-amp and crystal oscillator.

The virtual ground can be adjusted by selection of resistors R1 and R2, this is due to the adjustable voltage regulators U1 (positive voltage regulator) and U2 (negative voltage regulator). The virtual ground is created by connecting the outputs of the two regulators together, each output is loaded with a small resistance, R3 and R4, to avoid the outputs of the regulators from supplying the output of the other. A zener diode Z1⁶⁸ compensates for the +1.25 V and -1.25 V internal references of the two regulators U1⁶⁹ and U2⁷⁰ respectively. Resistors R1 and R2 create a voltage divider that is connected to the adjust pins of the voltages regulators, by making the resistors equal values the voltage supply to the adjust pins of the regulators will be 1/2 of whatever the rail to rail voltage is (+V and -V). The circuit was designed for a rail to rail voltage of ± 15 V, to protect the regulators from damage a relatively high resistance of 6.81 k Ω ⁷¹ for R1 and R2 was selected. With this setup the regulators split the supply voltage from 0V and 30V to ± 15 V with a relatively stable virtual ground. The diodes D1 and D2 are to keep the adjust pin of the regulators held in place by keeping the voltage output at half of the rail to rail voltage. With help from Ph.D. student Anton Grounds the capacitors C1⁷², C2/C3⁷³ and C4/C5⁷⁴ were selected to smooth the DC voltage signal from the rails and the diodes D1 - D4⁷⁵ were implemented to protect the regulators from the capacitors discharging when the circuit is turned off.

A voltage supply for the crystal oscillator can be created from a simple zener diode circuit (Z2⁷⁶ and R5⁷⁷) to step the voltage of the positive rail +V down to the required

⁶⁸Texas Instruments LM336Z-2.5/NOPB

⁶⁹Texas Instruments LM317T/NOPB

⁷⁰Texas Instruments LM337T/NOPB

⁷¹Vishay CMF606K8100FHEB

⁷²Panasonic P/N EEU-FM1H471

⁷³Panasonic P/N EEU-FM1E102

⁷⁴Panasonic P/N EEU-FM1H220

⁷⁵Vishay 1N4002-E3/54

⁷⁶Microsemi 1N942

⁷⁷Vishay CW01050R00JE12HE

voltage of the crystal oscillator. Although a crystal oscillator wasn't tested with this circuit, the zener diode voltage ($V_{Z2} = 11.7$ V) was chosen to step the +15 V of the positive rail down to +3.3 V. This is a typical supply voltage for most crystals but can be changed by selecting the zener diode voltage to be a different value. The resistor R5 is used to limit the current across the zener diode to protect it from breaking down. Most zener diodes come with a maximum current value I_Z , the minimum resistance required from R5 can be calculated from $R5 = (+V - V_{Z2})/I_Z$. With a linear voltage supply, the circuit was tested for a high impedance load. With a voltage supply of 30 V across the +V rail, the internal ground of the supply to the -V rail, the outputs of the circuit for a 1 k Ω load was ± 15 V for the positive and negative rails (referenced to the virtual ground) and 3.3 V at the output for the crystal.

The op-amp ⁷⁸ was chosen for its high current, high RF bandwidth and high gain capabilities. The op-amp was tested with the virtual ground circuit using an evaluation board⁷⁹ with a high 1 k Ω load and a signal generator at the input of the amplifier. The op-amp was setup in a non-inverting configuration where the gain of the amplifier can be changed by selection of two resistors, optimal resistance values are outlined in [115]. During testing the op-amp was setup to give a voltage gain of 5, this is the configuration used for testing with the resonant circuit discussed in the next section.

Miniaturised resonant circuit

The resonant circuit part of the design was created on a single PCB for test purposes, the circuit uses a voltage probing system like the one described in Sec. 4.3.2 and is calibrated the same way. The PCB hosts the auto-transformer capacitive probe and ion trap capacitor proxy. This represents the transformer, feedthrough and micro-fabricated ion trap components of the resonant circuit. Many of the equations used in Sec. 4.3.1 can be used to represent the components in the resonant circuit discussed here.

To maximise the voltage gain of the resonant circuit, the input of the resonant circuit is matched to 50 Ω to avoid any power being reflected back into the amplifier as the test circuit has a 50 Ω SMA input. Reflected power could result in an overheated op-amp and reduction in resonant circuit voltage gain. This also helps to minimise the total power consumption of the resonator circuit as power being reflected back into the amplifier is wasted energy. A single coated copper wire with a diameter of 0.71 mm is wrapped around a toroidal core⁸⁰ to form the auto-transformer, one end of the coil is grounded, and the other connected to the connector for the micro-fabricated ion trap and capacitive divider probing system as shown in Fig. 6.2. The transformer material and toroidal geometry

⁷⁸Analog Devices ADA4870

⁷⁹Analog Devices ADA4870ARR-EBZ

⁸⁰Fair-Rite Material 68

was chosen for its high Q for RF frequencies when used as an inductor.

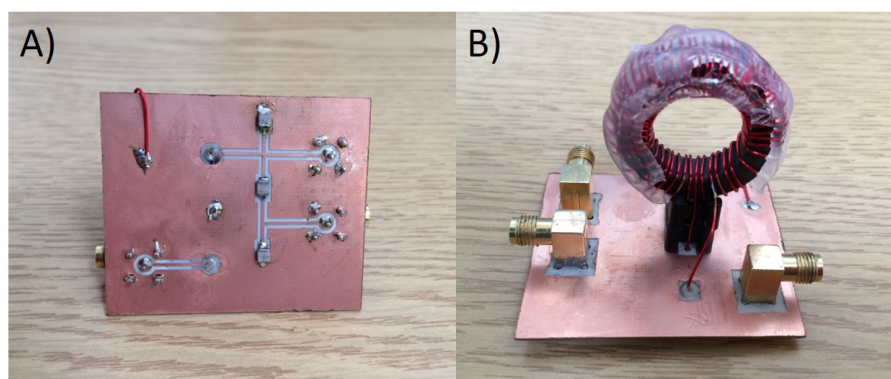


Fig. 6.4 A) Front PCB for toroidal test circuit, the capacitor at the top of the PCB is the chip proxy, the mid and bottom capacitors are the capacitive divider. The SMA on the left is the input, the two on the right are for calibration of the capacitive divider and readout of the voltage. B) The back side of the PCB, the toroidal auto-transformer can be seen, it was put on a stand to minimise magnetic properties of the PCB and covered in glue once the input impedance was closely matched to $50\ \Omega$ to stop the coil turns from moving.

To match the circuit to $50\ \Omega$, a pin used at the input for the resonant circuit is soldered to a position on the toroidal coil where the input impedance is $50\ \Omega$. This is done by connecting the input of the auto-transformer to a VNA⁸¹ and probe different positions on the coil until the S_{11} parameter impedance $Z = 50\ \Omega$, an example of this is shown in Fig. 6.5. The PCB circuit design can be seen in Fig. 6.4 and the corresponding s-parameters in Fig. 6.5 for a $20\ \text{pF}$ capacitor at the output of the auto-transformer and a $16\ \text{pF}$ capacitance from the oscilloscope for the capacitive probe. Note that the coil around the toroid can be moved closer to, or further away from the input probe to tune the input impedance of the circuit. This changes the coupling between the primary and secondary coils of the auto-transformer, thus, changes the inductance of the transformer; which is analogous to changing the coupling between the primary and secondary coils of the helical can resonator in Sec. 4.3.1.

⁸¹Rohde and Schwartz ZNB Vector Network Analyzer

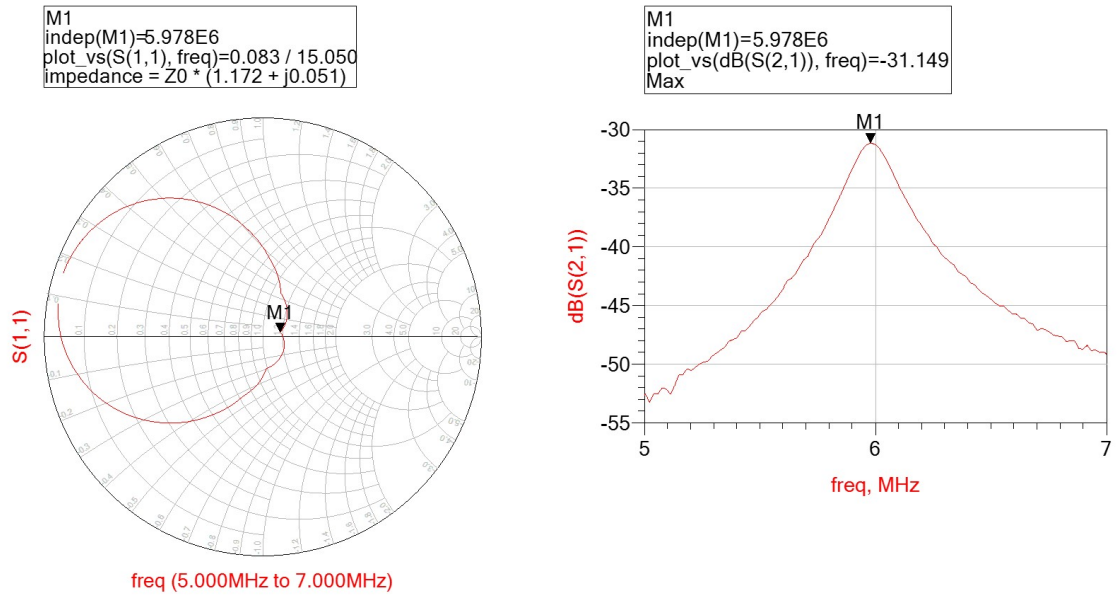


Fig. 6.5 S_{11} and S_{21} parameters for test resonant circuit using the larger toroid and a 20 pF load, The Q of the resonance circuit is ≈ 34 . Notice that the maximum output reflection coefficient (S_{21} is at the same frequency as the input reflection coefficient when closest to 50Ω , that the maximum gain of the circuit will be when the input is matched as closely to 50Ω as possible.

The toroidal geometry has a large influence on the voltage gain and resonant frequency of the circuit. This makes sense when looking at a typical equation for the resonant frequency of a LC resonant circuit $\omega = 1/\sqrt{LC}$. Generally a smaller toroid with less turns will have a lower inductance, resulting in a higher resonant frequency. Two toroid shapes were tested, one large $29.95 \times 19.45 \times 7.50$ mm and one small $12.70 \times 7.90 \times 6.35$ mm (outer radius, inner radius and height respectively). The large toroid was tested first, images of the toroid can be seen in Fig: 6.4 and s-parameters of it matched to $\approx 50 \Omega$ can be seen in Fig: 6.5. From the s-parameters we can see that the circuit resonates at 5.235 MHz (20 pF chip capacitance), though it is possible to trap ions at this frequency it is not ideal as it is quite close to the motional frequency of the ions in the radial direction (see Sec. 3.3.1). Increasing this value can be done by reducing the number of turns on the toroid coil or using a smaller toroidal core. It was observed that decreasing the number of turns only contributes to a slight increase in resonant frequency with minimal change in voltage gain, this can be seen in Table: 6.1.

Total Turns on Toroidal Coil	Voltage Gain	Resonant Frequency $\Omega/2\pi$ (MHz)
60	15.0	5.235
52	15.0	5.534
45	15.0	6.072
40	15.0	6.908

Table 6.1 Large toroid voltage gains and resonant frequencies for different total turns on the toroidal auto-transformer coil. Each time the input to the resonant circuit is matched as closely as possible to 50Ω by probing the coil at different positions, the input voltage for each test was 1V. For each test the toroid was connected to a chip capacitor 20 pF and a capacitive divider described in Sec. 4.3.2.

When testing the small toroid, the resonant frequencies achieved were much higher than the large toroid. Two small toroid auto-transformers with a different number of total turns were tested as seen in Table: 6.2. s-parameters for each test can be seen in Fig: 6.7 and Fig: 6.6. The capacitance of capacitor used to represent the ion trap was also varied to help understand how much of an effect this has on the resonant frequency of the circuit. The change that this has on the resonant frequency is minimal, which would make selecting a crystal oscillator for a portable RF supply easier.

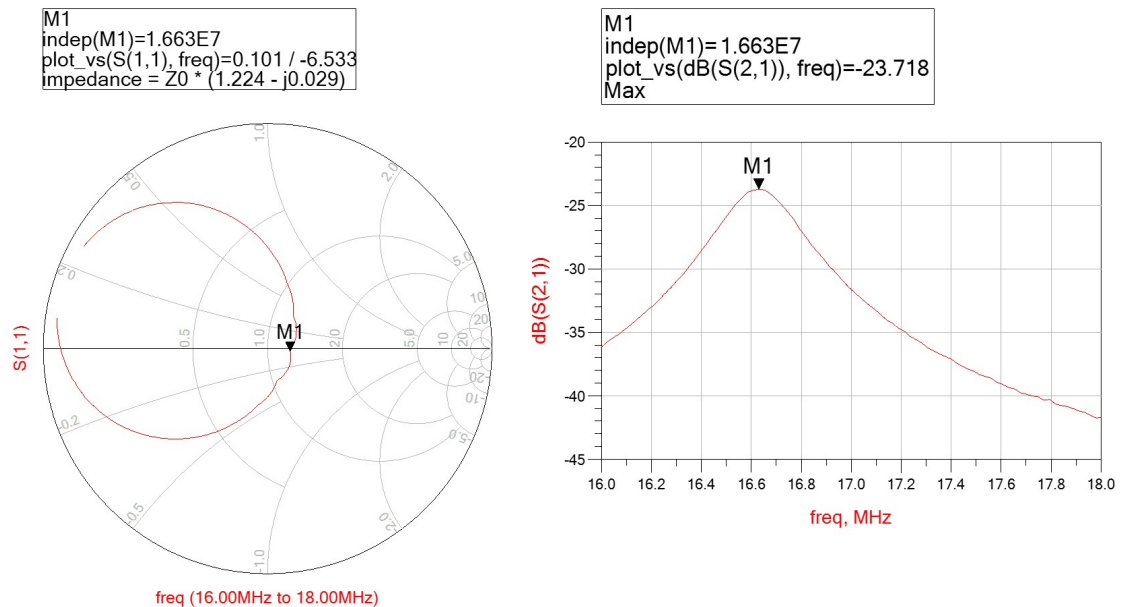


Fig. 6.6 S-parameters for small toroid with 19 turns and a 29 pF load. The Q of the resonant circuit is ≈ 52 .

Total Turns on Toroidal Coil	Chip capacitance (pF)	Voltage Gain	Resonant Frequency $\Omega/2\pi$ (MHz)	Q factor
29	20	16.8	12.67	67
29	29	17.1	12.65	70
19	20	13.1	16.75	51
19	29	13.5	16.63	52

Table 6.2 Small toroid voltage gains and resonant frequencies for different total turns on the toroidal auto-transformer coil. Each time the input to the resonant circuit is matched to 50Ω by probing the coil at different positions, the input voltage for each test was 1 V. For each test the toroid was connected to a chip capacitor and a capacitive divider described in 4.3.2.

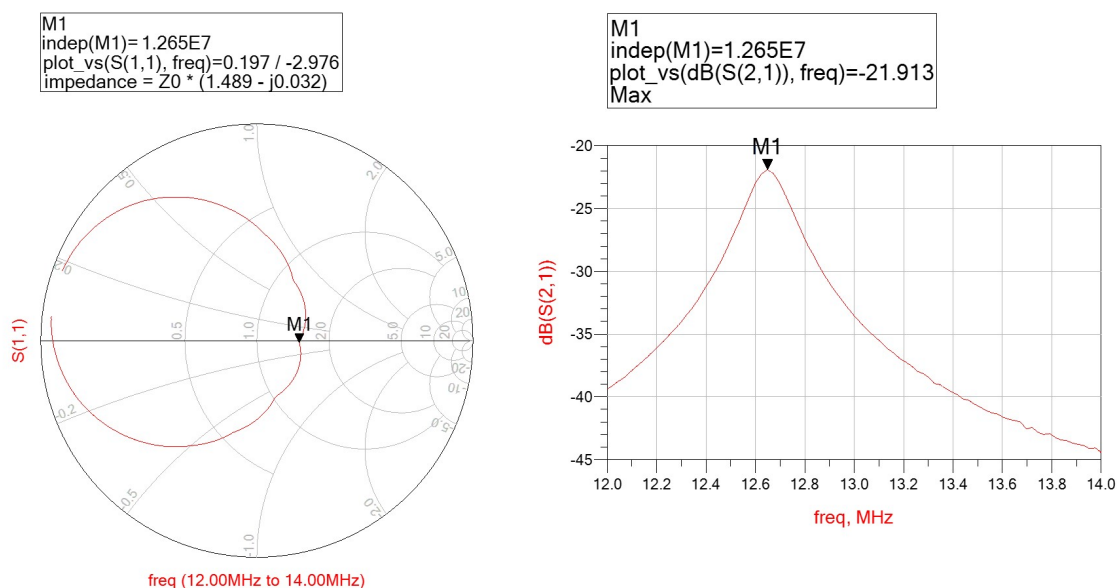


Fig. 6.7 S-parameters for small toroid with 29 turns and a 29 pF load. The Q of the resonant circuit is ≈ 70 .

From table 6.2 it is clear that a higher number of turns results in a much better voltage gain. This is likely because the transformer voltage gain is directly proportional to the ratio of primary and secondary impedances. A higher voltage gain is beneficial for ion traps, especially when power consumption of the entire device needs to be low. Unfortunately fewer turns would result in a preferable resonant frequency for ion traps, for this case though it is not too much of an issue as the resonant frequency of the circuit for both numbers of turns is significantly higher than the usual secular frequencies of the ions. There are significant improvements in the Q value of the higher turn, smaller toroidal structure; for the reasons mentioned in Sec. 4.3.1 this is beneficial for ion traps.

It appears that the smaller toroid with 29 turns is the best option for ion trapping applications as it provides the highest voltage gain and Q factor while maintaining a

trapping frequency far from the motional frequency of the ions. If higher frequencies are paramount, then less turns or an even smaller toroid can be used. From this the resonant circuit is tested for higher input voltages.

The gain of the autotransformer is likely to change at higher input voltages, this is due to the properties of the transformer core changing for higher magnetic fields. Typically, as the magnetic field induced on the transformer core doesn't scale linearly with the magnetic field flux density in the core, meaning that the voltage gain of the circuit would decrease for higher voltages. From Fig. 6.8 the core appears to be reaching its saturation point. This is where increases in induced magnetic field does not increase the magnetic flux density in the core. This is typically understood from the hysteresis loop of the transformer material. The maximum peak trap voltage V_T attained for an input voltage of 15 V is 114.9 V, this is lower than the ideal trapping voltages mentioned in Table 3.3 but could potentially still be sufficient for ion traps with ideal electrode geometries.

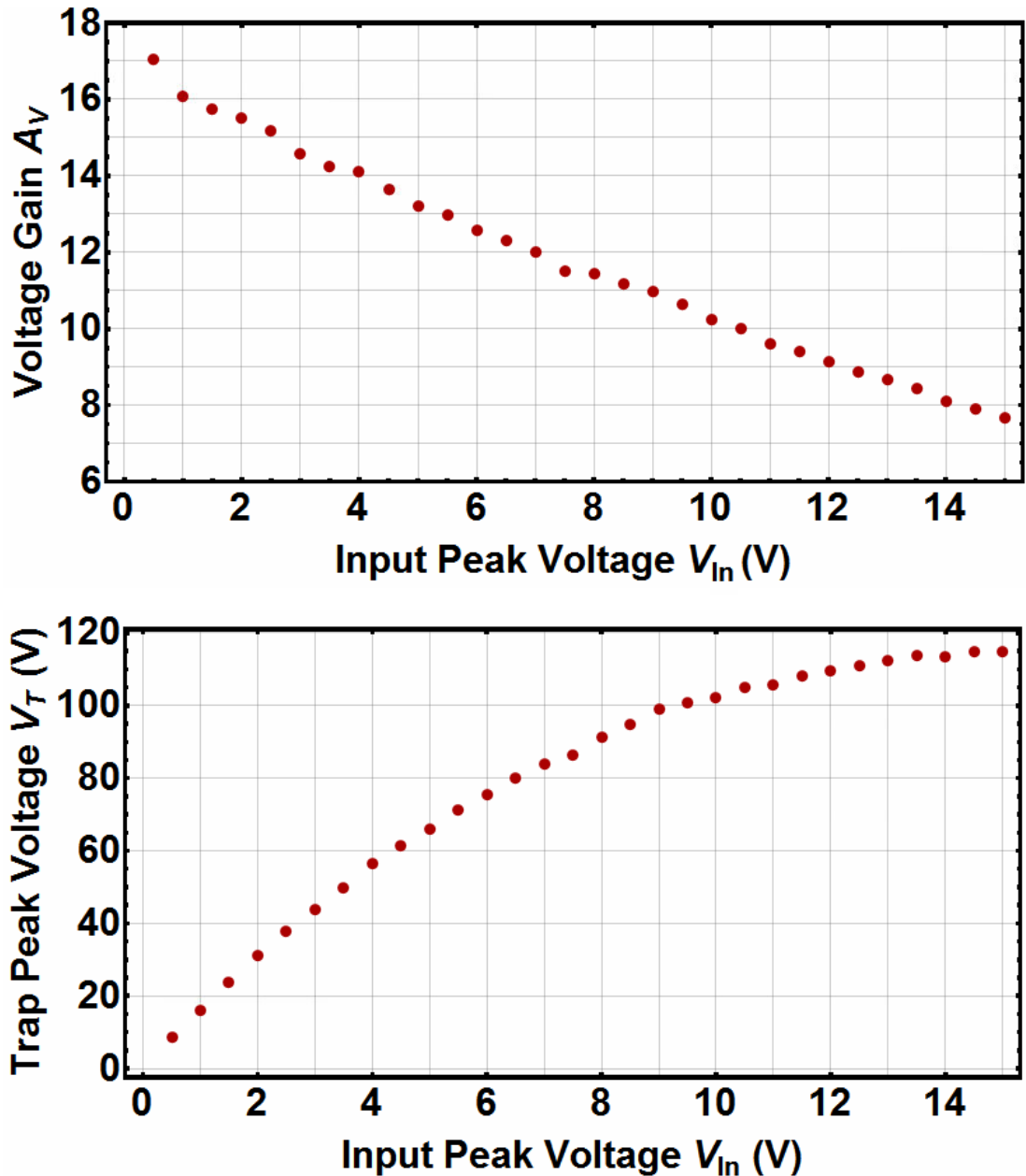


Fig. 6.8 (Top) Resonator circuit gain for different input voltages. (Bottom) Voltage measured in the resonant circuit for different input voltages. The input for the resonator is attached to a signal generator set at the circuit resonant frequency $\Omega/2\pi = 12.65$ MHz.

6.2.2 Testing of the developed components

Individual testing of the components mentioned in the previous section showed that they all work relatively well in isolation. When testing the developed components together a signal generator was used in place of the crystal oscillator to test the total gain of the circuit. Also, a linear power supply was used in place of the Li-po battery to test the power consumption of the circuit, A diagram of this can be seen in Fig. 6.9.

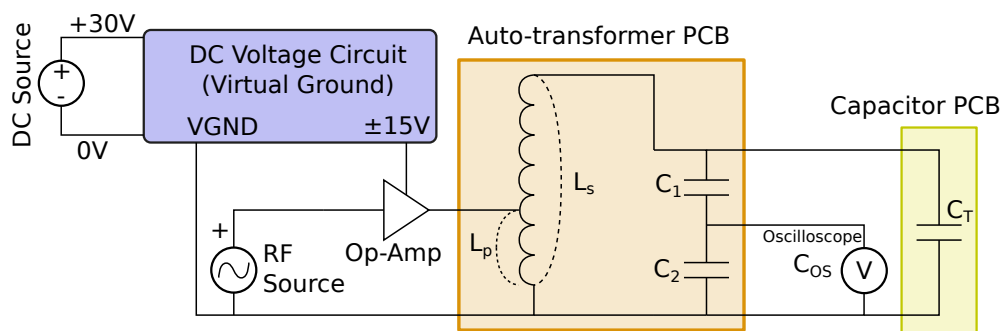


Fig. 6.9 Test circuit used for measuring power consumption of the portable RF supply and the potential voltages attainable by using the op-amp and auto-transformer together.

With the op-amp, non-inverting feedback loop resistors in a configuration that gives a voltage gain of $A_V = +5$, the total circuit gain and resonator circuit voltage can be seen in Fig. 6.10. The Voltage wasn't increased further due to the temperature shutdown of the op-amp being activated, meaning that the power dissipation within the op-amp exceeded its threshold automatically shutdown. The maximum trap peak voltage attained was $V_T = 74.9$ V. The total gain of the circuit matches well to the data recorded without the op-amp in Fig. 6.8, meaning that its likely that the transformer core would reach its saturation point at a similar voltage if the op-amp wasn't shutting down.

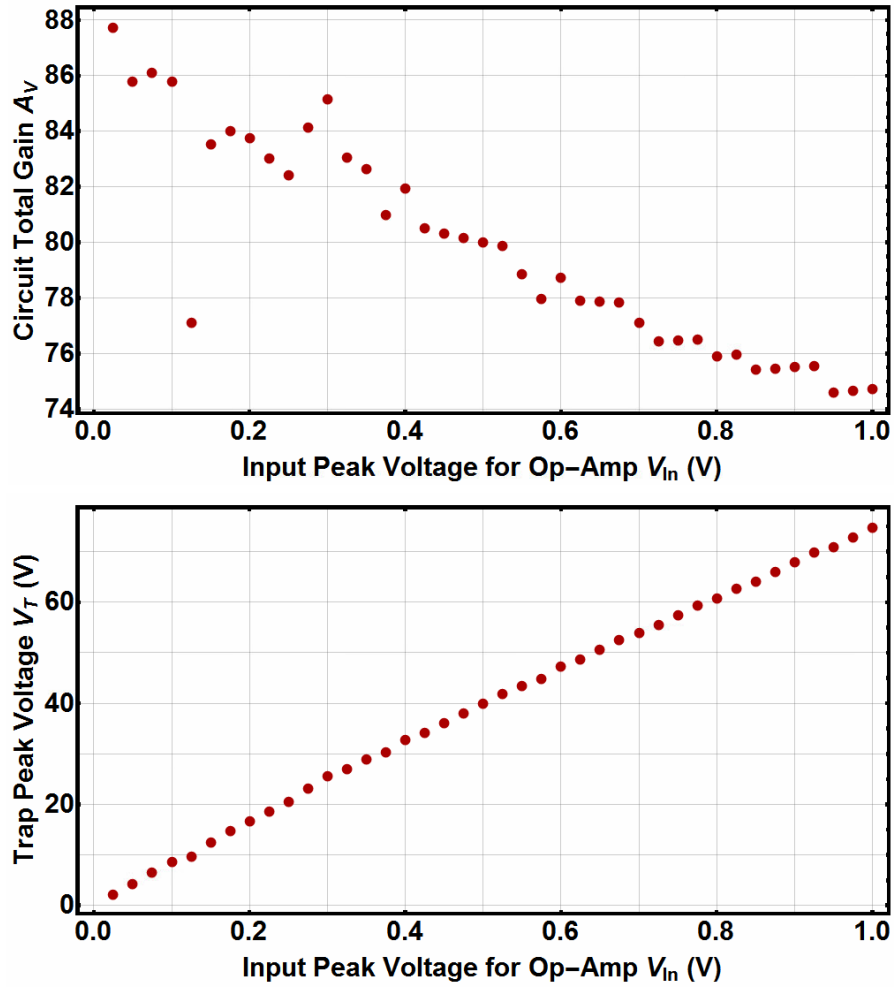


Fig. 6.10 (Top) Resonator circuit gain for different op-amp input voltages. (Bottom) Voltage measured in the resonant circuit for different op-amp input voltages. The input for the op-amp is attached to a signal generator set at the circuit resonant frequency $\Omega/2\pi = 12.65$ MHz.

It is also important to understand the power consumption of the device at different trapping voltages. This can be seen in Fig. 6.11 where the power consumption was calculated from the voltage and current pulled from the linear DC supply in Fig. 6.9. The power consumption of the RF source was not taken into account as it is being used as a proxy for the crystal oscillator; most crystal oscillators would have a very low power consumption relative to the power consumed by the op-amp as they typically consume μA currents and about 5 V max.

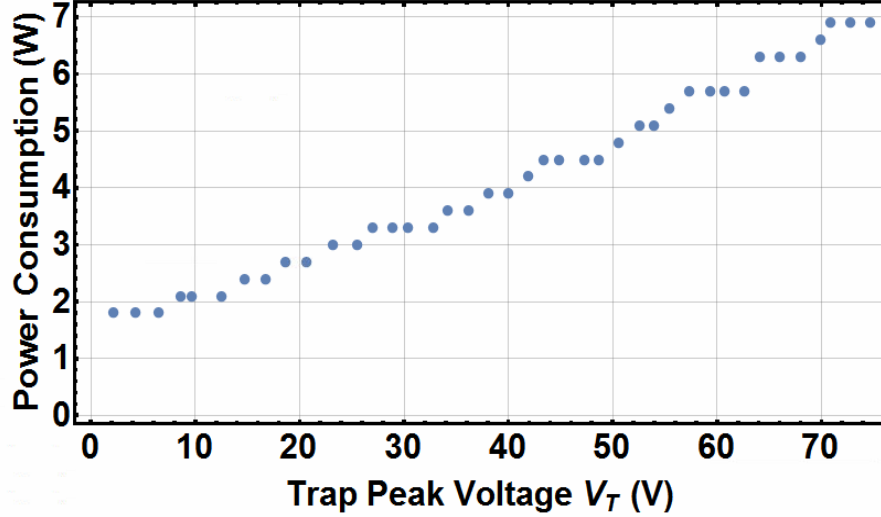


Fig. 6.11 Power consumption of the op-amp for different trap voltages, the DC rails for the op-amp are set to ± 15 V.

The power consumption is relatively high when compared to similar portable RF resonator technologies [116], potential improvements on the power efficiency of the resonator and options for increasing peak trap voltage are discussed in the next section.

6.2.3 Improving power efficiency of the portable RF generator

When the components were tested together the op-amp and resonant circuit could only attain a trap peak voltage of $V_T = 74.9$ V before the op-amp overheated. It is useful to understand why this is happening at such a low voltage input and how to mitigate this effect. It could be due to the mismatch of impedances between the op-amp source and the resonator load, this can cause power to be reflected back into the amplifier and is the likely cause of the excessive power dissipation being observed within the amp. Typically the power being reflected from mismatched sources Z_S and loads Z_L follows the equation

$$\Gamma = \frac{Z_L - Z_S}{Z_L + Z_S}, \quad (6.1)$$

where Γ is the reflection coefficient. For this case where the op-amp output impedance is $Z_S = 20 \Omega$ and the load impedance is $Z_L = 74.45 \Omega$, the reflection coefficient is 57.6, meaning that 57.6% of the power is being reflected back into the op-amp. From the op-amp data sheet, an equation for the average power being dissipated within the amp ($P_{AVG,SINE}$) is given as the sum of the power dissipated in the output stage of the amp plus the quiescent power minus the power being dissipated within the load, this can be modified by adding the power being reflected by the resonator load. The total power dissipated by the op-amp is then given by

$$P_{AVG,SINE} = (V_S \times I_q) + \left(\frac{2}{\pi} \times \frac{V_{CC} V_{peak}}{R_S} \right) + (\Gamma - 1) \left(\frac{V_{peak}^2}{2R_S} \right), \quad (6.2)$$

where V_S is the total supply voltage ($V_{CC} - V_{EE} = 30$ V), I_q is the quiescent current, V_{peak} is the peak voltage output of the op-amp, R_S is internal resistance of the op-amp and R_L is the real part of the load impedance. This gives a dissipated power of 5.62 W at the point in which the op-amp automatically shuts down. By matching these impedances ($\Gamma = 0$) the power dissipated in the op-amp would only decrease to 5.52 W, this is unlikely to improve the total power output of the op-amp as this is isn't a significant decrease in total power dissipation.

Upon further inspection of Eq. 6.2, a factor that could be reduced is the supply rail voltage as ± 15 V is much larger than the rail voltage required for an output peak voltage of 5 V. If the rail voltages were changed to ± 6 V then the total power dissipation for a matched load would reduce significantly. This would also result in a decreased power consumption. To optimise the rail voltage for the op-amp it is advised to use a linear power supply in place of the DC voltage circuit shown in Fig. 6.9 and to measure the output of the op-amp so that the RF signal isn't clipped. With this potential reduction in power dissipation, it is more likely that the saturation point of the transformer could be reached a much higher peak trap voltage.

6.2.4 Comparison with other portable RF resonator circuit

An alternative portable RF resonator that could be used for trapping ions has been developed by Sandia National Laboratories [116]. This system uses a simple LC resonant circuit has been used in combination with 12 CMOS inverters to generate peak trapping voltages of 250 V with a power dissipation of 900 mW at a comparable frequency of $\Omega/2\pi = 10.1$ MHz and on a small PCB of only a few cm^2 . When compared to the maximum voltage attained on the auto-transformer and the power dissipation of the op-amp this seems like a more preferable option for portable ion traps. Though auto-transformer system described here boasts a higher degree of tuneability in trap frequency, and the potential for higher trap voltages when optimised further.

Further investigation of potential amplifying stages in the setup mentioned here could result in a similar power dissipation, though a series of CMOS inverters may be the best option for an initial amplifying stage. An auto-transformer with a larger core or different ferrite material could also result in a higher maximum attainable trap voltage if the material doesn't reach its saturation point. The Q of the auto-transformer resonant circuit is also higher than the resonator described in [116] by > 10 . A hybrid in which CMOS inverters were used for the initial RF signal generation and the auto-transformer used for second stage amplification would likely be the best option. This would reduce the total size and power dissipation of the circuit while still attaining high Q values at higher frequencies.

7 Colclusion

7.1 Summary

The work presented in this thesis is part of the Ion Quantum Technology (IQT) groups efforts towards developing a miniaturised ion trap magnetometer as part of the UK National Quantum Technology Hub for Sensors and Metrology. The purpose of this thesis was to develop a table top magnetometer device that could be used to demonstrate novel magnetometry using a single ion. Additionally, work towards the development of a miniaturised ion trap magnetometer was conducted.

Initially, an understanding of the research problem was established. The metrics in which currently established quantum magnetometers measure their capabilities is key to understanding the potential of a trapped ion magnetometer. Current benchmarks for quantum magnetometers are discussed in order to understand the advantages and disadvantages a trapped ion magnetometer would comparatively have to other quantum magnetometers.

From this, the theoretical background for trapped ions was used to describe how an ion could be used as a magnetometer. Dressed state schemes comprised of the energy levels within the hyperfine ground state of $^{171}\text{Yb}^+$ ions were theorised in order to improve the sensitivity of the ion trap magnetometer by extending the T_2 coherence time. From this, a method for sensing radio-frequency (RF) magnetic fields based on current research was altered to create a novel method for sensing microwave magnetic fields with unprecedented sensitivities of the order of $\text{pT}/\sqrt{\text{Hz}}$. The ground work for sensing pulsed magnetic fields was also laid out in order expand upon potential applications for such a magnetometer.

Once the scheme for sensing magnetic fields using trapped ions was outlined, work towards adapting the current ion trap architecture for quantum sensing was conducted. The result of this was a novel, micro-fabricated ion trap capable of trapping up to 42 ions that could be theoretically imaged on a single charge-coupled device (CCD) camera. Demonstration of this would give a sensitivity improvement of $1/\sqrt{42}$.

Following this, a table top demonstrator device was constructed in order to demonstrate the trapped ion sensor capabilities. This included the ultra-high vacuum (UHV) system, laser setup, RF and DC electric fields for trapping ions, ion imaging setup, radiation sources for manipulating the hyperfine states of the ion and a master computer control setup. The ion imaging setup was developed to image multiple ions across a 1.018×1.018 mm surface with a $2 \mu\text{m}$ resolution. The computer control implements an Advanced Real-Time Infrastructure for Quantum physics (ARTIQ) system developed by M-Labs in order to perform fast experimental protocols.

Once the demonstrator device was operational, trapping parameters were optimised followed by initial experiments to characterise the system and a demonstration of the magnetometer capabilities for a single ion. Initial trapping of $^{174}\text{Yb}^+$ ions allowed for optimisation of the systems laser alignment, collection optics alignment and micro-motion

compensation. This was followed by trapping of $^{171}\text{Yb}^+$ ions in which laser and microwave field polarisation and Doppler cooling laser intensity could be optimised. Initial experiments involved performing frequency scans, Rabi oscillations and Ramsey T_2^* and T_2 coherence time measurements on the bare atomic states within the hyperfine ground state of $^{171}\text{Yb}^+$. This allowed for dressed state measurements of the dressed state transition frequencies, Rabi oscillations, and coherence time to be performed. The data from these dressed state measurements were used to calculate the sensitivity of the trapped ion system and the theoretically achievable sensitivity of this system. The best attained sensitivity for $\omega_{rf}/2\pi = 15.6161$ MHz was 125.860 pT/ $\sqrt{\text{Hz}}$ and for $\omega_{\mu w}/2\pi = 12.6584639$ GHz was 102.054 pT/ $\sqrt{\text{Hz}}$.

During the course of this thesis, efforts towards developing a portable concept and miniaturised components for a portable trapped ion system were made. This involved the development of a miniaturised, RF resonator that could be used for radial confinement of ions in Paul traps. The maximum peak voltage demonstrated for the resonant circuit was 114.9 V at a frequency of $\Omega/2\pi = 12.65$ MHz and a Q of ≈ 70 .

7.2 Future work

The demonstrator device developed during the course of this thesis has the potential to demonstrate further trapped ion magnetometer capabilities. The next step is to measure RF and microwave magnetic fields using multiple ions in a string as described in Sec. 2.2.6. This can be done on the micro-fabricated chip currently in the system, or it could be demonstrated on the dual linear rail chip described in Sec. 3.3 as this chip would eventually need to be placed in the system. From this, RF and microwave magnetic field gradient measurements would be conducted on the dual rail linear chip by trapping ions on separate trapping zones as described in Sec. 3.3.1.

Additional work on the demonstrator device can be performed with applications in mind. Pulsed magnetic field magnetometry would be demonstrated to show Nuclear quadrupole resonance (NQR) and nuclear magnetic resonance (NMR) imaging capabilities (Sec. 2.3). This would be further expanded upon by using a NQR or NMR sample located near the trapped ion magnetometer instead of a pulse generated by the direct digital synthesizer (DDS) board described in Sec. 4.5. Vector field magnetometry would also be demonstrated as described in Sec. 1.3.

Finally, the development of miniaturised trapped ion experiment components is required in order to make a portable trapped ion magnetometer. This involved the miniaturisation of all of the components outlined in chapter 4. Together, these efforts over the coming years could result in a state of the art trapped ion magnetometer capable of outperforming other quantum magnetometers across numerous benchmarks.

References

- [1] D. Delpy, J. Pritchard, and S. Till. Uk quantum technology landscape 2016. <http://uknqt.epsrc.ac.uk/files/ukquantumtechnologylandscape2016/>, (2016). DSTL/PUB098369.
- [2] K. Bongs and M. Turner. Annual report. <https://www.quantumsensors.org/wp-content/uploads/2017/08/qt-hub-annual-report-2015-2016-web.pdf>, (2016).
- [3] S. F. Huelga, C. Macchiavello, T. Pellizzari, A. K. Ekert, M. B. Plenio, and J. I. Cirac. Improvement of frequency standards with quantum entanglement. *Phys. Rev. Lett.*, 79(3865), 1997.
- [4] R. D. Dobrzański, J. Kolodyński, and M. Gută. The elusive heisenberg limit in quantum-enhanced metrology. *Nature Communications*, 3(1063), 2012.
- [5] B. M. Escher, R. L. de Matos Filho, and L. Davidovich. General framework for estimating the ultimate precision limit in noisy quantum-enhanced metrology. *Nature Physics*, 7(406-411), 2011.
- [6] L. T. Hall, C. D. Hill, J. H. Cole, and L. C. L. Hollenberg. Ultrasensitive diamond magnetometry using optimal dynamic decoupling. *Phys. Rev. B*, 82(045208), 2010.
- [7] G. Balasubramanian, I. Y. Chan, R. Kolesov, M. Al-Hmoud, J. Tisler, C. Shin, C. Kim, A. Wojcik, P. R. Hemmer, A. Krueger, T. Hanke, A. Leitenstorfer, R. Bratschitsch, F. Jelezko, and J. Wrachtrup. Nanoscale imaging magnetometry with diamond spins under ambient conditions. *Nature*, 455(648-652), 2008.
- [8] L. M. Pham nad N. Bar-Gill, C. Belthangady, D. Le Sage, P. Cappellaro, M. D. Lukin, A. Yacoby, and R. L. Walsworth. Enhanced solid-state multispin metrology using dynamical decoupling. *Phys. Rev. B*, 86(045214), 2012.
- [9] S. Kotler, N. Akerman, Y. Glickman, A. Keselman, and R. Ozeri. Single-ion quantum lock-in amplifier. *Nature*, 473(61-65), 2011.
- [10] M. Hirose, C. D. Aiello, and P. Cappellaro. Continuous dynamical decoupling magnetometry. *Phys. Rev. A*, 86(062320), 2012.
- [11] C. D. Aiello, M. Hirose, and P. Cappellaro. Composite-pulse magnetometry with a solid-state quantum sensor. *Nature Communications*, 4(1419), 2013.
- [12] P. Appel, M. Ganzhorn, E. Neu, and P. Maletinsky. Nanoscale microwave imaging with a single electron spin in diamond. *New J. Phys.*, 17(112001), 2015.

- [13] P. Wang, Z. Yuan¹, P. Huang, X. Rong, M. Wang, X. Xu¹, C. Duan¹, C. Ju¹, F. Shi¹, and J. Du¹. High-resolution vector microwave magnetometry based on solid-state spins in diamond. *Nature Communications*, 6(6631), 2015.
- [14] J. R. Maze, P. L. Stanwix, J. S. Hodges, S. Hong, J. M. Taylor, P. Cappellaro, L. Jiang, M. V. Gurudev Dutt, E. Togan, A. S. Zibrov, A. Yacoby, R. L. Walsworth, and M. D. Lukin. Nanoscale magnetic sensing with an individual electronic spin in diamond. *Nature*, 455(644-647), 2008.
- [15] G. de Lange, V. V. Dobrovitski D. Risté, and R. Hanson. Single-spin magnetometry with multipulse sensing sequences. *Phys. Rev. Lett.*, 106(080802), 2011.
- [16] K. Fang, V. M. Acosta, C. Santori, Z. Huang, K. M. Itoh, H. Watanabe, S. Shikata, and R. G. Beausoleil. High-sensitivity magnetometry based on quantum beats in diamond nitrogen-vacancy centers. *Phys. Rev. Lett.*, 110(130802), 2013.
- [17] J. M. Taylor, P. Capellaro, L. Childress, L. Jiang, D. Budker, P. R. Hemmer, A. Yacoby, R. Walsworth, and M. D. Lukin. High-sensitivity diamond magnetometer with nanoscale resolution. *Nature Physics*, 4(810-816), 2008.
- [18] I. M. Savukov, S. J. Seltzer, and M. V. Romalis. Tunable atomic magnetometer for detection of radio-frequency magnetic fields. *Phys. Rev. Lett.*, 95(063004), 2005.
- [19] I. M. Savukov and M. V. Romalis. Nmr detection with an atomic magnetometer. *Phys. Rev. Lett.*, 94(123001), 2005.
- [20] I. K. Kominis, T. W. Kornack, J. C. Allred, and M. V. Romalis. A subfemtotesla multichannel atomic magnetometer. *Nature*, 422(596-599), 2003.
- [21] I. M. Savukov, S. J. Seltzer, and M. V. Romalis. Detection of nmr signals with a radio-frequency atomic magnetometer. *Journal of Magnetic Resonance*, 185(214-220), 2007.
- [22] S. K. Lee, K. L. Sauer, S. J. Seltzer, O. Alem, and M. V. Romalis. Subfemtotesla radio-frequency atomic magnetometer for detection of nuclear quadrupole resonance. *Appl. Phys. Lett.*, 89(214106), 2006.
- [23] A. Horsley and P. Treutlein. Frequency-tunable microwave field detection in an atomic vapor cell. *Appl. Phys. Lett.*, 108(211102), 2016.
- [24] M. Koschorreck, M. Napolitano, B. Dubost, and M. W. Mitchell. High resolution magnetic vector-field imaging with cold atomic ensembles. *Appl. Phys. Lett.*, 98(074101), 2011.
- [25] N. Behbood, F. Martin Ciurana, G. Colangelo, M. Napolitano, M. W. Mitchell, and R. J. Sewell. Real-time vector field tracking with a cold-atom magnetometer. *Appl. Phys. Lett.*, 102(173504), 2013.

- [26] V. V. Yashchuk, J. Granwehr, D. F. Kimball, S. M. Rochester, A. H. Trabesinger, J. T. Urban, D. Budker, and A. Pines. Hyperpolarized xenon nuclear spins detected by optical atomic magnetometry. *Phys. Rev. Lett.*, 93(160801), 2004.
- [27] The spin exchange relaxation free (serf) magnetometer. <http://physics.princeton.edu/romalis/magnetometer/>. Accessed: 30-07-19.
- [28] R. C. Jaklevic, J. Lambe, A. H. Silver, and J. E. Mercereau. Quantum interference effects in josephson tunneling. *Phys. Rev. Lett.*, 12(159), 1964.
- [29] S. N. Ern e, H. D. Hahlbohm, and H. L ubbig. Theory of rf-biased superconducting quantum interference device for nonhysteretic regime. *J. Appl. Phys.*, 47(5440), 1976.
- [30] H. C. Seton, J. M. S. Hutchinson, and D. M. Bussell. A tuned squid amplifier for mri based on a doit flux locked loop. *IEEE Transactions on Applied Superconductivity*, 7(3213-3216), 1997.
- [31] D. Drung, C. Abmann, J. Beyer, A. Kirste, M. Peters, F. Ruede, and Th. Schurig. Highly sensitive and easy-to-use squid sensors. *IEEE Transactions on Applied Superconductivity*, 17(699-704), 2007.
- [32] T. Sch onau, V. Zakosarenko, M. Schmelz, R. Stolz, S. Anders, S. Linzen, M. Meyer, and H. G. Meyer. A three-axis squid-based absolute vector magnetometer. *Rev. Sci. Instrum.*, 86(105002), 2015.
- [33] Jorge Berger Omri J. Sharon, Avner Shaulov and Amos Sharoni. Current-induced squid behavior of superconducting nb nano-rings. *Scientific Reports*, 6(28320), 2016.
- [34] I. Baumgart, J.-M. Cai, A. Retzker, M. B. Plenio, and Ch. Wunderlich. Ultrasensitive magnetometer using a single atom. *Phys. Rev. Lett.*, 116(240801), 2016.
- [35] J. Accardo and M. A. Chaudhry. Radiation exposure and privacy concerns surrounding full-body scanners in airports, 2014.
- [36] L. Wang, H. Peng, and J. Ma. Microwave breast imaging techniques and measurement systems, 2017.
- [37] A. H. Nizamani, J. J. McLoughlin, and W. K. Hensinger. Doppler-free yb spectroscopy with fluorescence spot technique. *Phys. Rev. A*, 82(043408), 2010.
- [38] P. T. H. Fisk, M. J. Sellars, M. A. Lawn, and C. Coles. Accurate measurement of the 12.6 ghz-“clock” transition in trapped $^{171}\text{yb}^+$ ions. *IEEE Trans. Ultrason. Ferroelectr. Freq. Control*, 44(344-354), 1997.

- [39] P. Taylor, M. Roberts, S. V. Gateva-Kostova, R. B. M. Clarke, G. P. Barwood, W. R. C. Rowley, and P. Gill. Investigation of the $^2s_{1/2} - ^2d_{5/2}$ clock transition in a single ytterbium ion. *Phys. Rev. A*, 56(2699-2704), 1997.
- [40] S. M. Olmschenk. *Quantum Teleportation Between Distant Matter Qubits*. Ph. d. thesis, University of Michigan, 2009.
- [41] G. Breit and I. I. Rabi. Measurement of nuclear spin. *Phys. Rev.*, 38(2082), 1931.
- [42] J. Randall. *High-Fidelity Entanglement of Trapped Ions using Long-Wavelength Radiation*. Ph. d. thesis, Imperial College London, 2016.
- [43] N. Timoney, I. Baumgart, M. Johanning, A. F. Varon, M. B. Plenio, A. Retzker, and Ch. Wunderlich. Quantum gates and memory using microwave-dressed states. *Nature*, 476(185–188), 2011.
- [44] S. C. Webster, S. Weidt, K. Lake, J. J. McLoughlin, and W. K. Hensinger. Simple manipulation of a microwave dressed-state ion qubit. *Phys. Rev. Lett.*, 111(140501), 2013.
- [45] M. P. Fewell, B. W. Shore, and K. Bergmann. Coherent population transfer among three states: Full algebraic solutions and the relevance of non adiabatic processes to transfer by delayed pulses. *Aust. J. Phys.*, 50(281-308), 1997.
- [46] W. M. Itano, J. C. Bergquist, J. J. Bollinger, J. M. Gilligan, D. J. Heinzen, F. L. Moore, M. G. Raizen, and D. J. Wineland. Quantum projection noise: Population fluctuations in two-level systems. *Phys. Rev. A*, 47(5), 1993.
- [47] A. E. Webb, S. C. Webster, S. Collingbourne, D. Breaud, A. M. Lawrence, S. Weidt, F. Mintert, and W. K. Hensinger. Resilient entangling gates for trapped ions. *arXiv:1805.07351v1*, 2018.
- [48] W. L. Ma and R. B. Liu. Proposal for quantum sensing based on two-dimensional dynamical decoupling: Nmr correlation spectroscopy of single molecules. *Phys. Rev. App.*, 6(054012), 2016.
- [49] M. H. Levitt and R. Freeman. Compensation for pulse imperfections in nmr spin-echo experiments. *J. of Magnetic Resonance*, 43(65-80), 1981.
- [50] J. Zopes, K. Sasaki, K. S. Cujia, J. M. Boss, K. Chang, T. F. Segawa, K. M. Itoh, and C. L. Degen. High-resolution quantum sensing with shaped control pulses. *Phys. Rev. Lett.*, 119(260501), 2017.
- [51] T. N. Rudakov, V. T. Mikhaltsevich, and O. P. Selchikhin. The use of multi-pulse nuclear quadrupole resonance techniques for the detection of explosives containing rdx. *J. Phys. D*, 30(1377-1382), 1997.

- [52] S. D. Somasundaram, A. Jakobsson, J. A. S. Smith, and K. Althoefer. Exploiting spin echo decay in the detection of nuclear quadrupole resonance signals. *IEEE Transactions on Geoscience and Remote Sensing*, 45(925-933), 2007.
- [53] J. P. Yesinowski, M. L. Buess, and A. N. Garroway. Detection of ^{14}N and ^{35}Cl in cocaine base and hydrochloride using nqr, nmr, and squid techniques. *Anal. Chem.*, 67(2256-2263), 1995.
- [54] X. Zhang, N. Schemm, S. Balkir, and M. W. Hoffman. A low-power compact nqr based explosive detection system. *IEEE Sens. J.*, 14(497-507), 2014.
- [55] K. Włdkiewicz. Laser linewidth effects in intensity correlations in resonance fluorescence. *Phys. Lett. A*, 77(315-317), 1980.
- [56] A. Abragam. *Principles of Nuclear Magnetism*. Oxford University Press, 1961.
- [57] M. J. Duer. *Introduction to Solid-State NMR Spectroscopy*. Blackwell Publishing, 2004.
- [58] Z. P. Liang and P. C. Lauterbur. *Principles of Magnetic Resonance Imaging*. NY: IEEE Press, 2000.
- [59] J. A. S. Smith. Nuclear quadrupole resonance spectroscopy. general principles. *J. of Chemical Education*, 48(39), 1971.
- [60] E. Gudmundson. *Signal Processing for Spectroscopic Applications*. Ph. d. thesis, Uppsala University, 2010.
- [61] A. Jakobsson, M. Mossberg, M. D. Rowe, and J. A. S. Smith. Exploiting temperature dependency in the detection of nqr signals. *IEEE Trans. on Signal Processing*, 54(1610-1616), 2006.
- [62] W. Paul, O. Osberghaus, and E. Fischer. Ein ionenkäfig. *Forschungsberichte des Wirtschafts- und Verkehrsministeriums Nordrhein-Westfalen*, 415, 1958.
- [63] H. G. Dehmelt. Radiofrequency spectroscopy of stored ions i: storage. *Adv. At. Mol. Phys.*, 3(53), 1967.
- [64] S. Earnshaw. On the nature of the molecular forces which regulate the constitution of the luminiferous ether. *Trans. Camb. Phil. Soc.*, 7(97-112), 1842.
- [65] M. D. Hughes, B. Lekitsch, J. A. Broersma, and W. K. Hensinger. Microfabricated ion traps. *Cont. Phys.*, 52(505), 2011.
- [66] D. J. Wineland, C. Monroe, W. M. Itano, D. Leibfried, B. E. King, and D. M. Meekhof. Experimental issues in coherent quantum-state manipulation of trapped atomic ions. *J. Res. Nat. Inst. Stand. Tech.*, 103(259-328), 1998.

- [67] J. J. McLoughlin, A. H. Nizamani, J. D. Siverns, R. C. Sterling, M. D. Hughes, B. Lekitsch, B. Stein, S. Weidt, and W. K. Hensinger. Versatile ytterbium ion trap experiment for operation of scalable ion-trap chips with motional heating and transition-frequency measurements. *Phys. Rev. A*, 83(013406), 2011.
- [68] S. M. Olmschenk. *Quantum teleportation between distant matter qubits*. Ph. d. thesis, University of Michigan, 2009.
- [69] D. Gerlich. *Inhomogeneous RF Fields: A Versatile Tool for the Study of Processes with Slow Ions*. John Wiley and Sons, Inc., 2007.
- [70] M. J. Madsen, W. K. Hensinger, D. Stick, J. A. Rabchuk, and C. Monroe. Planar ion trap geometry for microfabrication. *Appl. Phys. B*, 78(639-651), 2004.
- [71] W. Paul. Electromagnetic traps for charged and neutral particles. *Rev. Mod. Phys.*, 62(531-540), 1990.
- [72] C. Donald. *Development of an ion trap quantum information processor*. Ph. d. thesis, University of Oxford, 2000.
- [73] M. Abramowitz and I. Stegun. *Handbook of Mathematical Functions*. Dover Publications, New York, 1964.
- [74] M. G. House. Analytic model for electrostatic fields in surface-electrode ion traps. *Phys. Rev. A*, 78(033402), 2008.
- [75] J. H. Wesenberg. Electrostatics of surface-electrode ion traps. *Phys. Rev. A*, 78(063410), 2008.
- [76] D. Hucul, M. Yeo, W. K. Hensinger, J. Rabchuk, S. Olmschenk, and C. Monroe. On the transport of atomic ions in linear and multidimensional ion trap arrays. *Quant. Inf. Comp.*, 8(501-578), 2008.
- [77] J. M. Amini, H. Uys, J. H. Wesenberg, S. Seidelin, J. J. Bollinger, J. Britton, D. Leibfried, C. Ospelkaus, A. P. VanDevender, and D. J. Wineland. Toward scalable ion traps for quantum information processing. *New J. Phys.*, 12(033031), 2010.
- [78] A. Nizamani and W. Hensinger. Optimum electrode configurations for fast ion separation in microfabricated surface ion traps. *Appl. Phys. B*, 106(327-338), 2012.
- [79] P. Fitzpatrick. *Advanced Calculus: A Course in Mathematical Analysis*. PWS Publishing Company, 1996.
- [80] R. B. Blakestad, C. Ospelkaus, A. P. VanDevender, J. H. Wesenberg, D. Leibfried, M. J. Biercuk, and D. J. Wineland. Near-ground-state transport of trapped-ion qubits through a multidimensional array. *Phys. Rev. A*, 84(032314), 2011.

- [81] J. Mikosch, U. Fruhling, S. Trippel, D. Schwalm, M. Weidemuller, and R. Wester. Evaporation of buffer-gas-thermalized anions out of a multipole rf ion trap. *Phys. Rev. Lett.*, 98(223001), 2007.
- [82] D. Gerlich. *Inhomogeneous RF Fields: A Versatile Tool for the Study of Processes with Slow Ions*. John Wiley and Sons, Inc., 2007.
- [83] A. Drakoudis, M. Sollner, and G. Werth. Instabilities of ion motion in a linear paul trap. *Int. J. Mass Spectrom.*, 252(61-68), 2006.
- [84] Y. S. Liao, S. W. Chyuan, and J. T. Chen. Fem versus bem. *IEEE Circuits Devices Mag.*, 20(25-34), 2004.
- [85] K. Singer, U. Poschinger, M. Murphy, P. Ivanov, F. Ziesel, T. Calarco, and F. Schmidt-Kaler. Colloquium: Trapped ions as quantum bits: Essential numerical tools. *Rev. Mod. Phys.*, 82(2609-2632), 2010.
- [86] M. Drewsen, I. S. Jensen, N. Kjaergaard, J. Lindballe, A. Mortensen, and K. Molhave. Non-stationary coulomb crystals in linear paul traps. *J. Phys. B*, 36(525-532), 2003.
- [87] L. L. Yan, W. Wan, L. Chen, F. Zhou, S. J. Gong, X. Tong, and M. Feng. Exploring structural phase transitions of ion crystals. *Nat. Sci. Rep.*, 6(21547), 2016.
- [88] D. F. V. James. Quantum dynamics of cold trapped ions with application to quantum computation. *Appl. Phys. B*, 66(181-190), 1998.
- [89] B. Lekitsch. *Development of Microfabricated Ion Traps for Scalable Microwave Quantum Technology*. Ph. d. thesis, University of Sussex, 2013.
- [90] L. Deslauriers, S. Olmschenk, D. Stick, W. K. Hensinger, J. Sterk, and C. Monroe. Scaling and suppression of anomalous heating in ion traps. *Phys. Rev. Lett.*, 97(103007), 2006.
- [91] D. Wineland, C. Monroe, W. Itano, B. King, D. Leibfried, D. Meekhof, C. Myatt, and C. Wood. Experimental primer on the trapped ion quantum computer. *Fortschr. Phys.*, 46(363-390), 1998.
- [92] Q. A. Turchette, D. Kielpinski, B. E. King, D. Leibfried, D. M. Meekhof, C. J. Myatt, M. A. Rowe, C. A. Sackett, C. S. Wood, W. M. Itano, C. Monroe, and D. J. Wineland. Heating of trapped ions from the quantum ground state. *Phys. Rev. A*, 61(063418), 2000.
- [93] M. Li¹, W. H. Li¹ and J. Zhang¹, G. Alici, and W. Wen. A review of microfabrication techniques and dielectrophoretic microdevices for particle manipulation and separation. *J. Phys. D*, 47(6), 2014.

- [94] Ligo vacuum compatible materials list. dcc.ligo.org/E960050/public. Accessed: 04-07-18.
- [95] D. F. Murgia. *Microchip ion traps with high magnetic field gradients for microwave quantum logic*. Ph. d. thesis, University of Sussex, 2017.
- [96] F. A. Shaikh. *Monolithic microfabricated ion trap for quantum information processing*. Ph. d. thesis, Georgia Institute of Technology, 2013.
- [97] E. D. Standing. *Design and fabrication of high magnetic field gradients towards fault tolerant two-qubit gates with trapped ions using long-wavelength radiation*. Ph. d. thesis, University of Sussex, 2016.
- [98] R. C. Sterling. *Ytterbium ion trapping and microfabrication of ion trap arrays*. Ph. d. thesis, University of Sussex, 2011.
- [99] S. Weidt. *Towards microwave based ion trap quantum technology*. Ph. d. thesis, University of Sussex, 2013.
- [100] J. D. Siversns. *Yb ion trap experimental set-up and two-dimensional ion trap surface array design towards analogue quantum simulations*. Ph. d. thesis, University of Sussex, 2011.
- [101] Annealed copper gaskets for cf flanges technical note. www.lesker.com/newweb/anges/angestechnicalnotesconat1.cfm. Accessed: 03-07-18.
- [102] T. Navickas. *Towards high-fidelity microwave driven multi-qubit gates on microfabricated surface ion traps*. Ph. d. thesis, University of Sussex, 2017.
- [103] Principles of spatial filters. https://www.thorlabs.com/newgrouppage9.cfm?objectgroup_id=1400. Accessed: 05-07-18.
- [104] J. D. Siversns, L. R. Simkins, S. Weidt, and W. K. Hensinger. On the application of radio frequency voltages to ion traps via helical resonators. *Appl. Phys. B*, 107(921-934), 2012.
- [105] K. G. Johnson, J. D. Wong-Campos, A. Restelli, B. Neyenhuis K. A. Landsman, J. Mizrahi, and C. Monroe. Active stabilization of ion trap radiofrequency potentials. *Rev. Sci. Instrum.*, 87(053110), 2016.
- [106] J. Simpson, J. Lane, C. Immer, and R. Youngquist. Simple analytic expressions for the magnetic field of a circular current loop, 2001.
- [107] Artiq 1.0. 10.5281/zenodo.51303. Accessed: 16-08-18.
- [108] D. J. Berkeland, J. D. Miller, J. C. Bergquist, W. M. Itano, and D. J. Wineland. Minimization of ion micromotion in a paul trap. *J. Appl. Phys.*, 83(10), 1998.

- [109] H. J. Metcalf and P. van der Straten. *Laser Cooling and Trapping*. Number 26-27. Springer, 1999.
- [110] J. H. Wesenberg, R. J. Epstein, D. Leibfried, R. B. Blakestad, J. Britton, J. P. Home, W. M. Itano, J. D. Jost, E. Knill, C. Langer, R. Ozeri, S. Seidelin, and D. J. Wineland. Fluorescence during doppler cooling of a single trapped atom. *Phys. Rev. A*, 76(053416), 2007.
- [111] K. Lake. *Yb ion trap experimental set-up and two-dimensional ion trap surface array design towards analogue quantum simulations*. Ph. d. thesis, University of Sussex, 2011.
- [112] R. Noek, G. Vrijsen, D. Gaultney, E. Mount, T. Kim, P. Maunz, and J. Kim. High speed, high fidelity detection of an atomic hyperfine qubit. *Opt. Lett.*, 38(4735–4738), 2013.
- [113] G. A. Alvarez, A. Ajoy, X. Peng, and D. Suter¹. Performance comparison of dynamical decoupling sequences for a qubit in a rapidly fluctuating spin bath. *Phys. Rev. A*, 82(042306), 2010.
- [114] J. Randall, S. Weidt, E. D. Standing, K. Lake, S. C. Webster, D. F. Murgia, T. Navickas, K. Roth, and W. K. Hensinger. Efficient preparation and detection of microwave dressed-state qubits and qutrits with trapped ions. *Phys. Rev. A*, 91(012322), 2015.
- [115] Analog devices high speed high voltage 1a output drive amplifier (ada4870) data sheet. <http://www.analog.com/media/en/technical-documentation/data-sheets/ADA4870.pdf>. Accessed: 30-07-18.
- [116] Y. Y. Jau, F. M. Benito, H. Partner, and P. D. Schwindt. Low power high-performance radio frequency oscillator for driving ion traps. *Rev. Sci. Instrum.*, 82(023118), 2011.
- [117] J. Randall, A. M. Lawrence, S. C. Webster, S. Weidt, N. V. Vitanov, and W. K. Hensinger. Generation of high-fidelity quantum control methods for multi-level systems. *arXiv:1708.02634v1*, 2017.
- [118] R. Barlow. Asymmetric errors. *arXiv:physics/0401042*, 2003.

Appendix

A Micro-fabricated chip numerical simulation meshes and mask

A.1 Numerical simulation meshes

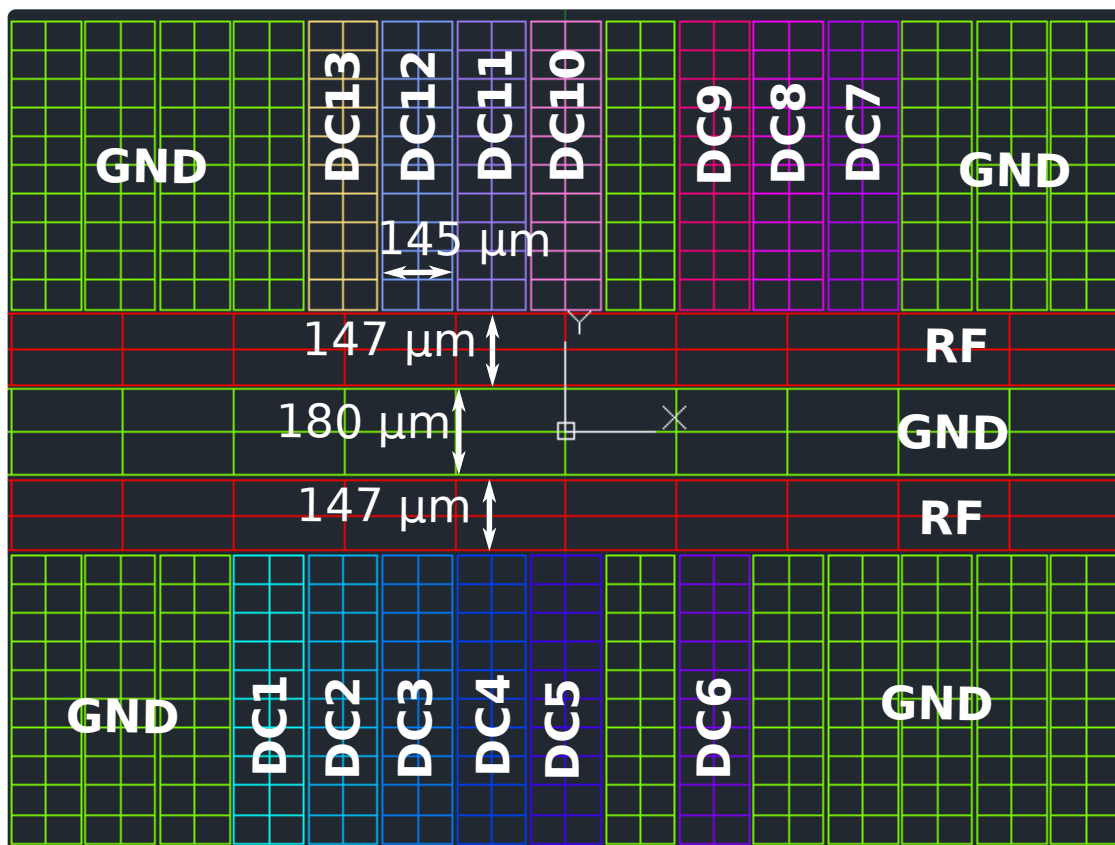


Fig. A.1 CAD file for dual linear chip design in Sec. 3.2.3, RF (red) ground (green) and DC electrode numbers and widths are labelled, all electrodes are separated by 10 μm . Grounded DC electrodes are due to disconnects that happened on the PCB after the baking process.

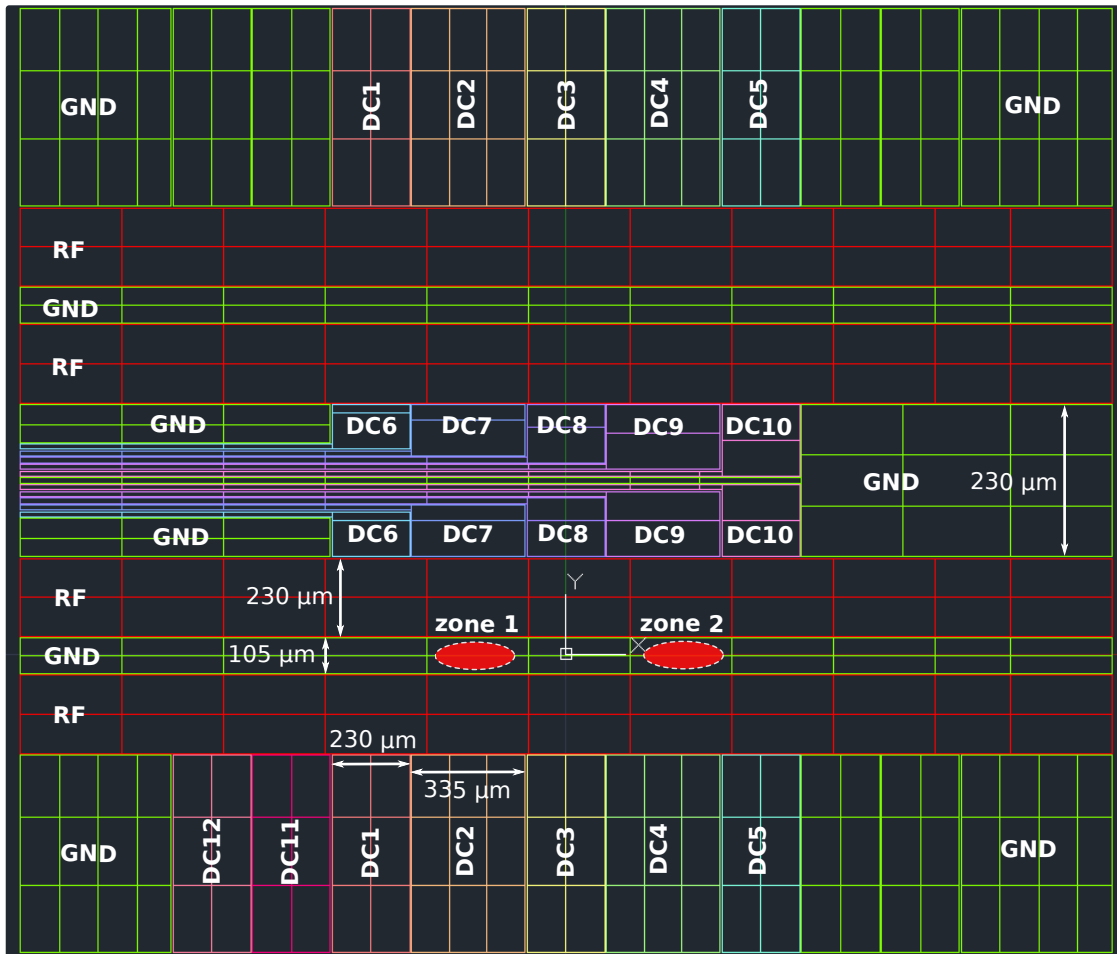


Fig. A.2 CAD file for simple linear chip design in Sec. 3.3.1, RF (red) ground (green) and DC electrode numbers and widths are labelled, all electrodes are separated by 5 μm, the thickness of the DC tracks on the inside of the two linear rails is 15 μm.

A.2 Mask design

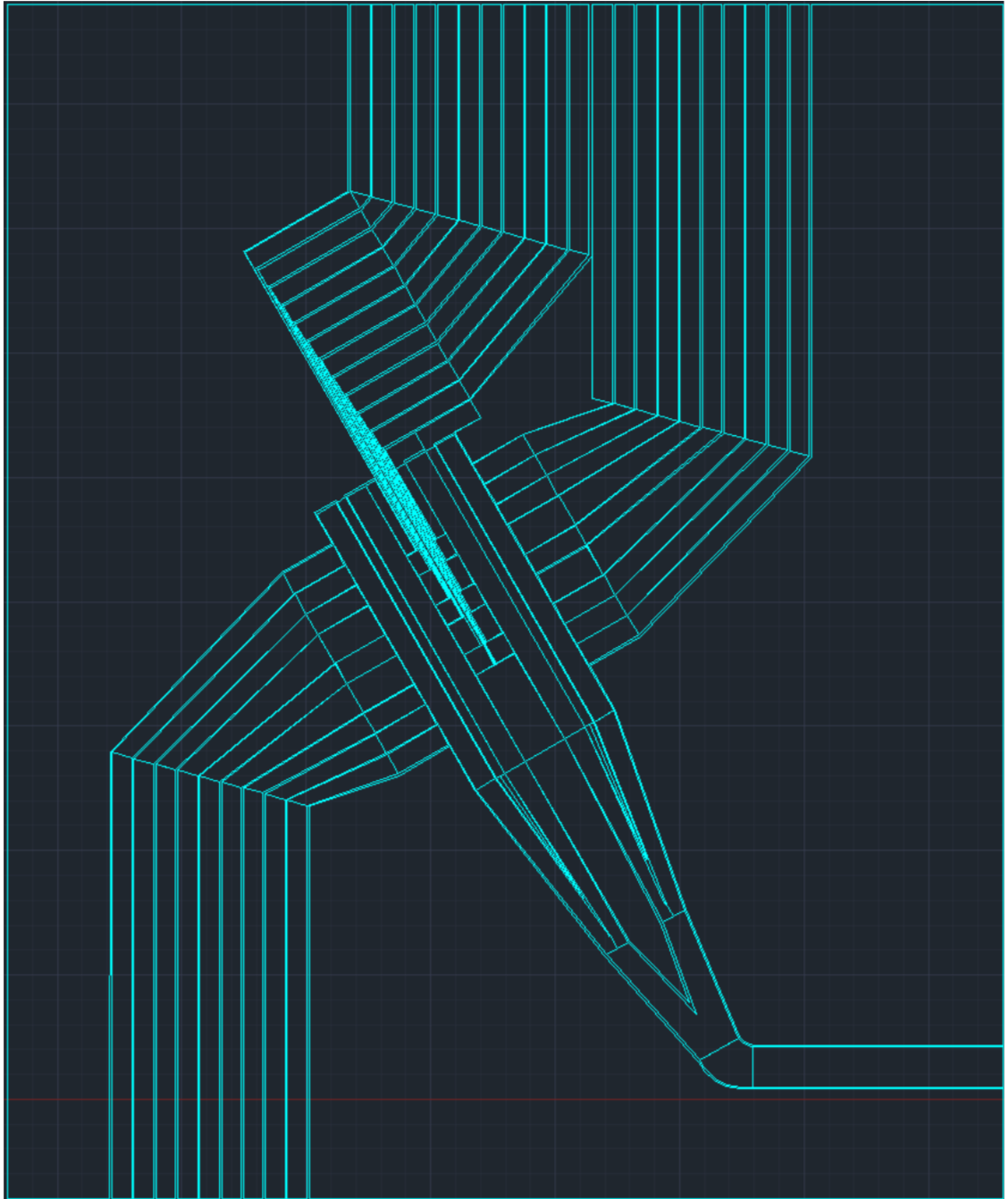


Fig. A.3 Dual Linear CAD design used for photo-lithography mask, chip design is 8×10 mm total size.

B Chip glow

Chip glow was a persistent issue for ion trap chip micro-fabrication, many chip batches fabricated by Weikang Fan exhibited an anomalous glow that made trapping on the dual linear sensor chip (Sec. 3.3) unattainable over the duration of this thesis. The latest fabrication outlined in Sec. 3.3.3 exhibited no glow, this process is identical to fabrication runs that did exhibit glow but was conducted in a different clean room facility. Because of this it is expected that the glow was due to an unknown chemical that was likely left in a dirty micro-fabrication machine. The glowing chips behaved as capacitors completing the resonant circuit and allowing large RF voltages to pass through them, but the glow caused a slow melting of the electrodes of many of the chips tested.

Examples of the melted electrodes can be seen in Fig. B.4, B.5 and B.6; note that this dual linear design deviates slightly from the one shown in Fig. 3.16 and A.3. The thin electrodes following the outside of the RF electrodes in B.5 and B.6 was intended for inducing a principal axis rotation. It was later confirmed from trapping on the simple linear chip design described in Sec. 3.2.3 that this is an unnecessary feature for trapping.

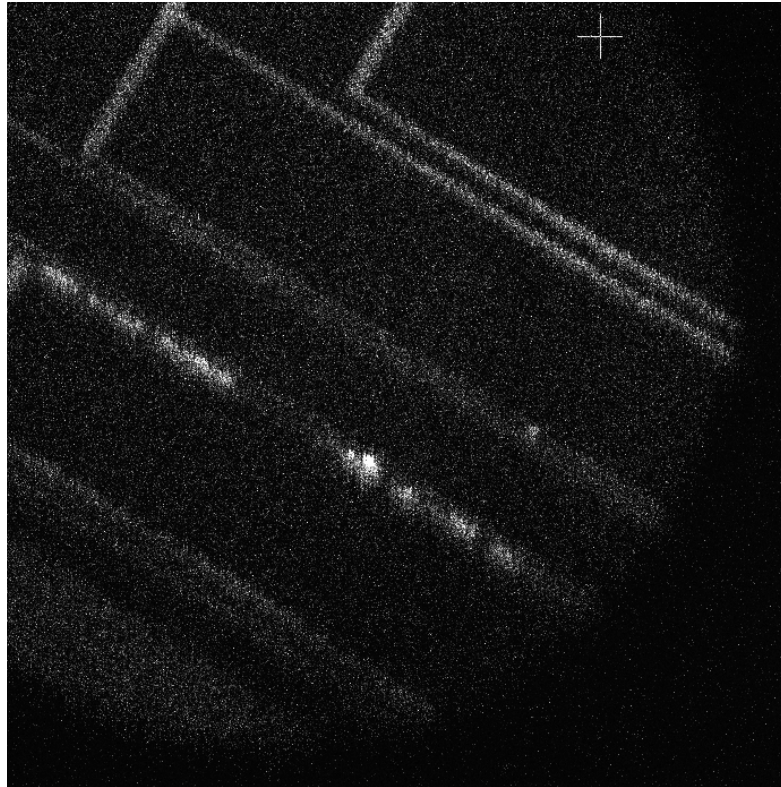


Fig. B.4 CCD camera image of the dual linear chip glowing with $V_{RF} = 200$ V applied at a trapping frequency of $\Omega/2\pi = 18.5$ MHz.

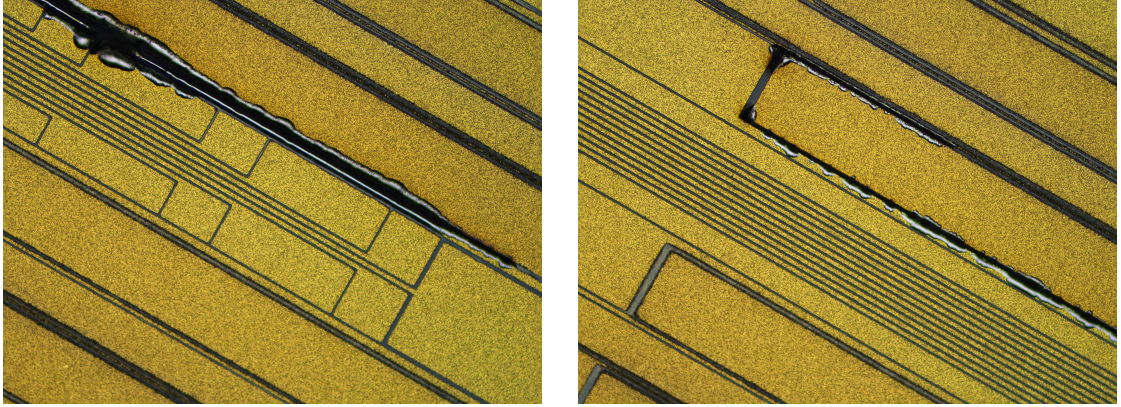


Fig. B.5 Dual linear chip electrodes outside the vacuum system after the glowing shown in Fig. B.4.

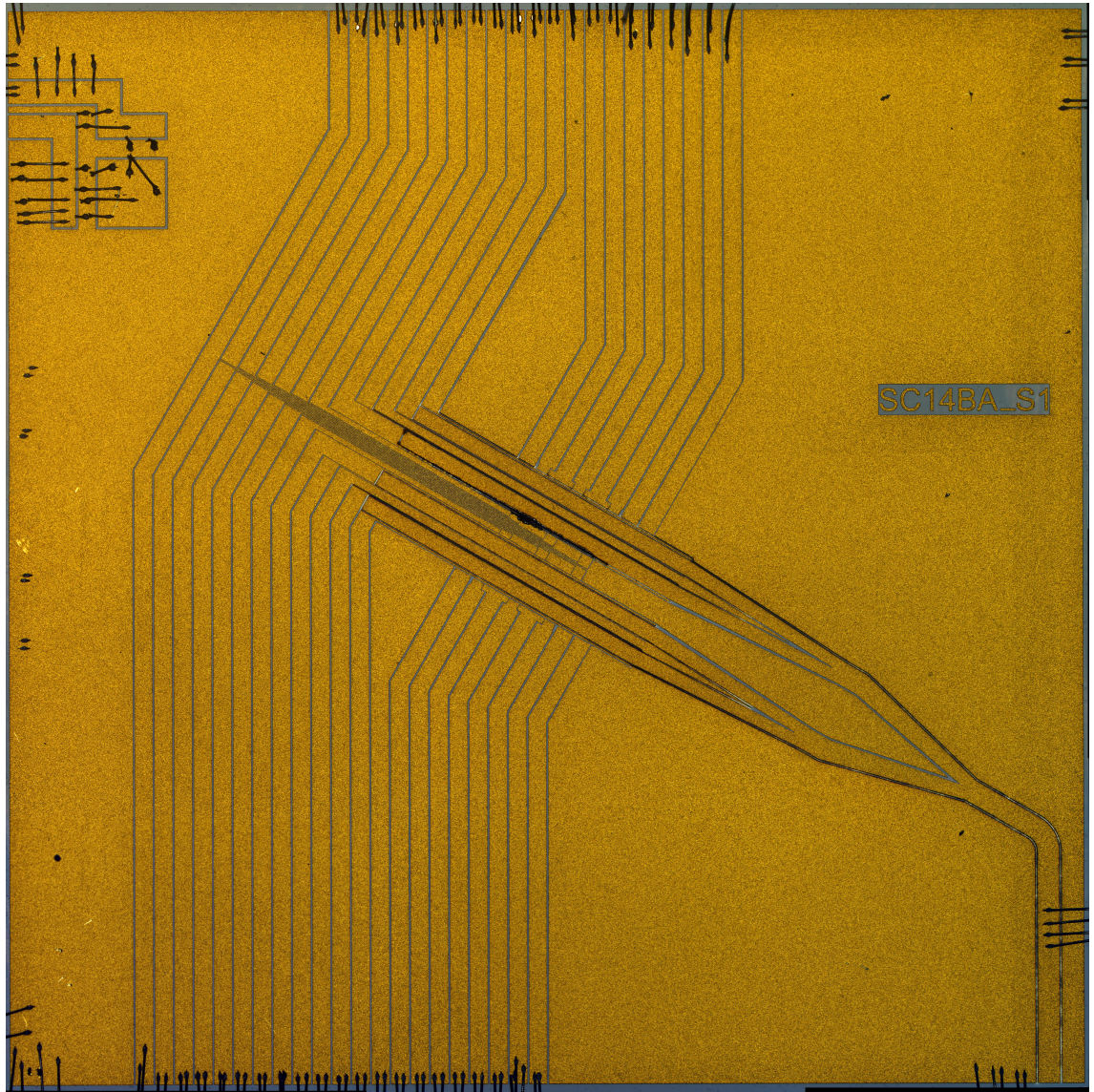


Fig. B.6 Entire dual linear chip electrodes outside the vacuum system after the glowing shown in Fig. B.4 had occurred.

Because of the major delays this caused it is advised that professional clean rooms of a high standard are utilised for chip fabrication.

C Workshop CAD designs

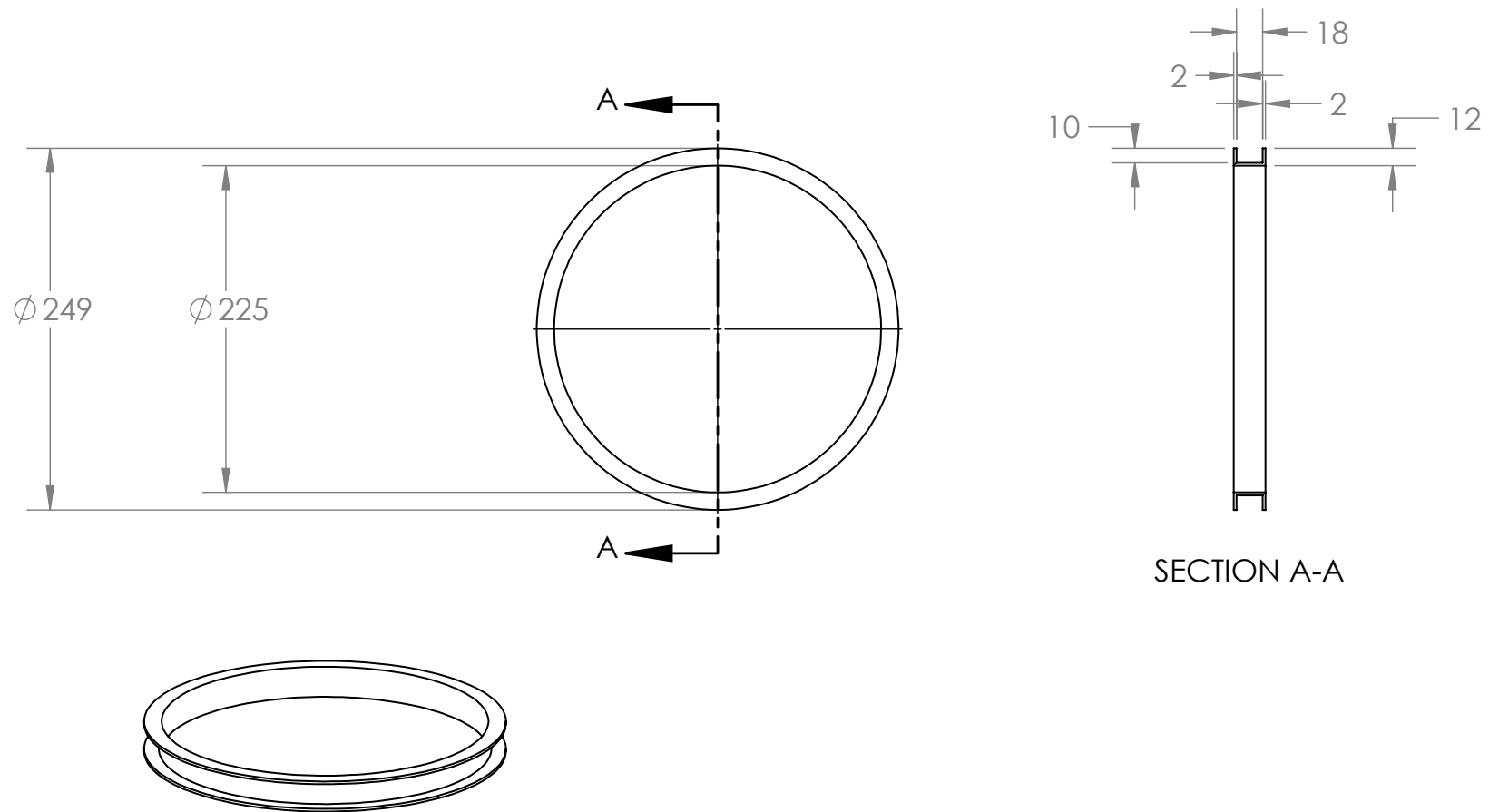


Fig. C.7 Single coil housing (Sec. 4.5.1) structure dimensions, units are in mm.

D Normalising detection errors

This appendix outlines two methods for normalising detection errors, the first uses an error matrix found from the conditional probabilities described in Sec. 5.2.1 to produce normalised population probabilities, along with a binomial distribution to calculate error bars on each measurement. The second uses a maximum log-likelihood method based on a binomial distribution to produce normalised population probabilities and errors alongside a fitted maximum log-likelihood function for any function fitted to the population measurements. The latter was chosen due to normalization and error calculation issues encountered in the former method.

D.1 Normalising detection errors conditional probabilities matrix

To normalise detection errors in this method, we take an error matrix constructed from the conditional probabilities described in 5.2.1 and use it to describe the relationship between measurement probabilities and state probabilities, given by

$$\begin{pmatrix} P(B) \\ P(D) \end{pmatrix} = \begin{pmatrix} P(B|1) & P(B|0) \\ P(D|0) & P(D|1) \end{pmatrix} \begin{pmatrix} P(1) \\ P(0) \end{pmatrix} = M_2 \begin{pmatrix} P(1) \\ P(0) \end{pmatrix}, \quad (\text{D.1})$$

where $P(B)$ and $P(D)$ are measurement probabilities, and $P(1)$ and $P(0)$ are state probabilities. From this the error matrix can be inverted to give the state probabilities

$$\begin{pmatrix} P(1) \\ P(0) \end{pmatrix} = M_2^{-1} \begin{pmatrix} P(B) \\ P(D) \end{pmatrix}. \quad (\text{D.2})$$

To translate this to experimental data points and their associated errors, we consider the measurement to be a Bernoulli trial with outcome $X \in \{B, D\}$. For N measurements, the probability to measure $X = B$; $P(B)$, can be estimated to be

$$P(B) = \frac{k}{N} \pm z \sqrt{\frac{P(B)[1 - P(B)]}{N}}, \quad (\text{D.3})$$

where k is the number of measurements with outcome B and z is approximately equal to 1 for a confidence interval of one standard deviation. The values of $P(B)$ and $P(D) = 1 - P(B)$ are then transformed using Eq. D.2 to find values of $P(1)$ and $P(0)$. Their associated errors represented by the \pm term in Eq. D.3 go under the same transformation to give errors to the probabilities $P(1)$ and $P(0)$. This is the typical procedure that has been used to normalise measurements and their detection errors, but this poses a few minor issues. Firstly, the error matrix M_2 doesn't always normalise probability measurements between 0 and 1, it could be argued that it's because the conditional probabilities within M_2 have changed due to some variable in the experiment changing, like the clock transition π time, or background photon count, or laser power drift etc. Though this could be true and the state detection experiment in Sec. 5.2.1 should be done periodically throughout the day to minimise these errors, this normally isn't the case as all the equipment that

could effect this is normally kept in a relatively stable state, this is observed by conducting multiple state detection experiments throughout the day. What's more likely is a statistical fluctuation, causing a $N = 100$ measurement to give $k = 100$ or $k = 0$ bright events, which would make the transformation in Eq. D.2 to output a value > 1 or < 0 .

This brings us to the second issue with this method, and that is the zero value errors that get produced when $P(B) = 0$ or 1 . If this were true, the currently established method for calculating sensitivities would output readings of zero as it is directly proportional to the population error. It would be expected to correspond to a fitted function value of 0 , which works in theory as described in Sec. 2.40; but in practice this is simply never this case, as the derivative of a fitted function almost always has a non-zero value when associated with said data point at given experimental time, unless the fitted function to the data is perfect at this measurement. For this reason, a maximum log-likelihood method has been implemented instead to give a more in depth understanding of the sensitivity of this system across all population measurements.

D.2 Normalising detection errors using maximum log-likelihood method

This method uses a maximum log-likelihood function based on a binomial probability distribution, similar to the one used in [117]. First, we can extract the probability to measure a bright event based on conditional probabilities extracted from the error matrix in the previous section, $p_B(p) = P(B|1)p + P(B|0)(1 - p)$ where p is the probability that the ion will be in the $F = 1$ manifold during readout. This is used in the binomial distribution for the maximum log-likelihood function, taking the form

$$f_B = \sum_{i=1}^{N_T} \log \left(\frac{N! p_B(p_i)^{k_i} (1 - p_B(p_i))^{N - k_i}}{k_i! (N - k_i)!} \right), \quad (\text{D.4})$$

where N is the number of repetitions per data point, N_T is the number of data points and k_i is the number of bright events for the i th data point. For individual data points, $N_T = 1$, allowing us calculate p_1 by maximizing f_B for k_1 . Errors for individual data points are then calculated by finding the two roots to the equation

$$\frac{f_B(p_1)}{f_B(p_1^{err})} = 0.5, \quad (\text{D.5})$$

where p_1^{err} has two non equal solutions, corresponding to $p_1 + \sigma^+$ where σ^+ is the error bar above than the most likely probability p_1 , and $p_1 - \sigma^-$ where σ^- is the error bar below the most likely probability p_1 . This finds approximately the 1 standard deviation point either side of the probability distribution.

There is a slight asymmetry of the function so a better understanding of the errors is needed when calculating the sensitivity. Due to the high fidelity readout of the state detection, asymmetries ($A = (\sigma^+ - \sigma^-)/(\sigma^+ + \sigma^-)$) are typically very low, making it a reasonable to take the mean of the two errors when calculating sensitivities $\Delta P =$

$(\sigma^+ + \sigma^-)/2$ [118]. It's worth noting the asymmetry of the population errors though when calculating sensitivities as it just gives more information about the system. This is introduced as a systematic error to the sensitivity calculation, this error is calculated from using the maximum and minimum errors σ^+ and σ^- in the sensitivity calculation to give the errors on sensitivity measurements.

For fitting functions to the data set, f_B is maximized for a given function of p_B across all N_T data points, the functions used are described in the results section of this thesis.